Asteroid Muon Tomography

A feasibility study on using galactic cosmic rays to map small Solar System body interiors.

Jules Antoine Reichert

January 2021

Master Thesis

Supervisor: Dr. A. Menicucci

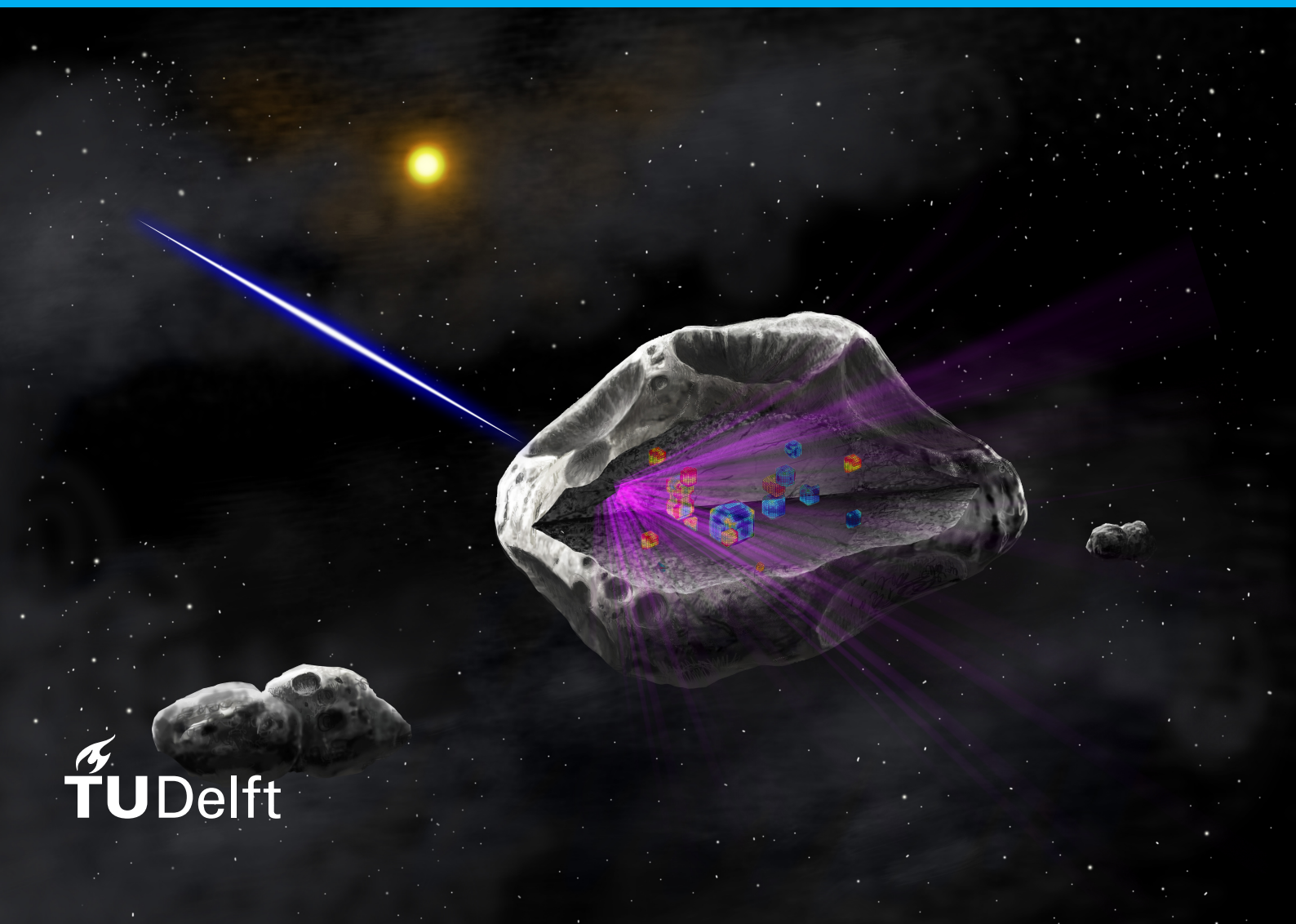

TU Delft

Asteroid Muon Tomography

A feasibility study on using galactic cosmic rays to map small Solar System body interiors.

by

Jules Antoine Reichert

to obtain the degree of Master of Science
at the Delft University of Technology,
to be defended publicly on Friday January 15th.

Student number:	4163605	
Project duration:	February 13, 2020 – January 15, 2021	
Thesis committee:	Dr. A. Menicucci,	TU Delft, Supervisor
	Prof. Dr. E. K. A. Gill,	TU Delft, Committee Chair
	Dr. D. M. Stam,	TU Delft, Examiner

An electronic version of this thesis is available at `http://repository.tudelft.nl/`.
Cover image: Artist rendition of asteroid Sylvia. (Credit original: Danielle Futselaar/SETI Institute; Adapted with permission.)

TU Delft Delft University of Technology

Preface

The first time I was presented the idea of applying muon tomography in space was during a course on planetary sciences back in 2017. My *curiosity* was peaked by the concept, even more so through the enthusiasm of our then supervisor Dr. Alessandra Menicucci. A little less then a year ago I got the *opportunity* to re-kindle this collaboration, by taking on the challenge of proving the feasibility of this technology as my Master Thesis. The concluding thesis for the Entrepreneurship Annotation allowed me to demonstrate the business opportunities of this technology, which formed an interesting tangent to this research.
With many hurdles on the way, I had to take on the role as a real *pathfinder* to avoid the obstacles put in place by the onset of the COVID-19 pandemic. I am grateful that I never lost my *spirit* during this endeavour, seeing as this project required *perseverance* to the very conclusion of it.

First of all, I would like to express my gratitude to Prof. Dr. E.K.A. Gill and Dr. D.M. Stam as members of my thesis assessment committee for taking the time to read my report and attend my defence. Similarly, want to thank Dr. L. Hartmann and Ir. J.A. Melkert for their supervision and assessment of the entrepreneurial addendum to this thesis.
Words fail to describe the love and support I received from family and friends over the course of this project. I would like to thank all my friends for the awesome time: restoring an oldtimer campervan with my cousin Gijs, backpacking through Asia with Floris, as well as the amazing student-life we enjoyed. I want to thank my sister Antoinette and my brothers Renier, Jurriaan and Marnix for being there for me. I sincerely thank my parents Louis and Elizabeth, who supported me my entire life and are always there when I need them. I especially want to thank my girlfriend Maaike, not only for the vital life-support she provided me in the final stages of this project, but for the countless fruitful discussions on the topic of particle physics as well.
Last but not least I wish to thank Dr. Alessandra Menicucci for her inspiring enthusiasm in the field of science, which helped me bring this project to its successful conclusion.

Jules Reichert
Nijmegen, January 2021

Abstract

The aim of this thesis to explore the feasibility of using a hodoscope muon detector system in a space environment to map the interior of asteroids.
Small Solar System bodies, a group where asteroids and comets belong to, are thought to provide a geological snapshot of the early Solar System, as their composition is largely unaltered by planet formation processes. No strategy has thus far succeeded in characterising their interior structure and composition from direct measurements. Knowledge on these interior properties could prove invaluable to the field of planetary sciences, planetary defence and in-situ resource utilisation. Muon tomography can fill this knowledge gap from measurements of the muon flux leaving the asteroid's surface.
Muons are charged elementary particles, two-hundred times more massive than their electron siblings, enabling them to traverse much larger amounts of solid matter. Measuring the alterations to this muon flux allows one to deduce the properties of the traversed material. On Earth, muons are generated continuously from collisions of galactic cosmic rays with the tenuous upper atmosphere. The muon production rate on airless bodies however is poorly characterised and thought to be very low. The available muon flux to the instrument is therefore unknown, but plays a pivotal role in the feasibility assessment.
The core research performed for this feasibility study therefore aims to characterise this radiation environment in the vicinity of asteroids. Numerical simulations were executed with *Geant4*, a software toolkit using Monte Carlo methods to simulate the passage of particles through matter [3]. Regarding the inputs of the simulations: extensive use was made of the numerical computing environment *MATLAB* [152] to create the three-dimensional asteroid and comet models, and the galactic cosmic ray flux model was created with ESA's Space Environment Information System (SPENVIS) [69][105].
Most asteroids with a $> 120m$ diameter are rubble-piles [184]: agglomerates of porous rocks and regolith. These rocks are found to be best modelled as tri-axial ellipsoids of 1:0.7:0.5 (Length:Width:Height) with a size-frequency distribution having a power-index of -3.5 ± 0.1. The coma surrounding outgassing comets interacts with the cosmic ray flux, positively affecting the muon production. The time-variable properties of this coma are hard to characterise and model.
Most of the simulations were performed on a ten meter diameter spherical asteroid with a variable interior structure and a composition similar to *25143 Itokawa*. The muon flux exiting the surface was found to be $1.2 m^{-2} s^{-1}$, resulting from the proton component of the full galactic cosmic ray flux. Including the smaller helium ion component leads to a 35% increase of this flux, to $1.62 m^{-2} s^{-1}$. It was possible to locate the asteroid's high-contrast interior features from these simulation results using straight track fitting. Simulations with a pure muon source resulted in sufficient data to empirically reconstruct these features in three-dimensional space using filtered back-projection tomography. Simulation of full size realistic asteroid models for a mission's duration requires vast amounts of high performance computing hardware.
It was deemed unfeasible within the scope of the project to perform particle experiments to aid the validation of the simulation results. As no real-world data is available on the muon flux near asteroids, the research outcome was validated with simulation results by T.H. Prettyman [187].
For asteroids in the $120m \sim 500m$ diameter range the available muon flux is shown to be large enough to distinguish different density regions in the interior, with a strong preference towards the lower end of this range. Due to their lower density and their coma's positive effect on muon production, this upper diameter limit is higher for comets. The preferred location and orientation for the hodoscope instrument are found to be close to the surface, aimed along the body's minor axis. Therefore, it is suggested to integrate the envisioned instrument on a lander-type spacecraft, preferably with hopping or roving capabilities. For sparse muon data, straight track fitting is found to be the preferred reconstruction method. Based on these results it was concluded that an extraterrestrial application of muography to map small Solar System bodies is ultimately feasible.

Contents

List of Figures

List of Tables

List of Symbols

Symbol	Description	Value	Unit
α	Spectral Index	–	$[-]$
β	Relativistic Velocity	–	$[-]$
γ	Lorentz Factor	–	$[-]$
θ	Scattering Angle	–	$[rad]$
θ	Elevation	–	$[rad]$
$\angle\theta$	Elevation	–	$[rad]$
Θ	Cherenkov Wave-Front Angle	–	$[deg]$
μ	Muon	–	$[-]$
ν	Neutrino	–	$[-]$
π	Pion	–	$[-]$
ρ	Density	–	$[kg/m^3]$
ρ_b	Bulk Density	–	$[kg/m^3]$
ρ_{bm}	Meteorite Bulk Density	–	$[kg/m^3]$
ρ_g	Grain Density	–	$[kg/m^3]$
ρ_p	Density of Primary	–	$[kg/m^3]$
ρ_s	Density of Satellite	–	$[kg/m^3]$
ϱ	Opacity	–	$[g/cm^2]$
σ	Standard Deviation	–	$[-]$
σ^2	Variance	–	$[-]$
τ	Mean Life	–	$[s]$
τ	Tau	–	$[-]$
ϕ	Porosity	–	[%]
ϕ	Azimuth	–	$[rad]$
$\angle\phi$	Azimuth	–	$[rad]$
Φ	Macro-Porosity	–	[%]
ω	Spin Rate	–	$[rad/s]$
ω_c	Critical Spin Rate	–	$[rad/s]$
a	Acceleration	–	$[m/s^2]$
a_c	Centrifugal Acceleration	–	$[m/s^2]$
a_g	Gravitational Acceleration	–	$[m/s^2]$
a_R	Roche Limit	–	$[m]$
A	Atomic Mass Number	–	$[-]$
AU	Astronomical Unit	$1.495978707 \cdot 10^{11}$	$[m]$
c	Speed of Light	299,792,458	$[m/s]$
d	Day	86,400	$[s]$
D	Diameter	–	$[m]$
e	Electron	–	$[-]$

Continued on next page

Continued from previous page

Symbol	Description	Value	Unit
eV	Electron-volt	$1.602176634 \cdot 10^{-19}$	$[J]$
E	Energy	–	$[eV]$
E_0	Rest Energy	–	$[eV]$
E_k	Kinetic Energy	–	$[eV]$
ΔE_W	Most Probable Energy Loss	–	$[eV]$
G	Gravitational Constant	$6.67408 \cdot 10^{-11}$	$[m^3 kg^{-1} s^{-2}]$
h	Hour	3,600	$[s]$
j	Flux	–	$[N/(m^2 s)]$
K	Kaon	–	$[-]$
l	Unit Path Length	–	$[cm]$
L	Path Length	–	$[cm]$
L_0	Radiation Length	–	$[cm]$
m	Mass	–	$[eV/c^2]$
m	Mass	–	$[kg]$
min	Minutes	60	$[s]$
m_0	Rest Mass	–	$[eV/c^2]$
M_b	Bulk Mass	–	$[kg]$
n	Refractive Index	–	$[-]$
n	Number of Samples	–	$[-]$
N	Number of Atoms	–	$[-]$
N	Number of Atoms per Volume	–	$[V^{-1}]$
p	Momentum	–	$[eV/c]$
r	Distance from SSSB Center	–	$[m]$
r	Radial Distance	–	$[m]$
$rand$	Pseudorandom Number Generator Output	$[0-1]$	$[-]$
$Rate$	Rate	–	$[day^{-1}]$
R_p	Radius of Primary	–	$[m]$
s	Sample Standard Deviation	–	$[-]$
s^2	Sample Variance	–	$[-]$
t	Time	–	$[s]$
t	Student's t-test	–	$[-]$
T	Kinetic Energy	–	$[eV]$
v	Velocity	–	$[m/s]$
v_p	Particle Velocity	–	$[m/s]$
v_{ph}	Phase Velocity	–	$[m/s]$
V_b	Bulk Volume	–	$[m^3]$
x	Distance Travelled	–	$[m]$
$\overline{\mathrm{X}}$	Sample Mean	–	$[-]$
yr	Year	31,556,952	$[s]$
Z	Atomic Number	–	$[-]$

List of Abbreviations

Abbreviation	Description
AIDA	Asteroid Impact & Deflection Assessment
AMICA	Asteroid Multi-band Imaging Camera
AMS	Alpha Magnetic Spectrometer
ASTORB	Asteroid Database
BIRA – IASB	Belgian Institute for Space Aeronomy
BNE	Brazil Nut Effect
BP	Back Projection
CAD	Computer-Aided Design
CBP	United States Customs and Border Protection
CERN	European Organization for Nuclear Research
CHAMP	Challenging Minisatellite Payload
CNEOS	Center for Near Earth Object Studies
COCA	Cost of Customer Acquisition
CONSERT	Comet Nucleus Sounding Experiment by Radiowave Transmission
COSIMA	Cometary Secondary Ion Mass Analyser
COTS	Commercial Off The Shelf
CPT	Charge-Parity-Time
CWMD	Countering Weapons of Mass Destruction Office
DART	Double Asteroid Redirection Test
DMU	Decision Making Unit
DONUT	Direct Observation of the Nu Tau
DSMC	Direct Monte Carlo Simulations
EAS	Extended Air Shower
ECAS	Eight-Color Asteroid Survey
ESA	European Space Agency
FBP	Filtered Back Projection
Fermilab	Fermi National Accelerator Laboratory
FOV	Field of View
GCR	Galactic Cosmic Ray
GDML	Geometry Description Markup Language
GECO	Geant4 Crystal Objects
GOCE	Gravity field and steady-state Ocean Circulation Explorer
GRACE	Gravity Recovery And Climate Experiment
GRACE – FO	Gravity Recovery And Climate Experiment - Follow-On
IAU	International Astronomical Union
ICQ	Implicitly Connected Quadrilateral
IDEX	Interstellar Dust Explorer

Continued on next page

Continued from previous page

Abbreviation	Description
IMAP	Interstellar Mapping and Acceleration Probe
IMPACT	Institute for Modeling Plasma, Atmospheres and Cosmic Dust
InSight	Interior Exploration using Seismic Investigations, Geodesy and Heat Transport
IR	Iterative Reconstruction
ITT	Invitation to Tender
KBO	Kuiper Belt Object
LASP	Laboratory for Atmospheric and Space Physics
LHC	Large Hadron Collider
LTV	Lifetime Value
MBSE	Model Based Systems Engineering
MIRO	Microwave Instrument for the Rosetta Orbiter
MT	Multi-Threaded mode
MVBP	Minimum Viable Business Product
NASA	National Aeronautics and Space Administration
NAVCAM	Navigation Camera
NDPF	Nikhef Data Processing Facility
NEA	Near Earth Asteroid
NEC	Near Earth Comet
NEO	Near Earth Object
NICM	NASA Instrument Cost Model
NIAC	NASA Institute for Advanced Concepts
NIKHEF	Dutch National Institute for Subatomic Physics
NIST	National Institute for Standards and Technology
NPR	NASA Procedural Requirements
NSI	NASA standard initiator
OSIRIS	Optical, Spectroscopic, and Infrared Remote Imaging System
OSIRIS – REx	Origins, Spectral Interpretation, Resource Identification, Security, Regolith Explorer
PDG	Particle Data Group
PDS	Planetary Data System
PHA	Potentially Hazardous Asteroid
PHO	Potentially Hazardous Object
PMT	Photo Multiplier Tube
ROI	Region of Interest
ROSINA	Rosetta Orbiter Spectrometer for Ion and Neutral Analysis
R_x	Receiver
SAMPEX	Solar Anomalous and Magnetospheric Particle Explorer
SDO	Scattered Disc Object
SDSD	Sloan Digital Sky Survey
SE	Systems Engineering
SEIS	Seismic Experiment for Interior Structure
SFD	Size-Frequency Distribution
SiPM	Silicon Photo Multiplier

Continued on next page

Continued from previous page

Abbreviation	Description
SPAD	Single-Photon Avalanche Diodes
SPENVIS	SPace ENVironment Information System
SPH	Smooth Particle Hydrodynamics
STS	Space Transportation System
STScI	Space Telescope Science Institute
SMASS	Small Main-Belt Asteroid Spectroscopic Survey
SMBAS	Subaru Main Belt Asteroid Survey
SSSB	Small Solar System Body
SUDA	Surface Dust Analyser
TAM	Total Addressable Market
TBR	To Be Resolved
TNO	Trans-Neptunian Object
T_x	Transmitter
USGS	United States Geological Survey
XML	Extensible Markup Language
YORP	Yarkovsky-O'Keefe-Radzievsky-Paddack

1 Introduction

Asteroids and comets are the primordial remnants of the birth of our Solar System. Their composition is thought to be largely unaltered over the past billions of years. Because of this, they provide geological snapshot of what the early Solar System might have looked like. To research these mysterious space bodies, mankind is launching an increasing number of space probes to image, measure, and scan their exterior. However, no interior scans have been made to fully map these objects' structures and compositions. One of the more promising methods to accomplish this feat revolves around the use of the already present muon particle flux caused by galactic cosmic radiation. Although similar technology has been put to use on Earth, no Solar System body has ever been scanned utilising such technology. This report therefore seeks to answer the question: what is the feasibility of using muons to map small Solar System body interiors?

1.1. Problem Description

In order to better understand the problem this thesis project aims to solve, it is often helpful to discover its origin and heritage.

Historical Background

Ever since the discovery of X-rays in 1895 by Wilhelm Röntgen, mankind has been expending their capabilities of using radiation to image the interior features of an object that are otherwise invisible to the naked eye. Today, scanners and detectors are used all over the world in the field of science, medicine, border security and many more. The various detectors use a plethora of different radiation types to scan objects, such as photons, protons and in a more niche application: muons.

Muons can be considered the quantum siblings of electrons. They share a lot of properties, in that they are both members of the lepton family, they both hold a charge and both are influenced by the same fundamental forces. Muons are however short lived and have a mass approximately 200 times larger than their electron counterparts. This mass increase allows them to travel through much more material as compared to electrons, which makes them much more suitable for radiography purposes.

Muons were first theorised as a particle in 1935 [238] and discovered a year later. It was quickly found that the ever present cosmic radiation on Earth's surface consists of quite a lot of these muons, with around 10,000 passing through a square metre every minute [30]. The first civil application of cosmic radiation took place in 1955 when muon radiography, or "muography" for short, was used by E.P. George to measure to overburden above a tunnel in the Snowy Mountains region of Australia [91]. The muon flux produced by cosmic ray collisions with Earth's atmosphere was found to be suitable to map structures and features in very large objects, such as volcanoes [215][149], the ancient pyramids [165], shipping containers [93][166] and even nuclear reactors [162][163]. Muon tomography has seemingly only once been applied in space, when the AMS-01 experiment aboard Space Shuttle *Discovery* was used to image the *Mir* space station in 1998, during the STS-91 mission [2].

In 2014, T.H. Prettyman submitted his NASA Innovative Advanced Concepts report "Deep mapping of small solar system bodies with galactic cosmic ray secondary particle showers." [186]. In this report, he postulates the feasibility of using the muons produced in secondary cosmic ray showers to infer interior features of small Solar System bodies. This work forms the inspiration and part of the foundation for this thesis. His recommendations for future work include, among other things, the creation of interior reconstruction methods

and their subsequent application to different data acquisition scenarios, to demonstrate that interior structure can be determined from muon measurements. Knowledge on the internal features and composition of these ancient space bodies could not only prove invaluable to our understanding of the Solar System, but to fields like planetary defence, asteroid mining and in-situ resource utilisation as well.

Problems
Similar to the well known CT-scan often used in hospitals, the concept of muon tomography is to infer an object's interior structure by measuring its effect on the particle flux passing through it, from multiple directions. Combining these measurements in a process called "tomography", the three dimensional features can be resolved from two dimensional images.
With the large muon flux on Earth's surface, multiple applications of muon tomography have been proven to be successful in resolving these structure. However, contrary to what one might think, there are practically no muons present in space. This is due to the fact that the muons are created in Earth's upper atmosphere, where primary cosmic rays often consisting of protons and alpha particles collide with gas molecules producing so-called cosmic ray showers. These showers consist of a plethora of particle species, most of which quickly decay or collide in the lower atmosphere. As muons travelling at a velocity close to the speed of light easily reach the surface, they are the most abundant surviving compound of these showers.
This is where the biggest problem for muon tomography in space originates. Without an atmosphere present to produce these muons in cosmic ray collisions, there are none to detect. Prettyman et al. (2014) [186] showed with simulations that the direct collision of cosmic ray particles with an asteroid's surface would still produce muons, although a few orders of magnitude less than produced in a tenuous medium.
Very little is known on the interaction of asteroid regolith with cosmic rays, and the simulations performed to date are in stark disagreement [186][125][109]. No in-situ measurements of the muon flux around small space bodies have been performed to date and recreating the local conditions in a physical test setup on Earth is very difficult. As the amount of muons to detect is unanimously thought to be very small, the actual number could prove to be pivotal for the feasibility of such an instrument. Additionally, no interior reconstruction methods have been applied to these simulation results, something that could aid proving the feasibility as well as showcase its capabilities.

1.2. Research Objective

In order to perform effective and focused research, it is vital to accurately describe its goal and therefore limit its scope to the subjects that will aid in the completion of the research objective. The main goal of this thesis project is formulated as follows:

> the main goal of this research is to show the feasibility of using a hodoscopic muon detector system in a space environment to tomographically map the interior of small Solar System bodies, by and proving its conceptual feasibility with simulations and using a systems engineering approach to discover relevant system constraints.

One sub-goal is to create high-level constraints and requirements for the muon detecting scientific package and space mission needed to perform its goal. The possibility of integrating the package on a cubesat platform is explored as well. A source imposing these requirements will be the simulation results of the passage of particles through a created 3D model representative of an asteroid.
Another sub-goal is to demonstrate the conceptual feasibility of asteroid muon tomography by using simulation results to reconstruct the asteroid model's interior.
In order to reach these goals, a set of research questions is formulated.

1.2.1. Research Questions

1. Which methods and techniques can be used to model small Solar System bodies for accurate particle transmission simulations?
   (a) What are the interior characteristics of asteroids and comets?
   (b) Which simplifications can be made to the model to increase performance with minimal loss of accuracy?
   (c) What are the characteristics of a comet's coma that are relevant to muon tomography?
2. How can the radiation environment responsible for muon production around small Solar System bodies be simulated?

   (a) Which simplifications can be made to simulation parameters to increase performance with minimal loss of accuracy?
   (b) What are the properties of the muon flux through a small Solar System body?
      i. How are the characteristics of the muon flux altered by various aspects of the small Solar System body interior?

3. How can the interior characteristics of a small Solar System body be reconstructed from muographic measurements?
   (a) Which current algorithms and techniques are best fit to reconstruct the interior of a muographically mapped small Solar System body?
   (b) Can the interior characteristics of an asteroid model be reconstructed from particle transmission simulation results?

4. Which constraints and requirements imposed by muon tomography are put on key design aspects of a space mission to a small Solar System body?
   (a) What type and size of small Solar System bodies are best suited to tomographically map using a hodoscopic muon instrument?
   (b) What instrument characteristics are required to fulfil a small Solar System body muon tomography mission?
   (c) What are the differences in performance between the application of a micro- or nanosatellite platform, versus a conventional spacecraft platform?

Ultimately, answering all these research questions will allow for a conclusion to be drawn on the main subject of the entire thesis project: The feasibility of Asteroid Muon Tomography.

1.3. Report Structure

Similar to the structure of this introduction, the report starts with the description of some background theory in chapter 2. The aim of this chapter is not only to provide some background information on the problem at hand, but it is also meant to bridge the gap from the field of space engineering to that of particle physics. This is followed by the asteroid modelling chapter 3, in which the process of creating an accurate 3D model of a small Solar System body for particle passage simulations is treated in detail. This is subsequently followed by the simulation chapter 4, where the setup and results of particle simulations with the before mentioned asteroid models are described. Additionally, this chapter treats the various reconstruction methods available, and applies them to the simulation results. Chapter 5 shows the assumptions and constraints necessary for a muon tomography mission design process. This "Top Level Requirements" chapter aims to show the feasibility of such a mission by applying the results to a few case studies and defining requirements. The next chapter 6 contains the verification and validation process run through during this thesis project. As is often the case with these types of feasibility studies, full validation of the results was not possible as constructing a prototype was not possible within the scope of the project. The next chapter 7, called "Business Plan", forms a tangent in a different field of study to this project. It describes the possible application of muon tomography technology in a business setting, such as a high-tech start-up. Although it displays some interesting findings on bringing space technology to market, it is to be considered as a separate addendum chapter, not to be included for the formal grading of this project. Its content is therefore marked with a blue banner on the top of each page. The report concludes with chapter 8, where the findings of the performed research are discussed, conclusions are drawn and recommendations for future work are made.

2

Background Theory

This chapter aims to provide an overview of the scientific background theory on which the research in this thesis project is based. The discussed literature formed part of the framework from which the rest of the literature research in this report arose. The first section treats the subject for the envisioned muon tomography: the small Solar System bodies. This is followed by section 2.2 on the involved particle and radiation physics for galactic cosmic rays. Additionally, this section provides a figurative stepping stone for readers not accustomed the field of particle physics, in order to better understand the problem at hand. The chapter concludes with section 2.3 on particle detection methods, focusing on the detection of muons.

2.1. Small Solar System Bodies

In order to start developing new scientific research technology, one first needs to know what the object or phenomenon of interest is. A survey on some proposed targets for this hodoscopic muon detector, small Solar System bodies (SSSB), is presented in this chapter. The classification and grouping schemes for small Solar System bodies will first be clarified, including a few paragraphs on physical SSSB properties and their origins. This is followed by an explanation of the interest in their respective interiors and compositions. The section continues with three case studies into possible mission targets. The section concludes with a few alternative proposed methods for SSSB interior mapping.

2.1.1. Classification based on Orbital Elements

Our understanding of the Solar System continuously evolves, as more and more discoveries of Solar System bodies are made. The more knowledge of the Solar System is gained, the more precise definitions of the objects within it are needed to classify them. One of the more recent changes of definition caused international uproar, as the International Astronomical Union (IAU) decided in 2006 by resolution B5 [115] and B6 [116] that Pluto would no longer be classified as the ninth planet, but as a dwarf planet. One of the reasons astronomers decided to change this definition was the then recent discoveries of more Pluto-like Trans-Neptunian Objects (TNO) such as Eris, Makemake and Haumea. As Eris is more massive than Pluto, it was initially considered to be the tenth planet, until the IAU redrew the definition. Ceres, the largest asteroid in the main asteroid belt, also fits the criteria for a dwarf planet.
This demonstrates the importance of clear definitions, and the definition changes new discoveries can cause. As SSSBs are many orders of magnitude smaller (making them harder to detect) and more abundant than planets or dwarf planets, their discoveries really accelerated in number with the advances of technology. The discoveries of Near-Earth Asteroids (NEA) alone has boomed in the past years, as visible in figure 2.1[78]. In this section a written overview of the current classification of SSSBs and their orbits is presented. This overview in table-form is shown in appendix A.
According to the IAU, all of the objects in the Solar System, except satellites and the Sun, can be put into 3 major categories: planets, dwarf planets and Small Solar System Bodies[78]. In short: every object in the Solar System that is not a star, planet, dwarf planet or satellite is called a Small Solar System Body (SSSB). This group of SSSBs encompasses the classical groups of comets, asteroids and meteoroids. Of these bodies, all that show a visible atmosphere or coma caused by outgassing of volatile ices when warmed by the Sun, are called comets. Of the rest, every object bigger than 1m diameter is called an asteroid, with the remainder

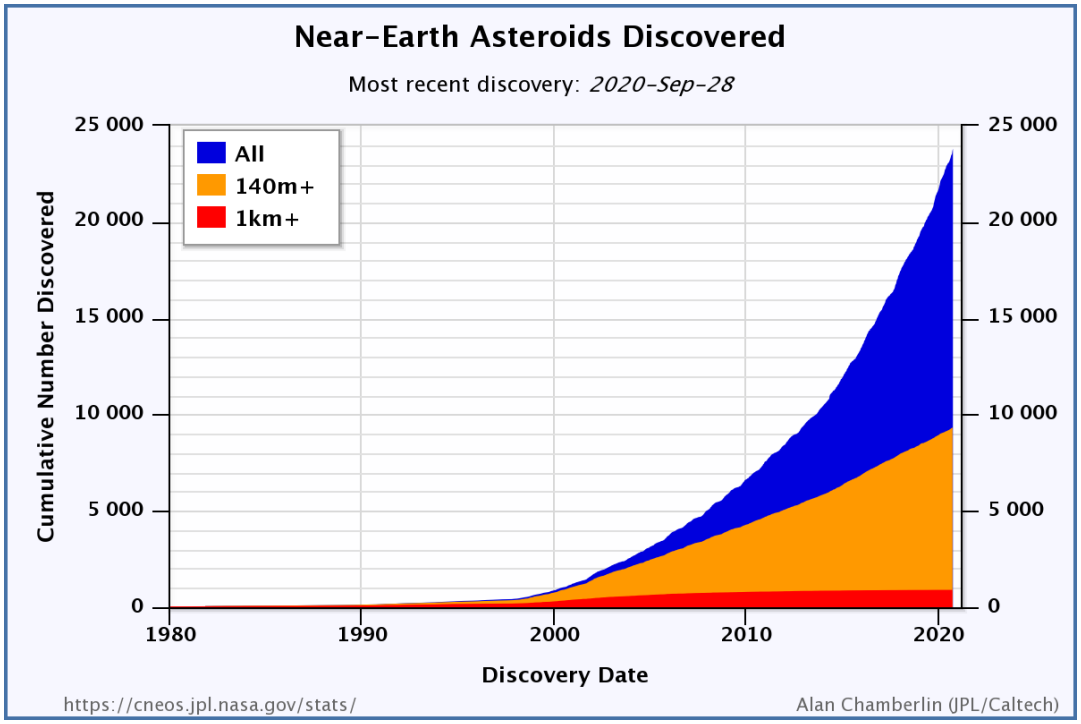

Figure 2.1: The cumulative number of known Near-Earth Asteroids (NEAs) versus time. From the Center for Near Earth Object Studies (CNEOS) [78].

being are called meteoroids. Often the word asteroid is used collectively to describe all types of SSSB, even though technically comets and meteoroids should not be called asteroid. Comets are usually found with highly elliptical orbits, allowing them to outgas only when close to the Sun. As comets can lose their volatiles after multiple perihelia, they may stop to produce a coma and will therefore evolve to be asteroids or meteoroids [183].
The asteroids, comets and meteoroids tend to live in specific locations and in specific orbits within the Solar System, and can be categorised accordingly.

Inner Solar System
The first groups to consider are located within the inner Solar System, shown in figure 2.2[156]. Even though some of these SSSB groups are not entirely located within Jupiter's orbit, they are still classified as belonging to the inner Solar System. The biggest of these groups is the Main Asteroid Belt, comprising the SSSBs that have an orbit between Mars and Jupiter, shown as white dots. A subgroup of this are the Hildas, shown in orange, which have a 3:2 resonance with Jupiter's orbit. Their orbit's aphelion is located in one of Jupiter's Lagrange points; L3, L4 or L5. The Hildas together show a triangular formation in the figure, co-rotating with Jupiter.
Another group of SSSBs co-rotates with Jupiter, called the Trojans and the Greeks, shown in green. They are not considered to be a part of the Main Asteroid Belt. These Trojans orbit in the L5 Lagrange point of Jupiter, trailing the gas giant, whilst the Greeks lead Jupiter's orbit in the L4 Lagrange point. In general, all asteroids located in Lagrange point L4 or L5 of any planet are called Trojans. Even the Greeks of Jupiter are called Trojans in some literature. Earth has one discovered Trojan as well, but Jupiter has by far the most.
The last group of inner Solar System SSSBs are the Near Earth Objects (NEO), often called Near Earth Asteroids (NEA). Their orbits bring them close to the Earth or its orbit, causing them to be a potential threat. The larger ones that cross Earth's orbit, with a diameter $> 140m$ [78], are called potentially hazardous objects (PHO). The NEOs have 5 subgroups, one of which are the Near Earth Comets (NEC) and the rest is sorted according to their orbits, as seen in figure 2.3. The orbits in this figure are mere examples to characterise the different groups. In reality, very little of these NEOs share the same orbit. The most numerous, comprising around 55% of the total number of discovered NEAs (as seen in figure 2.1), are the Apollos. Their perihelion lies within $1\,AU$ (Astronomical Unit), causing them to cross with Earth's obit. They differ from the Atens by having a semi-major axis larger than Earth's. The Atens comprise around 7.5% of the total number. As they cross Earth's

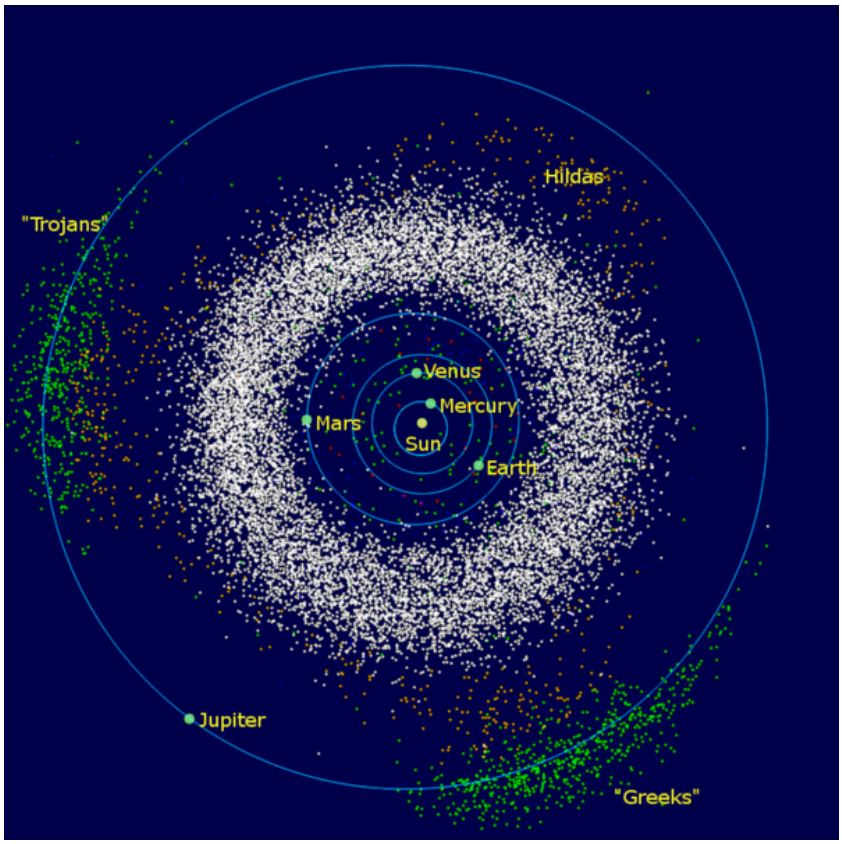

Figure 2.2: The asteroid groups and planets of the inner Solar System, including Jupiter. Main Belt Asteroids shown in white. Modified, from “Wikimedia Commons,” by Mdf, 2006[156]. Original from "Asteroid (and Comet) Groups" by P. Scheirich, 2005 [202]. Adapted with permission.

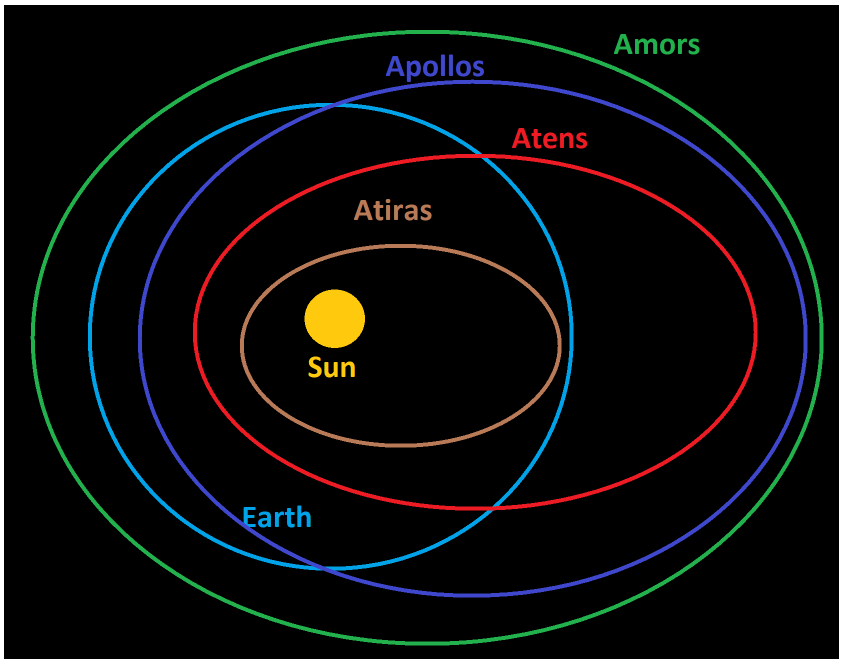

Figure 2.3: Schematic example of the orbits of Amors, Apollos, Atens and Atiras. (Own Work)

orbit as well, they form, together with the Apollos, the majority of the PHOs. The second biggest group with around 37% of the total are the Amors with their orbits entirely outside Earth's. The smallest group are the Atiras of which currently only 23 are discovered, which is even less than the NECs, of which 111 are found[78].

Outer Solar System and Beyond

The SSSBs of the outer Solar System are sorted according to their orbits as well. The Trojans of the the gas giants (apart from Jupiter) are one of these groups. A rather large group is called the Centaurs, which have at least a part of their orbit within the orbit of Neptune. As they cross one or multiple orbits of the giant planets, they tend to have unstable orbits.

Objects with an orbital radius on average larger than Neptune's are called Trans-Neptunian Objects (TNO) and lie in the trans-Neptunian region. The well-known Kuiper Belt contains TNOs, which are called Kuiper Belt Objects (KBO). The Kuiper Belt is doughnut-shaped and extends from around 30AU to 50AU from the sun. The objects within the belt can be split into two main groups: The classical KBOs and the resonant KBOs. The classical KBOs orbit unimpeded and uncontrolled by Neptune, and do not cross its orbit. The resonant KBOs do show resonance with Neptune and are grouped according to their resonance period. The $1:1$ resonance group are called Neptune's Trojans. The other named group are the Plutinos, which are named after dwarf planet Pluto and have a $2:3$ resonance with Neptune. Beyond the orbit of the KBOs there are another few families of SSSBs. The objects whose orbits are affected by Neptune, but are not in resonance, are named the Scattered Disc Objects (SDO). They have unstable and often eccentric and inclined orbits. The final group is located in a region called the Oort Cloud. This area is past the heliosphere and therefore classified as interstellar space. Objects within the Oort Cloud have never been observed directly, but its existence is theorised as an explanation for the origin and high inclination of long period and non-periodic comets. The Oort Cloud is thought to start at around $1000-2000AU$ from the Sun and extend all the way to around $100,000-200,000AU$, as is visible in figure 2.4. Because the objects within this cloud orbit so far from the Sun, they are thought to be icy SSSBs.

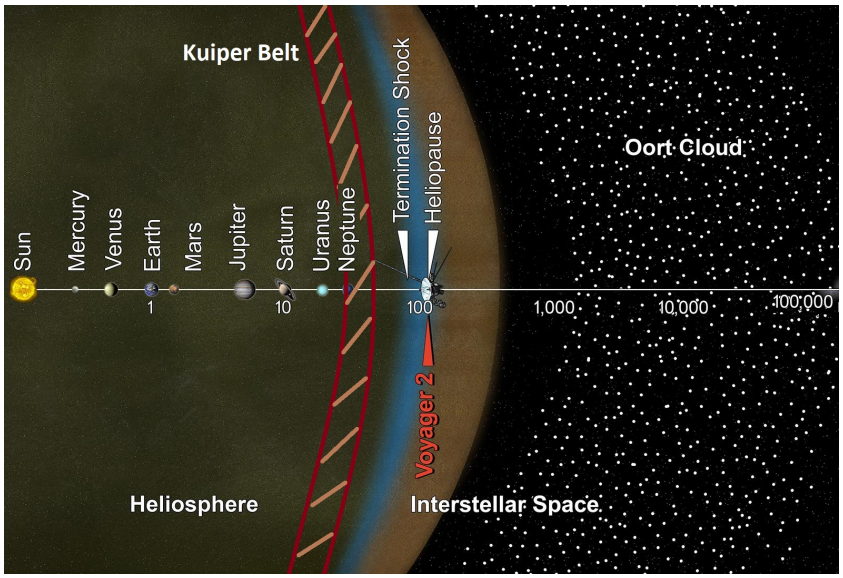

Figure 2.4: The Solar System, Kuiper Belt and Oort Cloud on a logarithmic scale. Modified, from "Photojournal" by NASA/JPL-Caltech, 2018 [173].

Currently, the only spacecraft to ever encounter a non-periodic comet was Ulysses in February 2007[174]. This comet was called Comet McNaught and was measured to have a hyperbolic orbit, but due to a drop in eccentricity once the comet moves far away from the sun, its period would be about 92,600 years. The rendezvous of Ulysses with McNaught's cometary tail was a chance encounter, as the probe's main purpose was to study the Sun. New Horizons is the only spacecraft to ever visit KBOs. This shows that only two spacecraft have encountered TNOs, demonstrating how few missions have gone there. The focus of the following sections will therefore lie on SSSBs within the inner Solar System, as these are easier to reach and far more missions will visit them.

2.1.2. Classification with Spectroscopy

Another method of grouping SSSBs is with the use of spectroscopy. This system classifies SSSBs based on their spectral lines and albedo. As these can be derived from properties readily observable from Earth, such as the apparent magnitude and colour spectrum, they allow for the creation of a taxonomy for these bodies in our Solar System.

The first scientists to come up with a spectral classifying scheme for asteroids did so in 1973. By comparing the spectral albedo curves of meteorites on Earth to those of SSSBs, they managed to predict the composition properties of these asteroids[42]. Their classifying system puts all SSSBs into two major groups: the Carbonaceous "C-Class" and the Siliceous "S-Class". These two groups encompassed about 90% of then discovered SSSBs. The others, some of which are fairly prominent asteroids such as Vesta, were designated "U" for unclassified.

A few years later, this system was augmented with a few new classes[31]. The main addition was the metallic "M-Class" of asteroids. Over the years, many different classification systems were put forward, most of them trying to comply with the older schemes. The two main ones are the Tholen Classification based on the Eight-Color Asteroid Survey (ECAS), and the Bus Classification based on the Small Main-Belt Asteroid Spectroscopic Survey (SMASS) and its second phase (SMASS-II). A summary of these two is shown in table 2.1 [41].

Tholen Class	Bus Class	Albedo	Spectral Features
A	A	Moderate	Very steep red slope shortward of 0.75 μm; moderately deep absorption feature longward of 0.75 μm.
B, C, F, G	B, C, Cb, Ch, Cg, Chg	Low	Linear, generally featureless spectra. Differences in UV absorption features and presence/absence of narrow absorption feature near 0.7 μm.
D	D	Low	Relatively featureless spectrum with very steep red slope
E, M, P	X, Xc, Xe, Xk	From Low(P) to Very High(E)	Generally featureless spectrum with reddish slope; differences in subtle absorption features and/or spectral curvature and/or peak relative reflectance.
Q	Q	Moderate	Reddish slope shortward of 0.7 μm; deep, rounded absorption feature longward of 0.75 μm.
R	R	Moderate	Moderate reddish slope downward of 0.7 μm; deep absorption longward of 0.75 μm.
S	S, Sa, Sk, Sl, Sq, Sr	Moderate	Moderately steep reddish slope downward of 0.7 μm; moderate to steep absorption longward of 0.75 μm; peak of reflectance at 0.73 μm. Bus subgroups intermediate between S and A, K, L, Q, R classes.
T	T	Low	Moderately reddish shortward of 0.75 μm; flat afterward.
V	V	Moderate	Reddish shortward of 0.7 μm; extremely deep absorption longward of 0.75 μm.
-	K	Moderate	Moderately steep red slope shortward of 0.75 μm; smoothly angled maximum and flat to blueish longward of 0.75 μm, with little or no curvature.
-	L, Ld	Moderate	Very steep red slope shortward of 0.75 μm; flat longward of 0.75 μm; differences in peak level.
-	O	-	Peculiar trend, known so far only for asteroid 3628.

Table 2.1: Summary of the Tholen and Bus asteroid taxonomy scheme, from "Spectroscopic Properties of Asteroid Families" by A. Cellino et al. [41].

2.1.3. Interior

Currently, no one has ever directly measured the interior structure of a SSSB, and there is no known way to do this with remote sensing. All information we have on their internal make-up is based on numerical models and a healthy dose of intuition.

So far, the main method of determining an asteroid's composition was by comparing its spectral signature, as seen in table 2.1, to that of meteorites found on Earth. There is however a big discrepancy between the density of these meteorites and their asteroid counterparts. The density estimates of a few well known SSSBs,

together with two of Mars's Moons, are shown in the following figure 2.5. The vertical lines show the measured density of meteorites.

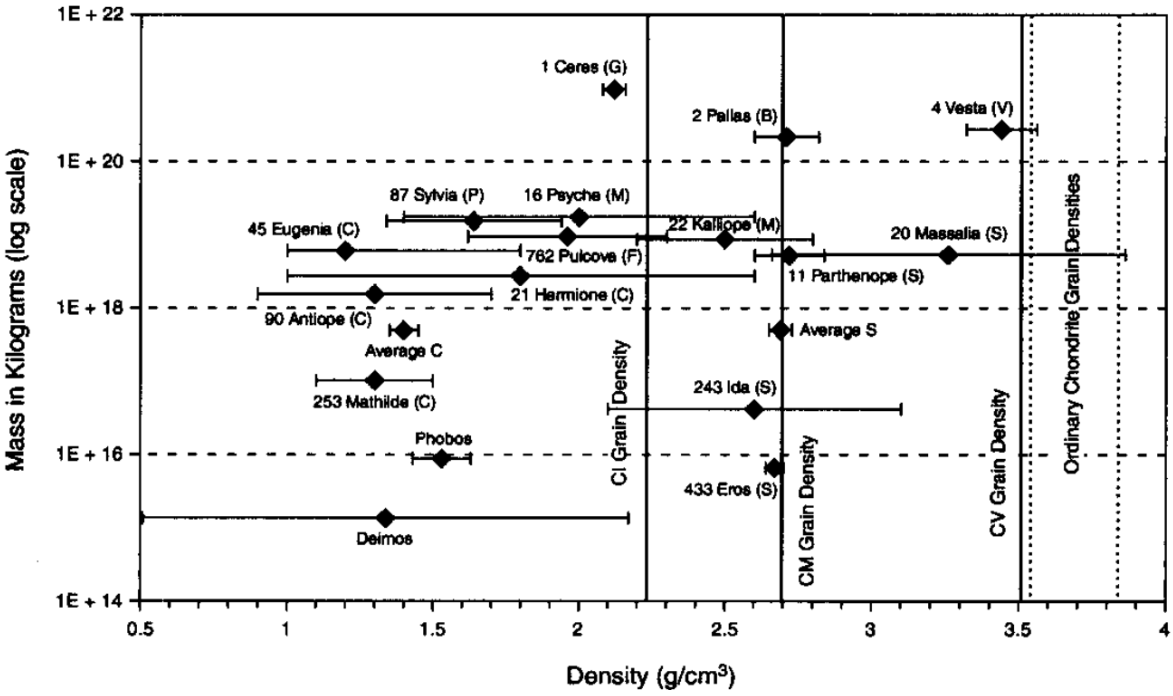

Figure 2.5: Density estimates for a few SSSBs, with error bars for clarity and vertical lines for average meteorite densities. From "Asteroid Density, Porosity, and Structure" by D.T. Britt, 2003 [34].

This shows that the density of these meteorites is generally much high than the bulk density of asteroids. This leads to the conclusion that either they are in fact different in composition to the meteorites on Earth, or that SSSBs contain a lot of porosity. The latter is the current leading theory, as a surface sample from the Itokawa Asteroid shows a similar composition to ordinary LL chondrite meteorites found on Earth [171], linking the two not only in spectral signature but in mineral composition as well.
Another argument for the existence of porosity in SSSBs is the so-called cohesion spin limit. If asteroids were made up of loose agglomerates of rocks and regolith with porosity, they would purely be held together by gravity and the Van der Waals force. This would implicate that they also have a cohesion spin limit, the maximum rotation period before they fly apart. This limit is calculated by first equating the gravitational acceleration on the surface ($a_g = \frac{G \cdot m}{r^2}$) with the centrifugal acceleration on the equator ($a_c = \omega^2 \cdot r$) [184]. Here, a_g and a_c are the acceleration due to gravity and the acceleration due to apparent centrifugal force respectively. G is the gravitational constant, m is the mass of the SSSB, r is its radius, and ω is its rotation rate.

$$\frac{G \cdot m}{r^2} = \omega_c^2 \cdot r \, [184] \tag{2.1}$$

Here, ω_c is the critical rotation rate at which the inward acceleration due to gravity is equal to the outward acceleration due to the rotation rate, which can be used to calculate the critical rotation period ($P_c = \frac{2 \cdot \pi}{\omega_c}$). Substituting the density ρ into the equation, we acquire the following:

$$P_c = \sqrt{\frac{3 \cdot \pi}{G \cdot \rho}} \approx \frac{375785}{\sqrt{\rho}} \approx \frac{3.3 \cdot h}{\sqrt{\rho \cdot 10^3}} [37][184] \tag{2.2}$$

In most literature on SSSBs, the density of regolith is taken in g/cm^3. Therefore, the 10^3 factor in the denominator is often not displayed in articles on this subject. The following image 2.6 shows a plot with the spin period of asteroids versus their diameter [231].

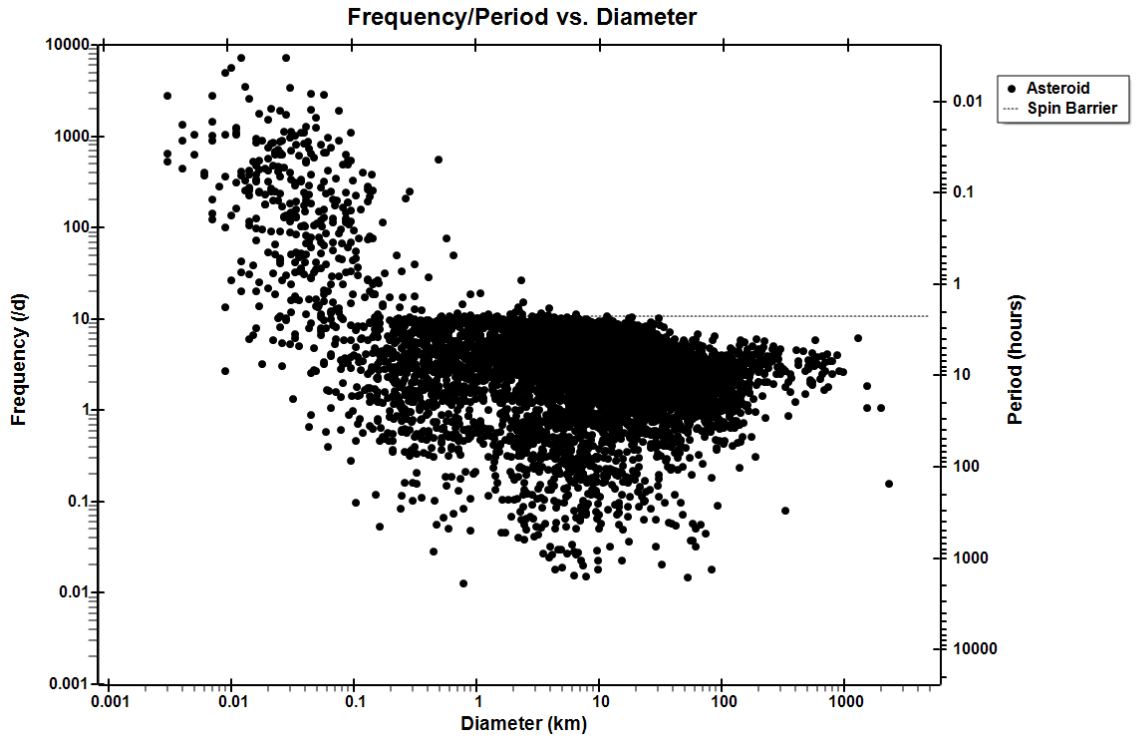

Figure 2.6: Rotation periods and frequencies of a large number of SSSBs, including a line showing the observed spin barrier/limit. From "The asteroid lightcurve database" by D. Warner et al., 2009 [231].

The horizontal dashed line shows the average spin period limit of the observed asteroids, at 2.2 hours. Using equation 2.2, this corresponds to an average density of $2.25 g/cm^3$, which is approximately the expected value for these SSSBs. As most observed bodies clearly adhere to this spin limit, the conclusion is drawn that most must be loosely bound rubble-pile type asteroids, and therefore contain porosity. Only the very smallest bodies, with a diameter of $< 0.12 km$, seem to be able to spin faster, which can be explained by them being monolithic. Also, Van der Waals forces play a bigger role in smaller SSSBs, allowing for a higher spin limit. Of the 8022 asteroids entered in the lightcurve database as of December 2020, 409 were smaller than the $120 m$ diameter limit [231], made out from figure 2.6. Of these, 318 have a lower spin period than 2.2 hours, which accounts for 78%. One can therefore assume the majority of sub $120 m$ asteroids to be monolithic.
To determine a SSSB's porosity, its bulk density (ρ_b) is compared to its grain density (ρ_g). Bulk asteroid density is calculated by dividing its total mass by its total volume.

$$\rho_b = \frac{M_b}{V_b} \tag{2.3}$$

The methods used to estimate the two constituents of the fraction in this equation are listed as follows by B. Carry, 2012 [40].
The bulk volume (V_b) is approximated in four main ways. One method is performed by comparing an SSSB's absolute magnitude to its expected albedo based on spectral type. The most used and second method is the thermal modelling of SSSBs from observations made with mid-infrared radiometry. The third method is a direct measurement of a single geometry, for instance by observing stellar occultation. From this single 2D geometry, the 3D geometry is extrapolated, giving the volume. The final method is performed by combining multiple 2D geometries, as for instance observed by a spacecraft or radio telescope.
The mass approximation (M_b) is done using one of four different methods as well: orbit deflection by other bodies, planetary ephemeris, tracking a spacecraft near the body, or observing the orbit of a Satellite of the body. As most of these methods decrease in precision with decreasing asteroid size, the error bars can be quite large.
The grain density of an asteroid is the density it would have if it was monolithic and is generally based on the density of the minerals in their meteorite spectral counterparts. These meteorites themselves often contain a lot of microporosity, so even meteorite bulk density is different from meteorite grain density. The average

grain density for most meteorites was found to be $\rho_g = 3 \sim 4 \cdot 10^3 kg/m^3$, with ordinary LL chondrites being $\rho_g = 3.48 \pm 0.08 \cdot 10^3 kg/m^3$ [33]. This is in stark contrast to two asteroids visited by spacecraft, as they were found to be much less dense. Eros is measured to have a density of $\rho_b = 2.67 \cdot 10^3 kg/m^3$[236] and Itokawa has a bulk density of $\rho_b = 1.9 \cdot 10^3 kg/m^3$ [83]. The current hypothesis is that these asteroids therefore must contain a lot of porosity (ϕ), which is calculated using the following equation:

$$\phi(\%) = 100 \cdot (1 - \frac{\rho_b}{\rho_g}) \tag{2.4}$$

In some cases, only the macroporosity is of interest, as microporosity possibly does not effect the internal strength of the SSSB as much. This is demonstrated by the fact that meteorites survive Earth entry, even with their internal microporosity. The following equation is used to estimate the macroporosity (Φ):

$$\Phi(\%) = 100 \cdot (1 - \frac{\rho_b}{\rho_{bm}}) \tag{2.5}$$

Here, ρ_{bm} is the measured average bulk density of meteorites, including their microporosity. The ordinary LL chondrites, comparable to Itokawa's composition, show an average measured (micro-) porosity of 9.3% ± 8.5%, with an average bulk density of $3.21 \pm 0.22 \cdot 10^3 kg/m^3$[33]. Using these and earlier mentioned values in equation 2.4 and 2.5, we get a porosity of $\phi \approx 45.4\%$, and a macroporosity of $\Phi \approx 40.8\%$ for Itokawa, which corresponds to the 40% mentioned in "Fundamental Planetary Science" by Jack J. Lissauer and Imke de Pater[143]. The estimated porosities and macroporosities for the SSSBs from figure 2.5 are shown in the following figure 2.7.

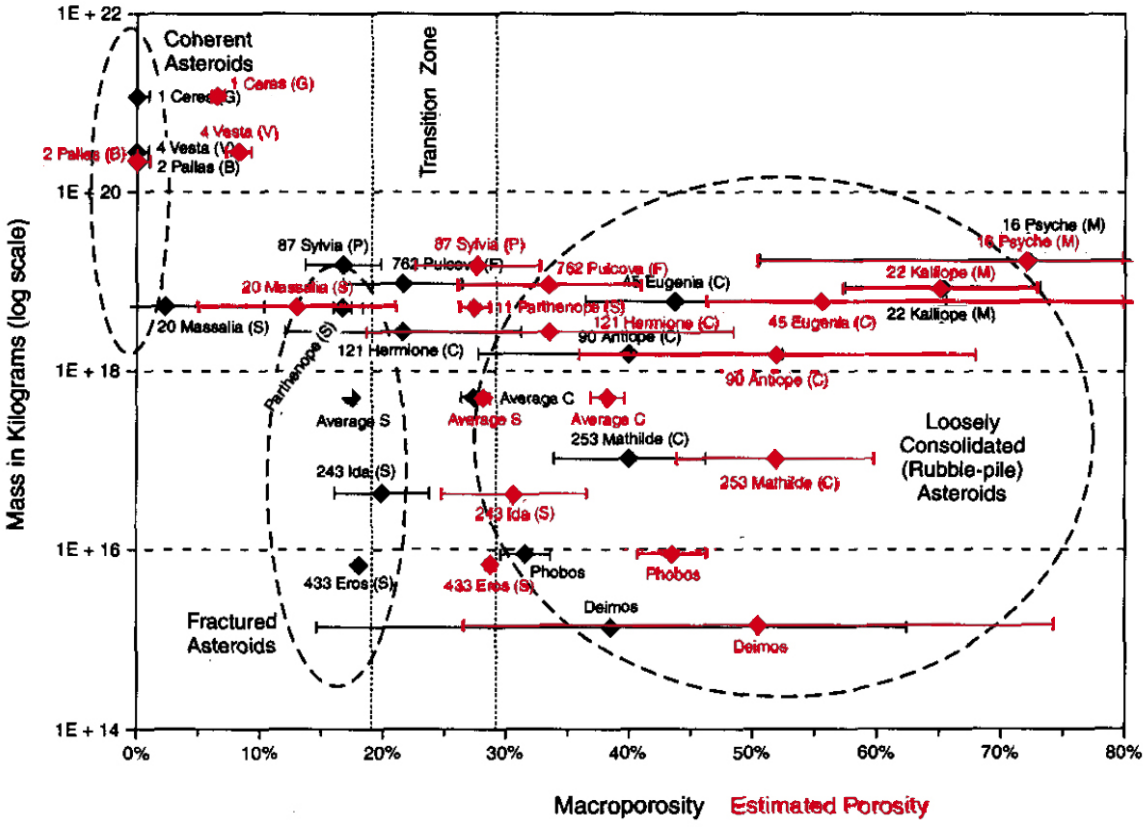

Figure 2.7: Porosity (Black) and macroporosity (Red) estimates for a few SSSBs, with error bars for clarity and encircled areas for suspected interior type. Edited, from "Asteroid Density, Porosity, and Structure" by D.T. Britt, 2003 [34].

This leads to the conclusion that, apart from the most massive asteroids, SSSBs are not monolithic and thus contain areas within their interior with a lower density, henceforth called "voids". According to A. Herique et al. [103], there are three main reasons gathering knowledge on SSSB interior structure and composition is crucial. This directly implies the necessity of devising a method to measure this.

The first reason is the previously discussed lack of information on micro and macro porosity, or even voids, within asteroids. From surface observations of asteroids it is known that many have a large variation in boulder and grain sizes. The distribution of these different sized rocks and regolith within the interior of the asteroid, together with data on its porosity and voids, can provide clues on its collisional history and therefore its formation and origin.

The second reason stated by A. Herique et al. [103] is to confirm hypotheses and numerical models on internal asteroid dynamics. The movement of particles within the SSSB could explain the abundance of fine regolith on asteroids. Verified numerical models of their interior will improve our understanding of their dynamics, which will aid fields like planetary defence, asteroid mining and planetary sciences.

A final reason A. Herique et al. [103] provide is the improvement of our understanding of SSSB constitutive materials. Interior dynamics such as the Brazil Nut Effect [153] can cause rocks of bigger sizes to end up on top of the asteroid's surface, which in turn can create a composition change of surface materials as compared to interior materials. Knowing how much deviation there is from a homogeneous distribution of materials within an SSSB interior will greatly improve our models, improving the conclusions that can be drawn from remote sensing and surface samples.

2.1.4. Target Case Studies

The selection of the small Solar System Body for the muography mission is of paramount importance. In this section, three different possible mission target will be discussed. This preliminary selection is governed by the space missions that have been or are planned to go to these bodies.

25143 Itokawa

Itokawa is one of the few asteroids already visited by spacecraft. As it belongs to the group of Apollos, who's orbital characteristics are shown in 2.3, it did not require too much delta-V to visit (a minimum of $4.632 km/s$) [134]. In 2003, the Hayabusa spacecraft was launched with the purpose of studying 25143 Itokawa and bringing a small surface sample back to Earth, making this the first asteroid sample return mission. A few of the asteroid's properties are shown in the following table 2.2:

Property	Value	Source
Dimensions	$535m \times 294m \times 209m$ $(\pm 1m)$	[83][143]
Spectral Type	S	[23][171]
Rotation Period	12.1324 ± 0.0001 $hours$	[175][231]
Mass	$3.51 \cdot 10^{10} \pm 0.105 \cdot 10^{10}$ kg	[83]
Volume	$1.84 \cdot 10^{7} \pm 0.092 \cdot 10^{7}$ m^3	[83]
Density	$1.9 - 1.95 \pm 0.13 - 0.14$ $g \cdot cm^{-3}$	[83][1]

Table 2.2: Summary of Itakawa's observed properties. Modified, from "The Rubble-Pile Asteroid Itokawa as Observed by Hayabusa" by A. Fujiwara et al. [83].

Images taken by the Hayabusa spacecraft clearly show Itokawa's surface structure, as displayed in figure 2.8. The areas with relatively few big boulders are thought to be "fresh" areas, where the Brazil Nut Effect did not yet run its course[153]. This supports the theory that Itokawa is made up from two constitutive pieces: The "head" (the smaller section left of the Muses Sea in 2.8A) and the body (the bigger section right of the Muses Sea in 2.8A). The Muses Sea would then be the not yet settled regolith in the neck of Itokawa [83] . Another observation supporting this theory is the strange spin up caused by the Yarkovsky-O'Keefe-Radzievsky-Paddack (YORP) effect. This effect causes a change in rotation rate for bodies differentially radiating away thermal energy imposed on them by solar radiation and the differential solar pressure exerted on them. Modelling the YORP effect on Itokawa's surface, it was found that observations would only fit the models if the "head" and the "body" of Itokawa would have significantly different densities [145].
Another deduction made from the observed YORP effect is mainly made due to its magnitude; The deceleration of Itokawa's rotation is so great, that it would cause seismic events to take place on a regular bases. Extrapolating the rotational deceleration back in time, it is found that approximately $100,000 - 180,000$ years ago, Itokawa would have had a rotational period of 6.5 hours, causing the head and body to be in orbit around

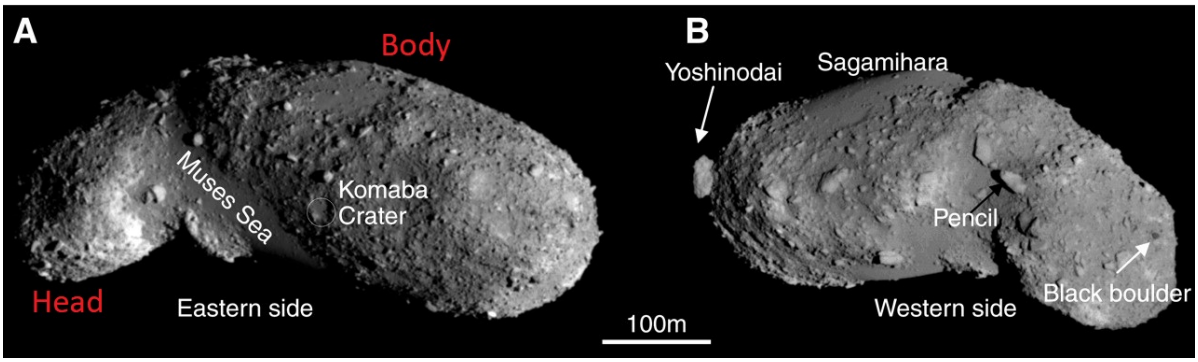

Figure 2.8: Images of Itokawa taken by Hayabusa. Two areas lacking large boulders are denoted as the Muses Sea and Sagamihara. A few prominent boulders and a crater are denoted as well. Modified, from "Detailed Images of Asteroid 25143 Itokawa from Hayabusa" by J. Saito et al. 2006 [198].

their mutual centre of mass [201]. Any faster and the two parts would have separated. It is therefore thought that around this period in time, Itokawa was reshaped into the morphology we observe today. As the YORP effect seems to influence asteroids dramatically on relatively short time scales, it is thought to be one of the biggest shaping forces for asteroid morphology [201]. It is worth mentioning that impacts from other bodies on the asteroid also have an effect on its rotation period [150].
An extra clue on Itokawa's history is the almost complete lack of impact craters [143], also visible in figure 2.8. As craters are present on practically all Solar System Bodies, the only ones with relatively few craters must have experienced some form of resurfacing [219]. On planets such as Earth and Venus this can be caused by atmospheric erosion, plate tectonics and other volcanic activity. As asteroids do not have an atmosphere or a "liquid" core, some other force must have caused the relatively recent resurfacing of Itokawa.
Quite a bit is known already about Itokawa; surface samples have already been studied and many articles have been written. Based on these articles, models and assumptions have been made on Itokawa's origin and composition. A tomographic muography mission will definitely help fine-tune these models and fill the gap of our current knowledge. A mission to Itokawa would not need as much instruments as a mission to a "new" asteroid would, as the Hayabusa mission already did quite a bit of the legwork needed for a muon tomography mission to be successful. Additionally, Itokawa is much smaller than the preliminary muography "Asteroid diameter limit" posed by T.H. Prettyman et al.; $D < 1km$[185]. This should cause Itokawa to let some of the much more abundant lower energy muons pass through, providing significantly better contrasting abilities and lower integration times to the instrument as compared to larger, more massive asteroids.

65803 Didymos

Another interesting asteroid for a muon tomography mission would be 65803 Didymos. Discovered in 1996, it is a sub-kilometre binary asteroid and therefore a potential target for muography. The perihelion of Didymos lies between the perihelion and aphelion of Earth, causing it to belong to both the Amor group and the Apollo group, seen in figure 2.3. As its orbit crosses that of Earth and its diameter exceeds $140m$, Didymos is considered a Potentially Hazardous Asteroid (PHA). This creates an extra incentive to visit Didymos and gather information on its interior structure. A few of Didymos's properties are displayed in the following table 2.3:

Property	Value	Source
Dimensions Primary	$D_{Primary} = 780m \pm 10\%$	[71]
Dimensions Secondary	$D_{Secondary} = 163m \pm 18m$	[71]
Spectral Type	Xk	[24]
Rotation Period Primary	$2.2600 \pm 0.0001\ hours$	[71]
Mass	$(5.278 \cdot 10^{11} \pm 0.04 \cdot 10^{11}\ kg$	[71]
Density	$2.1 \pm 30\%$, $1.77 \pm 0.4\ g/cm3$	[71], [44]

Table 2.3: Summary of Didymos's properties deduced and observed with remote sensing. Modified, from "Dynamical and Physical Properties of 65803 Didymos." by D.C. Richardson et al. [71].

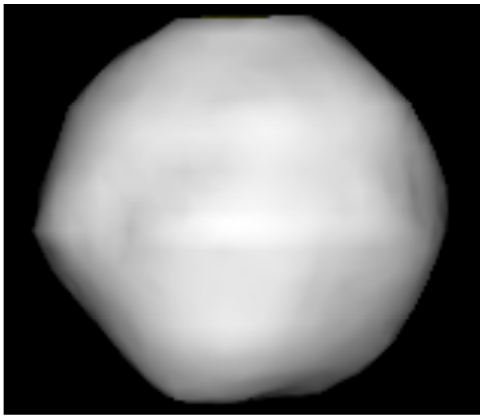

Figure 2.9: Rendering of the three-dimensional model of the Didymos primary, generated from radar and lightcurve date. From "Dynamical and Physical Properties of 65803 Didymos." by D.C. Richardson et al. [71].

For visualisation, a computer generated model of the Didymos primary based on radar and lightcurve data, is shown in figure 2.9[71]. The amount of Delta-V required for a spacecraft to rendezvous with Didymos is comparatively low: only about $5.102 km/s$ [134], which is less than what is needed to reach the Moon.
A double mission to Didymos is currently in the making, called the Asteroid Impact & Deflection Assessment (AIDA). It is a collaborative mission, with NASA and ESA both supplying a space probe. The probe supplied by NASA, called the Double Asteroid Redirection Test (DART), will be a 300kg impactor spaceprobe set to impact the smaller secondary of the Didymos binary system, called Dimorphos as of June 2020 [117], with $6.25 km/s$ [44]. It will be used to study the effects of such an impactor for asteroid redirection. The change in velocity caused by the impactor is expected to be only $0.4 mm/s$, but in the very low gravity environment around the Didymos primary, it will have a significant and measurable effect on the orbit of the secondary [44]. The European part of the mission is a mission called Hera. This spaceprobe, along with possible CubeSats or additional impactors hitching a ride, will arrive a few years later after the dust has settled from the DART impact [158]. It will study the effects of the impact in great detail, but there are still a lot of options left open for additional payload.
The Hera mission and therefore the Didymos binary system will be an excellent candidate for a muon tomography mission.

67P/Churyumov–Gerasimenko
Comet 67P/Churyumov–Gerasimenko is currently the only comet to have been orbited by a spacecraft. It is one of the 409 short-period numbered comets discovered as of December 2020, according to the IAU. Although an order of magnitude more non-periodic comets have been discovered, denoted with letter C, one can quickly limit the selection of possible mission targets for a rendezvous to the short-period comets, denoted with the letter P. This is caused by the huge difference in required Delta-V for a rocket to rendezvous with a C type comet versus a P type comet.
A few of 67P's properties are shown in table 2.4. As comets often have a coma surrounding their nucleus, especially when they get close to the Sun, their surface is obscured from view by this tenuous atmosphere. This negates the effectiveness of spectroscopy on most comets, which is why no spectral type is shown for 67P.

Property	Value	Source
Dimensions	$4.34 \pm 0.02 \times 2.60 \pm 0.02 \times 2.12 \pm 0.02 km$	[121]
Spectral Type	N/A	
Rotation Period	$\sim 12.4041 \pm 0.0001\ hours$	[121][77]
Mass	$9.982 \pm 0.003 \cdot 10^{12}\ kg$	[121]
Volume	$18.8 \pm 0.3 \cdot 10^{9}\ m^3$	[121]
Density	$0.532 \sim 0.535 \pm (0.07 \sim 0.035)\ g \cdot cm^{-3}$	[121]

Table 2.4: Summary of comet 67P's properties as observed by the Rosetta spacecraft. Sources are stated in right-most column.

The rotation period of the comet was found to vary much more than that of asteroids. This is most likely caused by the torque imposed on the comet from outgassing volatiles. The magnitude of this outgassing force is much larger than the YORP effect. The rotation period reached a maximum of $12.430h$ in May 2015 after which it dropped rapidly to $12.305h$ in a 3 month period [121]. Compared to Itokawa, which experiences a decrease in rotation period of $\sim 45ms$ per year [145], the percentage of change in rotation period is 6,192 times larger. Comet 67P/Churyumov–Gerasimenko is chosen as the main subject for the comet modelling process, described in section 3.3. The specific properties as well as its shape model will therefore be treated in further detail in the aforementioned section.
For a future launch, comet 320P/McNaught would be a good target. According to NASA Ames Research Center Trajectory Browser, a launch in June of 2024 would require $5.8km/s$ of Delta-V from low Earth orbit, which is achievable with current technology. Another daring and interesting target would be 73P/Schwassmann-Wachmann, a comet which is currently in the process of disintegrating. Such a comet in the process of breaking up will continuously reveal new virgin comet material to the surface, allowing for direct measurements of the interior composition. Most of the 73P fragments can be reached with less than $7km/s$ Delta-V from low Earth orbit, which is again achievable with current technology.

2.1.5. Asteroid Interior Mapping Methods

The focus of this thesis project lies mostly on the potential use of muons to map asteroid interiors. However, muography is not the only method to accomplish this. In this section, the alternative methods are discussed. The following table 2.5 [187][185] shows a comparison between different methods to map the interior of SSSBs. The three alternative methods to muography are discussed in the following paragraphs.

Method	Physical Parameter	Object Size/depth	Resolution limit	Issues
Radar	Dielectric constant, conductivity	Kilometres	Meters	Contrast detection, ambiguous
Gravimetry & Radio Science	Gravity field	Whole-body, regional mass anomaly	?	Model based
Seismic	Seismic velocity, density	Kilometres	Thin structures challenging	Contrast detection, ambiguous
Muon Imaging	Density (electron)	<3 km	Meters	Long integration times

Table 2.5: Comparison of prospective deep mapping methods for small Solar System bodies, from "Deep mapping of small Solar System bodies with galactic cosmic ray secondary particle showers" by T.H. Prettyman et al. [187].

Radar
Radar has already been put to use for this specific purpose in the field. It was used to map the interior of comet 67P/Churyumov-Gerasimenko. A radar instrument called CONSERT (COmet Nucleus Sounding Experiment by Radiowave Transmission) was flown on the Rosetta spacecraft with its Philae lander. This instrument used electromagnetic radio waves to measure the permittivity of different parts of the comet. The composition and interior structure of the comet, as well as any voids present, will effect the amplitude and velocity of these radio waves [104]. Thus, once the radio signal has passed through the comet, it will contain information concerning the comets properties. Measurements of these radio wave alterations can subsequently be used to create a model of the comet's interior. The CONSERT instrument required both the Philae lander and the Rosetta spacecraft to function, as the working principle of the instrument required signal transmission.
A study by P. Sava and E. Asphaug proposed the use of radar reflection caused by interior physical contrasts, in addition to radar transmission, to measure interior structure and composition of SSSBs. The following figure 2.10 schematically shows the difference between transmission and reflection experiments [200], with

T_x being the transmitter and R_x the receiver.

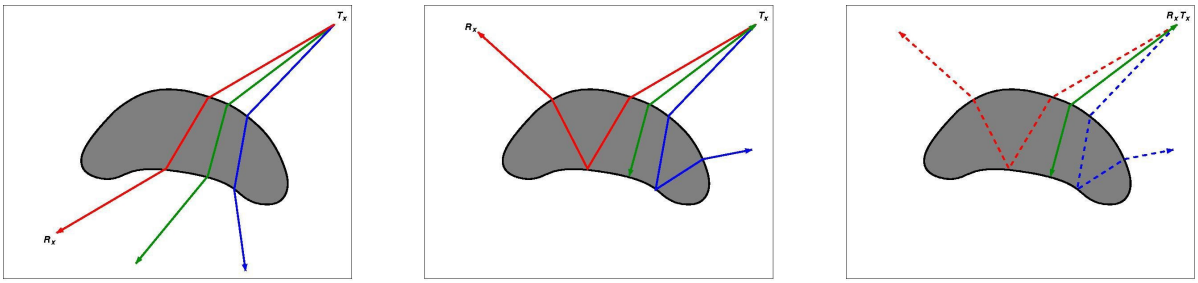

Figure 2.10: "Schematic representation of (a) transmission experiments, (b) bistatic reflection experiments, and (c) monostatic reflection experiments." Caption and image from "3D radar wavefield tomography of comet interiors" by P. Sava and E. Asphaug, 2018[200].

As a radar instrument can only be used to map the dielectric properties, the permittivity and conductivity, of the medium it traverses. Although deductions on density distributions can be made from these measurements, the dielectric property of a medium depends on material type as well. This creates a problem, as material composition is generally not known. Radar in this application is therefore only a tool to create boundary conditions for the interior structure.

Gravimetry

The gravitational acceleration caused by Earth's mass is not uniformly distributed around the globe. This is caused by differences in mass distribution, which in turn are the result of differences in interior density, tides, surface irregularities and other effects. By mapping these anomalies in gravity, a model can be made of the interior structure of Earth. Multiple space missions have measured the anomalies of Earth's gravity field, such as CHAMP, GRACE, GOCE and the GRACE-FO mission [76]. Based on observed morphological irregularities, SSSBs should also have gravitational anomalies which can give clues to their interior density distribution and structure. However, to measure the Earth's anomalies, very sensitive accelerometers were used. Earth's anomalies in mass distribution are much larger than even the total mass of a SSSB. Measuring gravitational anomalies of an asteroid will therefore require much more sensitive equipment than used on the Earth observation spacecrafts, rendering accelerometers for asteroid interior mapping ineffective with the current technology. A spacecraft in orbit of an SSSB will also experience acceleration from sources other than gravity, such as solar pressure. Additionally, the further away from the surface it gets, the lower the gravity signal ($\propto r^{-2}$). This will further reduce the signal to noise for such an accelerometer [38]. A solution might be the use of a gravimeter, which is essentially an accelerometer on the object's surface. This creates the need for multiple landings on the SSSB or a rover solution, as measurements from multiple positions will be needed to create the interior map [39].
All in all the use of gravimetry seems only feasible for only the largest SSSBs. In fact, a model of the interior structure of one of the biggest known asteroids, Vesta, has been made using data on its gravitational anomalies. A shape model of Vesta was made from images obtained with the Dawn spacecraft and a gravity model was produced by radio tracking the spacecraft location and acceleration in relation to Vesta. With these two models, a three layer interior structure model was computed [65]. This does not prove the usefulness of this technique for other SSSBs as Vesta is the second biggest asteroid currently known and most other SSSBs are many orders of magnitude smaller, which is clearly visible in figure 2.11. This graph shows the cumulative size distribution of main-belt asteroids, with Vesta's spot on this graph indicated. The line represents observed asteroids from the Asteroid Database (ASTORB). The diamonds and circles are extrapolations from the Sloan Digital Sky Survey (SDSD) and the Subaru Main Belt Asteroid Survey (SMBAS) [217].

Seismic

In the early years of the 20th century, seismology was used for the first time to draw conclusions on Earth's interior. R. Oldham identified different wave types in earthquakes and deduced that Earth must have a liquid core [205]. Many scientist have since used the waves from earthquakes and explosions to make a model of Earth's interior structure and composition. Seismology is also used in planetary sciences. As of 2018 scientist have put a seismometer on Mars; the Seismic Experiment for Interior Structure (SEIS) on the Mars Interior

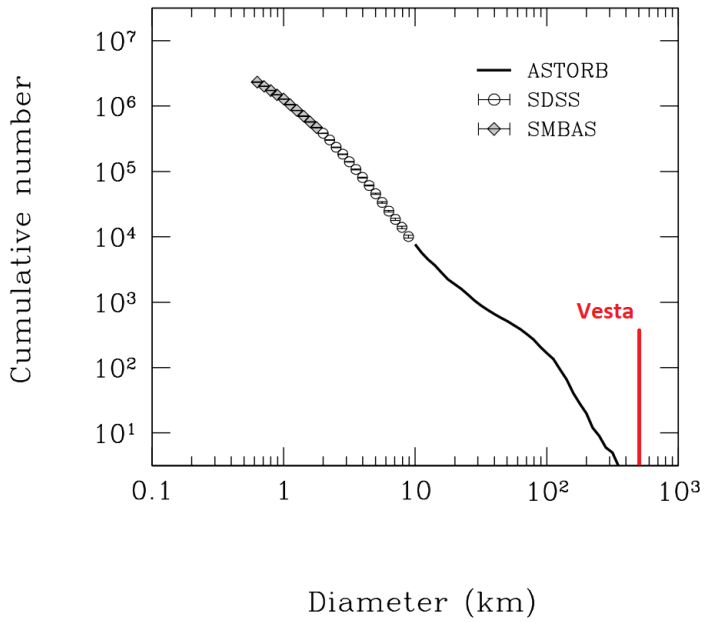

Figure 2.11: Graph of the cumulative size distribution of main-belt asteroids [217]. Vesta's diameter is indicated on the horizontal axis.

Exploration using Seismic Investigations, Geodesy and Heat Transport (InSight) lander. This instrument will try to detect seismic waves travelling through Mars' interior, revealing new information on its core structure. SSSBs are not expected to have very many measurable seismic events, caused in part by the lack of a liquid core and the poor wave propagation through loosely bound rubble. In order to measure seismic wave propagation trough such a body, the waves will most likely have to be man-made. This can be accomplished with an impactor or an explosion. To create a map of the interior, multiple sensors, multiple sources, or a combination of both must be used. The explosion needed to create enough seismic energy to be picked up by sensors on a SSSB is quite small. A NASA standard initiator (NSI), an explosive device used to break connections on a spacecraft, should already provide enough energy [182]. Similarly, small meteorite impacts could also suffice, although these events cannot be planned and their properties such as mass and impact velocity are often not known.
A paper by P.C. Thomas and M.S. Robinson [219] suggest that observations of a SSSB surface can show how seismic waves travel through its interior, and therefore provide clues on its interior structure and composition. The crater count on an Asteroid varies along its surface and is effected by resurfacing events. The straight-line distance from a young and large crater to a specific area on the SSSB surface seems directly proportional to the crater count in said area. The seismic energy released by a meteorite impact decreases with the aforementioned straight-line distance from the point of impact, suggesting seismic energy plays a quantifiable role in the resurfacing of the SSSB. Therefore, there is a passive way of observing past seismic events on an asteroid and thus a passive way to determine its interior from seismic waves.

2.2. Galactic Cosmic Ray Physics

In order to understand why muons might be such useful particles for asteroid interior mapping, we first have to understand what they are, where they originate from, and how muons compare to other particles for this specific purpose. This chapter starts off with a very top-level study on the leptons in the current standard model of particle physics. This is followed by a more detailed review of the muon particle. The chapter concludes with a study on the interactions that can be expected, and possibly used for interior mapping, between these cosmic ray particles and small Solar System bodies.

2.2.1. Particle Physics

The theoretical basis for using muons to map interior structures and density distribution lies not only within classical physics, but in quantum physics as well. In order to understand how muons interact with other particles, what forces act upon them, and how to detect them, a top-level look into quantum physics is war-

ranted. This section discusses the standard model of particle physics, the fundamental forces acting on these particles, and a muons place within both. It concludes by describing cosmic rays as the mechanism that creates these muons.

Standard Model

The standard model of particle physics describes all the currently found elementary particles, and three of the four known fundamental forces. The weak force is a very short range (diameter of proton) force that acts between two elementary particles and causes radioactive decay. The strong force is the force that holds matter together. The electromagnetic force acts between charged particles. The only "missing" fundamental force is the gravitational force, which brings together all things with mass or energy. A graphic explanation of the standard model is shown in figure 2.12.

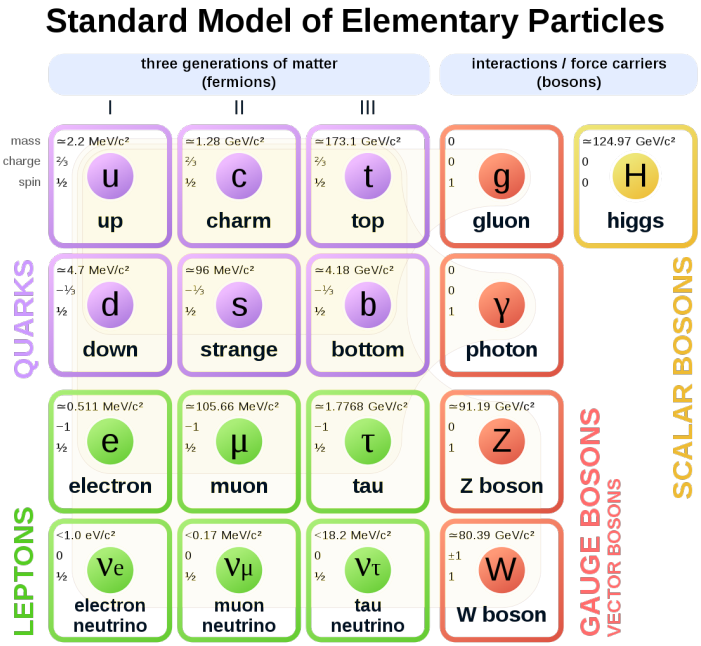

Figure 2.12: Standard model of Elementary Particles. From “WikimediaCommons,” by MissMJ, 2006[161].

The particles in this model can be separated into two main groups: the fermions and the bosons. Splitting the two is their spin, as bosons are defined to have an integer spin in contrast to fermions.
All elementary bosons had a spin of 1, until the discovery of the elementary Higgs boson, which has a spin of 0. Theoretically, a spin of 2 should be possible as well, but is yet to be observed in elementary bosons[178]. The graviton, hypothesised carrier of the gravitational force, is predicted to have a spin of 2 if it exists. Bosons are known as the "force carriers". The photon is the carrier of the electromagnetic force, the gluons are the carriers of the strong force and the Z and W boson carry the the weak force. These are considered gauge bosons, whilst the Higgs boson is seen as a scalar boson. It carries the so-called Higgs field, which causes particles to have mass.
The fermions all have a half-integer spin following $n+\frac{1}{2}$, and are generally considered the elementary particles that make up matter (with some exceptions). The fermions can also be in the form of an anti-particle, essentially doubling their number in figure 2.12 to 24 elementary fermions. There are two types; quarks and leptons. The quarks are the fundamental part of matter, and usually combine to form hadrons, which are combinations of two or more quarks, and are held together by the strong force. Mesons are a combination of one quark and an anti-quark. Baryons are a combination of three quarks, such as the well known neutron and proton. In atomic nuclei, the protons and neutrons are held together by the strong force as well. They are affected by all four of the fundamental forces. The other type of fermions are the leptons, which will be discussed in the following subsection.

Leptons
In contrast to quarks, leptons are not affected by the strong force. They are comparably much less massive as well, especially neutrinos, which were long thought to have no mass at all. The latter are not even charged, so neutrinos are only affected by the weak and the gravitational force. As muons are a type of lepton, it is not more than fitting to get to know their family. In this section, the leptons are discussed; their properties, similarities, differences and their discoveries. The following table 2.6 shows a few important properties and values on the 6 types of lepton and their respective antiparticles.

Particle Name	Symbol	Antiparticle	Spin	Mass (MeV/c^2)	Mean Life (s)
Electron	e^-	e^+	$\frac{1}{2}$	0.511	Stable
Neutrino (e)	ν_e	$\bar{\nu}_e$	$\frac{1}{2}$	0(<0.14eV/c^2)	Stable
Muon	μ^-	μ^+	$\frac{1}{2}$	105.7	$2.20{\cdot}10^{-6}$
Neutrino (μ)	ν_μ	$\bar{\nu}_\mu$	$\frac{1}{2}$	0(<0.14eV/c^2)	Stable
Tau	τ^-	τ^+	$\frac{1}{2}$	1777	$2.91{\cdot}10^{-13}$
Neutrino (τ)	ν_τ	$\bar{\nu}_\tau$	$\frac{1}{2}$	0(<0.14eV/c^2)	Stable

Table 2.6: Properties and numerical data on Leptons [92]

As a sidenote to this table, it must be mentioned that (anti-) electrons also have a mean lifetime. This lifetime however is in the order of $\tau > 6.6 \cdot 10^{28} yr$, which is considered stable[178]. The best known of these leptons is the electron, discovered in 1897 by J.J. Thompson [221] and the first of the subatomic particles to be observed by mankind. The next particle to be discovered was the anti-electron, also known as the positron. Its existence was predicted in 1928 by P.A.M. Dirac [63], although initially he only posed that electrons could be either negatively or positively charged. The anti-electron was observed 4 years later by C.D. Anderson [5], which earned him the Nobel prize for Physics.
In 1935 Hideki Yukawa, a theoretical physicist, predicted the existence of a particle with a mass of around 200 times that of an electron [238]. He thought this particle might be the carrier of the strong nuclear force. A year later, C.D. Anderson and S. Neddermeyer discovered the muon, which they called the mu (μ) meson. They found the new particle to be of either positive or negative charge and behave as higher mass states of electrons. Its existence was confirmed a year later [213]. The term meson would be used up until the formation of the standard model in the 1970's, as it described particles with a mass in between that of a proton and an electron. This mu meson did have Yukawa's predicted mass but did not interact with the strong nuclear force and therefore was not the actual particle Yukawa predicted.
In 1971 Yung-su Tsai predicted the existence of the tau (τ) particle [223]. Four years later a team headed by M.L. Perl discovered the tauon [181]. It was not directly observed but proven from the results of anomalous events in their experiment.
The existence of neutrinos was first theorised in 1930 in a letter from W. Pauli to the Physical Institute of the Federal Institute of Technology in Zürich [188]. He predicted these particles as a solution to the problem of a violation of the law of conservation of energy in beta decay. Because neutrinos have a very small mass and no charge, they were very hard to detect. The first neutrino, later called the electron neutrino, was discovered a quarter of a century after Pauli's letter in 1956, by Frederick Reines and Clyde L. Cowan [188][189]. The muon neutrino was shown to be a distinct neutrino in 1962 by a team led by Leon Lederman [57]. The tau neutrino has only been observed very recently by a team of the Fermilab, in an experiment called DONUT, in the year 2000 [128].

Muons
Muons are short-lived particles, but compared to the other unstable particles they are the second longest lived, after the neutrons [133]. According to the Particle Data Group (PDG), the lifetime of a muon is $\tau = (2.19698811 \pm 0.0000022) \cdot 10^{-6} s$ [178], and the ratio between its lifetime and that of an antimuon is $(\tau_{\mu^+})/(\tau_{\mu^-}) = 1.00002 \pm 0.00008$. However, a discrepancy between these two lifetimes would indicate a violation of Charge-Parity-Time (CPT) symmetry [111]. CPT (the details of which are out of scope for this thesis project) is a fundamental physical symmetry which holds for all physical phenomena and is currently widely accepted as true. Therefore, this ratio in lifetime is to be read as equal, proven to a factor of 10^{-4}. Muons almost always decay to electrons and neutrinos by one of the processes in the following list.

- $\mu^- \rightarrow e^- + \bar{\nu}_e + \nu_\mu$
- $\mu^+ \rightarrow e^+ + \nu_e + \bar{\nu}_\mu$

Almost 100% of the muon decay follows these processes [178]. The other processes involve the additional production of photon pairs or electron-positron pairs. A muon's mean travelled distance at the speed of light is $c \cdot \tau = 658.6384m$ [178] in its own reference frame.

2.2.2. Cosmic Rays

On Earth, the primary source for muons are the cosmic rays reaching its atmosphere. In 1912, Victor Hess discovered these rays during his famous balloon flight. Ever since, this field of research has flourished, but a lot is still unknown. For this thesis project, the focus will lie on the muon production by cosmic rays.
Cosmic rays are all stable charged particles and atomic nuclei moving through space at nearly the speed of light. These can be divided into three groups based on their origin. The first group are the particles expelled by the Sun in Solar flares and coronal mass ejections, and consist predominantly of protons. The second and most common group are the Galactic Cosmic Rays (GCR), whose origin lies within the Milky Way Galaxy. The last group are the Extra-Galactic Cosmic Rays, with their origin outside of our Galaxy. Very little is known about the last group, as their flux is very small.
These cosmic rays can again be divided into primaries, which are the primary accelerated particles and mainly consist of protons and alpha particles, and secondaries, which are created when primaries interact with interstellar gas[178]. The flux of the major components of primary GCRs is shown in the following figure 2.13.

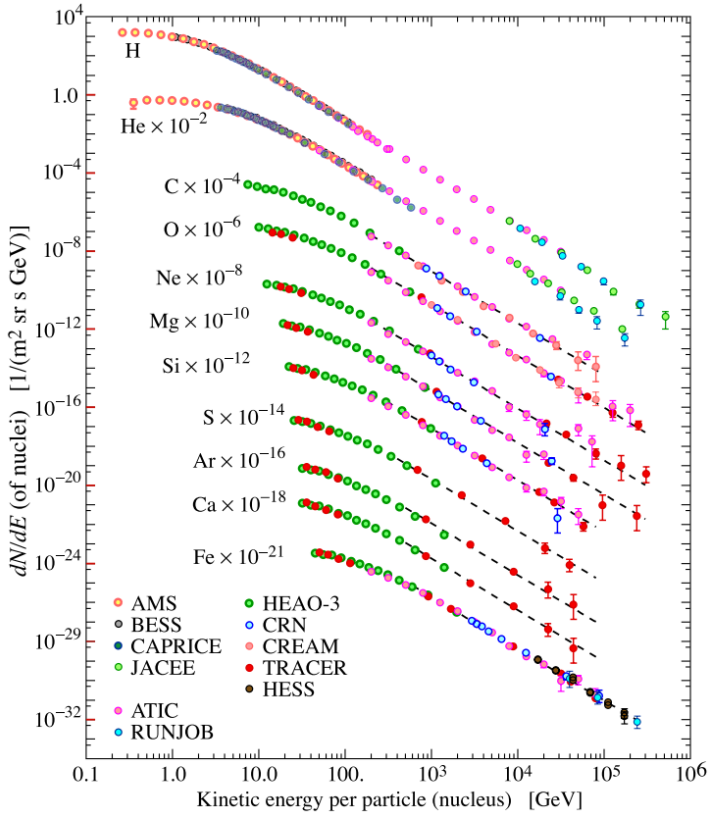

Figure 2.13: Fluxes of nuclei of the primary cosmic radiation in particles per energy-per-nucleus plotted vs energy-per-nucleus. The data sources are indicated in the legend. Caption and figure from "Chinese Physics C", figure created by P. Boyle and D. Muller, 2016 [178].

This figure is made from data of multiple sources, as indicated in the legend. It is clearly visible that the most abundant particles are protons. Atomic nuclei from secondary cosmic rays, such as lithium, beryllium and boron, are not included in this graph.

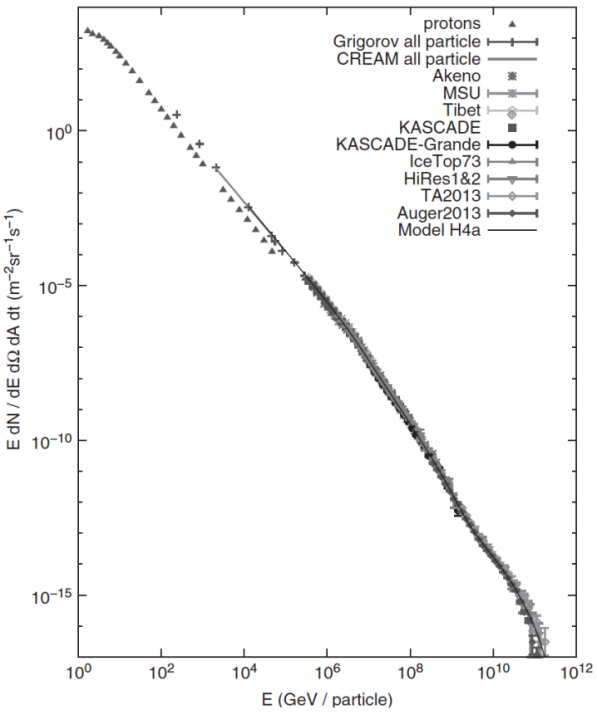

Figure 2.14: The cosmic ray energy spectrum. The triangles indicate data only for protons, the rest of the graph is the cumulative of all particles. From "Cosmic Rays and Particle Physics", by T.K. Gaisser et al., 2016 [220].

These cosmic rays arrive nearly uniformly distributed over all possible arrival directions. This is caused by the diffuse propagation of said rays through the galactic magnetic field [178]. There are however a few factors causing anisotropy for some ranges of the energy spectrum. The intensity of the particles in the low GeV range fluctuates with Solar activity [178][220]. This effect however is stronger closer to the Sun, and the low GeV range particles are not that interesting for muography as their penetrating depths are generally too low. In the energy range of a few TeV, the anisotropy level is found to be about 10^{-3} [178], and therefore not of great effect on muography. The Pierre Auger Collaboration found that at energies above $8 \cdot 10^{18} eV$, or 8 EeV, there is large scale anisotropy. They concluded that at these energies, the particles are of extra-galactic origin [72]. These particles however, as seen in figure 2.14, arrive in very small numbers, in the order of 1 per km^2 per year or less. Therefore this anisotropy will not be great influence on muography.
Once a primary particle undergoes nuclear interaction with particles in the upper atmosphere, a cascade of new particles is created. This cascade is schematically depicted in the following figure 2.15:

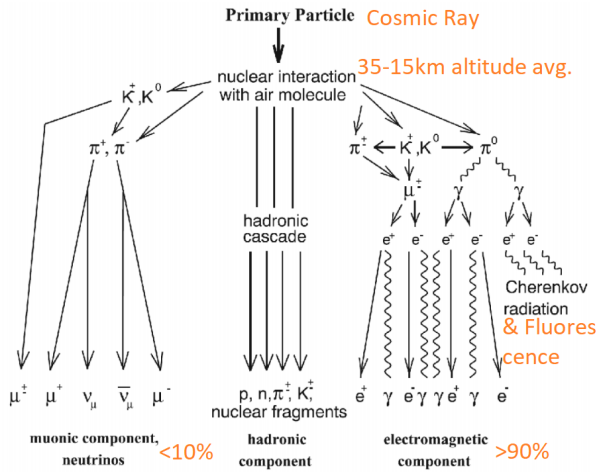

Figure 2.15: Schematical display of processes involved in cosmic ray air showers. Modified, from "Cosmic Ray Physics at MATHUSLA", by J.C. Arteaga-Velázquez et al., 2018[8]

This cascade of particles is called an air shower and sometimes called an Extended Air Shower (EAS), as the components reaching the Earth's surface can be spread out over many kilometers. The three main components are the hadronic component, the muonic component and the electromagnetic component [8]. Other components are generally very difficult to detect, such as the neutrinos and very low energy particles.
The hadronic component consists of nucleons like neutrons and protons, as well as other hadrons like pions and kaons. Pions form the majority of the hadrons produced after the first interaction with the atmosphere. As pions and kaons are not stable, they decay to form particles for the muonic and electromagnetic component. The kaon can also decay to pions, commonly following one of the processes depicted in the list shown hereafter [8][178].

- $K^{\pm} \rightarrow \pi^{\pm} + \pi^{0}$
- $K^{\pm} \rightarrow \pi^{\pm} + \pi^{\pm} + \pi^{\mp}$
- $K^{+} \rightarrow \pi^{0} + e^{+} + \nu_{e}$
- $K^{-} \rightarrow \pi^{0} + e^{-} + \bar{\nu}_{e}$
- $K_S^0 \rightarrow \pi^{+} + \pi^{-}$
- $K_S^0 \rightarrow \pi^{0} + \pi^{0}$
- $K_L^0 \rightarrow \pi^{\pm} + e^{\mp} + \nu_{e}$
- $K_L^0 \rightarrow \pi^{\pm} + \mu^{\mp} + \nu_{\mu}$
- $K_L^0 \rightarrow \pi^{0} + \pi^{0} + \pi^{0}$
- $K_L^0 \rightarrow \pi^{+} + \pi^{-} + \pi^{0}$

These are the decay processes with 5% or more probability. The decay processes for the antikaon K^{-} are the charge conjugates or antiparticles of the results of K^{+} decay above. The neutral kaon K_0 exists in two forms (L for long lifetime, S for short) with different decay processes and lifetimes. The energetic hadrons can also interact with atmospheric particles, creating a cascade by themselves. The hadronic component tends to follow the same general line the primary particle did, and therefore forms the "core" of the shower.
The muonic component is created by decaying pions and kaons, by one of the processes depicted in the following list [8][178].

- $K^{+} \rightarrow \mu^{+} + \nu_{\mu}$
- $K^{-} \rightarrow \mu^{-} + \bar{\nu}_{\mu}$
- $K_L^0 \rightarrow \pi^{\pm} + \mu^{\mp} + \nu_{\mu}$
- $\pi^{+} \rightarrow \mu^{+} + \nu_{\mu}$
- $\pi^{-} \rightarrow \mu^{-} + \bar{\nu}_{\mu}$

Again, only the processes with a fraction of 5% or more are shown. The created muons are comparably stable and often manage to traverse many kilometres of atmosphere before decaying or destructively interacting with other particles. At sea level, around $10,000 m^{-2} min^{-1}$ muons reach the ground. Controversially, the mean travelled distance at the speed of light should only be $c \cdot \tau = 658.6384 m$[178], as stated in subsection 2.2.1. This distance however does not take time dilation and length contraction from the special relativity theory into account. The effect of these can be calculated using the Lorentz factor, calculated in equation 2.6.

$$\gamma = \frac{1}{\sqrt{1 - \frac{v^2}{c^2}}} = \frac{dt'}{dt} \tag{2.6}$$

Here, γ is the Lorentz factor, c is the speed of light, v is the relative velocity between the two frames of reference, dt' is the time past in the reference frame of the moving body, and dt is the proper time past in the reference frame of the observer. The Lorentz factor is also the factor between a particles rest mass m_0 (or rest energy E_0) and its moving mass m (or moving energy E and kinetic energy E_k). The following list shows the relevant equations.

$$dt' = \gamma \cdot dt \tag{2.7}$$

$$dx' = \frac{dx}{\gamma} \tag{2.8}$$

$$m = m_0 \cdot \gamma \tag{2.9}$$

$$E = \gamma \cdot E_0 = \gamma \cdot m_0 \cdot c^2 \tag{2.10}$$

$$E_k = E - E_0 = (\gamma - 1) \cdot m_0 \cdot c^2 \tag{2.11}$$

So, calculating for a muon with a kinetic energy of $4 GeV$, we get a mean lifetime in the frame of the observer of $\tau \approx 83 \cdot 10^{-6} s$, which would indicate a mean travel distance of $x \approx 25 km$. Therefore, muons are able to travel significant distances if energetic (fast) enough. Most muons only lose around 2 GeV in energy before reaching the ground[178], leaving enough for most to relativistically survive the distance.

2.2.3. Particle Interaction with Asteroid Material

The choice to use muons to make observations of SSSB interiors is not only made based on its availability through cosmic rays, as discussed in section 2.2.2, but on its properties concerning the interaction with matter as well. In order to provide information on the interior structure, the particle has to interact with the matter inside the SSSB. In other words, once the muon has passed through the SSSB, it must contain information concerning the interior properties. This interaction has to fulfil three requirements:

- the interaction must alter the characteristics of the incoming particle spectrum;
- at least some of the affected particles must be able to fully traverse the interior of the SSSB;
- the magnitude and/or type of effect from the interaction must have some correlation to the interior structure characteristics.

It is worth noting that the interaction of the radiation with matter in the sensing instrument is also of importance, which will be discussed in chapter 2.3.

The interaction between energetic particles and matter is governed by energy transfer from the moving particle to the matter it traverses. How this energy is transferred depends first and foremost on which fundamental forces act upon the particle. Of the four fundamental forces, gravitational force is so weak, many orders of magnitude smaller than the electromagnetic force, that it can be ignored for our intends and purposes. The weak force is also quite a few orders of magnitude smaller than the electromagnetic force, mostly because its range is very limited. Only at a distance of around $10^{-18}m$, which is around 10^{-3} times the diameter of a proton, its magnitude is comparable to that of the electromagnetic force [179]. The strong force is a few orders of magnitude larger than the electromagnetic force, but is very limited in range as well. Because leptons, and therefore muons, are not affected by the strong force, it can be assumed that the electromagnetic force is the major carrier of energy transfer during a muon's transit through matter. Neutrinos are not charged, and therefore do not even transfer energy this way. They can therefore transit through vast amounts of matter, but are very hard to detect. The amount of energy transferred depends on a number of factors, one of which is the kinetic energy of the particle. The following figure 2.16 shows a graph of the energy transfer (or stopping power) of a positive muon in copper.

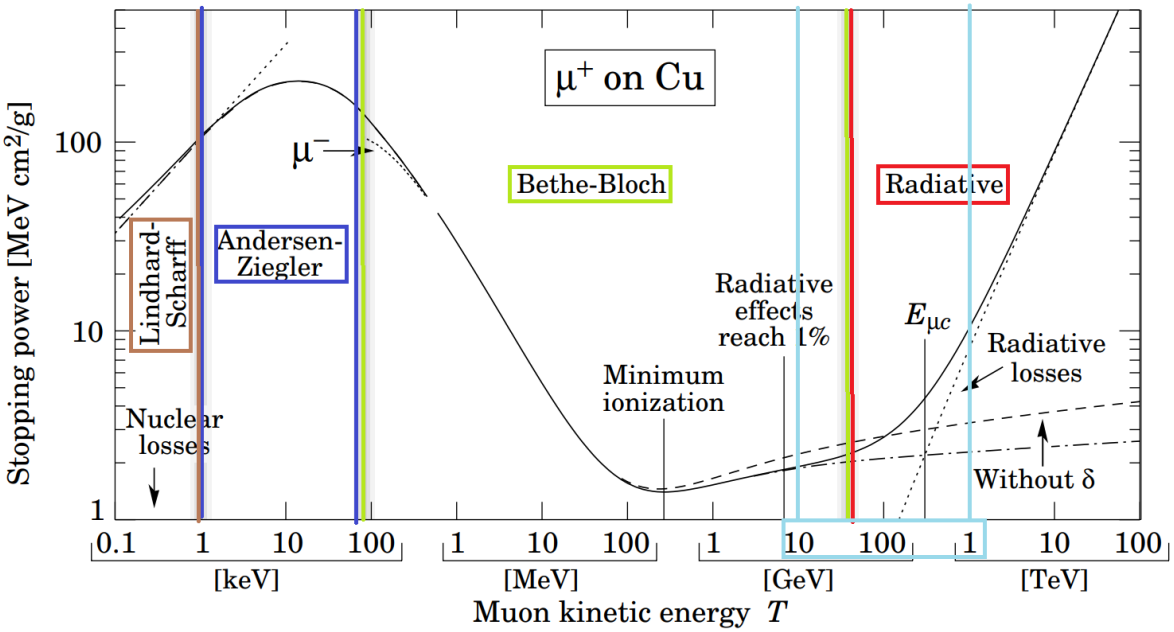

Figure 2.16: The positive muon stopping power of copper versus kinetic energy. Modified, from "Muon Stopping Power and Range Tables 10 MeV-100 TeV", by D.E.Groom et al., 2001[95]

The vertical axis depicts the energy lost per traversed centimeter, per density. This is shown as follows:

$$\frac{dE}{\rho dx} \rightarrow \frac{MeV}{cm \cdot \frac{g}{cm^3}} \rightarrow \frac{MeV \cdot cm^2}{g} \tag{2.12}$$

The graph is split into multiple regimes depending on the kinetic energy T. Each regime is covered by a primary "method" of energy transfer to the surrounding material. There is a slight difference between the stopping power for positive and negative muons, called the Barkas effect[18]. This causes negative muons to have a slightly longer range, and is denoted by a dashed line and a μ^- in figure 2.16. The energy loss of a particle traversing material is a random process and therefore does not always yield the same result for the same starting condition. Integration of the energy loss found in the graph over the travelled distance yields the most probable energy loss. The true kinetic energy loss is distributed following an asymmetric Landau distribution[135].

$$L(\lambda) = \frac{1}{\sqrt{2 \cdot \pi}} \cdot \exp(-\frac{1}{2} \cdot (\lambda + e^{-\lambda})) \tag{2.13}$$

$$\lambda = \frac{\Delta E - \Delta E_W}{\xi} \tag{2.14}$$

Here, ΔE is the actual energy loss, ΔE_W is the most probable energy loss from the Bethe equation, and ξ is the width of the distribution.

2.3. Muon Detection

Particles are detected by the direct or indirect effects of their interactions with the medium they traverse. These interactions, as described in section 2.2.3, can take place via one or more of the four fundamental forces. Depending on the type of detector, different interactions are observed with the material inside the instrument, giving information on the particle type, energy and/or trajectory. In this section, the most promising muon detection methods for asteroid tomography based on current literature are treated. All discussed techniques of detecting muons rely on their interactions via the electromagnetic fundamental force.
There exists a wide variety of instruments capable of detecting muons and some of their properties. In order to constrain this search for background literature to the scope of asteroid muography, a set of top-level preliminary requirements are formulated which the instrument must meet. The detector instrument:

- must be able to withstand the environment around a SSSB without damage;
- must be able to operate in the environment around a SSSB without mission critical performance loss;
- must provide good directional information on the arriving muons;
- must provide good energy resolution for particle discrimination;
- must be compact and light-weight;
- must be low-energy consuming;
- must be able to operate continuously;
- must be able to detect a sufficient range of muon energies.

Even though these requirements are very crude and top-level, they already rule out quite a few detection techniques. Fully passive detectors using photographic film for instance, such as nuclear emulsions, will not allow the spacecraft to (easily) register and send its data. Instruments like Geiger counters only count the particles and give no information on trajectory or energy [133]. However, some detection techniques that by themselves do not provide information on the trajectory of the particle, can be fitted in such a way in the instrument to overcome this issue. Such an instrument is called a "hodoscope", and is discussed in the following section.

2.3.1. Hodoscope

To easily deduce what a hodoscope is, a bit of enthymology can be used. The word itself is made from two ancient Greek words; the word ὁδός (hodós), which translates to "way" or "path" and the word σκοπός (skopós), which means "one that watches" and in turn comes from the verb σκέπτομαι (sképtomai), "I observe". A hodoscope is used in particle detection instruments and it watches or observes the path these particles follow to determine their trajectory. Figure 2.17 schematically shows the detection of a muon ($\mu^{\pm}$) by a hodoscope.

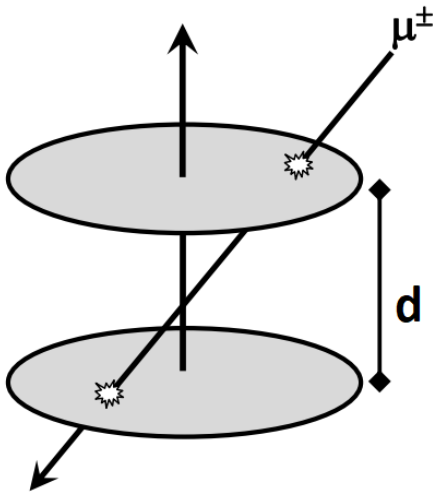

Figure 2.17: Diagram of a hodoscope using two, position-sensitive, particle detection layers [186].

The charged particle transects both layers, and its incident angle can be determined from the positions of the interaction on the layers [186]. Each type of muon detecting layer allows for different and sometime multiple ways of determining the position of the muon path intersection with its detection layers. The multiple types of muon detecting layers are discussed in the sections hereafter. Temporal arrival differences between the two (or more) interaction events of the plates allow for discrimination of the flight direction of the particles, therefore aiding the instrument in ignoring particles arriving from the other side.

2.3.2. Scintillation

Scintillation is most commonly seen in the every-day life in fluorescent or "glow-in-the-dark" materials. In the former, light of wavelengths often outside of the spectrum visible by the human eye, is absorbed by the fluorescent material, and re-emitted in a wavelength within the visible spectrum. This causes fluorescent materials or dyes to appear much brighter then materials without this fluorescence and is therefore most often used in safety equipment. The latter "Glow in the dark", known as phosphorescence, shows the same basic principle as fluorescence, but involves a notable time delay in the re-emission, causing the material to "glow" minutes and sometimes hours after absorbing the excitation radiation. Both these forms of scintillation can be seen in the following figure 2.18.

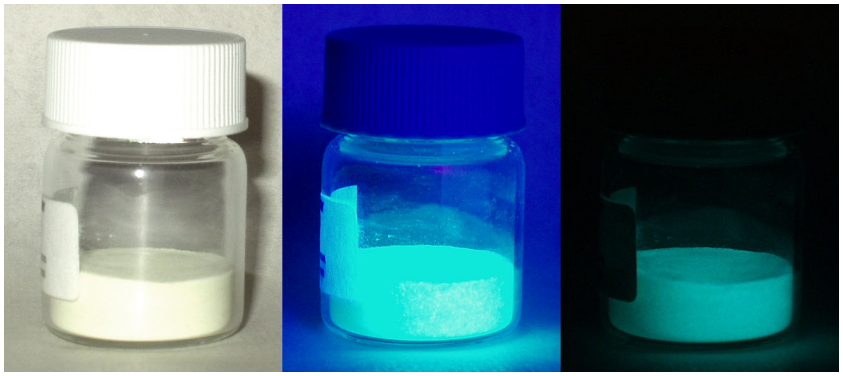

Figure 2.18: Examples of scintillation. Left image shows the sample material under visible light, the middle image shows the same sample fluorescing under long wave Ultra-Violet light. The right image shows the material glowing in total darkness: Phosphorescence. Image from “Wikimedia Commons” by Sparka, 2005[211].

In short, scintillation is the phenomenon where a particle moves through a material, and this material’s electrons absorb some of the energy of said particle. These electrons are then "excited" into higher states of energy, which are sometimes unstable or meta-stable. Once these electrons return to a lower energy state, they emit the difference in energy as a photon or photons. These photons can then be picked up by sensors,

indicating the passage of a particle through the material. "Glow-in-the-dark" materials indicate the presence of invisible UV light, to the human eye, by transmitting visible light after radiated upon by said UV.
For particle detectors, a scintillating material can be used to indicate the passage of an energetic particle. This material, called a scintillator, will emit photons once such a particle passes through. Two types of scintillating material exist, organic and inorganic scintillators. Although they similarly produce photons from energetic particles, the fundamental difference in working principal traces back to where the scintillation process takes place. Inorganic scintillators require a crystal structure to work, whereas organic scintillators do not. The photon production for the latter takes place on a molecular level, removing the need for a crystal lattice. This allows organic scintillators to be produced as liquids and polymers, increasing their range of applications [20].
The produced photons can subsequently be picked-up by a photo-multiplier, amplifying their emitted signal so that it can be read by an analogue to digital converter. This process will be treated in further detail in section 2.3.4. Preferentially, the chosen material shows no phosphorescence, as that will significantly decrease the timing precision of the instrument. A known relation between the amount of photons emitted by the scintillator and kinetic energy of the transiting particle is also of paramount importance, as this will prove crucial information to the instrument. The chosen material must also be transparent to the emitted photons, as otherwise only photons created on the surface of the material will be able to reach the photo-multiplier, significantly lowering the yield.

2.3.3. Čerenkov Radiation

The second physical phenomenon by which muons can produce photons, is called Čerenkov radiation. This is commonly associated with the cool blue light radiating from the pools in active nuclear reactors, as seen in image 2.19.

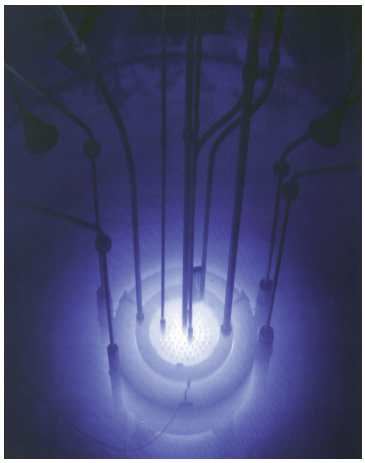

Figure 2.19: Nuclear Regulatory Commission picture of Cerenkov radiation surrounding the underwater core of the Reed Research Reactor, Reed College, Oregon, USA. Image and caption from “Wikimedia Commons” by United States Nuclear Regulatory Commission, 2007[52].

This emitted light is caused by charged particles moving through a dielectric medium faster than the local phase velocity of light. This velocity is defined as the speed at which one phase of a frequency component of the electromagnetic wave travels. Even though the speed of light in a vacuum (c) is a universal constant, it can be significantly lower in some materials. How fast light travels through a medium, its phase velocity v_{ph} is denoted by its refractive index (n), which as calculated as follows:

$$n = \frac{c}{v_{ph}} \tag{2.15}$$

Since the refractive index of water is $n \approx 1.33$, we know that light travels through water with only $v_{ph} \approx \frac{3}{4}c$. Therefore, particles with a greater velocity (v_p) will cause cause Cerenkov radiation:

$$\frac{c}{n} = v_{ph} < v_p < c \tag{2.16}$$

The radiation itself is caused by the polarisation of the dielectric medium. At particle velocities lower than the phase velocity of light in said medium, the polarisation is symmetrical around the particle, and no net electric field is formed. Once the particle velocity becomes greater than the phase velocity, the polarisation "can not keep up", shown in figure 2.20. This causes an electric field to form behind the particle. The energy stored in this polarisation is emitted as Čerenkov radiation once the polarisation relaxes.

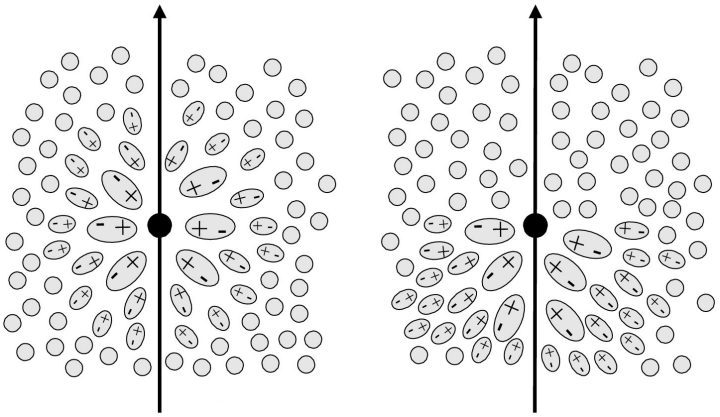

Figure 2.20: In both figures, the particle moves along the arrow upwards. Left: Schematic depiction of the polarisation in a dielectric medium caused by a negatively charged particle when $v_{ph} > v_p$ Right: The polarisation lagging behind, when $v_{ph} < v_p$. Modified, from "Ground-based detectors in very-high-energy gamma-ray astronomy" by M. de Naurois & D. Mazin, 2015[58].

A common analogy for Čerenkov radiation is the supersonic shockwave caused by objects travelling faster than the speed of sound through air. The angle of the shockwave (Θ), as shown in 2.21, gives information on the velocity of the object, which holds true for Čerenkov radiation as well.

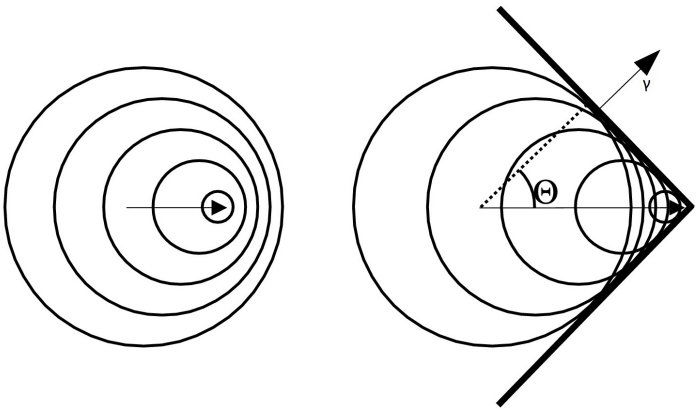

Figure 2.21: In both figures, the arrow shows the moving direction of the charged particle. Left: Schematic depiction of polarisation waves radiating from the particle when $v_{ph} > v_p$ Right: Construction of the Čerenkov wave-front when $v_{ph} < v_p$. γ shows the direction of the Čerenkov radiation propagation, Θ shows the angle between this direction and the velocity vector of the charged particle. Modified, from "Ground-based detectors in very-high-energy gamma-ray astronomy" by M. de Naurois & D. Mazin, 2015[58].

The particle velocity v_p can be calculated from the shockwave angle Θ as follows:

$$v_p = \frac{c}{n \cdot \cos\Theta} \tag{2.17}$$

It is worth noting that the angle the emitted photons make with the wave-front (the thick black line in figure 2.21) is 90°. This is however only true in non-dispersive media. For dispersive media, this angle is not equal to 90°, causing the radiation to "side-slip" along with the particle [167]. This change in angle must be considered when calculating the particle velocity using equation 2.17 for dispersive media.
Čerenkov detectors can be used in many configurations. Prettyman et al. proposed the use of aerogel Čerenkov detectors as a part of the muon tomography image[187]. These detectors would be used to create a threshold

kinetic energy level. Only muons with the kinetic energy of interest would then be detected, allowing for the removal of backscattered particles from the SSSB's surface from the measurements.

2.3.4. Photon Signal Conversion

The previous two sections 2.3.2 and 2.3.3 both treated physical phenomena by which a muon can produce photons within a medium it traverses. These photons can not be detected by the spacecraft directly and therefore their signal needs to both be amplified and converted into an electrical signal. Two methods are discussed, starting with the classical Photo Multiplier Tube (PMT) followed by the more modern Silicon Photo Multiplier (SiPM).

Photo Multiplier Tube

A photo-multiplier tube, or PMT for short, is very similar in its workings to an electron multiplier tube, the type of input signal setting them apart. A PMT includes a photocathode, which is a thin material capable of converting the incident photon to a free electron by means of the photoelectric effect. This photocathode often doubles as the negatively charged first electrode.
The small group of electrons is subsequently accelerated in the tube's vaccuum to the first dynode through an electric field caused by the approximately $+100V$ potential difference between said dynode and the cathode. This acceleration increases the kinetic energy of the electrons to approximately $100eV$. Upon impact with the first dynode, a number of low energy electrons is knocked loose, which will in turn accelerate towards the second dynode. This process repeats, increasing the number of electrons with every dynode until the current reaches the positive anode, where it is absorbed and subsequently read-out by the spacecrafts electronics. A schematical representation of a PMT is shown in figure 2.22.

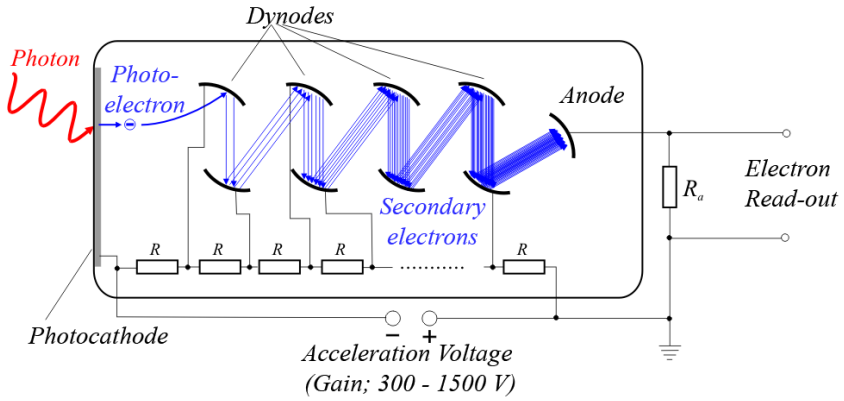

Figure 2.22: Simplified schematic of a photomultiplier tube. Image from "Wikimedia Commons" by Jkrieger, 2007 [120].

Photomultiplier tubes have been used for many years, some of their first designs are still being produced today. Their high levels of gain, low noise and fast response makes them especially suited for situations where the expected photon intensity (and therefore muon flux) is expected to be very low. However, these PMTs are quite bulky and need a high voltage to work, which are both undesirable for spacecraft applications.
Miniaturised PMTs exist such as the "Micro PMT® " range from Hamamatsu. Although these all-in-one packages even contain the high voltage supply needed to operate the PMT, they smallest one still has a mass of $11g$ [98]. For a hodoscope with two layers and a 100×100 resolution per layer, this would total $220kg$ for the PMTs alone. Naturally, other methods can be applied to resolve a muons location, such as time of arrival differences between two opposing PMTs. However, another solution exists which could replace the need for PMTs altogether.

Silicon Photo Multipliers

Silicon photomultipliers, or SiPM for short, are essentially a miniature grid of semi-conductors, each capable of converting an incoming ionising photon into an electric current. These semi-conductors are called Single-Photon Avalanche Diodes (SPAD), and operate with the same basic principle as other photo diodes, which are the inverse of the well known LED. Photo diodes operate by converting electromagnetic radiation to an electric current, by absorbing photons via the photoelectric effect. The magnitude of electric current produced relates linearly to the incoming light flux for normal photo diodes. However, SPAD rely on an effect called

impact ionisation, through which a single photon's effect can avalanche into a much larger current [240]. The SPAD is in a non-conducting state, but kept very close to its breakdown voltage. An electron with sufficient kinetic energy can knock another electron from its bound state in the semi-conductor molecular lattice. This creates a so-called electron-hole pair, a combination of a free electron and a positively charged volume in the lattice. The newly freed electron is subsequently accelerated in the electric field. In SPADs, this electric field is strong enough to impose sufficient kinetic energy on the electron to knock another one from its bound state, producing the electron avalanche.
SPADs, and therefore SiPMs, are a good alternative to the conventional PMTs. They are small and require a much lower voltage to operate, which can be as low as $10 \sim 50V$ whilst maintaining a photon detection efficiency of over 45% [240]. They provide an even better time resolution compared to PMTs and can be used to detect very small signals, which should them ideal for use on the envisioned muon tomography instrument.

2.3.5. Ionisation Detector

The heretofore discussed detection methods all relied on the direct or indirect creation of photons through energy loss processes undergone by the detector traversing muon. There is however a related but conceptually different method to detect these charged particles. This section treats the electric signal production by muons due to their ionising effects in the detector material.

Gaseous Detector

Similar to the electron excitation effects discussed in the section on scintillation, charged particles such as muons can even knock electrons free from their host atom. This causes ionisation, with positively charged particles and free negatively charged electrons. In gaseous detectors, these charged atoms are quickly separated in space from the electron by means of an electric field. The electrons, much lower in mass than their ex-host now-ions, are attracted to the positively charged part of the detector, which they often reach quickly. They are absorbed by this positive anode, producing a signal which can be read with electronics.
Various implementations of gaseous detector technology exist, of which the variants capable of tracking are of special interest to this project. The single chamber, multiple wire setup called the Multi-Wire Proportional Chamber uses a grid of thin, parallel anode wires to collect the electrons produces by an ionising particle [222]. A schematic representation of the workings of such a chamber is shown in figure 2.23.

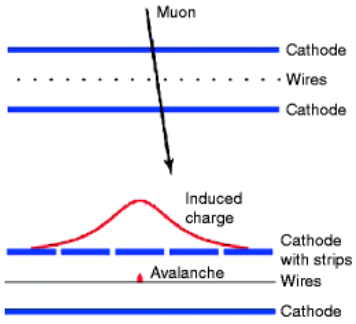

Figure 2.23: Simplified schematic of a gaseous Multi-Wire Proportional Chamber detector. Modified, from "Muon Spectrometers" by T. Hebbeker, K. Hoepfner, (2012) [102].

The magnitude of the electronic pulse is proportional to the incident particle's energy, allowing for the determination of muon energy. The signal distribution over the anode wires in turn allows for positional information to be retrieved. If more chambers are used, a hodoscope can be created for particle tracking.
In Drift Chambers, the time it takes for the created electrons to reach the anode wires is used to calculate the muon track [131]. With this method, positional accuracy levels of up to $100\mu m$ can be achieved [222]. If a second drift chamber is placed in the same charged particle beam, with its anode wires orthogonal to the previous, an even more precise track can be determined. This process is aided with knowledge on the exact event time, which is why a simple event detection layer is often put in front of both drift chambers. In this configuration, the instrument is called a Time Projection Chamber [131][222].
The superior application of gaseous detection methods is called a Micro-Pattern Gas Detector [222]. These detector configurations utilise a sub-mm electronic grid structure with very short distances between the cathode and anode. The can provide spatial resolutions up to $30\mu m$ and time resolutions in the order of nanosec-

onds [222]. A combination of such a Micro-Pattern Gas Detector with a CMOS imaging sensor couples the advances of the microelectronics industry to particle physics. This combination would result in a highly miniaturised charged particle detector capable of tracking and would provide easy integration onto a spacecraft.

Semiconductor Detector
The semiconductor ionisation detector working principal is very similar to that of the SPADs discussed in section 2.3.4. An energetic charged particle traverses the semiconductor, creating electron-hole pairs due to ionisation effects. These subsequently cascade to a detectable current. As semiconductors can be created to be very small, a high spatial resolution can be achieved. When multiple of these detectors are used in a hodoscope configuration, the charged particle's track can be resolved as well [131].

3

Asteroid Modelling

An accurate simulation setup of the Small Solar System Body environment is needed in order to validate designs for future muon tomography, numerically show its feasibility, provide reconstruction bias correction data and create a proving ground for reconstruction algorithms. The 3D asteroid and comet models used as inputs in such a simulation are discussed in this chapter. The details of the running of the simulation and its results are treated in chapter 4, which will revolve around the use of the core simulation tool used during this thesis project: *Geant4*, a software toolkit using Monte Carlo methods to simulate the passage of particles through matter [3].
The centrepiece and possible the most important input for the entire simulation will be the 3D model representing the SSSB. Due to computational constraints in this preliminary phase of feasibility exploration for the muon hodoscope technology, no efforts have been made thus far to create an accurate, realism-driven asteroid model to be used within a *Geant4* Monte Carlo simulation. Previously mentioned reports simplified their simulation asteroid model by a sphere (D. Hodge [109] and T.H. Prettyman [186]) or a cuboid (J. Keerl [125]), allowing for comparably easy computing.
The available computing power for this thesis project is not sufficient to perform *Geant4* simulations on a full sized accurate asteroid model within the project time-frame. The process of creating such a model is explored nonetheless as a stepping stone for future work to build upon and allow for a better overview of what can and cannot be simplified in smaller models. In order to ease the human workload during the simulation process, the models are created using the coding language GDML (Geometry Description Markup Language) [73], as this allows for easy adjustments of model parameters without altering the simulation setup within Geant4 [49].
Throughout this chapter, terms describing the different parts and aspects of small Solar System bodies are often used to indicate what is covered. As a terminology guideline, the following drawing 3.1 provides a graphical overview of the different parts and terms covered in this chapter. Each window showcases an enlargement of a small section of the image to the left. The average scale of each window is denoted underneath the figure. Individual feature sizes not drawn to scale for clarity.

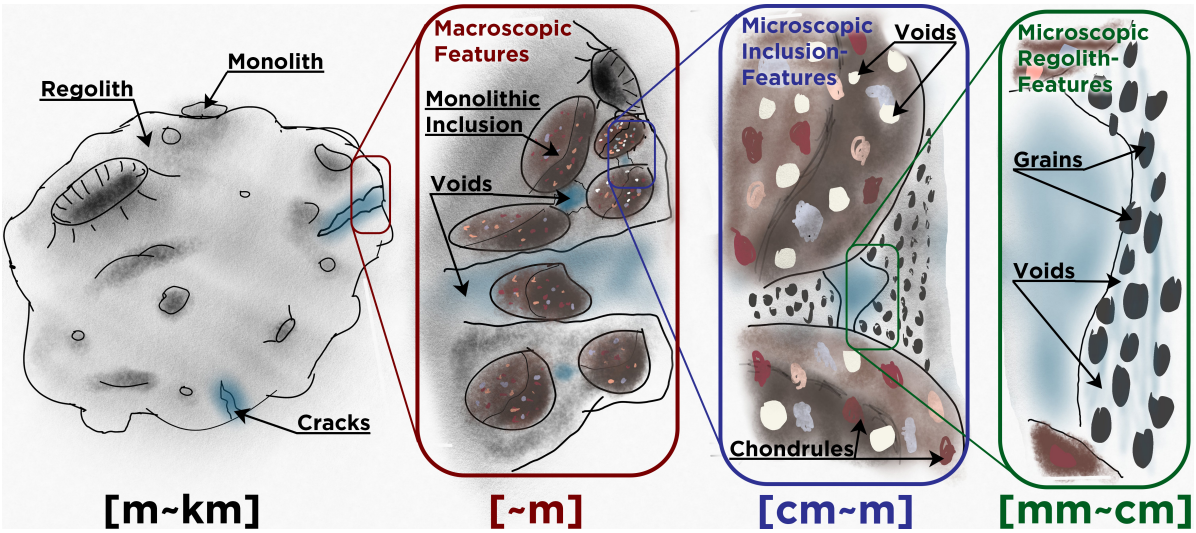

Figure 3.1: Schematic drawing of asteroid, with zoom-in windows from left to right. Features not to scale.

3.1. Realistic Asteroid Model

For the asteroid model to be realistic, quality data is needed on its composition, structure and shape. For most asteroids, all the available data is based on remote sensing data, which is generally only good for first order approximation. This limits the available choices broadly to the asteroids that have been visited by a spacecraft. A good argument for this restriction is a visual comparison between the predicted shape model, created from remote sensing, for Comet 67P/Churyumov–Gerasimenko in 2012 [144], versus its actual shape model as observed by the Rosetta spacecraft [208].

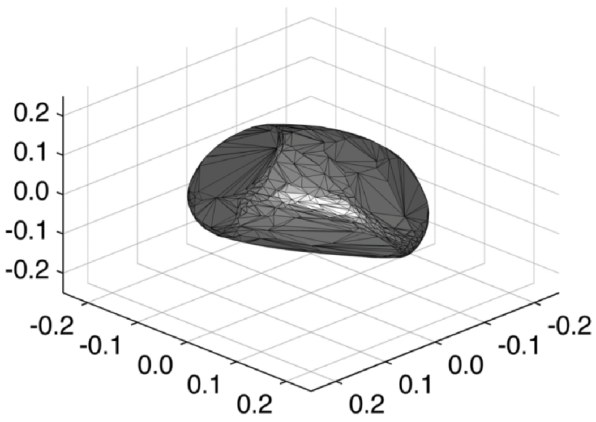

(a) Predicted shape model using optical lightcurve inversion techniques. Modified, from "The nucleus of Comet 67P/Churyumov-Gerasimenko" by S. Lowry et al., 2012[144].

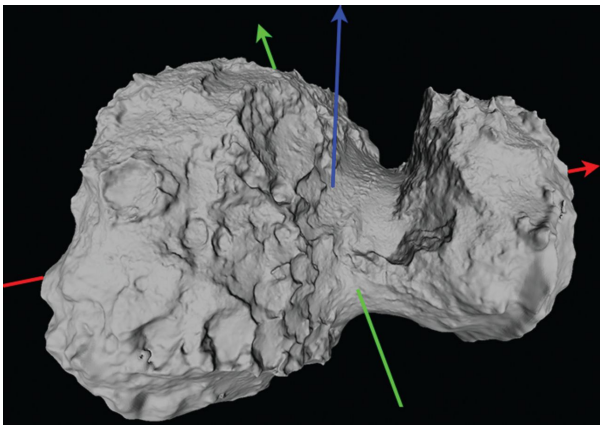

(b) Stereophotogrammetric shape model of Comet 67P from in-situ measurements by the Rosetta spacecraft. From “On the nucleus structure and activity of Comet 67P/Churyumov-Gerasimenko” by H. Sierks et al., 2015[208].

Figure 3.2: A visual comparison between two Comet 67P/Churyumov–Gerasimenko shape models.

Figure 3.2 clearly shows the major lack of detail in shape model predictions, as well as broad shape discrepancies. It is worth noting however that the size and orbit of the SSSB, as well as its albedo and possible presence of a coma, influence our ability to perform shape model predictions. The quality of said predictions will therefore generally be lower for heavily outgassing comets orbiting far from the sun, than for large asteroids with close-to-Earth Orbits. Nevertheless it must be said only SSSBs observed up close by spacecraft will have accurate shape models available, and therefore the selection for the realistic asteroid model is constrained to these.

Another argument for this constraint is posed by knowledge on the asteroid’s density and composition. To create an accurate model, knowledge on both these properties is paramount. As shown in subsection 2.1.3,

a decent approximation on material composition can be made by linking an asteroids spectral signature to those of meteorites found on Earth with known compositions. However, the distribution of the material within the SSSB, and its density, cannot be accurately calculated from remote sensing results. This once again leaves us with little choice but to create the accurate asteroid model based on ones that have been observed in-situ.
Future prime candidates for this model creation will be 162173 Ryugu and 101955 Bennu. Both are quite spherical "spinning-top" asteroids, have sub-kilometer diameters and were recently visited by a spacecraft. Asteroid 162173 Ryugu was visited in the year 2018 by the Hayabusa2 spacecraft [232], which is currently on its cruise back to Earth to complete its sample return mission and set to touch down in December of 2020. The high resolution shape model created from data transmitted by Hayabusa2 is shown in the following figure 3.3:

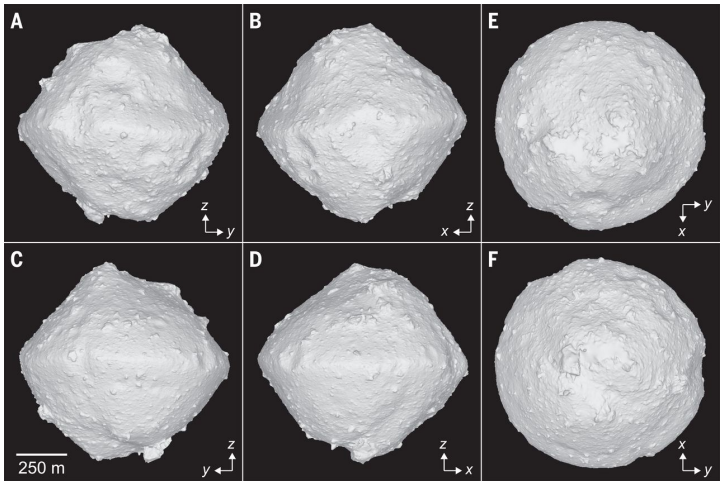

Figure 3.3: 162173 Ryugu shape model. From “Hayabusa2 arrives at the carbonaceous Asteroid 162173 Ryugu—A spinning top–shaped rubble pile” by S. Watanabe et al., 2019[232].

Another spacecraft, called OSIRIS-REx (Origins, Spectral Interpretation, Resource Identification, Security, Regolith Explorer), is currently in orbit around 101955 Bennu and set to conclude its sample return mission in the year 2023 [139].
Unfortunately, both Hayabusa2 and OSIRIS-REx have not finished their sample return missions at the time of writing. Even though both missions have provided very detailed shape models of their targets, the choice is made to focus on another asteroid for this thesis project. Once these two missions are concluded, the available amount of information on the composition of their asteroid targets will increase greatly, allowing for far more detailed model creation in the near future.
The most recently visited SSSBs with shape model and composition data available are the Comet 67P Churyumov–Gerasimenko and the Asteroid 25143 Itokawa, by the Rosetta and Hayabusa space missions respectively. As the application of muon tomography technology in orbit near comets comes with its own set of caveats, discussed in section 3.3, the primary realistic asteroid model for this thesis project will be based upon Asteroid 25143 Itokawa.

3.1.1. Itokawa Shape Model

The construction of the asteroid model of Itokawa for use in Geant4 starts with its shape model (its 3D surface shell model) as presented by Gaskell et al. [85] in NASA’s Planetary Data System (PDS), see figure 3.4. This model was constructed from around 770 images taken by the Asteroid Multi-band Imaging Camera (AMICA) instrument onboard Hayabusa[198]. A detailed description of the construction process is provided in "Landmark Navigation Studies and Target Characterisation in the Hayabusa Encounter with Itokawa" by R. Gaskell et al., 2006[86].
The model is available in both the implicitly connected quadrilateral (ICQ) format as well as the vertex-facet format in the PDS [85], both supplied as a list of shape data with the table ($*.tab$) extension. The latter of the two is used to create the 3D model, by converting the vertex-facet format (similar to Plate-Vertex format) to the *Alias|Wavefront* OBJ ($.obj$) format, which is a more commonly used geometry definition file format. This

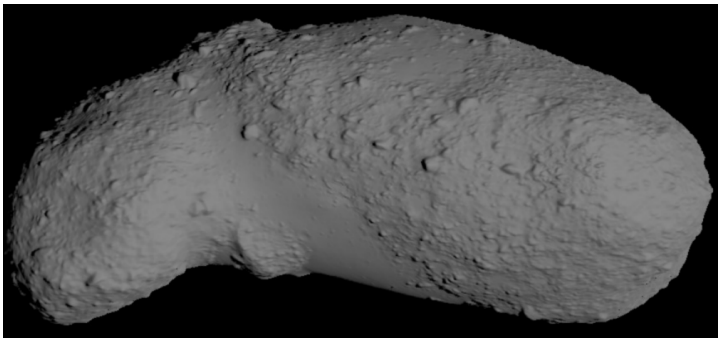

Figure 3.4: Browse view of the Itokawa shape model as presented by Gaskell et al., 2008 [85].

conversion is performed using the "PlateVertext2Obj.py" *Python* script, provided by Trent Hare of the United States Geological Survey (USGS) Astrogeology Science Center[100]. The resulting OBJ file is very similar in format to the "Tesselated Solid" available for use in GDML [49], as described in the GDML User's Guide [73]. A piece of *MATLAB* code is written to convert the OBJ file data into a text file with the GDML Tesselated Solid format. The contents of this file can be inserted into the main GDML file to be used in the Geant4 simulation.This essentially concludes the conversion from a Gaskell shape model to GDML code. The following figure 3.5 shows the flow chart depicting the steps of this conversion.

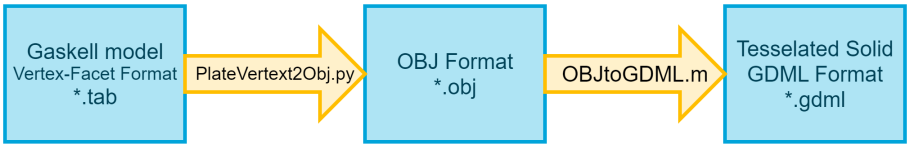

Figure 3.5: Flow diagram of conversion steps from Gaskell shape model [85] to GDML code. (Own Work)

As a footnote to the heretofore described process, it must be said that every mentioned conversion step requires some manual adjustment of the input code as well as the conversion scripts, as not all PDS shape model data is presented in the exact same formatting.

3.1.2. Itokawa Chemical Composition

For the model of Itokawa to be accurate, the GDML code needs to contain information on its composition as well. To facilitate quick adjustments of the used materials in a GDML file, the language allows the use of a separate "materials" file in the Extensible Markup Language (*.xml*) format. All the entities described in the main file will be linked to a material, which in turn can be a combination of other materials.
Itokawa's mineral composition will mostly be based on the results of the analysis of regolith samples, returned to Earth by the Hayabusa mission. The sample collection mechanism of Hayabusa however did not perform as expected [235], resulting in less than 1 mg of material being collected [94]. Due to this less then desirable amount of regolith analysed, the composition and micro-porosity data will be augmented with data from spectral and meteorite analyses as described in section 2.1.2.
The meteorite classification scheme used henceforth, partially similar to the spectral classification scheme used for asteroids (table 2.1), will follow the naming used in the corresponding source for each citation. The choice of a single naming scheme would complicate the readability of the text when comparing with the sources, as there is still a lack of consensus within the scientific community on how to classify meteorite beyond the naming of groups.
The modal mineralogical abundances contained within a 40-particle sample subset of Hayabusa's returns, as described by A. Tsuchiyama et al. [225] and shown in table 3.1, show remarkable similarities to ordinary LL chondrites, which is in line with predictions based on spectral analyses of Itokawa.

Mineral	Modal Abundance [vol.%]	Density [g/cm^3]	Percentage by Mass [wt.%]
Olivine	64	3.57	67
Low-Ca pyroxene	19	3.36	18
Plagioclase	11	2.63	9
High-Ca pyroxene	3	3.16	2
Troilite	2	4.83	3
Others (Taenite, Chromite, etc)	≈1	3.20~8.38	≈1

Table 3.1: Modal mineral abundances in Itokawa samples according to A. Tsuchiyama et al. [225].

Not all similar named minerals are comprised from the same ratio of their respective constituents. Olivine for instance is generally made up from fayalite (Fe_2SiO_4) and forsterite (Mg_2SiO_4), often abbreviated to Fa and Fo respectively. The ratio between these two is described with a subscript of their molar percentages within the olivine. In the case of the Itokawa samples this is depicted as $Fa_{28.6\pm1.1}$ and $Fo_{71.4\pm1.1}$[171]. The densities and percentages by mass mentioned in 3.1 are calculated from their average chemical composition from T. Nakamura et al. [171]. The chemical bulk composition mass percentages are shown in table 3.2 and compared with values from ordinary chondrite meteorite falls.

[wt%]	Itokawa	LL Chondrite	L Chondrite	H Chondrite
SiO2	42.5	40.6	39.7	36.6
TiO2	<0.1	0.1	0.1	0.1
Al2O3	1.8	2.2	2.3	2.1
FeO	20.6	17.4	14.5	10.3
MnO	0.4	0.4	0.3	0.3
MgO	29.5	25.2	24.7	23.3
CaO	0.9	1.9	1.9	1.7
Na2O	0.8	1.0	1.0	0.9
K2O	0.1	0.1	0.1	0.1
Cr2O3	0.1	0.5	0.5	0.5
P2O5	<0.1	0.2	0.2	0.3
Oxides:	96.8	89.7	85.3	76.2
Fe	0.3	2.4	7.0	16.0
Ni	0.3	1.1	1.2	1.7
FeS	3.0	5.8	5.8	5.4
Total:	100.3	99.0	99.3	99.4

Table 3.2: Bulk composition of Itokawa particles compared with those for L-, LL- and H ordinary chondrite falls [118]. All displayed values in wt%. From "The Rubble-Pile Asteroid Itokawa as Observed by Hayabusa", Table S5, by T. Nakamura et al. [171]

These bulk composition values will be used in the *materials.xml* file and used in conjunction with the *.gdml* file as input for the Geant4 simulation.

3.1.3. Itokawa Interior Microstructure

The solids present in Itokawa's interior have their own structural properties and variations. This subsection reviews the microstructures present within said solids, from the smallest regolith dust to the largest monolithic rocks.

Microporosity
One of the first things to look into concerning Itokawa's microstructure is microporosity. This is defined as the percentage of void space within solid features such as regolith grains and monoliths. As posed by T.H. Prettyman et al. [186], it is likely that relativistic mesons created from cosmic rays will collide within solids, such as monolithic material in asteroids, before having a chance to decay. As the main source of muon production from cosmic rays is the decay of mesons, as indicated in section 2.2.2, porosity within the solids might provide void space for these particles to decay without let or hindrance. Therefore the incorporation of microporosity in the Itokawa model might have a tremendous effect on the simulation outcome. This type of porosity, discussed in section 2.1.3, is thought to be the result of shock-induced compaction in the asteroid's early lithification process, a process asteroids must have gone through to form monolithic structures as opposed to loose dust, as their current internal pressures are not high enough to account for lithified rocks [59]. This shock-induced porosity can also be the result of later impact cratering of said asteroids, but as the present microporosity is fairly consistent throughout chrondrites, the former is thought to be the main culprit, as the latter would depend to much on the number of impacts experienced by the chondrite. These microporosities are often found in the form of microcracks spreading through grain boundaries (figure 3.6) [53].

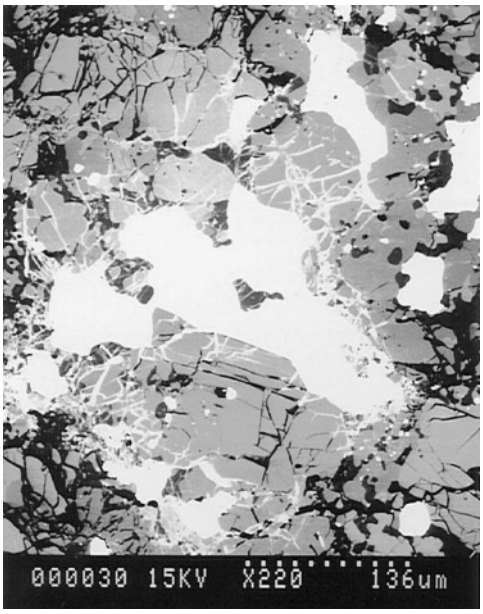

Figure 3.6: Slice image of an H5 ordinary chondrite. The black veins show the cracks accounting for the microporosity. The white areas show grains of Iron and Nickel. The partial filling of the microcracks with white material is thought to be the result of oxidation of the metallic grains with terrestrial Oxygen. From "The significance of meteorite density and porosity", by G.J. Consolmagno et al. [53].

The size of these porous cracks is the governing parameter in their effect on the muon count as shown by J. Keerl [125]. Voids much smaller than $1mm$ have an effect far below 1% on the overall muon count, whilst larger voids have an increasing effect, with $1mm$ creating an increase of 1%, 8.5% for $1cm$, and 58.4% for $10cm$. The cumulative effect of 10.000 $1mm$ voids was found to add up to a 12.5% muon increase, and is expected to be much lower for smaller voids. As the voids accounting for the microporosity are scaled in the order of μm, a thousand times smaller than voids creating a 1% increase in muons, their effect on the overall homogeneity of the asteroid is thought to be small. Their effect on material density will therefore be simulated in the model by using the average meteorite bulk density found in LL ordinary chondrite falls ($\rho_{bm} = 3.21 \pm 0.22 \cdot 10^3 kg/m^3$[33]) as opposed to their higher grain density ($\rho_g = 3.48 \pm 0.08 \cdot 10^3 kg/m^3$ [33]), for monolithic structures within the asteroid. The microcracks together with their monolithic parent material are consequently approximated by a homogeneous material with their combined average density.

Crystalline Structures
Another point of interest for the model generation, is the effect of microstructures within its material makeup. Geant4 was initially, up to version 10.2, limited to simulating only the interactions of particles with amorphous matter. As crystalline structures can and do have an effect on the path of charged particles, and asteroids contain a lot of these structures, the ability to simulate these effects is of importance to this project. The

mentioned effect is called "channeling" and creates a difference in charged particle stopping power dependant on solid-state structure orientation[90]. This could cause muons to lose less energy traversing a mineral from one angle as opposed to another, influencing the measurements performed. The GECO (GEant4 Crystal Objects) project created a general framework for use within the Geant4 environment, allowing for the simulation of interactions between particles and detailed geometric structures[15]. This framework can be used to mitigate the problem, and is included with the Geant4 package since version 10.3. However, as the size of the crystalline structures within an asteroid is many orders of magnitude smaller than the overall asteroid size, the effect of these structures on particles will average out during its traversion. Chondrules, round igneous crystalline grains found in chondrites, average a size of 0.9mm diameter in LL chondrites such as Itokawa, which is much less than the asteroid's diameter [141]. An overview of average chondrule diameters in chrondrites is shown in the following table 3.3.

Chondrite	Average Chondrule Diameter	Chondrite	Average Chondrule Diameter	Chondrite	Average Chondrule Diameter
CI	N/A	CR	0.7 mm	LL	0.9 mm
CM	0.3 mm	CH	20 μm	EH	0.2 mm
CO	0.15 mm	CB	0.2-1 cm	EL	0.6 mm
CV	1.0 mm	H	0.3 mm	R	0.4 mm
CK	1.0 mm	L	0.7 mm	K	0.6 mm

Table 3.3: Average chondrule diameters of major chondrite groups. (NA=Not Applicable). Modified, from "Systematics and Evaluation of Meteorite Classification", 2016, Table 1, by M.K. Weisberg et al. in "Meteorites and the Early Solar System II", by D.S. Lauretta and H.Y. McSween (Eds.), (p.26) [141].

Chondrules themselves can be mono-crystalline, but can contain various smaller crystalline structures as well (figure 3.7), which decreases the average geometric structure size within asteroids even further. The assumption is therefore made that muon channelling will not have a significant effect on measurement results and is hence omitted from the GDML model.

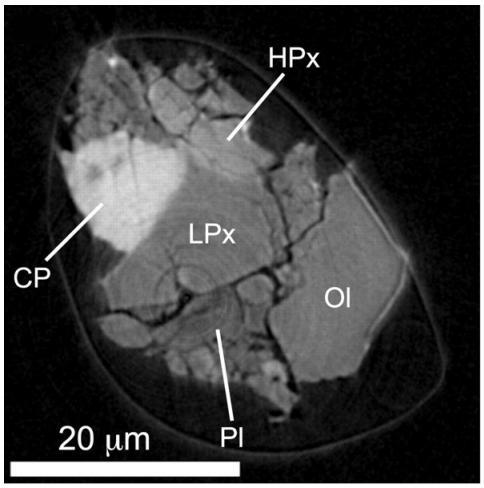

Figure 3.7: Slice image of Itokawa particle sample RA-QD02-0063, obtained by microtomography, showing different mineral structures within said particle. Modified, from "Three-Dimensional Structure of Hayabusa Samples: Origin and Evolution of Itokawa Regolith", by A. Tsuchiyama et al. [225].

Caveats

It must be noted that the available information on both crystal structures and microporosity is based in large parts on the returned samples from the Hayabusa space mission and meteorite falls on Earth. Both sample types are not an error-free source to base asteroid interior microstructure on, as both are not a representative subset of the asteroid's material. The in-situ collected samples by Hayabusa are only taken from the upper

surface, where the material is exposed to space weathering. This weathering, physical and chemical changes caused by the space environment, will have affected the upper surface more than material buried deep within the asteroid. The changes brought forth by electromagnetic radiation will mostly effect the optical properties of the surface regolith, whilst micrometeorite and particulate impacts will alter its microstructure [99]. T. Hiroi et al. [107] show that space weathering altered the surface samples of Itokawa, even to different degrees per sample site, proving surface samples are at least partially altered from their sub-surface origins.
In the case of meteorite falls, the discrepancy between its microstructure and that of asteroid interiors would be caused by the selection process taking place during atmospheric entry, where monoliths with high structural integrity (less porosity) show a higher chance of entry survival than their more porous counterparts, lowering the average porosity of Meteorites reaching Earth's surface. Atmospheric weathering causes structure changes as well, which is shown in figure 3.6. The oxidation of metals within the meteorites fills up the porous cracks, lowering their porosity. The average porosity of all ordinary "chondrite falls" (Meteorites seen to fall) is $7.4 \pm 5.3\%$ whilst among ordinary "chondrite finds" (Meteorites not seen to fall) this value equals $4.4 \pm 5.1\%$ [53]. In other words, prolonged exposure to Earth's atmospheric weathering lowers Meteorite porosity.

3.1.4. Itokawa Interior Macrostructure

This subsection treats the macrostructures thought to be present in Itokawa and other SSSBs, ranging from monoliths to voids. The homo- or heterogeneous distribution of these structures within the asteroid is discussed as well.

Rubble Pile

Most asteroids in the Solar System are not thought to be monolithic bodies, but are rather made up from numerous smaller fragments and called rubble piles, as posed in section 2.1.3. To support this claim, three observations serving as key evidence are summarised [61].
The first is existence of the clear "Spin Barrier" seen in asteroid rotation periods (figure 2.6[231]). Spinning faster than this "Spin Barrier" would let aggregated asteroids lose cohesion. Most with diameters larger than $120m$ stick to this limit, supporting the rubble pile theory.
The second argument is based on the in-situ observed macroporosity derived from surface morphology by the Hayabusa spacecraft on 25143 Itokawa [198], the Hayabusa2 spacecraft on 162173 Ryugu [232] and the OSIRIS-REx spacecraft on 101955 Bennu [140]. A large literature survey by B. Carry (2012) [40], compiling the data on 287 different SSSBs from Earthbound surveys and comparing it to known Meteorite bulk densities, shows with varying degrees of accuracy macroporosity values of up to 70%. Notable examples of these macroporosity estimates are shown in figure 2.7[34]. This asteroidal larger-than-meteorite-counterpart porosity is most likely caused by voids between solid fragments, again supporting the rubble pile theorem.
The third argument is the tidal breakup of SSSBs venturing within the Roche limit. This limit dictates the radius of a sphere around a celestial body within which a second celestial body will experience higher tidal forces than its own force of gravity, disintegrating it. This limit is vastly different for gravitationally bound fluid bodies compared to gravitationally bound rigid bodies. For fluid bodies, the tidal forces are allowed to disrupt the shape to form a prolate spheroid. Due to this deformation, the effect of the tidal disruption will increase on such a spheroid whilst its own gravitational forces on the tips will decrease, compounding the overall effect. The rigid bodies are assumed to stay spherical until their point of disintegration. The equations for Roche's limit applying to initially spherical, fluid ($a_{R_{fluid}}$) and rigid ($a_{R_{rigid}}$) bodies are as follows, where R_p is the radius of the primary, ρ_p the density of the primary and ρ_s the density of the satellite of interest.

$$a_{R_{fluid}} \approx 2.456 \cdot R_p \cdot \sqrt[3]{\frac{\rho_p}{\rho_s}} \text{[143]} \tag{3.1}$$

$$a_{R_{rigid}} = R_p \cdot \sqrt[3]{2 \cdot \frac{\rho_p}{\rho_s}} \approx 1.26 \cdot R_p \cdot \sqrt[3]{\frac{\rho_p}{\rho_s}} \text{[207]} \tag{3.2}$$

It is visible from these equations that the Roche limit for fluid bodies is approximately twice that of rigid bodies. In reality, most bodies will not respond to the tidal forces as fully rigid or fully fluid bodies, but something in between. The closer to the primary a body disintegrates, the higher the rigidity, and visa-versa. Bodies with significant structural integrity can even venture within the rigid Roche limit without disintegrating, their tensile strength holding them together.
It is known that many comets break up during their perihelion. The Roche limit can however not be used to accurately draw conclusions on the structural integrity of said comets, as thermal stresses from Solar radiation can also be a major culprit in the disintegration process. Luckily, other massive bodies in the Solar

System are known to break up SSSBs that venture within their Roche limit. One such event took place in 1994, when comet D/Shoemaker-Levy 9 (SL9) broke up into 21 fragments due to the tidal effects of Jupiter's gravity, shown in figure 3.8.

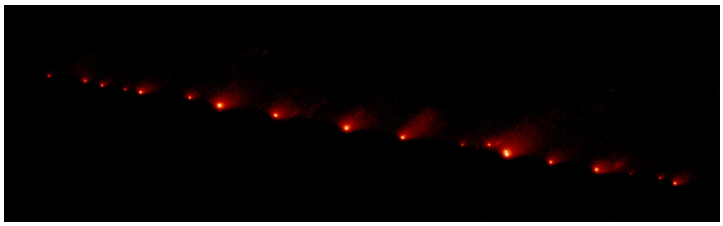

Figure 3.8: "A NASA Hubble Space Telescope (HST) image of comet P/Shoemaker-Levy 9, taken on May 17, 1994, with the Wide Field Planetary Camera 2 (WFPC2) in wide field mode." From "PANORAMIC PICTURE OF COMET P/SHOEMAKER-LEVY 9" by NASA, ESA, STScI; H. Weaver and E. Smith, 1994[172].

Using Roche limit equations 3.1 and 3.2 together with assumptions on density and measurements of its size, E. Asphaug and W. Benz concluded Comet SL9 must have been a weakly bound rubble pile body [10], as it broke up closer to the "fluid" limit. The presence and numerosity of crater chains on Jupiter's moons Ganymede and Callisto, an example shown in figure 3.9, led P.M. Schenk et al. to conclude that most, if not all comets have rubble pile nuclei[203].

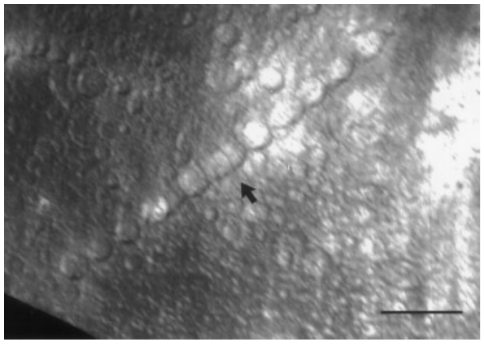

Figure 3.9: Crater chain Gipul Catena on Callisto. The scale bar depicts $100km$. Modified, from "Cometary Nuclei and Tidal Disruption: The Geologic Record of CraterChains on Callisto and Ganymede" by P.M. Schenk et al., 1996[203].

A comprehensive overview of evidence supporting the rubble pile theorem is given "Gravitational Aggregates: Evidence and Evolution" by D.C. Richardson et al., 2002 [193].

Macroporosity

The aggregated rubble pile theorem fits nicely to observations of Itokawa. Its overall bulk density is much lower than the bulk density of ordinary LL chondrites and the bulk density of the retrieved surface samples. As shown in section 2.1.3, this leads to the conclusion Itokawa has an average macroporosity of $\Phi = 40.8\%$. This means around 40.8 percent of Itokawa's volume is thought to be void space, excluding the microscopic voids within monolithic material as discussed in section 3.1.3. The parallel grooves present on Mars' moon Phobos, and the large faults of Asteroid 433 Eros, indicate some form of body-scale macroscopic voids could be present on small Solar System bodies[53]. Whether the macroporosity in Itokawa is made up from merely small scale inter-granular voids, or if the asteroid indeed does contain macroscopic cracks and voids, is not currently known. Gaining a method to reveal such features on asteroids is one of the research incentives for this thesis project.

An interesting conclusion drawn from observations made by the Hayabusa spacecraft, briefly discussed in section 2.1.4, is the difference in density between the head and body of Itokawa, shown graphically in figure 3.10. Multiple publications based on different techniques point out that the so-called head of Itokawa must have a much higher density than its body.

The first technique, mentioned in section 2.1.4, measured the acceleration of Itokawa's spin rate over a 12 year period. This change in spin rate is assumed to be caused by YORP-induced radiative torques, which

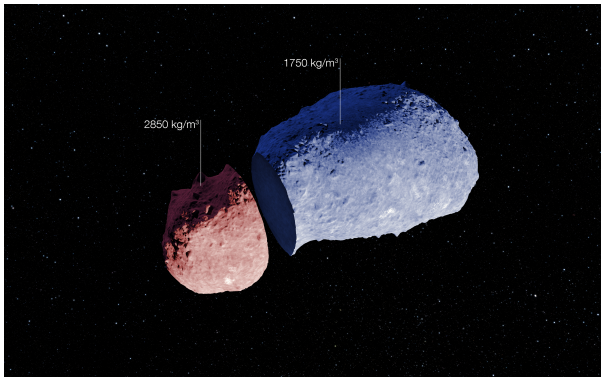

Figure 3.10: Schematic view depicting the density differences between the "head" and "body" of Itokawa, with their corresponding bulk densities[145]. From “Schematic view of asteroid (25143) Itokawa” by European Southern Observatory, 2014[74].

can be predicted using the highly detailed surface and shape topography model provided by the Hayabusa mission. This led to the conclusion by S.C. Lowry et al.(2014)[145] that the observed change in spin rate could only take place if the center of mass was shifted by $21m$ with respect to what would be expected with a homogeneous density distribution. This shift is assumed to be caused by density differences. Two different density distributions are considered, one where Itokawa is separated into a head ($\rho_b = 2.850 g/cm^3$) and body ($\rho_b = 1.750 g/cm^3$), and one where a third "neck" region is added.
The second technique, employed by M. Kanamaru et al. [123], assumes the smooth terrain areas on the surface of Itokawa comprised of centimeter sized regolith (such as the Muses Sea 2.8 [198]) to be gravitationally equi-potential surfaces. Based on this assumption, a mascon gravity model was made, from which a density distribution was proposed. This head-body difference is less dramatic than shown in figure 3.10, with the density of the head region equal to $\rho_b = 2.450 g/cm^3$, and the body region density equal to $\rho_b = 1.930 g/cm^3$. This is however based on an overall bulk density of $\rho_b = 2.020 g/cm^3$, which is calculated from the overall mass [1], divided by the Gaskell shape model volume [85]. This value is slightly higher than the $\rho_b = 1.9 \pm 0.13 g/cm3$ from A. Fujiwara et al.(2006)[83] and the $\rho_b = 1.95 \pm 0.14 g/cm3$ from M. Abe et al.(2006)[1]. The density distribution from S.C. Lowry et al.(2014)[145] is based on the latter.
To conclude, the bulk density is assumed to be higher near the head of Itokawa and the model will need to account for this.

Monoliths

Itokawa's surface is littered with numerous boulders, varying widely in shape and size. The largest, called Yoshinodai and depicted in figure 2.8[198], is observed to be $\sim 50m$ by $\sim 30m$ by $\sim 20m$. Asteroid-scale grooves or troughs are not visible on Itokawa, suggesting a lack of large internal structures. The cumulative boulder size distribution on the surface is shown in figure 3.11.
These graphs are both unbinned cumulative plots as advised by the "Crater Analysis Techniques Working Group" [96] for creating size-frequency distributions of craters, applied here on features with positive relief. The boulder size for both graphs was determined from images taken by Hayabusa, albeit with different methodologies. For figure 3.11a, J. Saito et al., 2006[198] based the graph off the maximum boulder size that could be visually determined. In figure 3.11b, T. Michikami et al., 2008[159] used the mean of the boulder's maximum size and its maximum size perpendicular to the axis of the first measurement. This not only leads to generally smaller boulder sizes for the latter, but also to a change in log-log slope, which is -2.8 for the left graph and -3.2 ± 0.1 for the one on the right. The conclusion drawn here is that larger boulders tend to be more elongated compared to their smaller counterparts[159].
Boulders formed in fragmentation events are experimentally shown to have an average aspect ratios of $1 : 0.7 : 0.5$ (Length:Width:Height), approximately $2 : \sqrt{2} : 1$ [160], assuming average tri-axial ellipsoid shapes. A selection of boulders on Itokawa larger than $6m$ show similar aspect ratios of $1 : 0.7$ (Length:Width)[155], and for another arbitrary selection of 21 boulders larger than $8m$ it equalled $1 : 0.66 : 0.46$ (Length:width:Height)[160], again showing larger boulders to be more elongated.

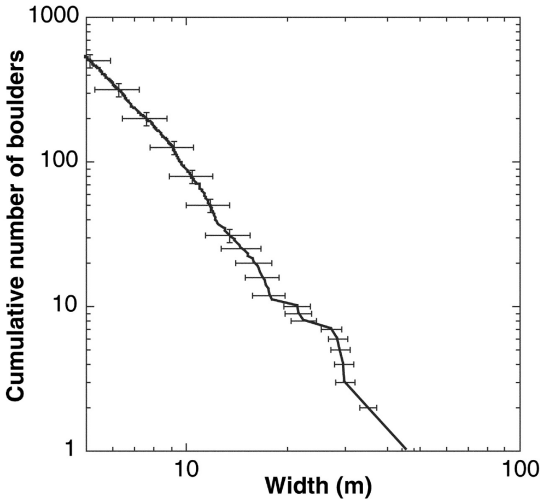

(a) Horizontal axis shows the maximum size of the boulder in meters, the vertical axis shows the cumulative number of boulders on the entire surface. From “Detailed Images of Asteroid 25143 Itokawa from Hayabusa” by J. Saito et al., 2006[198].

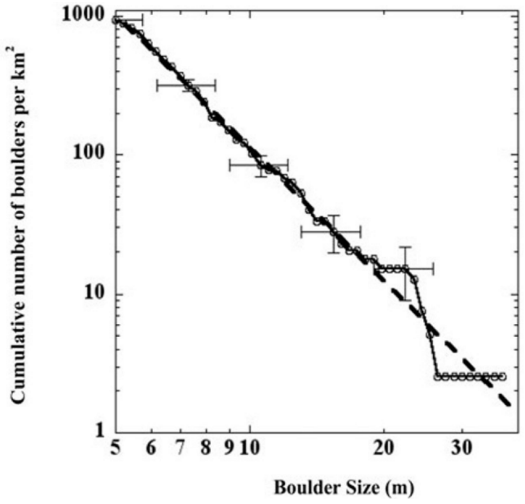

(b) Horizontal axis shows boulder size as its mean horizontal dimension in meters. Vertical axis shows cumulative number of boulders per square kilometer. From "Size-frequency statistics of boulders on global surface of asteroid 25143 Itokawa" by T. Michikami et al., 2008[159].

Figure 3.11: Cumulative boulder size distribution on the surface of 25143 Itokawa.

To account for these size-dependant shape irregularities, S. Mazrouei et al., 2014[155] created a cumulative block size distribution graph (figure 3.12) by assuming the unknown vertical height of each block to be equal to its horizontal minor axis, and calculated the diameter of a sphere of equal volume to said block.

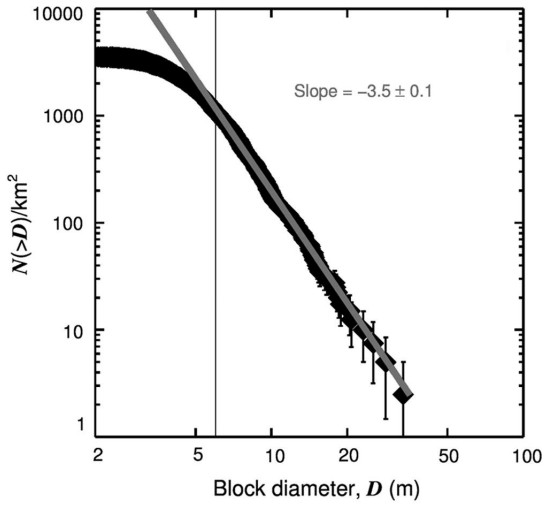

Figure 3.12: Itokawa cumulative size–frequency distribution of blocks as a function of block diameter representative of its volume. The vertical line indicates $6m$ block diameter, below which data incompleteness is assumed. The diagonal grey line shows the best-fit power law of -3.5 ± 0.1. Modified, from "Block distributions on Itokawa" by S. Mazrouei et al., 2014[155].

The term "block" is used to describe rocks and features larger than a few meters in size with distinctive positive relief, and is often used interchangeably with "boulder". The resulting graph shows an even steeper slope for the size distribution: -3.5 ± 0.1.

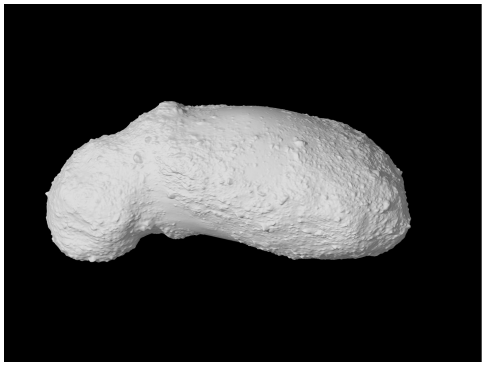

(a) Image of Itokawa rendered using the detailed topographical dataset from Gaskell et al. [85].

(b) Shape model interpreted by subroutines in the software package PKDGRAV and ray-traced with the Persistence of Vision Raytracer (POV-Ray). Region of spherical rubble pile carved out by this shape model(N=61,601).

Figure 3.13: Topographic and N-body model of Itokawa. Images and captions from "The NEOTωIST mission (Near-Earth Object Transfer of angular momentum spin test)" by L. Drube et al., 2016[64].

3.1.5. Interior Model

It is clear from section 3.1.4 that most asteroid and comets are in fact gravitationally bound rubble piles, consisting of regolith, larger monoliths of varying shapes and sizes, and void spaces. The glaring omission thus far is the available data on the size and distribution of the material making up the interior of the rubble pile. As posed in section 2.1.3, there is currently no detailed information on asteroid interior composition and macro structure available, apart from what can be sensed up to a few meters below the surface. The intricate balance between all the forces acting on the regolith, regulating this distribution, is poorly understood. Multiple theories exist describing the interior macrostructure of asteroids and some apply to Itokawa as well. There is currently no scientific consensus on which of these theories is the most likely for a given SSSB. Thus, an effort is made to allow for the creation of multiple models, simulating all probable scenarios. Model adjustments for these different scenarios are treated later in this section.

Spherical Boulder Representation

As mentioned by S. Van Wal et al. (2017) [229], it is numerically infeasible to generate and store the millions of differently shaped and sized rocks on the entire surface of a small body, let alone for the entire interior. Therefore, as a starting point for the interior structure model creation, a leaf is taken from the book of asteroid collision and formation modelling. Work in this field was pioneered by W. Benz and E. Asphaug in 1994 [9], who applied numerical methods to model the breakup of rubble pile Shoemaker-Levy 9 and later in 1995 [21] created a method of simulating brittle solids numerically by using Smooth Particle Hydrodynamics (SPH). In essence, the porosity and material distribution are simulated by using a multitude (N) of particles, often in the form of spheres. Successors to this numerical N-body simulation were later employed to simulate rubble pile asteroid physical phenomena such as tidal disruptions [192][230][241], granular dynamics due to vibrations [194][153][180][169] and catastrophic impact disruptions [16][61][64][14]. The bases for Planetesimal dynamics simulations is comprehensively shown in "Direct Large-Scale N-Body Simulations of Planetesimal Dynamics" by D. Richardson et al. (2000) [191].
To summarise, N-body spherical representations of rubble pile asteroids are the go-to solution in many fields of asteroid dynamics research, an example shown in figure 3.13[64]. Even though muon tomography simulation does not require N-body dynamics, the same modelling basis can still be applied. The choice is therefore made to model the many differently sized monolithic structures and voids within the realistic asteroid model with spheres. Packing these spheres within an asteroid model is no easy feat. In 1611, Johannes Kepler conjectured in his paper "Vom sechseckingen Schnee" (On the six-cornered snowflake)[126] that the packing density of equally sized spheres in never greater than $\frac{\pi}{3\sqrt{2}} \approx 0.74$. It took more than 400 years for a formal proof to be published [97], illustrating the shear difficulty of sphere packing. In order to solve this numerically, multiple algorithms were considered. The "Protosphere algorithm"[218] is known for its fast sphere packing capabilities, using the computing power of NVIDIA CUDA enabled GPU's for fast parallel packing. With this algorithm, which is an extension to Apollonian sphere packing, spheres will not overlap. This algorithm has already been applied to the field of planetary science, used for asteroid surface generation in

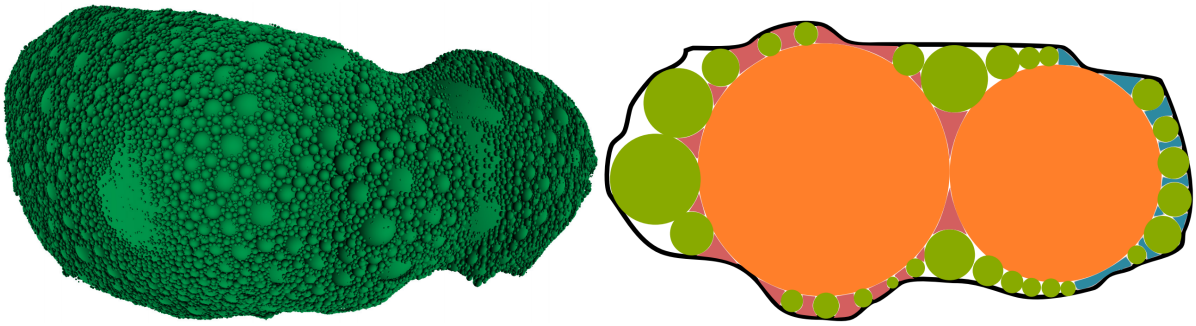

(a) 3D mesh representation.

(b) 2D schematic representation.

Figure 3.14: Itokawa Protosphere algorithm with default parameters, 100.000 spheres. Modified, from "Fast and Accurate Simulation of Gravitational Field of Irregular-shaped Bodies using Polydisperse Sphere Packings." by A. Srinivas et al., (2017)[212]

software called "AstroGen" [142]. However, as visible in figure 3.14, the algorithm starts by filling the biggest voids with the largest possible sphere. This is unwanted behaviour for interior modelling. Another downside to "Protosphere" is the lack of control over sphere size and positioning.
PKDGRAV can be used to simulate sphere packing as well, in which case gravity and dynamics will regulate the packing (figure 3.13). This soft and hard sphere discrete element simulation software package is oft-used for collision research[241]. Having gravity and inter body dynamics control the packing unfortunately removes sphere positioning control from the user and is therefore deemed unfit as a sphere packing algorithm for this application.
To mitigate this, a fully customisable code was written in *MatLab* to control the sphere positioning and dimensions. The procedural generation process of the spheres and different functions of this code are discussed in the following section.

Base Interior Model Creation
The base interior model creation process branches off from the shape model creation process described in section 3.1.1, by taking the OBJ file as shown in figure 3.5 as its starting point. The OBJ geometry file is loaded into *MeshLab*, an open-source 3D mesh processing software system[50]. *Meshlab* can be used in turn to convert the OBJ file format to a broad range of other file extensions, such as the *3D Systems* STereoLithography ($.stl$) format, which is of particular interest as it is an oft-used extension for Computer-Aided Design (CAD) and 3D modelling. In this situation, *MeshLab* will be used to check the model's surface for continuity. Any holes in the model's mesh can be patched using the software's features.
Next, the OBJ file data is imported into *MatLab* as two separate matrices. The first, called $S.vertices$, contains the x, y and$z$ coordinates of the mesh model vertices. The $S.faces$ matrix contains pointers to the row numbers of vertices in matrix $S.vertices$. Each row contains three vertices to create the triangular faces of the polyhedral mesh. The resulting mesh is shown in figure 3.15. To create the random distribution of spherical voids and monoliths within the shape model of Itokawa, the Mersenne Twister pseudorandom number generator, included in *MatLab*'s rng function, is used to generate horizontal spherical coordinates for a points distribution within a unit sphere of $1km$ radius. The following equations for azimuth ($\angle\phi$), elevation ($\angle\theta$) and radial distance (r) were used.

$$\angle\phi = 2 \cdot \pi \cdot rand \tag{3.3}$$

$$\angle\theta = \arcsin(2 \cdot rand - 1) \tag{3.4}$$

$$r = \sqrt[3]{rand} \tag{3.5}$$

In these equations, $rand$ depicts the output of the random number generator. *MatLab*'s "rng" function has a range between 0 and 1, so modifications are made to adjust its regime to what is needed for the horizontal spherical coordinates. Even though r needs a range between $[0-1]$ as well, using the distribution provided by "rng" would lead to more points towards the centre of the spherical distribution, following a power of 3 function, calling for a correction in the form of a cube root. These point coordinates are in turn converted to Cartesian coordinates, with each value equally scaled to create a sphere completely enveloping the model. In this case, the unit sphere distribution is scaled by 0.35 to more closely envelop the Itokawa model. A *MatLab* code based on "in_polyhedron.m" by J. Tuszynski [227] is used in turn to check which points are inside the model, and which are outside. This code uses the algorithm proposed in "Fast, Minimum Storage

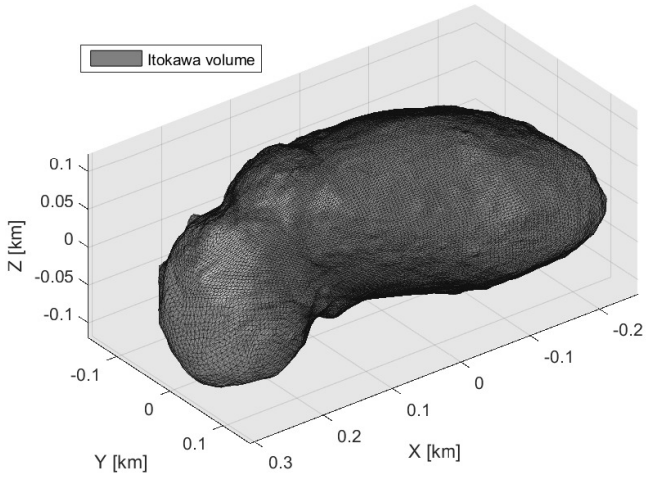

Figure 3.15: Itokawa polyhedral mesh shape model in *MatLab*.

Ray-Triangle Intersection" by T. Moeller and B. Trumbore (1997) [170], to efficiently find the points inside the model. The core of this algorithm is the counting of the number of times a random ray shot from one of the points, intersects the model's surface. If this is an odd number, the point lies inside the model, and visa-versa. The results of this process for 2000 points is shown graphically in the following figure 3.16. A relatively low number of initial points is used in the upcoming example figures to support clarity and ease of viewing.

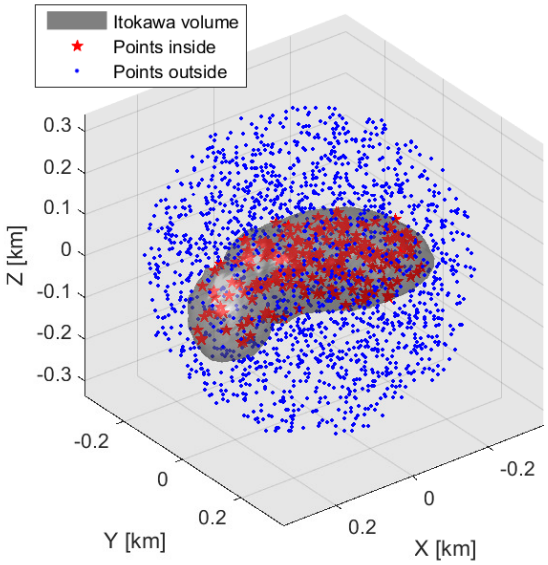

Figure 3.16: Itokawa polyhedral mesh shape model with random distribution of 2000 points within a sphere of $0.35km$ radius in *MatLab*. Points determined to be inside the model are depicted as red stars, their counterparts outside as blue dots.

The points outside the model are discarded for the rest of the interior creation process. The next step involves turning the points into spheres, without protruding from the surface or overlapping. The code used for "growing" these points into spheres without overlap is based on "growbubbles.m" by S. Holcombe [110]. The code uses a "Nearest Neighbour" algorithm, which is a sub graph-type of Delaunay triangulation, to find each point's nearest neighbouring point. Each point is then "grown" into a sphere with a radius equal to half the distance to the nearest neighbour. All sets of points that are each-others nearest neighbour are now finalised. All other spheres are grown one by one, by their distance to the closest sphere's surface minus their

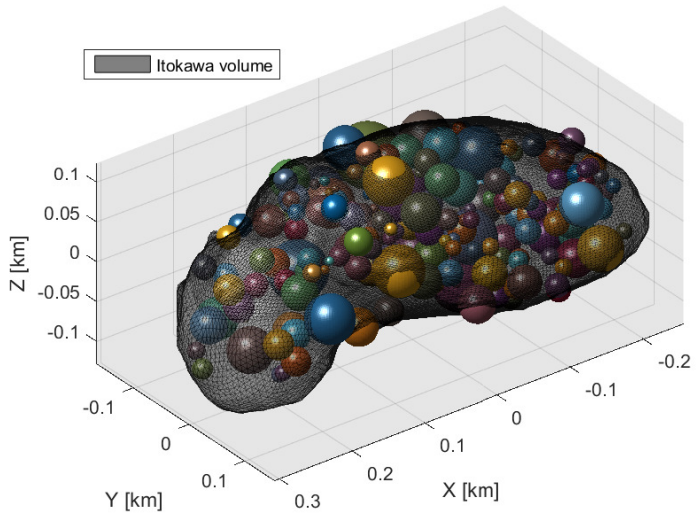

Figure 3.17: Itokawa polyhedral mesh shape model with non-overlapping packing of 215 randomly distributed spheres.

own radius. The 2000 points shown in figure 3.16 resulted in 215 points inside the Itokawa model, which after the sphere growing process are shown in figure 3.17. From this image, spheres can clearly be seen protruding from the surface. As the number of points increases, the average sphere diameter will decrease, and as each sphere's centre will lie beneath the surface of the model, this will lead to less protrusion by volume. However, to stay true to the shape model and prevent overlap within the GDML model, an effort is made to mitigate this problem. For every point inside the model, the shortest distance to the surface of the model is calculated. The algorithm finds the nearest vertex, the nearest point on an edge and the nearest point on a triangle surface. The shortest distance of these three is returned, defining the shortest distance to the model's surface (figure 3.18). The *MatLab* code used is based on "points2trimesh.m" by D. Frisch [82].

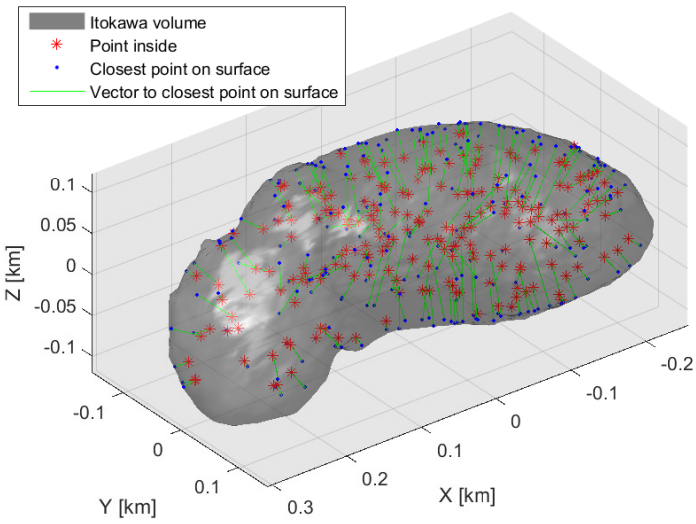

Figure 3.18: Itokawa polyhedral mesh shape model with green vector lines depicting the shortest distance from interior points (red asterisk) to points on surface features(blue dot).

In the final step, all spheres with radii larger than the distance value returned in the previous step, will either be shrunk accordingly or removed altogether. Both of these solutions have implication for the sphere size distribution throughout the asteroid. Removal leads to less spheres the closer to the surface, whilst shrink-

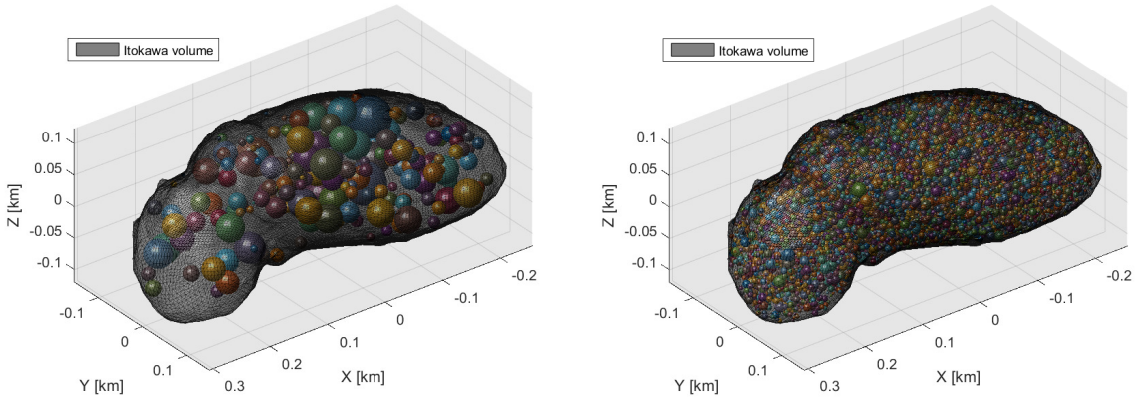

(a) 215 spheres

(b) 9907 spheres

Figure 3.19: Itokawa polyhedral mesh shape model with non-overlapping, non-protruding random sphere packing.

ing results in on average smaller spheres close to the model's outer layer. The results of the shrinking process applied to the same initial conditions as the previous figures are shown in figure 3.19a. The resulting spheres adhere to all constraints posed by GDML. For the "Base Model", the model on which all alternative models discussed in this chapter are based on, we assume no macroscopic voids to be present. The total volume of the spheres is determined and their density is set to the bulk density of LL ordinary chondrites ($\rho_{bm} = 3.21 \pm 0.22 \cdot 10^3 kg/m^3$ [33]). From this, and the total average density of $1.9 - 1.95 \pm 0.13 - 0.14$ $g \cdot cm^{-3}$[83][1], the density of the non-monolithic regolith is determined. Table 3.4 shows per example these results and density inputs for the Itokawa model with 9907 spheres (figure 3.19b).

Data	Value	Unit	Data	Value	Unit
Number of Spheres	9907	[-]	Fill Percentage	16.26	[%]
Maximum Diameter	22.68	[m]	Density Model	1.925	$[g/cm^3]$
Minimum Diameter	10.86	[mm]	Density Spheres	3.21	$[g/cm^3]$
Mean Diameter	6.95	[m]	Density Regolith	1.675	$[g/cm^3]$
Median Diameter	6.6	[m]	Log-Log Slope (D>6m)	-3.7654	[-]

Table 3.4: Data on Itokawa model with 9907 procedurally generated spheres.

The fill percentage denotes the fraction of the total volume of the model filled with sphere volumes. The coordinate and radius data of all the spheres is exported to a GDML file, where the loop function as described in the GDML User's Guide [73] is used to create "parameterised orbs", reading the parameters from the table containing said data. These orbs are nested within the Itokawa tessellated solid, therefore passing the overlap check and allowing them to be placed inside the volume of the model. The schematic flow diagram in figure 3.20 graphically shows the steps taken in this process.

This base model adheres to all density, volume, composition, porosity and mass constraints. However, the size-frequency distribution as well as the location dependant size-frequency distribution of the spheres is not fitted to promising theorems. The following subsections will show the modifications that can be made to this universal interior model to fit the multitude of theorems governing SSSB interiors.

Homogeneous Interior Distribution

An unbinned log-log plot of the size-frequency distribution (SFD) of the 9907 spheres shown in figure 3.19b, adhering to the crater analysis SFD standards[96], with modifications to work with cumulative count per volume instead of area, yields the following graph 3.21. The slope of the polynomial curve fit applied to the spheres with diameter $6m$ and up, yields a comparable value to what was found by S. Mazrouei et al.[155] in figure 3.12: -3.7654 versus -3.5 ± 0.1 respectively. Comparing the two graphs visually does show a few mismatches, mostly caused by the concave downward nature of the SFD for the model, whereas the Mazrouei et

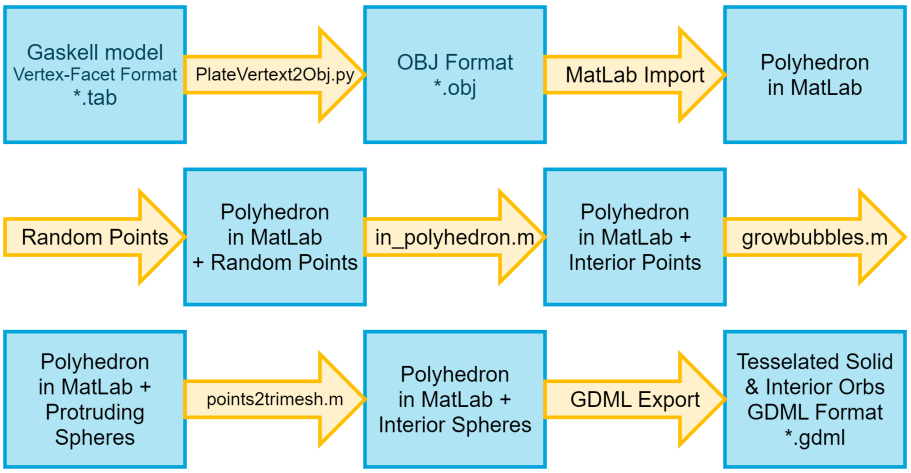

Figure 3.20: Flow diagram of conversion steps from Gaskell shape model [85] to GDML code containing interior sphere size, density and distribution information. Mentioned code files are often heavily modified before use, the code file names are mentioned nonetheless for clarity. (Own Work)

al. graph seems to follow a linear trend in log-log scale. In comparing, the assumption is made that cumulative distribution per area scales linearly with cumulative distribution per volume.

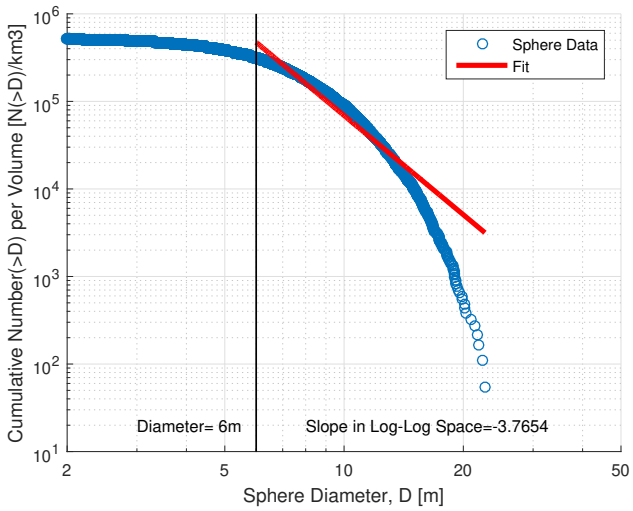

Figure 3.21: Unbinned cumulative size-frequency distribution of sphere diameters. The vertical line indicates a sphere diameter of $6m$. The diagonal red line shows the best-fit power law of -3.7654.

If one assumes the surface size-frequency distribution (SFD) of boulders to be representative of the SFD of its sub-surface monoliths, then the model needs to be adjusted to fit measurement data. A polynomial fit of the graph between $6m$ and $20m$ diameter is made, to stay true to the lower limit of linearity found by S. Mazrouei et al.[155], and remove outliers above $20m$. The process of adjusting the SFD is performed by adjusting the sphere population according to a calculated formula. The effect of removing a sphere in a certain location causes the curve to lower in the y axis. The best linear fit in log-log scale shown in 3.21 is shifted until it lies completely beneath the polynomial fit (figure 3.22). The equation governing the difference between the two is used in turn to remove certain spheres, until the entire sphere population adheres to this log-log linearity. The same method is applied to different best-fit power laws, such as the previously mentioned -3.5 ± 0.1[155] found on the surface of Itokawa.

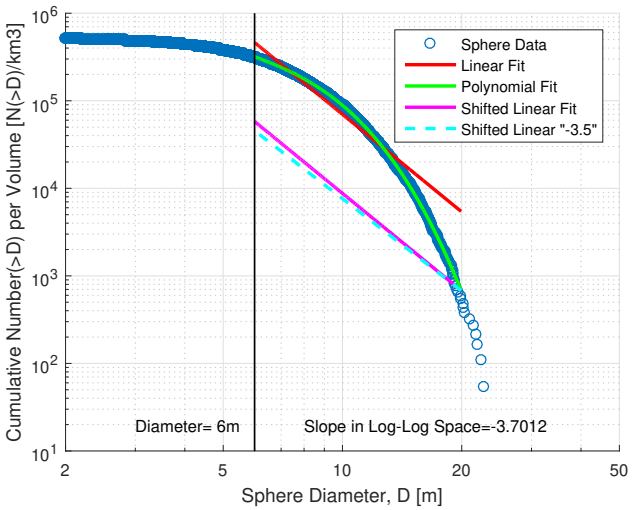

Figure 3.22: Unbinned cumulative size-frequency distribution of sphere diameters. The vertical line indicates a sphere diameter of $6m$. The green curve shows the best-fit polynomial between $6m < D < 20m$, the diagonal red line shows the best-fit power law of -3.7012 for this section. The magenta line shows the same power law and the dashed cyan line shows a power law of -3.5, both shifted to lie beneath the green polynomial.

This method allows for the adjustment of the model to fit data of surface boulders SFD for SSSBs.

Inhomogeneous Interior Distribution

Thus far, a homogeneous distribution of boulders throughout the SSSB has been assumed in the model creation process. Many theorems however show that this might not be the case. As a first example, S. Mazrouei et al. [155] state that the surface boulders are much more exposed to the harsh space environment. They are subjected to large thermal fluctuations and (micro-)Meteorite impacts, causing fractures and dis-aggregation. This in turn would lead to, on average, smaller boulder diameters on the surface.
Other papers speak of granular convection or subsidence, analytically and numerically showing that at least some form of size-dependant granular transport is assumed to take place within SSSB interiors (figure 3.23). The vibrations [164] caused by (micro-)Meteorite impacts, thermal stresses [154] and tidal forces are thought to be the driving force behind this granular transport. These vibrations could cause smaller pebbles to fill voids deep in the interior, whilst larger boulders, too large to fill the many smaller voids, stay on top[180], as shown in figure 3.23.

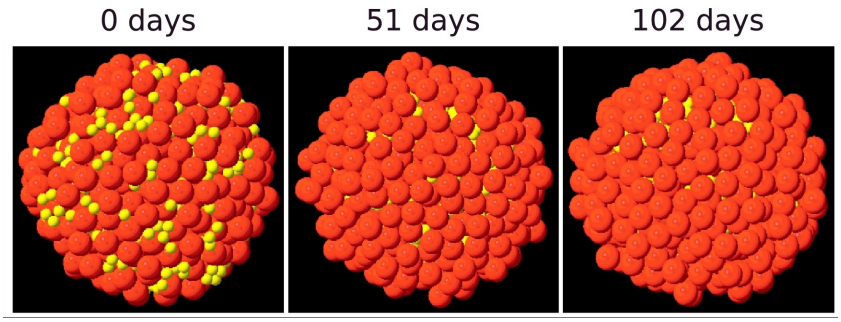

Figure 3.23: Brazil Nut Effect simulation. Larger particles (radius 80 m) are coloured red and the smaller particles (radius 40 m) are coloured yellow. The maximum magnitude of shaking was 46.21% of the escape speed (34.7 cm/s). Three stages (0, 51, and 102 days) of the simulation are shown. Modified, from "The spherical Brazil Nut Effect and its significance to asteroids" by V. Perera et al., (2016)[180].

Another oft-used theorem is called the Brazil Nut Effect (BNE), a granular convection and sorting theorem that describes how the largest particles in a granular material seem to end up on the surface after vibration induced convection. The effect is named after Brazil Nuts, an edible large South-American seed often found on top of store-bought nut mixes. This effect could cause on average larger boulders to appear on an asteroid surface[169]. The reverse BNE, where larger particles subside, could also take place, as BNE is quite poorly

understood in a low gravity, low friction environment. T. Shinbrot et al.[206] think the vibrations needed to drive the Brazil Nut Effect within a sensible time frame would be higher than the escape velocity of smaller SSSBs such as Itokawa, proposing ballistic sorting as a granular convection alternative. In this proposed scenario, smaller pebbles are more likely to rebound after an impact and subsequent end up in lower regions on the surface, essentially sinking the smaller pebbles versus larger boulders. This is visually quite clear in lower regions such as the Muses Sea and Sagamihara on Itokawa (figure 2.8).
As the construction algorithm of the asteroid interior uses a growing sphere method, the process of creating a size-dependent sorting within the interior is fairly simple. For larger boulders near the surface, the number of points from which spheres are grown is decreased further out from the center, to simulate interior dynamics governed by large boulder convection. The reverse is used to simulate an environment governed by subduction of larger rocks. All three scenarios are depicted graphically in figure 3.24.

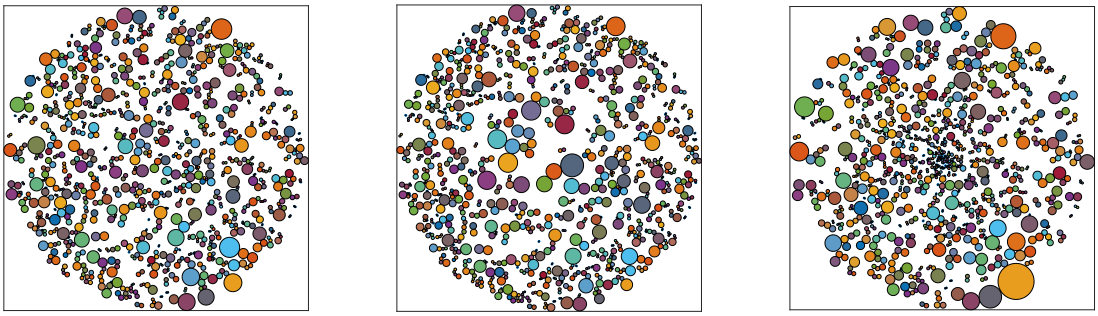

(a) Homogeneous Distribution (b) Subductive Distribution (c) Convective Distribution

Figure 3.24: Graphical 2D representation of three slices of sphere distributions within arbitrary models dependant on ruling size-sorting theorem. Made with 1000 circles.

Body-Sized Voids and Features
Large macroscopic, body-sized features, can be manually placed within the model before the sphere growing process is initiated. Using the inverse of the "in_polyhedron.m" code [227] (figure 3.16), all points remaining within the newly placed feature can be removed. This is followed up by the "points2trimesh.m" code [82], after the sphere growth process took place, to remove intersections and overlaps. The material of such features can be chosen to differ from the surrounding mineralogical make up. This can therefore be used to simulate foreign inclusions such as exotic Meteorite captures. The notable "Black Boulder" on Itokawa (figure 2.8) is thought to be one such rock [106], indicating the presence of foreign inclusions.
Voids within the model can be manually generated as well, by setting the material of chosen sphere or feature to "G4_Galactic", retrieved from the *Geant4* Materials Database [89]. This online database is directly accessible by GDML code in *Geant4* and contains simple atomic elements as well as complex compounds provided by the National Institute of Standards and Technology (NIST). This "Galactic" material simulates the near-perfect vacuum of space.

3.2. Simplified Asteroid Model

The realistic asteroid model creation process shown in the previous section 3.1 yields a computationally very demanding GDML model. In some cases, such as a parametric or sensitivity analysis, a fast simulation time is required for rapid testing. Slow simulation time can be mitigated by the use of more computing power, but sometimes this is not available, expensive or plainly not required for the analysis. Therefore a simplified version of the realistic model is presented in this section. This is not only computationally less intensive, it also provides the basis for a parametric study, yielding relatively comprehensible results.

3.2.1. Model Simplifications

In order to create a less complex, computationally less intensive model, simplifications are made to asteroid size and shape parameters.

Model Size

Decreasing the size of the model results in faster simulation times, but only from a certain size threshold. Table 3.5, created from research results of J. Keerl [125], shows simulation time versus asteroid size, the increase of which stagnates at $10m$ depth and up. This simulation time ceiling is attributed to the fact that the most computational intensive calculations are performed for interactions taking place in the first few meters of regolith; the collision of protons with regolith.

Depth [m]	0.5	1	2	5	10	20	50	100	200	500
Time [s]	18.46	93.18	387.82	786.72	839.94	833.4	846.4	849.3	841.3	839.88

Table 3.5: "Simulation time of 250.000 protons with an energy of 50 GeV for different depths of asteroid material." Caption and table from "Characterisation of radiation in the proximity of small celestial bodies and the respective implication on muon tomography in space", appendix A, by J. Keerl (2020) [125]

Table 3.5 only shows the simulation time for 250.000, $50GeV$ protons hitting a $500m$ by $500m$ surface of varying thickness. As no sensitivity study was performed on the effects of parameters such as proton energy, material composition, density and model shape, no logical conclusion for an optimal model size can be drawn. Used as empirical evidence however, it shows the decrease in simulation time for smaller asteroid sizes. For fast simulations, asteroid diameters of less then $10m$ will therefore be used.

Model Shape

Asteroids are often represented in simulations by simple spherical models, as shown previously in section 3.1.5. Research into asteroid muon tomography by D. Hodge [109] and T.H. Prettyman [186] was based upon simulation runs on a spherical representation of an asteroid. In other fields of SSSB research, this approach for surrogate asteroid models is oft-used as well [180]. This well-defined shape can therefore be used to compare results with other studies and is hence chosen as the proxy asteroid for the *Geant4* simulations.

3.2.2. Simplified Model Creation

The process of creating the simplified asteroid model is largely derived from the realistic asteroid model creation process, which is schematically shown in figure 3.20. The few differences will be discussed in this section.

The procedure starts with the creation of the shape model. For this step, the 3D modelling and rendering package *Blender* [25] is utilised to create a sphere model. The "icosphere" mesh object creation is chosen, which creates a spherical polyhedron with 20 triangles, called an icosahedral sphere. These 20 faces are then subdivided 7 times to create a more detailed representation. The model is exported as *Alias|Wavefront* OBJ ($.obj$) format, after which it can be imported into *MatLab*. The interior creation steps following the model import are identical to the steps discussed in section 3.1.5. The resulting simplified asteroid is shown in figure 3.25. The outer shape model will be represented in GDML as a "parameterised orb" as opposed to a "tessellated solid"[73], which is used for the realistic shape models.

3.3. Comet Model

It is clear from previous performed studies on the feasibility of muon tomography for SSSB interior characterisation that the expected muon flux created by primary cosmic ray interaction with solid asteroid material is very low [109][125][186][187]. So low in fact, that it is one of the main points on which the entire project's feasibility hinges. In low density regions such as Earth's upper atmosphere, a significant portion of the mesons produced in cosmic ray collisions is allowed to decay to muons. In solid, dense matter, these mesons tend to collide before decaying, greatly decreasing the muon flux available to the hodoscope instrument.

Comets generally have a much lower density than asteroids, which could allow a larger number of mesons to decay before colliding in the upper surface layers. Additionally, comets have a coma around them which could create cosmic ray showers, increasing the muon count even further. This possibly greater muon flux could greatly improve the feasibility of the project and therefore comets are a very interesting subject to model and use in the *Geant4* simulation.

The most recent close observations of a comet were made with the Rosetta spacecraft. For this section, its mission target Comet 67P/Churyumov–Gerasimenko is chosen as the main subject for comet modelling.

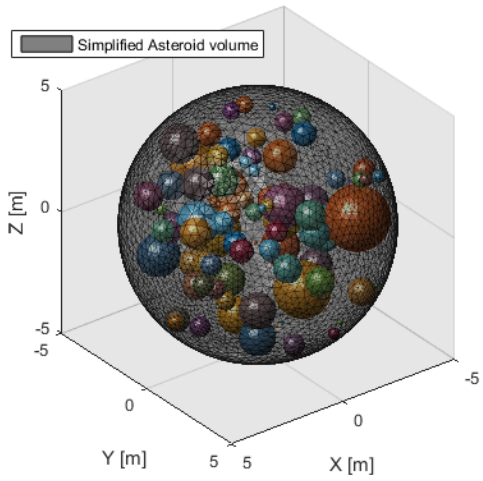

Figure 3.25: Simplified asteroid model of a 10m diameter sphere, with 96 non-overlapping, non-protruding spheres.

3.3.1. Comet Interior

At the time of writing (2020), there is no direct composition information available on comet surface and interior material. The Philae lander of the Rosetta mission did not touch down as planned and in-situ composition studies of the surface could not be fully completed [77]. Data from other missions is also lacking and the little that is available could be considered indirect. The Stardust mission for instance, the only sample return mission to a comet to date, captured the dust particles present in the coma of Comet 81P/Wild [224], which is telling of a comets surface composition but not conclusive in-situ evidence. The collected dust samples from Stardust showed similarities with carbonaceous chondrites, but smaller than expected in size [32].

Dust and Refractories

The elemental abundances found in 30 selected dust particles of Comet 67P, based in part on deductions from atomic ratios, are shown in table 3.6[17].

Element	67P	(−)	(+)	CI chondrite	(±)
C/Fe	19	14	25	0.87	0.11
N/Fe	0.66	0.69	1.1	0.064	0.011
O/Fe	19	11	22	8.8	1.1
Na/Fe	0.28	0.18	0.56	0.07	0.01
Mg/Fe	0.4	0.2	0.4	1.2	0.1
Al/Fe	0.061	0.037	0.095	0.1	0.01
Si/Fe	3.5	1.7	3.7	1.1	0.1
K/Fe	0.0074	0.0035	0.0069	0.0042	0.0003
Ca/Fe	0.019	0.008	0.015	0.069	0.006
Cr/Fe	0.0093	0.0035	0.0062	0.015	0.001
Mn/Fe	0.015	0.003	0.003	0.011	0.001
Fe	≡ 1			≡ 1	

Table 3.6: "Elemental abundances relative to Fe in 67P's dust and in the CI-type chondrite." Table and caption from "Carbon-rich dust in comet 67P/Churyumov-Gerasimenko measured by COSIMA/Rosetta" by A. Bardyn et al., (2017) [17].

On a preliminary best effort basis, the composition of the comet will be modelled using this data, as obtained by the Rosetta mission. The on-board COSIMA (Cometary Secondary Ion Mass Analyser) instrument was used to detect the composition of these solid dust particles ejected from Comet 67P's surface. The val-

ues show that, to within a factor of 3, most abundances can be compared to carbonaceous chondrites, with carbon being the notable exemption.

Ices

The composition of the ices present within the comet is largely derived from volatiles within its coma. These cometary "atmospheres" can in part be researched with IR and UV long-slit spectroscopy and radio mapping from Earth and Earth orbit. With this spectroscopy data, enhanced with in-situ measurements of past missions, D. Bockelée-Morvan et al. (2004) [27] created figure 3.26, containing the relative abundances of cometary ice "parent" molecules (molecules thought to exist in the ices, before disintegration by per example photolysis [26]). The main component of this comet nuclear ice is water ice (≈ 80%), followed by carbon monoxide ice and carbon dioxide ice.

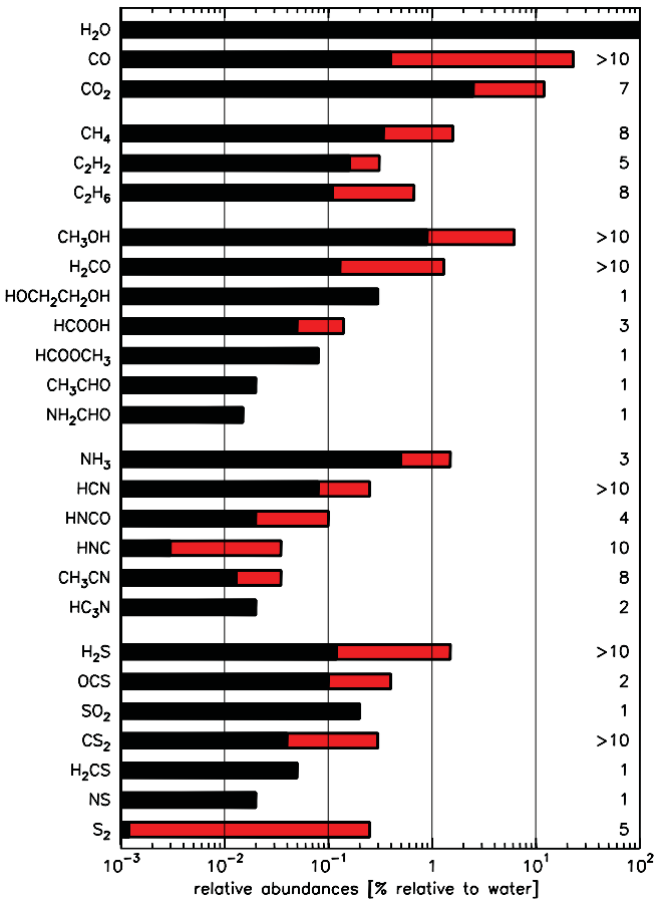

Figure 3.26: Abundances relative to water of cometary parent molecules. The range of measured values is shown in the red portion. The number of comets in which the molecule has been detected is given on the right (adapted from Bockelée-Morvan et al. (2004)[27]). From "An Overview of Comet Composition" by D. Bockelée-Morvan et al., (2011) [26]

Parent Molecule	W.r.t. H_2O[%] (Summer)	W.r.t. H_2O[%] (Winter)
H2O	100	100
CO	2.7	20
CO2	2.5	80
CH4	0.13	0.56
C2H2	0.045	0.55
C2H6	0.32	3.3
CH3OH	0.31	0.55
H2CO	0.33	0.53
HOCH2CH2OH	0.0008	<2.5e-3
HCOOH	0.008	0.03
HCOOCH3	0.004	0.023
CH3CHO	0.01	0.024
NH2CHO	<1e-4	<1e-3
NH3	0.06	0.15
HCN	0.09	0.62
HNCO	0.016	0.031
HNC	[i]	[i]
CH3CN	0.006	0.016
HC3N	<2e-5	<5e-4
H2S	0.67	1.75
OCS	0.017	0.098
SO2	0.011	0.041
CS2	0.003	0.024
H2CS	[N/A]	[N/A]
NS	[N/A]	[N/A]
S2	0.0004	0.0013

Table 3.7: Abundances relative to water of cometary parent molecules in Comet 67P/Churyumov-Gerasimenko. The two columns show the summer and winter hemisphere. Values are derived from ROSINA instrument measurements, taken at 3AU from the sun. Adapted from "Inventory of the volatiles on comet 67P/Churyumov-Gerasimenko from Rosetta/ROSINA" by L. Le Roy et al., (2015)[197].

L. Le Roy et al. (2015) [197] created an inventory (table 3.7) for these abundances measured on Comet 67P by the ROSINA (Rosetta Orbiter Spectrometer for Ion and Neutral Analysis) instrument. HNC, denoted with *[i]* in the table, cannot be distinguished from HCN by the ROSINA instrument. It is clear that large differences exist between the chemical composition of the coma on the summer versus the winter hemisphere. This dissimilarity is thought to be caused by the difference in sublimation temperatures of the different volatiles. As water has a much higher sublimation temperature when compared to carbon dioxide, the latter is expected to show up in higher relative abundances to water on the winter hemisphere, where temperatures are lower and water sublimates much less. Nonetheless, the relative abundance of CO_2 and C_2H_6 is considered high even for winter hemispheres. Molecules with relatively high sublimation temperatures, such as $(CH_2OH)_2$, ethylene glycol, are largely underrepresented. This is attributed to the fact that most of the ROSINA measure-

ments were taken at a heliocentric distance of $3\,AU$, whereas the measurements for values in figure 3.26 were often taken at distances less than $2\,AU$[197]. Coma measurements can not be used as a one-to-one indication of comet volatiles composition, due to these distance effects and space weathering. Effects of the latter can also be deduced from ROSINA instrument data. The relative lack of CO and CO_2 on the comet's summer hemisphere could not only be caused by the previously mentioned difference in sublimation temperature. It could also indicate that the persistent heating by Solar radiation has depleted parts of the carbon-chain on the surface, which in turn alters the signature present in the coma.

Porosity and Macrostructure

Tables 3.6 and 3.7 present a good first order approximation for the composition of cometary dust and ice respectively. To finish the comet model, information on the volume ratio between the two is needed, as well as information on the interior macrostructure. Based on data from the CONSERT instrument on-board Rosetta, W. Kofman et al. (2015) [129] calculated the electromagnetic permittivity of the material make-up of Comet 67P. This allowed for a relationship to be quantified between ordinary chondrites or carbonaceous chondrites, ice and porosity, based of their respective known permittivity. The two ternary diagrams shown in figure 3.27 show the relationship between dust, ice and porosity, with areas corresponding to CONSERT measurements marked in yellow and red.

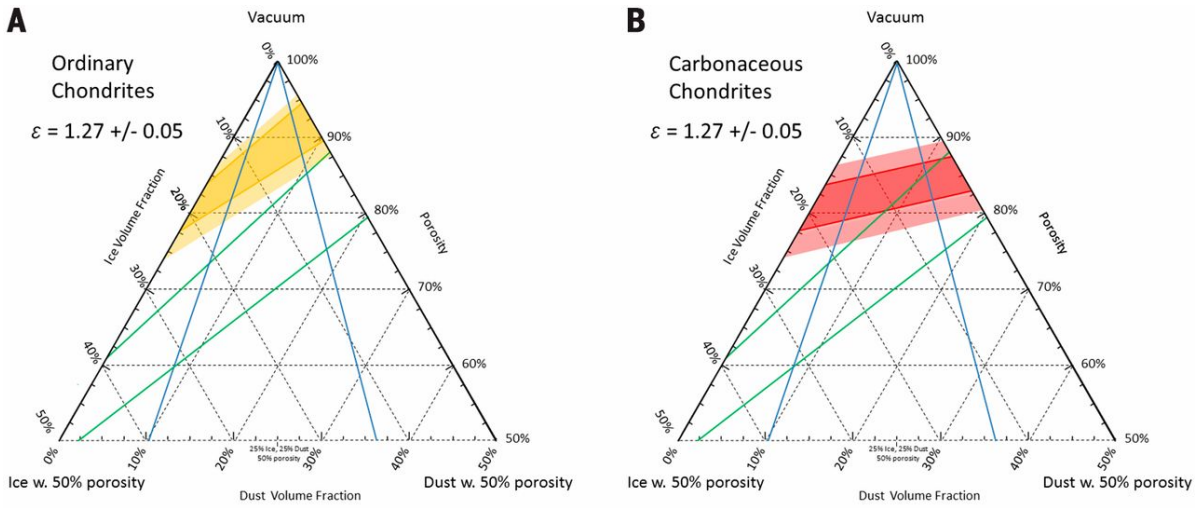

Figure 3.27: Two ternary diagrams showing the volumetric fractions of dust, ice and porosity for cometary material. Porosity is the sum of micro and macroporosity. The yellow and red areas delimit regions of equal permittivity to 67P. The green and the blue lines delimit possible densities and possible dust/ice ratios respectively. **A:** Ordinary chondrite dust. **B:** Carbonaceous chondrite dust. From: "Properties of the 67P/Churyumov-Gerasimenko interior revealed by CONSERT radar" by W. Kofman et al., (2015)[129].

The volume ratio of dust versus ice (refractory-to-ice) ranges from 0.4 to 2.6 while the porosity ranges from 75% to 85%. Based on CONSERT measurements the interior seems to have no inclusions or voids larger than a few times the signal wave length ($10\,m$) [28]. Unfortunately, deductions made on interior refractory-to-ice ratios based on data from other instruments, or using different analytical techniques, end up with much broader ranges and different values [46]. The discussion on who is right and whether a conclusion can even be drawn based on available data is still very much ongoing. For the creation of the comet model, refractory-to-ice and porosity ranges can be easily adjusted to test a variety of theories. The number of spheres is increased to account for the maximum inclusion size of $10\,m$. The resulting model is shown in figure 3.28.

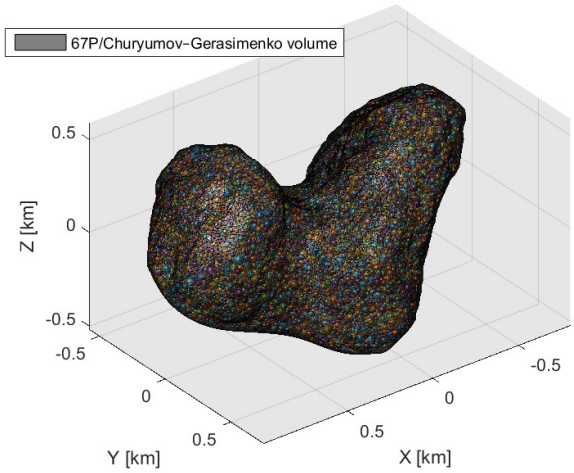

Figure 3.28: 67P/Churyumov-Gerasimenko polyhedral mesh shape model with non-overlapping, non-protruding sphere packing. Mesh model from Rosetta's OSIRIS and NAVCAM data, by ESA - European Space Agency (2014) [70].

3.3.2. Comet Coma

Comas are a comet's atmosphere, consisting of outgassed volatiles and dust particles. The density of this tenuous atmosphere is high enough for it to measurably interact with incident photons and particles. The scattering and reflection of photons in the tail and coma of some comets is visible with the naked eye from Earth. The ionisation of molecules and atoms in the coma, by photons, produces an often green glow, visible from Earth as well. This ionising green glow, together with photon reflection and scattering by the coma of Comet C/2020 F3 (NEOWISE), is shown in figure 3.29a.

(a) Image of Comet C/2020 F3 (NEOWISE), with zoom of coma. Captured with a Canon EOS 700D, 50mm, f/2.5, ISO-800 and 6 second exposure time, on the 20th of July 2020, 22:35 CEST, near Grado, Italy. (Own work)

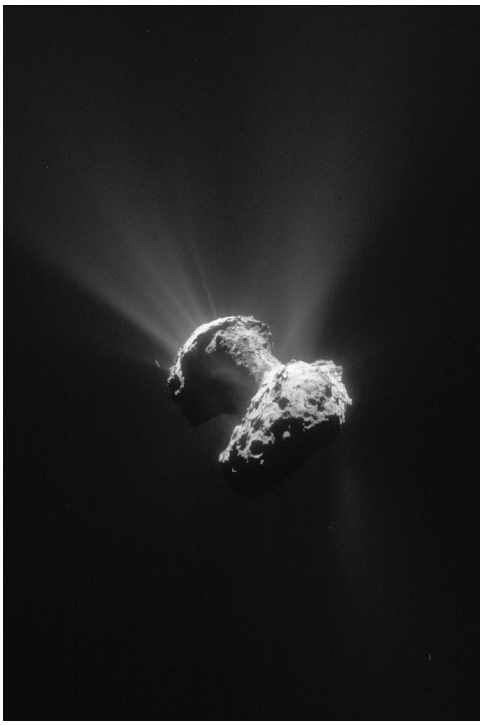

(b) Image of Comet 67P activity, taken by the Rosetta navigation camera on June 21st 2015. Cropped, from "Comet activity, 21 June" by ESA - European Space Agency[67]. Licensed under CC BY-SA 3.0 IGO.

Figure 3.29: Images of Comet C/2020 F3 (NEOWISE) and Comet 67P/Churyumov-Gerasimenko indicative of radiation interaction with the coma.

This empirically proves the significant interaction between photons and particles in the coma. Interactions between particle radiation and the coma was not observed until very recently, when data from the ALICE instrument showed the existence of a far-UV aurora around Comet 67P, likely caused by energetic electrons from Solar wind [84]. Cosmic rays should therefore, although lower in number than photons and Solar wind electrons, interact as well with the dusty gaseous cloud around a comet. How to model such a coma and whether this interaction has any measurable effect on the muon flux through the comet are questions that will be answered in this subsection.
Comet comas can be very large in radius, with molecules detected at distances greater than $r = 10^5 km$ from the nucleus [54]. In such a tenuous gaseous environment, muons are expected to lose very little energy trough particle interactions. The decay times of muons, produced by primary cosmic ray collisions with outer coma particles, are therefore expected to be the governing factor controlling the muon count near the nucleus. A heuristic calculation shows the average muon travel range in a vacuum versus muon energy graphically in figure 3.30. This calculation takes relativistic effects into account, and uses the energy of "once per hour per square metre" muons, derived from the energy spectrum of muons arriving on Earth's surface [185], as upper limit of interest.

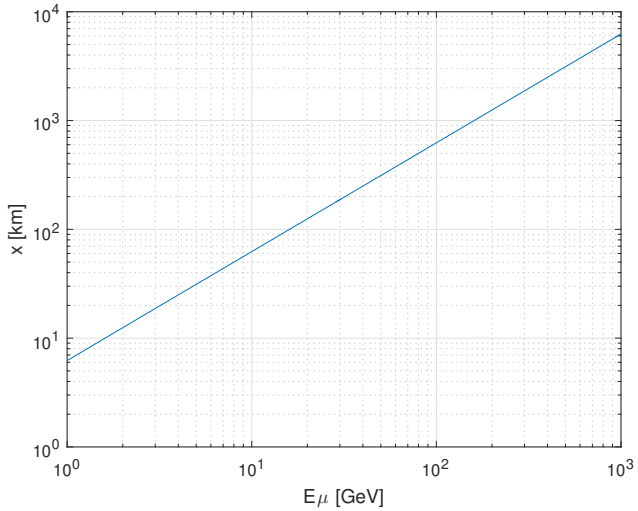

Figure 3.30: Muon energy E_μ versus mean travel range x in a vacuum.

The graph was created using equation 2.6 for the Lorentz factor and kinetic energy, together with muon rest energy E_0 and mean muon lifetime τ_0.

$$x = \frac{c \cdot \tau_0 \cdot \sqrt{E^2 - E_0^2}}{E_0} \tag{3.6}$$

From this graph it is clear that even relatively common energies seen in muons reaching Earth's surface can travel vast distances through a coma. The radius of coma to be modelled can therefore not be significantly limited by muon decay. Modelling a coma radius of millions of kilometres is expected to be computationally very intense and possibly not feasible. A more practical solution will be to limit the radius to where the amount of interactions between primary cosmic rays and coma particles becomes negligible and analytically approximate the muon flux produced by interactions outside this radius.
A deduction can be made based on Direct Monte Carlo Simulations (DSMC) models, which predict the number density of one or more species in a comet's coma. Some of these models are adjusted with measurements from Rosetta's instruments, such as the MIRO (Microwave Instrument for the Rosetta Orbiter)[147]. The graphs in figure 3.31 show altitude number density profiles for H_2O in the coma around Comet 67P.

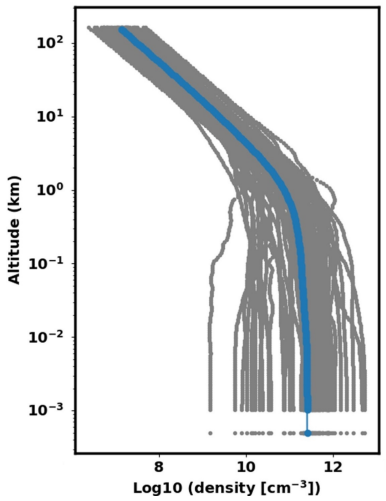

(a) Graph based on selected events from the MIRO database. Measurements taken between May 1st and 20th 2015, at 1.73 – 1.59 AU heliocentric distance. Modified, from "A comparison of multiple Rosetta data sets and 3D model calculations of 67P/Churyumov-Gerasimenko coma around equinox (May 2015)", by R. Marschall et al. (2019)[147].

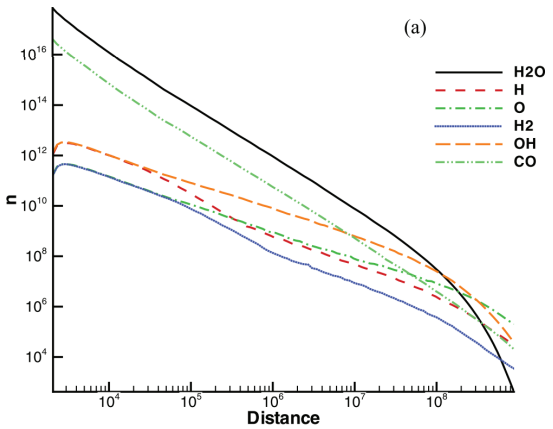

(b) Simulation based on a heliocentric distance of 1.29 AU. Modified, from "A global kinetic model for cometary comae: The evolution of the coma of Rosetta target Comet Churyumov-Gerasimenko throughout the mission" by V. Tenishev et al., (2008) [216].

Figure 3.31: DSMC simulated altitude profile of H_2O number density per cubic meter in coma of Comet 67P/Churyumov-Gerasimenko.

Combining both graphs, adjusting for difference in comet activity, and integrating the number density per volume over the altitude, yields the column number density (n/m^2); the number of particles in a square meter column from the comet's surface up until the corresponding altitude. Integrating the data to a coma radius of $10^8 m$ gives an approximation for the total column number density, which, set at 100%, yields the following graph 3.32.

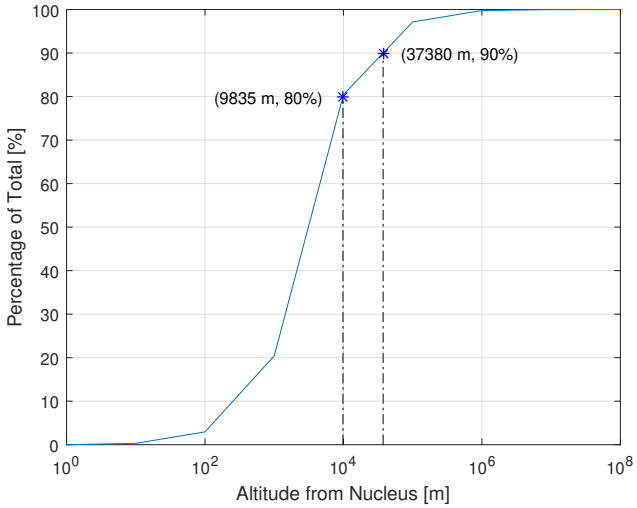

Figure 3.32: Heuristic approximation of the percentage of the total number of H_2O molecules in a square meter column extending radially outward from Comet 67P's surface to $10^8 m$, located beneath the specified altitude.

This shows that ≈ 80% of the total column density is located in the first $10km$ of altitude and ≈ 90% within $40km$. This back-of-the-envelope approach shows nonetheless that incoming primary cosmic rays encounter much more particles within a radius of a few tens of kilometres around the comet, than outside this radius. These cosmic rays therefore have a much higher chance of colliding with a particle close to the comet. As a first order estimation, the radius of the coma to be modelled for numerical simulations should not have to be much larger than $10-100km$ to simulate ≈ 80% of the primary cosmic ray collisions from rays that have a velocity vector through the comet's nucleus. This approach does not take coma variability, cosmic

ray scattering, volatile daughter species, dust and other factors into account. Cosmic ray primaries colliding with volatiles in the outer regions of the coma can create particle showers, which can contain stable hadrons. These newly produced, lower kinetic energy hadrons should be accounted for when modelling the cosmic ray spectrum at the outer edge of the decided upon coma radius. A more precise coma radius decision can and should therefore be made based on time dependent states of the coma, and the incoming particle spectrum should be adjusted to account for tenuous outer coma effects.
The coma around a comet can have large variations in composition and density throughout its orbit, clearly visible in figure 3.29b. One of the first attempts to analytically model the coma around a comet was made in 1957 by Ludwig Haser in his "Distribution d'intensité dans la tête d'une comète"[101]. He modelled the distribution of secondary particles, such as a volatile radicals, from being photo-dissociated from their parent molecule to the moment they are destroyed by a photo-destruction process. The photo-dissociation of OH from its parent species H_2O and the the following photo-dissociation into H and O is an example of this process. For the quantitative equation, Haser assumes the comet to be a symmetrical, spherical point source of uniformly outflowing parent molecules with radial outwards flow velocity v[51]. The lifetime of the molecules is assumed to be exponential until its destruction. The density of parent molecules n_p is related to the distance from the comet point source r with the following equation 3.7[51].

$$n_p(r) = \frac{Q}{4\pi r^2 v} \cdot (e^{\frac{-r}{\gamma_p}}) \tag{3.7}$$

The variable γ_p is the parent molecule scale length, which is equal to its exponential lifetime τ_p times its velocity radially outward v. Q is the comet's global parent molecule production rate. The next equation 3.8 calculates the daughter particle density. Variables dealing with daughter species are denoted with subscript "d".

$$n_d(r) = \frac{Q}{4\pi r^2 v} \cdot \frac{\gamma_d}{\gamma_p - \gamma_d} \cdot (e^{\frac{-r}{\gamma_p}} - e^{\frac{-r}{\gamma_d}}) \tag{3.8}$$

Haser's model is still widely used and modifications have been made to account for multiple generations, the creation of granddaughter species. Direct Monte Carlo Simulations (DSMC) are more often used today together with advanced analytical methods, to create more detailed models. These models can account for comet geometry, local heating by Solar radiation, composition fluctuations, "active areas" and much more factors[54].

Homogeneous Coma

The easiest but least accurate technique of describing the tenuous coma in GDML is by using a spherical atmosphere around the comet. This is achieved creating a spherical world volume in GDML, in which a single composition and density can be used. The composition should be taken from figure 3.26 with slight modifications to more closely resemble the data in table 3.7, as no heterogeneity can be applied to model the difference between the summer and winter hemisphere.

Radially Heterogeneous Coma

A radially heterogeneous coma model can represent the decrease in number density radially outward, whilst a homogeneous coma model can not. This so-called onion model uses homogeneous number density and composition in each layer, but varies these values for each different layer. According to the Haser model [101], parent molecules are expected to be more disintegrated farther from the comet. The number of daughter species increases radially outward whilst the parent molecules number decreases. This changes the coma composition for each layer. As multiple daughter species can be formed from a single parent molecule, the number density will not scale with mass density, which should be taken into account. An example of such an onion model applied to gas densities around Comet 67P is shown in figure 3.33. This figure is created with a DSMC model by V.V. Zakharov et al. (2018) [239] and adjusted with data from the ROSINA instrument[197].

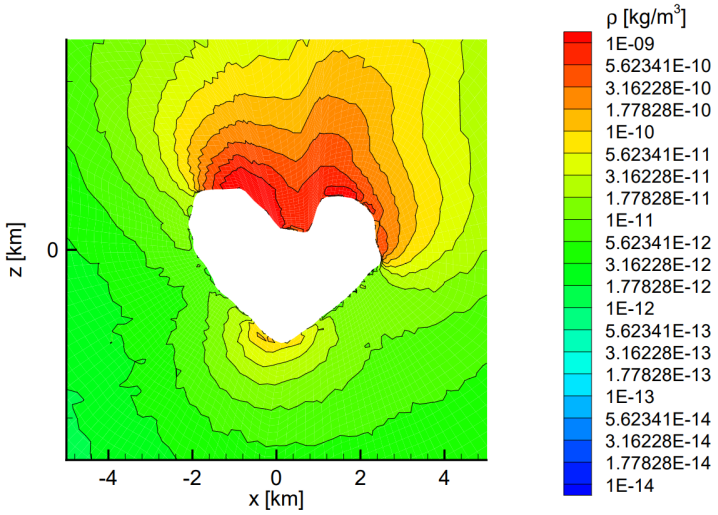

Figure 3.33: Gas densities around Comet 67P modelled with DSMC and adjusted with in-situ measurement data by the ROSINA instrument[197], represented in a non-spherical onion model. Simulation of comet at 3.21 *AU* heliocentric distance, October 10th, 2014. From "The near-nucleus gas coma of comet 67P/Churyumov-Gerasimenko prior to the descent of the surface lander PHILAE" by V.V. Zakharov et al., (2018)[239].

In the GDML model, spherical onion layers will have to be used. This creates discrepancies between the model presented by Zakharov[239] and the GDML coma model. To mitigate this, a third angle of attack is presented in the following subsection.

Angular Heterogeneous Coma

The third, most accurate and most computationally intensive option, uses small sphere chunks of heterogeneous composition and number density to describe the comet's coma. GDML provides the "Sphere" volume to be used for this[73]. The coordinate inputs for such a sphere shell section are radius "rmin" (r), azimuth "startphi" (ϕ) and elevation "starttheta" (θ), whilst the size inputs are maximum radius "rmax" ($r+dr$), "deltaphi" ($d\phi$) and "deltatheta" ($d\theta$), graphically shown in figure 3.34a [112].

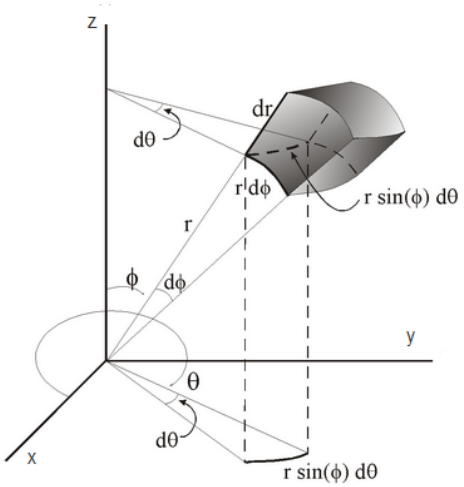

(a) Spherical coordinate system with spherical shell section "chunk" description. From "Algorithms - Uniform Distribution of Points on the Surface of a Sphere" by K. Hong, (2019) [112].

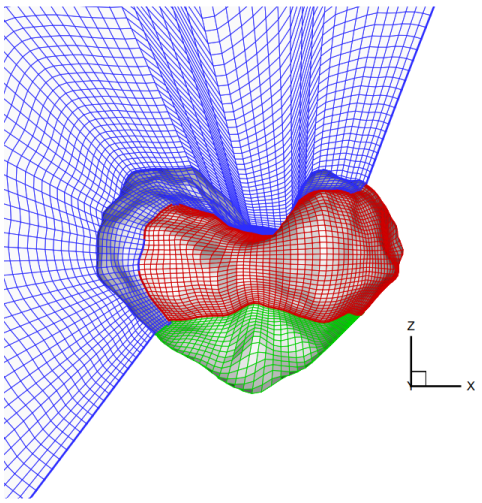

(b) Graphic representation of the computational grid used near the surface of Comet 67P by Zakharov to model the gas densities. From "The near-nucleus gas coma of comet 67P/Churyumov-Gerasimenko prior to the descent of the surface lander PHILAE" by V.V. Zakharov et al., (2018)[239].

Figure 3.34: Spherical shell sections.

The shell sections used in GDML will have a radially outward, spherically symmetrical construction. The computational grid used by A.V. Rodionov et al. [195], on which the grid used by V.V. Zakharov et al. (figure

3.34b) is based, follows the contours of the comets near the surface but approaches spherical symmetry further out. This grid structure was designed to implement the cometary activity model proposed in the paper "An advanced physical model of cometary activity" by A.V. Rodionov et al. (2002)[196]. The discrepancy between the GDML grid structure and the grid used for cometary activity modelling near the surface can be mitigated by reallocation of section parameters.

3.3.3. Dust Coma

The dust present in the coma can be modelled in two different manners, either with the inclusion of its mass and composition within the GDML description of the gaseous coma, or by discreet spherical dust particles. The former has a clear computational advantage, as the sheer number of dust particles to be described in the GDML file will require huge amounts of computation resources. However, it will provide a more accurate representation of reality and might be the preferred method if smaller sections of coma and comet are isolated for simulation in *Geant4*.

The mass of dust per unit volume, considered in the previously mentioned two methods, can be calculated from the dust-to-gas mass ratios provided by M. Choukroun et al. (2020) [46]. The number density and distribution of dust particles within the coma, if chosen for the discreet representation, can be calculated from a given mass using the size distribution and average dust density. R. Marschall et al. (2020) [148] show a relationship between the dust-to-gas mass ratio and the power law exponent of dust particle radii, allowing for the calculation of the size distribution for a given dust-to-gas mass ratio.

As the dust coma around Comet 67P is clearly not isotropic [138], the difference in number density can be modelled with spherical shell sections in GDML as previously explained. Kramer and Noack (2016)[130] modelled the heterogeneity of the dust distribution around Comet 67P. In their model, jets of dust such as the ones visible in figure 3.29b are predicted over one diurnal period. The model shows a very high correlation of on average 0.8 between the predictions and observational values, making it a prime candidate for dust heterogeneity value calculation to be used in the GDML model.

4

Simulation

A few major gaps in the currently available knowledge need to be bridged to prove the feasibility of the heretofore mentioned muon tomography technology. One such a gap is the available amount of useful muons for the instrument to detect near a small Solar System body, and how these muons can be used to reconstruct the interior structure. Most muons arriving on Earth are produced in collisions between Galactic Cosmic Rays(GCRs) and the tenuous upper atmosphere, as described in section 2.2.2. The muon production rate of direct GCR collisions with regolith on a small Solar System body's (SSSB) surface as compared to the production rate in a low density gaseous environment is one of the poorly understood variables essential to asteroid muon tomography.
The goal of the work performed for this chapter is to discover which factors affect the muon flux characteristics near SSSBs, and to what extent. The setups of the simulations for this thesis project were initially planned with the future use of server time at *Nikhef* in mind (Dutch National Institute for Subatomic Physics). The available computing power at this facility governed the level of detail provided in the asteroid and comet models presented in chapter 3. Unfortunately, due to restrictions caused by the onset of the COVID-19 pandemic, physical presence at the *Nikhef* facilities was deemed less than desirable. Attempts to run *Geant4* simulations on their servers remotely were only partially successful. Due to the lack of time within the allocated time frame for this thesis to properly debug the arisen problems for remote server control, it was decided in consultation with the involved parties to run *Geant4* exclusively on locally available hardware. This thesis project is therefore performed exclusively on a Hewlett-Packard EliteBook 8560w laptop with an Intel i7-2630QM processor, NVIDIA Quadro 1000M graphics and compute card and 12 gigabytes of RAM. These computational limitations eliminated the possibility of running full scale, no-compromise simulations with the accurate asteroid models.
This limited computing power required creative approaches to reach critical, enlightening results. The choice was made to redirect the focus from resolving an accurate muon count from realism driven simulation conditions, to a more tangible result driven approach.
This chapter starts with a description of the simulation setup and tools used during this thesis project, showing the inputs created, simplifications made, and displays the simulation results. The chapter concludes with a preliminary look at the process of creating a reconstruction algorithm. A high-level version of such an algorithm is applied to the simulation output data, creating a tentative result, aiding the perceived feasibility of the muon hodoscope project. The core of this simulation chapter relies on the software platform *Geant4*, a software toolkit using Monte Carlo methods to simulate the passage of particles through matter [3], as well as extensive use of the numerical computing environment *MATLAB* [152].

4.1. Geant4

The main core of this project is the software toolkit *Geant4*, a C++ library for numerical Monte Carlo particle simulation through matter, mostly used in the world of particle physics. The specific version utilised for all the simulations in this chapter is *Geant4* 10.06, patch 2, May 29th 2020. The package was compiled and build with the [MT] (Multi-threaded mode) option enabled, allowing for faster computation times. This software package merits some explaining and background information in this space engineering oriented thesis.

The first version of "Geometry and Tracking" *GEANT* was created in 1974 [35] at CERN and used computational resources that would be considered archaic in today's world to compute the passage of particles through matter. The last descendant of this code, *GEANT3*, was actively maintained by CERN until the last version of its programming language *FORTRAN* was released in the 2000's [36], ushering in the conclusion of its useful life-cycle. This version aided in the design of the Large Hadron Collider (LHC) experiments such as the famous ATLAS detector [11], and remained in use for some experiments for more than a decade in the 21^{th} century. As the separate but nonetheless spiritual successor to *GEANT3*, the C++ object-oriented *Geant4* was written in 1994-1998 [3]. This simulation toolkit was still in use in the year 2020, and is maintained by CERN and the *Geant4 Collaboration*.

4.1.1. Physics Lists

The so-called "physics list" used in *Geant4* is a C++ code object that lists a subset of physics computation modules (from the modules available within *Geant4*), geared for use in a specific application. Even though *Geant4* provides quite a large array of different physics modules, not all of them should be utilised all of the time. Since not every application demands the same level of accuracy, smaller or more specialised subsets of physics modules can be chosen to lower the computational intensity. Different modules can also describe similar processes but rely on different underlying theorems and approximations, which often have different energy regimes in which they are deemed most accurate. Processes such as radioactive decay or optical photon transportation are generally not included with the most commonly used physics lists, but can be added either manually or by choosing a more extensive physics list.
Validation studies of these physics lists are performed at the LHC experiments, showing that a string model coupled to a cascade model is in closest agreement to testbeam data. Multiple string models are available, such as the Quark-Gluon-String-Model *QGS* or Fritiof *FTF* model. The first operates mainly above $12GeV$ for protons, neutrons, pions and kaons, while the latter model is applied above $4GeV$. For the lower energy intra-nuclear cascades, 2 main models are used: The Bertini type cascade model *BERT* and the Binary cascade model *BIC*. These models handle energies up to $10GeV$, with the *BERT* model providing a larger range and higher accuracy at the cost of performanc e[6]. These physics lists often include extra models not necessarily abbreviated and shown in the name. Models regularly used in common physics lists include standard electromagnetic physics, muon-nuclear interaction, the Precompound *P* model for the precompound and evaporation phases of the residual nucleus [6] and some parameterised models used for edge cases. When more precise electromagnetic models are required, the suffix *EMY* will provide higher precision compared to the standard model, oft-used for medical applications, and *EMZ* will provide the highest level of precision available. The suffix *EMV* slightly reduces the precision and induces a slight bias [7], but greatly increases its performance and is still deemed valid for high energy physics from keV to PeV. The energy region where the chosen string model and cascade model overlap, displays the largest mismatch between simulation and testbeam data. The oft-used *QGSP* model has good validation above $\sim 15GeV$, but the cascade models are validated up to $3-10GeV$. There is a need for a model describing this range, as existing codes are not fully satisfactory [228]. To mitigate this problem for now, a Low Energy Parameterised model *LEP* is used to cover this region. This is graphically shown in figure 4.1.

Figure 4.1: The probability a given model is used by *Geant4* versus the kinetic energy in GeV of the incident hadron, for the *QGSP_BERT* physics list. From "GEANT4 Physics Lists for HEP", by J. Apostolakis et al., (2008)[6].

Parameterised models are generally low in their energy response, but give great CPU performance compared to theory-driven models. A High Energy Parameterised model *HEP* exists as well, which combined with *LEP* forms one of the fastest physics lists available: *LHEP*. This fully parameterised physics list is generally the least computationally intensive, but at the cost of accuracy in energy response. This physics list is deprecated since *Geant4* version 10.0 [87], but can still be manually compiled for use as a physics list.
Four different physics lists are considered for use during this thesis project: the *FTFP_BERT* and *QGSP_BERT* physics lists, and their *EMV* suffixed variants *FTFP_BERT_EMV* and *QGSP_BERT_EMV*. The first two are the preferred physics lists used at CERN at the ATLAS and CMS experiments. *FTFP_BERT* has its transition be-

tween the Fritiof string model and the Bertini cascade model at $4-5GeV$, while for *QGSP_BERT* this transition between *LEP* and Bertini cascade lies at approximately $9-10GeV$ (figure 4.1). As these transition regions show the least smooth energy response, the choice between one of these two will depend on the energy region of interest.

Performance Analysis

The simplified asteroid model as shown in section 4.2.2, a 5 meter radius sphere with ten inclusions, was used for a performance analysis between the four considered physics lists for muon transmission. The results of said analysis are tabulated in table 4.1. The difference in performance between the *FTFP* and *QGSP* based physics lists is marginal when only muons of 5 GeV are used. However, the Fritiof model shows a slight increase in performance once higher energy protons are used as the primary particles and it is therefore the model of choice for most of the proton simulations. The results show the clear advantage of using *EMV* suffixed physics list, as this results in a $23-43\%$ increase of performance. With CPU performance being a major constraint in this thesis project, the *FTFT_BERT_EMV* physics list is used as the model of choice for most of the simulations performed, as this performance increase is deemed to outweigh the loss in precision.

Particles↓PhysicsList→	FTFP_BERT	QGSP_BERT	FTFP_BERT_EMV	QGSP_BERT_EMV	Units↓
4k 5GeV $\mu^{\pm}$	46.2	45.9	33.6	33.8	[s]
10k 5GeV $\mu^{\pm}$	108.3	109	76.3	76.1	[s]
25 50GeV Protons	34.5	35.2	26	25.7	[s]
100 50GeV Protons	123.3	123.4	89.4	100.2	[s]
250 50GeV Protons	290.8	293.1	211.9	217.4	[s]

Table 4.1: Performance analysis of four different physics lists in *Geant4*, performed on Hewlett-Packard EliteBook 8560w.

For proton transmission, a setup of a homogeneous $250 \times 250m^2$ slab of $50m$ thickness was used, with a composition of 20% FeO and 80% SiO_2 by mass. The total density of this slab is set to $1.6g/cm^3$. The performance results for proton transmission are tabulated in table 4.1. This setup is similar to the performance analysis setup used by J. Keerl[125] in his research, and is therefore chosen to allow for a performance comparison between the Hewlett-Packard EliteBook 8560w laptop used during this thesis project and the "Magdalena" server from the Detector Research and Development group at *Nikhef*. This server, with an Intel Xeon E5-2697 2.60 Ghz, 28 core, 56 threads processor, was initially considered to perform most of the simulation work for this project and could be made available for future simulations, justifying this comparison. The following table 4.2 compares the extrapolated performance analysis results of both systems.

Total 50Gev Protons→ CPU↓	25	100	250	250K
Intel i7 2630QM 2.00 GHz	25.7 s	100.1 s	217.4 s	**~60.4 h**
Intel Xeon E5-2697 2.60 GHz	**~85 ms**	**~34 ms**	**~85 ms**	846.5 s[125]

Table 4.2: Performance comparison in *Geant4*, Intel i7 2630QM (Hewlett-Packard EliteBook 8560w) versus Intel Xeon E5-2697 (Magdalena server at *Nikhef*[125]). Physics list *QGSP_BERT_EMV* was utilised in both simulations. Values in **bold** are extrapolated.

These results clearly show the advantage of using specialised hardware for *Geant4* simulations. The Magdalena server shows a ~ 25782% improvement of simulation times, allowing for much more complex simulations to be run in a working day's time. The *Nikhef* Data Processing Facility (NDPF) is one of the twelve centres around the world that forms the computational backbone of *CERN*. It has thousands of CPU cores at its disposal, the use of which could put full simulation runs of the entire asteroid model within reach.

4.2. Setup and Simplifications

The numerous simulations performed over the course of this thesis project used varying inputs, models, simplifications and assumptions to achieve results. This section includes said inputs, the assumptions their values are based on, the rationale behind them and their creation process. The asteroid and comet models presented in chapter 3 are created with the main focus on the accuracy of their representation of the real world, with some simplifications included thought and shown not to affect realism significantly. This section differs in that it focuses in depth on which model parameters can and cannot be simplified to yield realistic simulation results, deviating from the overall realism of the models in the modelling chapter.

4.2.1. Surface Porosity

One of the first simplifications covered in this section revolves around the use of homogeneous material of lower overall density, to simulate higher density but porous material. This assumption is used both for the simulation of microporosity in monolithic structures (section 3.1.3) and macroporosity between monolithic structures.

The modelling of microporosity by use of non-porous, lower density, solid material is justified when considering the physics model basis *Geant4* utilises to compute the probability a particle has of encountering another particle or nucleus in the stationary medium it is transiting. The mean rate of energy loss for charged particles for instance scales directly and linearly with the number of atoms per volume ($dE \propto N$)[88]. Any eccentricities in the distribution of these small porosities and their effects on muon energy loss will average out over the macroscopic distances a muon has to traverse through the asteroid. As the dimensions of such microporosities are in the order of μm and vacuum inclusions of this size are shown to barely effect muon production[125], the substitution of microporosity with lower density homogeneous material is deemed justifiable.

Macroporosity, as discussed in section 3.1.4, is defined as the vacuum pockets contained between monolithic grains and boulders. These pockets can be in the form of large macroscopic features such as cracks and voids, but can be merely the void space between regolith as well. As large scale structures and features are of particular interest for this research, they are simulated in full by use of vacuum spherical inclusions. The simplification here is the use of spheres to simulate generally amorphous features, justified in section 3.1.5.

The small scale macroporosity between the regolith allows for some partial, basic simplification. Apart from neutrinos, muons are the only particles surviving their journey through the material of the asteroid. Almost all other particles created in particle shower events are destroyed within the upper 10m depth layer of the surface[125], and therefore most of the muons are created in this layer as well (figure 4.2).

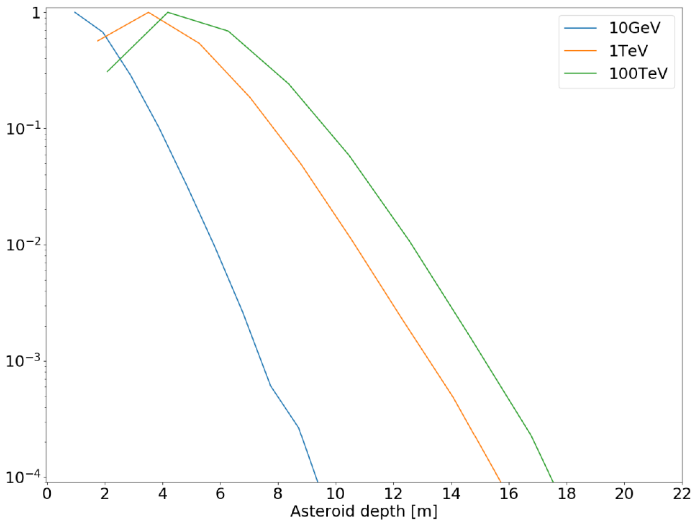

Figure 4.2: The normalised depth distribution for muon creation, for three different incident proton energies. Muon creation depth taken from precursor particle decay. From "Characterization of radiation in the proximity of small celestial bodies and the respective implication on muon tomography in space", by J. Keerl (2020)[125]

Even though muons are seemingly created at depths up to ~ $18m$ for $100TeV$ protons, the $10m$ limit is mentioned due to the low frequency of these $100TeV$ events, as seen in figure 2.14; equal to approximately

once every 2 ~ 3 hours per square meter per steradian. Below this $10m$ layer, the accuracy of the asteroid model is therefore mostly determined by muon interactions, and not the interaction with other particles. David Hodge (2018) [109] restricted the muon creation volume in his *Geant4* asteroid simulation to the upper 3m layer of regolith, simplifying his model:

> *"The thickness of 3m was decided partly as a guess of a reasonable regolith thickness (once again, there is very little data available with which that guess could be improved into a semi-accurate estimate), but mostly because 3m of regolith proved enough to stop virtually all secondary particles generated by GCR primary impacts on the surface except for the elusive muon, a panoply of neutrinos, and the odd very-very high energy heavy-nucleus primary."*
>
> From "Asteroid Muography: Design feasibility of a hodoscopic, spacecraft-based, detector intended for muon tomography of asteroid interiors.", p.45, by D. Hodge (2018)[109].

As previously mentioned, the energy loss and scattering of muons passing through matter is approximately averaged out over longer distances, allowing for the interior small scale macroporosity to be modelled as lower density homogeneous material [88]. However, the same small scale macroporosity is shown to positively affect the muon creation efficiency [125] (section 3.1.3) when situated in the upper surface layers. The upper $10m$ layer can therefore not be simplified by using a lower density substitute, although this simplification is nonetheless suggested for differing reasons by T.H. Prettyman [186] and D. Hodge [109]. One of the plausible mechanisms causing the increase of the muon creation efficiency is thought to be the much rarer but faster decay of charmed hadrons such as D mesons, and short-lived neutral kaons. Both of these have decay mechanisms that allow them to decay to muons, and both have much shorter average lifetimes than charged kaons and pions [178] (table 4.3), the particles thought to create the bulk of the muons in Earth atmospheric cosmic ray showers.

Particle	Mean Life $c \cdot \tau_0$[m]
$\pi^{\pm}$	7.80
$K^{\pm}$	3.71
K_S^0	$2.68 \cdot 10^{-2}$
$D^{\pm}$	$3.12 \cdot 10^{-4}$

Table 4.3: Particle decay constants. Decay length is found by multiplying mean life with Lorentz factor. [186][178]

Muons produced by the very fast decay of charmed hadrons have never been observed experimentally, but are thought to form the majority of muons produced by cosmic rays in Earth's atmosphere at high energy levels, i.e. higher than $100GeV$[186]. At similar velocities, the decay length of a charged D meson is a factor of 10^4 shorter than that of charged kaons and even twice that for pions. This increases the chances of D mesons decaying in the small microporosities present between regolith grains compared to pions and kaons, in turn increasing the fraction of muons created by D mesons. This non-linear muon creation efficiency scaling when porosities are present could be the main cause for the muon increase seen in the porosity simulations run by J. Keerl (2020) [125].

4.2.2. Models

In order to ease the computational intensity, to better facilitate parameter manipulation and to allow for comparably more comprehensible and tangible simulation results, a simplified asteroid model is used for most of the simulation runs. The creation process for this model is run through in section 3.2. As shown in table 3.5, simulation time and therefore computational intensity does not rise significantly when increasing the material thickness above $10m$. This is based on simulations with $50GeV$ protons as the primaries, but poses a good starting point nonetheless. The choice was made to create a $10m$ radius simplified asteroid, as this would lower the computational intensity but still allow for full development of some of the cosmic ray showers.
The model is based on Itokawa for its material composition and density, with the overall density and monolith inclusion density set to $1.925g/cm^3$ and $3.21g/cm^3$ respectively. The regolith density is subsequently adjusted to have the model match the required overall density. For the simulations in this chapter, four different

models are used. The first model is the control, where a homogeneous density distribution and homogeneous material composition is assumed. This is similar in size and shape to the models visible in figure 4.4, but without the inclusions. Its regolith density is equal to the overall density. The second and third models employ the random spherical inclusion distribution process of section 3.2, limited to 10 inclusions for result clarity. As visible from the comparison in figure 4.3, using less spheres for imaging with single plane creates far more intelligible results. For the third model (figure 4.4b), some of the inclusions are set as voids, whereas in the second model (figure 4.4a) all of the inclusions are monolithic structures. The fourth model includes four symmetrically distributed spheres, shown in figure 4.3b, where two of these spheres are voids and two are monolithic. This model is created to further increase the contrast, ease of use and possible intelligibility of results.

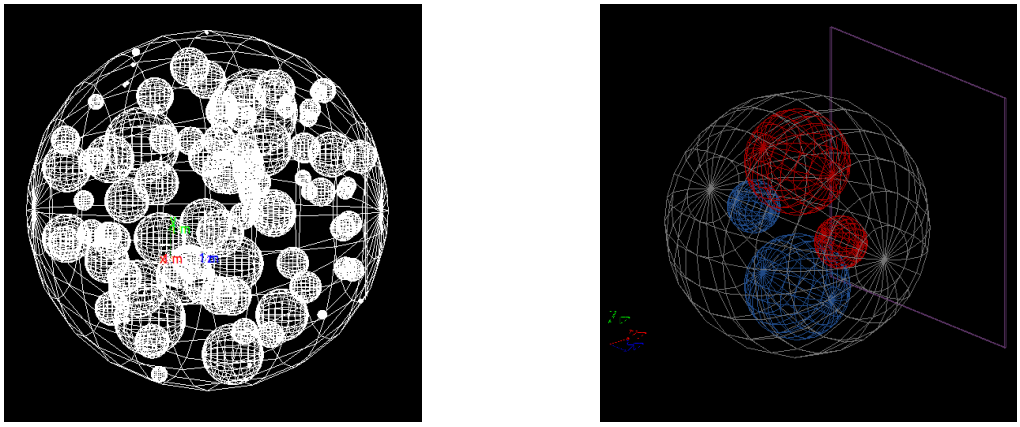

(a) 97 spherical inclusions

(b) 2 monolithic and 2 void inclusions

Figure 4.3: Comparison between renderings of two simplified 5 meter radius asteroid models with varying number of spherical inclusions. Red denotes monolithic solids, blue shows void inclusions. The purple frame shows the detector plane. Axis in positive direction, XYZ in red, green and blue respectively.

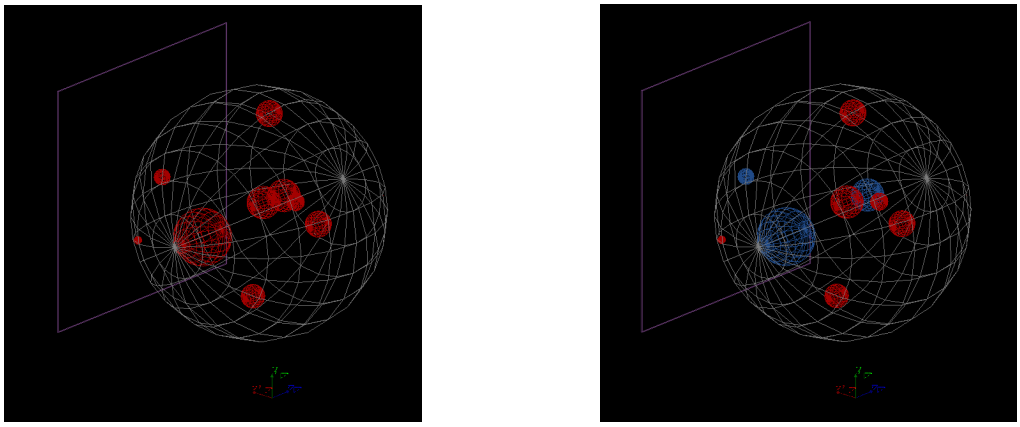

(a) 10 monolithic inclusions.

(b) 7 monolithic and 3 void inclusions.

Figure 4.4: Rendering of two 5 meter radius simplified asteroid models in wireframe. Red denotes monolithic solids, blue shows void inclusions. The purple frame shows the detector plane. Axis in positive direction, XYZ in red, green and blue respectively.

All of the simulations performed in this chapter use a thin silicon plate as the sensitive detector volume. This plate has a $5cm$ thickness, a $10x10m^2$ area aligned orthogonal to the axis of interest, and its centre is positioned at $6m$ positive on said axis. In figure 4.4 for example, the plate is positioned at $X = 6m$. The origin for each model lies at the centre of the asteroid. The *Geant4* code checks which particle has entered the sensitive volume, and only write to the output file when this particle is a muon. Of this muon, the charge, position, velocity vector and energy properties are stored. It is important to note that *Geant4* works with steps. Each step is a change added to the information of the particle, such as location, energy and velocity

vector. For each step of each particle, the code checks whether the track crosses the silicon plate. To prevent a particle from getting counted more than once if it has multiple steps through the volume, a flag is set to ignore that particle after it has been counted.

4.2.3. Galactic Cosmic Rays

The first major simplification made for the simulations in this project, is the use of a pure proton spectrum for the simulation of galactic cosmic rays. The two major constituents of the the primary cosmic ray flux are protons and Helium nuclei (alpha particles), approximately 90% and 10% respectively, as shown in figure 2.13. Previous literature on the subject of muon tomography (T.H.Prettyman [187], D.Hodge [109] and J.Keerl [125]) utilised a source which only emitted protons, to simulate the GCR spectrum. In order to be able to validate results with said literature, the choice was made to use a similar GCR setup for most of the simulations, therefore consisting of only protons. For some of the GCR simulation runs, the alpha particle spectrum is included as well.
Geant4 allows for the use of easily adjustable macro files (**.mac*) that describe the size, shape, position, orientation and flux for a radiation source. These macros can be created to accurately simulate the galactic cosmic ray flux (figure 2.14) for any location within the Solar System, at a given time. The SPace ENVironment Information System (SPENVIS), an online interface run by ESA and BIRA-IASB (Belgian Institute for Space Aeronomy) providing access to models of the space environment and its effects [105], is used to generate these particle source macros of GCR spectra. SPENVIS itself bases its GCR particle fluxes on multiple models, shown in figure 4.5, to be chosen by the user. The ISO-15390 model is often used in literature, and was modified by Nymmik et al. (1996) [177] to match the increase in flux seen at lower energies, comparable to the CREME96 model. The four models provided by SPENVIS align nicely from $1GeV$ and up, three of the models even align from $20MeV$ and up.

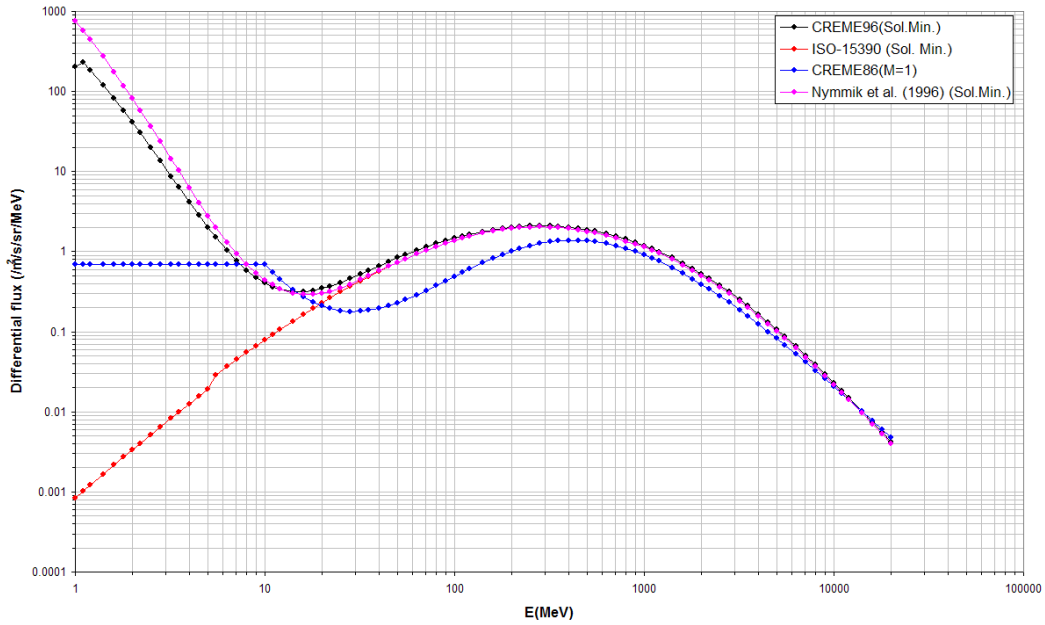

Figure 4.5: The proton galactic cosmic ray flux models near Earth at Solar minimum. From "GCR particle models", by the Belgian Institute for Space Aeronomy, (2018) [69].

As luck would have it, the kinetic energy range of GCRs of interest is higher than $1GeV$. Below this lower limit, it becomes very difficult to distinguish penetrating muons from backscatter [186], the angular deviation from the initial trajectory of the muon through the asteroid increases dramatically and the muon creation efficiency is practically zero[125]. Additionally, as shown in section 2.2.2, the flux of lower $\sim GeV$ primary GCRs fluctuates inversely with Solar activity [178][220]. As GCR protons in this below GeV energy range are not of interest for muon tomography, a lower limit is put on the GCR energies created at the particle source, simplifying the simulation. This also avoids having to model the effect of Solar activity fluctuations. As a side effect, it allows for a practically free choice of GCR particle flux model as they all very much align at high

energies (figure 4.5).
The upper limit for the GCR particle flux is imposed by the limitations of the physics lists available for *Geant4*. All of the physics modules mentioned in section 4.1.1, as well as others available for use with *Geant4*, have an upper energy limit of $100TeV$ for hadronic processes [29]. Luckily, the flux of GCR particles with energies higher than this is very low, justifying the simplification of omitting energies above this limit. The famous "knee" present in the cosmic ray energy spectrum (figure 2.14) lies at approximately $\sim 3PeV$ [220]. Different energy regions of the spectrum can be described by inverse power laws, where this so-called knee depicts a transition area between two energy regions. The region from $\sim 10GeV$ to $\sim 1PeV$, before the "knee", has a differential spectral index of $\alpha \approx -2.7$ [220]. As the $100TeV$ limit lies below the aforementioned transition region, a power law with α can be used to relatively easily extend the differential flux plots produced with SPENVIS, as these are limited to GCR energies of $10^5 MeV$. The resulting proton galactic cosmic ray flux is shown in figure 4.6.

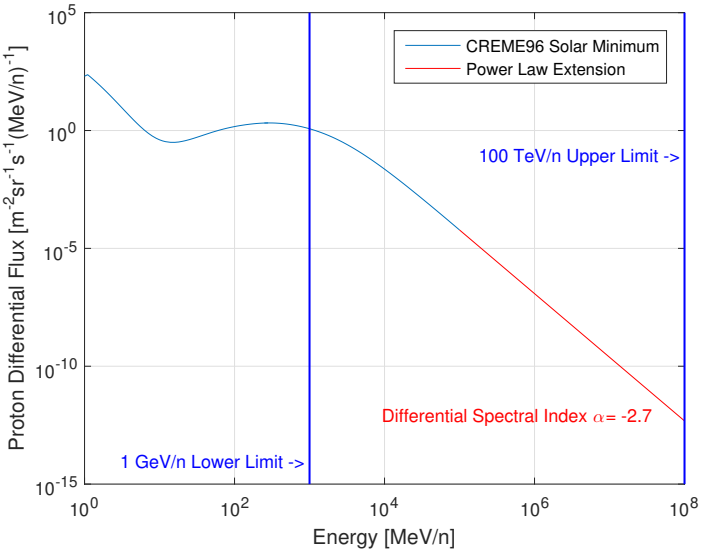

Figure 4.6: The proton galactic cosmic ray flux from SPENVIS[105], utilising the CREME96 model. Augmented in red, starting from $10^5 MeV$, with a power law using differential spectral index $\alpha = -2.7$[220]. Blue lines show the limits of energy region of interest, at $1GeV - 100TeV$.

The *Geant4* macro files produced by SPENVIS specify a point-wise distribution of differential particle flux versus energy. Normalisation of this distribution is critical for creating a particle source that can be related to time. The normalisation terms for the energy range in the macro file are calculated by SPENVIS, using the following equations[146][68].

$$n_1 = (F|_{E_{min}}^{\infty} - F|_{E_{max}}^{\infty}) \tag{4.1}$$

$$n_2 = \frac{1}{4\pi}\int_0^{2\pi} d\phi \int_{\theta_{min}}^{\theta_{max}} \cos\theta \sin\theta d\theta = \frac{1}{4}(\sin^2\theta_{max} - \sin^2\theta_{min}) \tag{4.2}$$

For an energy spectrum, such as the GCR spectrum produced by SPENVIS, the energy normalisation factor n_1 is produced by subtracting the maximum integral fluence $F|_{E_{max}}^{\infty}$ (integral flux times duration) from the minimum integral fluence $F|_{E_{min}}^{\infty}$ (Equation 4.1) [68]. The resulting energy normalisation factor n_1 is essentially the number of real world particles emitted within the energy distribution between $E_{min} - E_{max}$, for the entire real-world duration of the simulation or measurement. SPENVIS takes care of the unit transformations so that n_1 is presented in the number of particles per cm^2. The angular distribution for the particle fluence created by SPENVIS is omnidirectional. The macros from SPENVIS per standard use a cosine-law dependent source, and restrict the zenith angle θ between 0 and 90 degrees. This limits particle vectors to one hemisphere as seen from the source. The cosine-law dependent emission, similar in effect to the Lambert's cosine emission law oft-used in optics, makes sure the target receives the same radiance (flux per unit projected area per steradian) no matter its angle to the emitter surface. As the differential flux in the macro is already integrated over a full sphere, the $1/(4\pi)$ term in equation 4.2 reverts the solid angle dependence, and

the angular distribution normalisation factor n_2 is then equal to 1/4. These two normalisation factors can be used to determine the real-world number of particles expected, based on simulation results. The quantitative simulation result X_s can be scaled to a value expected in a real-world scenario X_r with equation 4.3. N_s is the number of particles in the simulation and N_r is the expected number of real-world particles through the geometry. The latter is analytically determined by multiplying the energy normalisation factor n_1 with the angular normalisation factor n_2 and the surface area of the source S, shown in equation 4.4.

$$X_r = X_s \frac{N_r}{N_s} [199] \tag{4.3}$$

$$N_r = n_1 n_2 S [146] \tag{4.4}$$

In the by SPENVIS presented particle source macros, the n_1 factor is denoted as NORM_FACTOR_SPECTRUM, the n_2 factor as NORM_FACTOR_ANGULAR. Dividing the former by the total "real-world run-time" of the cosmic ray spectrum calculation performed by SPENVIS, yields the flux integral of the point-wise histogram in said macro file. Per example, a 1 year calculation of the GCR spectrum in vicinity of Earth was performed, ignoring the effects of solar activity, Earth's magnetic field and its cosmic ray shadow. This yielded the differential proton galactic cosmic ray flux seen in figure 4.6. This flux in turn is used as the basis for the *Geant4* macro file. The values noting the weights of the histogram points in the macro correspond to the values of the calculated galactic cosmic ray flux. The conversion between the two is performed by SPENVIS. With the default settings enabled an omnidirectional source is assumed and the differential flux per steradian is integrated over a sphere, by multiplying the value with 4π. As *Geant4* requires the use of flux per cm^2, the trivial conversion from m^2 is executed by SPENVIS as well [68], completing the conversion from differential flux to macro input values. The final conversion is from energy-per-nucleon MeV/n to energy-per-particle MeV, which is trivial for protons. The trapezoidal integral over particle energy of the point-wise histogram yields almost the same value as the result of the division of the n_1 factor (NORM_FACTOR_SPECTRUM=1.477696E+08) by the run time of 1 year. The discrepancy between both values is most likely caused by the use of a trapezoidal integration.

$$\int_{E_{min}}^{E_{max}} w_i \, dE = 4.6826 \tag{4.5}$$

$$\frac{n_1}{yr} = \frac{1.477696 \cdot 10^8}{31,556,952} = 4.6858 \tag{4.6}$$

Equation 4.6 yields a factor of 4.6858, by which each of the histogram weights w_i can be divided to get a probability density distribution, as the integral of this new histogram is now equal to 1. The weight of each point of the histogram now depicts the probability a generated particle within the energy range has the corresponding energy to that point. This histogram can be adjusted again to closely match the spectrum created with SPENVIS by multiplying the weights w_i with the integral (normalisation factor) of the differential spectrum.

The SPENVIS created macro does not represent the full particle energy spectrum of interest ($1GeV - 100TeV$), but is limited to $1MeV - 100GeV$. A new macro is created from the extended proton differential flux as shown in figure 4.6. The values between the energy range of interest are then converted for use in the *Geant4* macro, with the previously mentioned method, from units $[m^{-2}sr^{-1}s^{-1}(MeV/n)^{-1}]$ to units $[cm^{-2}s^{-1}(MeV/n)^{-1}]$, for an omnidirectional source. The resulting point-wise histogram is shown in figure 4.7, where the energy $[MeV]$ of each point denotes the abscissa of the corresponding point in the histogram, and the ordinate of each point denotes the weight w_i of the histogram bars. In total 74 histogram points are depicted in the figure, and the same number is used in the macro.
A *Geant4* macro for alpha particles is created using the same method. The notable difference is the fact that a single alpha particle consists of four nucleons, so the energy-per-nucleon $[MeV/n]$ to energy-per-particle $[MeV]$ conversion requires multiplying the energy with 4.

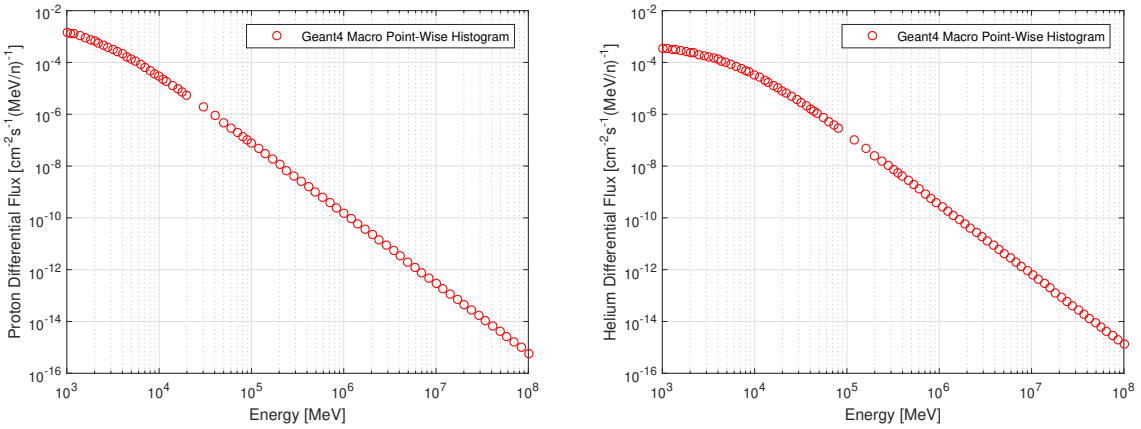

(a) Proton differential flux.

(b) Helium ion differential flux.

Figure 4.7: Inputs for the *Geant4* source macro point-wise histogram. Based on the galactic cosmic ray flux from SPENVIS[105], utilising the CREME96 model, augmented starting from $10^5 MeV$ with a power law using differential spectral index $\alpha = -2.7$[220]. An omnidirectional source is used for the macro.

The normalisation factor n_1 for the proton flux, shown in figure 4.7a, is calculated with equation 4.1, and multiplied with the expected real-world run time in seconds for use in the macro. For the unconverted flux from figure 4.6, in the energy region of interest, the normalisation factor is $n_1 = 1.9566 \cdot 10^3 [m^{-2} sr^{-1} s^{-1}]$, whereas for the converted flux this equals $n_1 = 2.4587 [cm^{-2} s^{-1}]$, or $n_1 = 7.7589 \cdot 10^7 [cm^{-2}]$ when a real-world run time of 1 year is considered. Comparing this value for n_1 to the value found in equation 4.6 for the standard energy region provided by SPENVIS, we find a 47.5% decrease in particle count. However, the more numerous particles removed on the lower end of the energy spectrum require much less computation time per particle compared to the less numerous, higher energy particles. The resulting decrease in total particle count might therefore not positively effect computation time when all factors are considered.

The normalisation factor n_1 for the alpha (Helium ion) flux, shown in figure 4.7b, is calculated with equation 4.1 as well, but with one slight alteration. The normalisation factor governs the amount of particles expected in a real world scenario. As the flux used for the weights in the histogram is defined per-nucleon, we need to divide the result of the integral by 4 to find the flux per-particle. The resulting normalisation factor then equals $n_1 = 0.3382 [cm^{-2} s^{-1}]$, or $n_1 = 1.0674 \cdot 10^7 [cm^{-2}]$ for 1 year real-world run time.

The mentioned normalisation factor between $E_{min} = 1 MeV$ and $E_{max} = 10^5 MeV$, is equal to $3.7293 \cdot 10^3 m^{-2} sr^{-1} s^{-1}$. Assuming the use of a spherical particle source, with a total solid angle of 4π, the particle count rate per square meter can be calculated: $4.6864 \cdot 10^4 m^{-2} s^{-1}$. As a final step this value is multiplied by the surface area $4\pi R^2$ of the volume of interest. In this scenario, the $10m$ diameter spherical simplified asteroid model shown in section 3.2.2 is used to showcase the sheer computational intensity of the endeavour. The total GCR primary count on such an asteroid would be $1.4723 \cdot 10^7 s^{-1}$. A sphere of equal volume to asteroid Itokawa (table 2.2) would have a radius of $163.77m$, which results in a GCR primary count rate of $1.5795 \cdot 10^{10} s^{-1}$. Simulating this environment in *Geant4* has a computation rate of $5 \cdot 10^5$ GCR primaries per $1-2$ hours on the aforementioned laptop used for this project. One real-world second of simplified asteroid simulation would require ~ 44 hours of computation time, whereas the Itokawa sized sphere would require an unrealistic ~ 5.4 years. The use of simplifications is therefore a must for this thesis project.

In some simulations the cosmic ray primaries can be omitted altogether. As shown in table 3.5, the simulation time depends mostly on the amount of interactions between primary cosmic rays and their subsequent cascade showers with the first $\sim 10m$ of regolith, and much less on the interaction between the muons and the interior of the asteroid. In simulations where merely the passage of muons through matter is of interest, such as the testing of a preliminary reconstruction algorithm, the use of a muon source instead of a cosmic ray source will vastly improve performance. This improvement is visible in table 4.1 as well, where even accounting for the energy difference between the protons and the muons, the required simulation time per particle is much lower. Additionally, the amount of muons reaching the detector per incident proton is much lower than when muons of similar total energy are used. The use of muons as primaries is understandably at

a major cost of realism, but shows to be useful for some if not most of the simulations.

4.2.4. Linear Representation

Tomography is performed by imaging sections of a subject from multiple angles and integrating to find the 2D shape or 3D interior structure. As a major simplification, all of the simulations run in this project will image the model only from a single angle. For most simulations, the particles will be created in a square plane orthogonal to the axis of interest, similar in size to the asteroid model, and start with a velocity vector along said axis. As the scattering angle of most energetic muons is low [125], the detector plane will be placed behind the subject, orthogonal to the velocity vector of the particles originating from the source.
The spacecraft in an asteroid observation mission will most definitely orbit its subject, and the asteroid will likely rotate at some rate [231], resulting in many time-dependant observation parameters. Even though this aids in observing the asteroid from all angles, it will increase the complexity of the simulations. As this will require either a particle source fully enveloping the simulation volume, or a co-rotating particle source, it will increase simulation time as well.
As tomographic reconstruction merely requires multiple angles to be observed, the decision is made to use three orthogonal principal axis along which the simulations should be run. Using discreet, non time-dependant observation angles will lower simulation complexity, computational intensity and yield much more intuitive results. Multiple angles will need to be imaged to aid the reconstruction process (section 4.4), but this will involve multiple, different, simulation setups with shifted particle sources and detector planes.

4.3. Asteroid Simulation

As previously mentioned in section 4.2.2, the $5m$ radius simplified asteroid model is used as the subject in most of the simulations performed in this thesis project. Four different versions are used, three of which are graphically shown in figures 4.3b and 4.4. The fourth model is the "control", which does not feature any inclusions and is therefore a homogeneous sphere similar in size, mass and composition to the other three models. This section displays the simulation results of these models, applying different data processing techniques and algorithms case-by-case to reveal the internal structures and features. Figure 4.8 shows graphically what a particle shower caused by a single $1TeV$ proton looks like in the visualisation feature of *Geant4*. For clarity, only protons and muons are displayed, as additional particle tracks would completely clutter up the image.

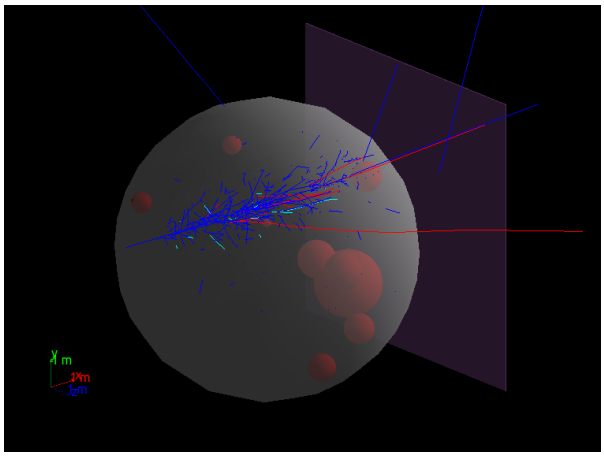

Figure 4.8: Simulation particle shower caused by a single $1TeV$ proton colliding with the 10 inclusions simplified asteroid model. Proton tracks shown in blue, μ^- in red and μ^+ in turquoise.

For all of the simulations, apart from the ones using galactic cosmic ray primaries (section 4.3.4), the particle source is a $10 \times 10m^2$ plane positioned at $-5.1m$ from the model's origin on the axis of interest. The plane, in which all the primaries originate, is positioned orthogonal to said axis. The initial velocity vector is parallel to the axis of interest. For each simulation, the particle detection plate (shown in figure 4.8) and the particle source are placed parallel and at opposite sides of the model. The use of such a linear representation of a much more complex real-world situation is justified in section 4.2.4.

4.3.1. Tomography Working Principal

With the different methods of muon detection, described in section 2.3, the properties of each muon passing through the detector can be measured with varying degrees of accuracy. A muon's properties and travel path are affected by the type and density of material it passes through. These interactions are described in section 2.2.3. This subsection shows the working principal of muon tomography by describing the various methods, analytically applying the knowledge from the two previously mentioned sections.

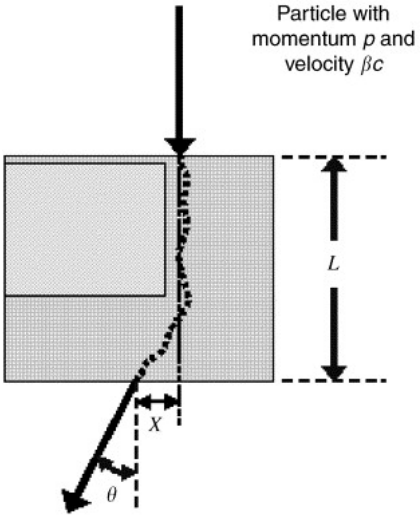

(a) Muon scattering through matter. Angle is exaggerated for clarity. From "Image reconstruction and material Z discrimination via cosmic ray muon radiography" by L.J. Schultz et al., (2004)[204].

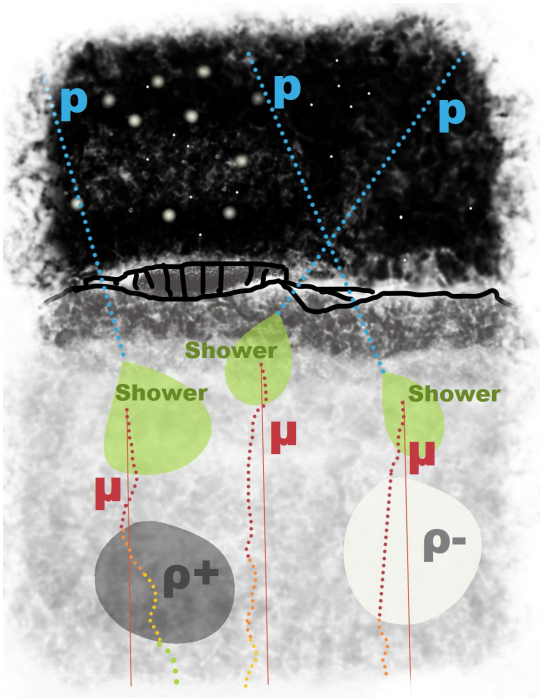

(b) Cosmic ray induced muon transmission through asteroidal material. The straight red line shows the extrapolated path and energy of the muon from starting conditions. The dashed line shows the actual path, where increasing hue angle (red→green) shows decreasing kinetic energy. Higher and lower density regions are indicated with $\rho+$ and $\rho-$ respectively. Not to scale.

Figure 4.9: Schematic representations of muon travel path through matter.

Scattering Tomography

One of the methods used for muon tomography is called scattering tomography. The muon's path through an asteroid is not a straight track due to multiple Coulomb scattering. This causes the muon's exit point on the asteroid's surface to be shifted by a distance x, and the angle to be offset from its initial velocity vector by a cumulative scattering angle θ, as shown in figure 4.9a. The many small scattering interactions a muon undergoes on its journey through the asteroid add up to an angular deviation distribution that roughly follows a Gaussian curve. This curve has long tails, but its centre 98% can be described by a width σ_θ and follows equation 4.7.

$$\frac{dN}{d\theta} = \frac{1}{\sqrt{2\pi\sigma_\theta}} e^{-\frac{\theta_x^2}{2\sigma_\theta^2}} [30] \tag{4.7}$$

The mean θ of the angular scattering distribution is 0 degrees, and the standard deviation σ_θ is calculated with equation 4.8.

$$\sigma_\theta = \frac{13.6[MeV]}{\beta c p} \sqrt{\frac{L}{L_0}} \cdot [1 + 0.038 \cdot \ln \frac{L}{L_0}][204] \tag{4.8}$$

In this equation, L is the depth of material (figure 4.9a), L_0 is the radiation length of the material, p and $\beta \cdot c$ are the momentum and velocity of the muon respectively. The spatial shift of the exit point can be described by a Gaussian distribution as well, where the standard deviation σ_x relates to σ_θ:

$$\sigma_x = \frac{L}{\sqrt{3}} \cdot \sigma_\theta [204] \tag{4.9}$$

It is important to note that these equations are for the scattering angle and displacement in a single plane. The values for these in a plane orthogonal to the previous are independent, but follow the same distributions. The total spatial displacement is therefore a Pythagorean combination of x and y, assuming the muon's velocity vector was along the $z-axis$. The radiation length depends on the type of material and increases with increasing atomic number Z, atomic mass number A and density ρ, as shown in equation 4.10.

$$L_0 \approx \frac{A \cdot 716.4[g/cm^2]}{\rho \cdot Z \cdot (Z+1)\ln(287/\sqrt{Z})}[81] \tag{4.10}$$

The amount of scattering can therefore be used to draw conclusions on material type versus density, as materials containing heavier elements will scatter the muons more. For example, the radiation length of platinum group metal Rhodium, a very rare and very expensive metal on Earth, would be only ~ 2/3 of the radiation length of Iron at the same density. The resulting scattering standard deviation would then be ~ 24% higher for Rhodium.
A caveat to this process is the fact that the muons are created with an initial angular and spatial offset as compared to their primary cosmic ray particle's velocity vector. This is due to the conservation of momentum in the decay off their precursor particle. Relating a muon's exit angle to its cosmic ray primary is therefore much more complex than merely applying equation 4.7. A basic version of muon scattering tomography, which is essentially fitting a straight track to all muon velocity vectors at the detector and finding the locations where strongly scattered muons cross paths [204], is applied in section 4.3.3 and 4.4.

Absorption Tomography
A much more fitting technique for this research is called energy absorption tomography. As a muon travels through the asteroid it loses kinetic energy, the amount of which depends mostly on material density, muon energy and travelled distance. As described in section 2.2.3, the approximate total kinetic energy loss is found by integrating over figure 2.16, and the actual total kinetic energy loss is governed by a Landau distribution (equations 2.14). As muons lose more energy per travelled distance in denser materials, graphically shown in figure 4.9b, this muon property can be used to detect higher and lower density inclusions. The material property recovered from this type of tomography is called the opacity $\varrho[g/cm^2]$, similar to column density, and quantifies the amount of matter the muon encountered on its path. It is found by integrating the local density per unit length l over the total muon path length L, shown in equation 4.11.

$$\varrho = \int_L \rho(l)\,dl\,[122] \tag{4.11}$$

Transmission Tomography
A subset of energy absorption tomography is called transmission tomography, where one looks at the amount of muons that survive their journey through the subject material. Once a muon's kinetic energy approaches zero, it will be stopped in its path. Volumes through which relatively less muons survive will therefore logically have more stopping power and thus a higher density. Using this muon count property for imaging is the third method applied in this chapter.
To conclude, the most important properties to be measured at the detector in the simulation are the muon's kinetic energy, its velocity vector, its intersection location with the detector and their number total.

4.3.2. Muon Primaries

The use of muons as primaries will yield far more tangible results as compared to protons and GCRs, as there is much better control over the muon's parameters such as energy and velocity vector, and much more particles can be simulated within a certain timeframe. For all the muon simulations, an equal number of positively and negatively charged particles is used.

Muon-Count Mapping
The stopping power of muons in regolith not only depends on density and material, but on muon energy as well. This is clear from figure 2.16, where the Bethe-Bloch dominated section is of most interest. From research performed on a $250 \cdot 250 m^2$ slab of $50m$ thickness, with a composition of 20% FeO and 80% SiO_2 by mass, and a density of $1.6 g/cm^3$, it is known that the average stopping power for $20GeV$ muons is $346 MeV/m$,

while for $100GeV$ muons this equals $430MeV/m$ [125]. Muons lose typically $2.5MeV$ per $1g/cm^2$ opacity when atmospheric muons are considered [122]. As the average density for the simplified asteroid model in this section is slightly higher, it will logically have more stopping power. For this $10m$ diameter sphere, a minimal muon kinetic energy of around $3 \sim 4GeV$ at the source must therefore be assumed. However, the minimum stopping power according to Bethe-Bloch lies close to this energy range. Muons in this energy range will therefore experience less stopping power compared to more energetic muons. Using lower energy muons will increase computational efficiency. Thus, to find the optimal muon energy, a transmission test was performed on the homogeneous asteroid, using 4 different muon kinetic energies. The 3D muon count histograms of the results, using 100 by 100 bins, are shown in the following figure 4.10.

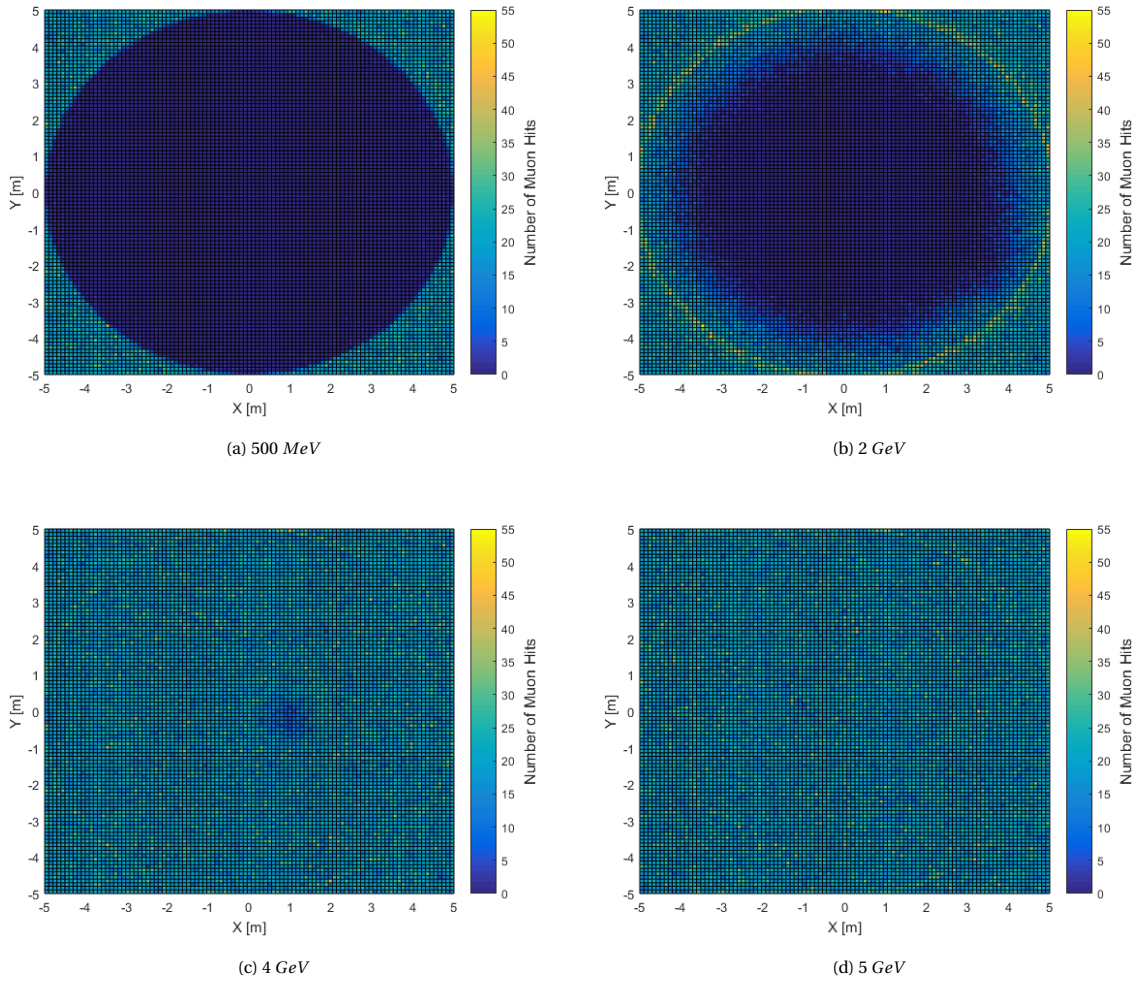

(a) 500 MeV

(b) 2 GeV

(c) 4 GeV

(d) 5 GeV

Figure 4.10: Transmission test of 200k muons along the Z-axis, at 4 different kinetic energy levels. The ten monolithic inclusion model was used as the simulation subject. Each histogram bin has a corresponding detector area of $10 \times 10cm^2$.

Figure 4.10a and 4.10b reveal large areas of the detector that did not receive any muons, whereas figure 4.10c only shows a small spot of decreased muon count and figure 4.10d displays no visible muon count variations on the detector's surface. These results shows that at least $4GeV$ muons are needed, and at least $5GeV$ muons are preferred, to fully penetrate the simplified asteroid model. The opacity of the simplified asteroid is calculated to be $\varrho \approx 1900g/cm^2$ through the centre, where the energy loss of the $4GeV$ and $5GeV$ muons is $\Delta E \approx 3.6GeV$ and $\Delta E \approx 3.8GeV$ respectively. These findings adhere to Bethe-Bloch as the higher energy particles lost more energy. The muons dissipated $1.9 \sim 2MeV$ per $1g/cm^2$ of opacity, predictably less than the values found in previously mentioned literature where on average higher energy muons were used. The dark spot visible in the $4GeV$ histogram (figure 4.10c), at approximately $[X,Y] \approx [1m,-0.2m]$, coincides with two spherical inclusions of $\sim 1.2m$ diameter, "stacked" in the Z direction. This already indicates that muon count can be used to find inclusions, as more muons will be stopped in denser material.

Another interesting finding is the increase in muon count at $\sqrt{X^2+Y^2} \approx 5m$, the outer rim of the model, most prominently visible in figure 4.10b. This is most likely due to the scattering effect of the asteroidal matter on the particles. The muons that hit the surface near this rim, can deviate from their original velocity vector. The ones that scatter towards the model's origin are more likely to be completely stopped as they encounter more matter than the ones scattering outwards, creating the higher muon count ring on the detector.

Energy Absorption Mapping

It is clear from figure 4.10d that once the muon kinetic energy surpasses the minimum level needed to fully penetrate the asteroid, not much information on its internal structure can be deduced based on muon count alone. The flux through an asteroid will contain a range of different muon energies, allowing for some muon-count mapping to be performed. However, the applicable energy range of muons is quite small, rendering most of the detected muons exceeding this range useless for this type of tomography. For example, in the case of the ten meter diameter asteroid, only muons within the $2 \sim 4GeV$ energy range (figure 4.10b & 4.10c) can be used for this purpose.
A technique called absorption tomography [204] can be used to reveal such internal structures based on their difference in muon energy absorption. This technique, further discussed in section 4.4, requires the energy of each detected muon to be mapped. Similarly to figure 4.10, 100 by 100 bins are used to create a histogram, where the weight of each of the histogram points is determined by the average energy of all the muons that transected that specific $10 \times 10cm^2$ bin area. The resulting histograms for both the 10 monolithic inclusions model and the 3 voids, 7 monoliths model simulations are shown in figure 4.11.

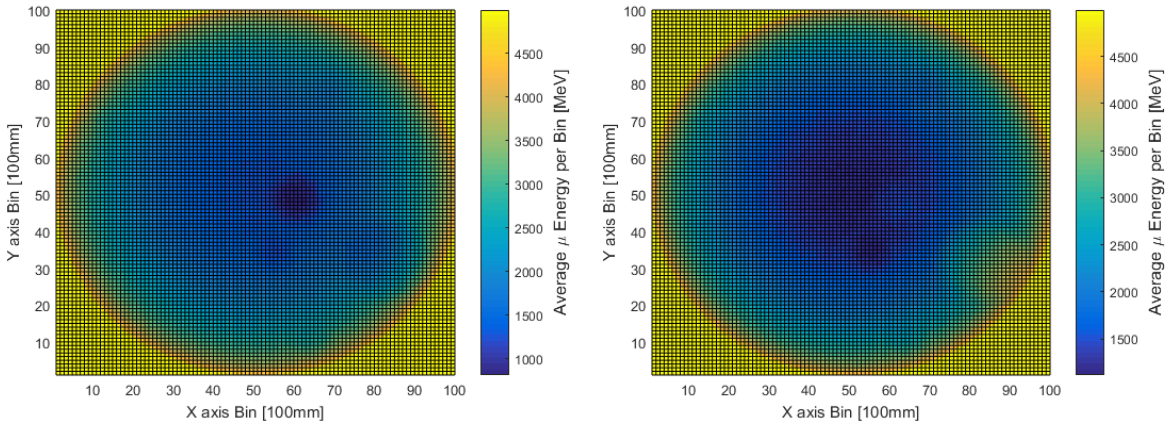

(a) 10 monolithic inclusions

(b) 7 monolithic and 3 void inclusions

Figure 4.11: Average remaining kinetic energy per muon. Simulation of 500k $5GeV$ muons through $5m$ radius simplified asteroids (figure 4.4), along the Z-axis. Average taken from all muons hitting a corresponding detector area bin of $10 \times 10cm^2$.

The computation time needed for the simulation of these 500,000 $5GeV$ muons is approximately 1 hour, per axis, per model. The presence of the inclusions in figure 4.11 is much more prominent compared to the transmission count based figure 4.10c. Increasing the contrast will reveal the inclusions even more. However, a much more effective technique can be used to isolate the inclusions from the figure.
For the most part, the energy absorption is caused by the sheer bulk of the material present in the asteroid. The small internal deviations from the homogeneous distribution are not clearly distinguishable in the measurement results. By the use of a "control" simulation, a bias file can be constructed which can remove the averaged effect of the asteroid on the muon energy absorption. For this simulation, the control model is used, which has the same shape model, average composition and average density as the asteroids in figure 4.4. It is important to note that this "control" model can be constructed from information available from spacecraft sensors, such as the asteroid shape model and mass, and is therefore a very useful data manipulation tool. The bias file for the simulations in figure 4.11 is shown in figure 4.12.

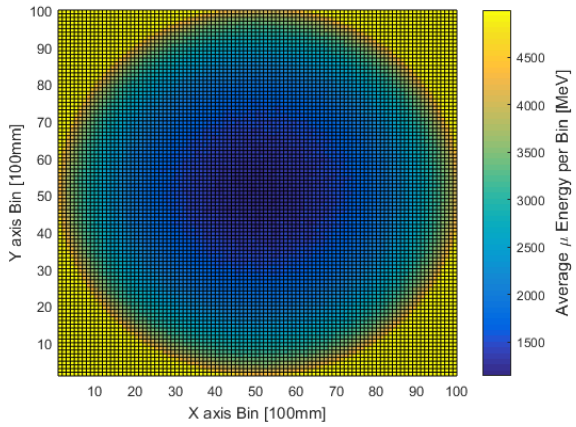

Figure 4.12: Average remaining kinetic energy per muon. Simulation of 500k $5GeV$ muons through $5m$ radius simplified "control" asteroid, along the Z-axis. Average taken from all muons hitting a corresponding detector area bin of $10 \times 10cm^2$.

Without any inclusions, the simulation time for 500k $5GeV$ muons is approximately 11% shorter ($3200s$) compared to the simulation for the models with inclusions. The resulting bias file of 100 by 100 average energy bins is subtracted from the simulation results in figure 4.11, yielding the energy difference per muon per bin as compared to a homogeneous asteroid.

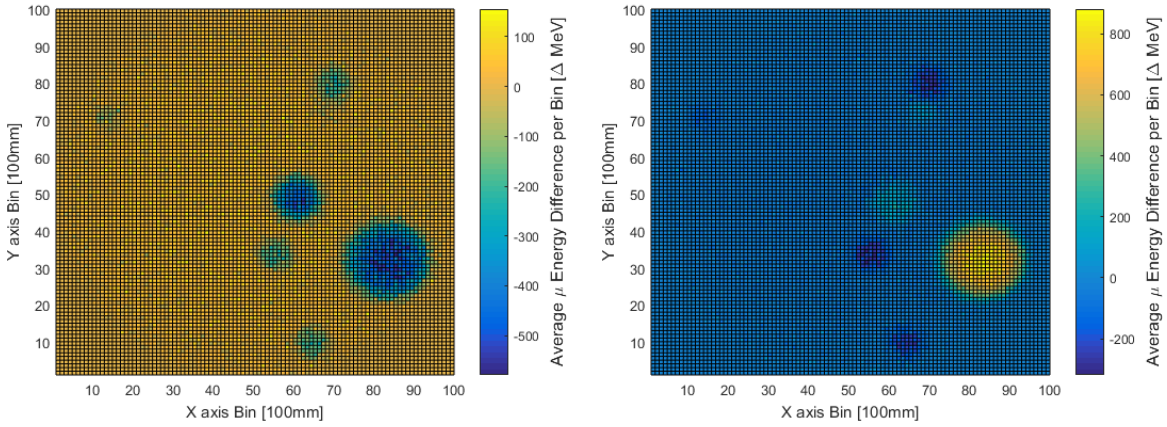

(a) 10 monolithic inclusions

(b) 7 monolithic and 3 void inclusions

Figure 4.13: Average kinetic energy difference per muon per bin, heterogeneous asteroid (figure 4.11) compared to homogeneous asteroid (figure 4.12).

The resulting histograms in figure 4.13 clearly show the location and size of the inclusions. To enhance the clarity even further and isolate the inclusions, a threshold can be used to remove all the bins with a close-to-zero energy difference with the bias file, of which the resulting histograms are shown in figure 4.14b. In this case, a $\pm 50MeV$ threshold was applied. For subsequent easy comparison, the 2D view along the Z-axis of both asteroid models are overlaid on their respective histograms.

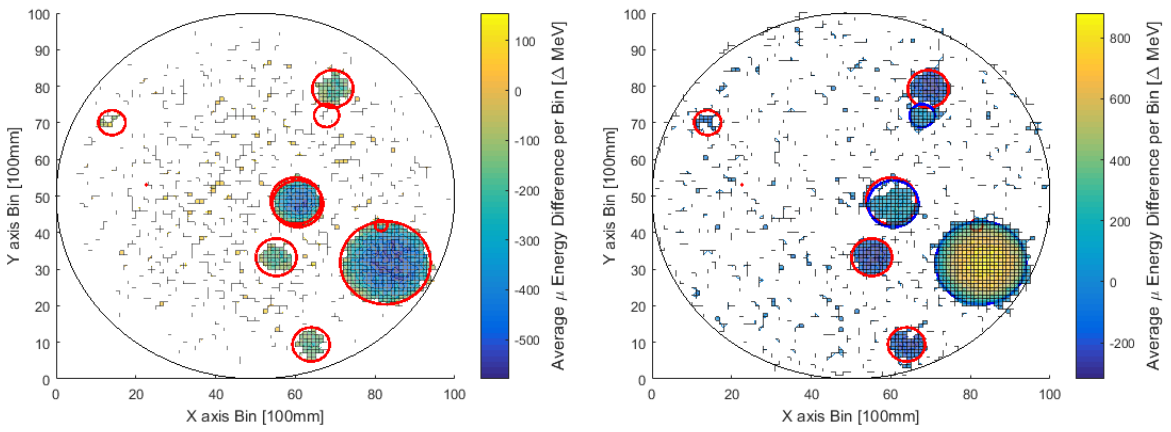

(a) 10 monolithic inclusions

(b) 7 monolithic and 3 void inclusions

Figure 4.14: Figure 4.13 with a $\pm 50 MeV$ threshold removed. 2D circular representation of spherical inclusions shows their location and size in the $X-Y$ plane. Red circles denote higher density monoliths, blue circles depict void inclusions.

4.3.3. Proton Primaries

The use of a pure proton source is considered a good trade-off between the realism of using galactic cosmic ray source, and the level of control gained by using a pure muon source. For this reason, a pure proton particle source was used in multiple asteroid muon tomography studies [125][186].

Energy Absorption Mapping

Continuing on with the $5m$ radius simplified asteroid, a quick performance test shows that higher energy protons will yield more muons per simulation second than lower energy ones. The results of this performance test are shown in table 4.4.

Proton Kinetic Energy	50 GeV	75 GeV	100 GeV	200 GeV	200 GeV *
100 Proton Simulation	72.2 s	99.2 s	126.9 s	253 s	222 s
Muon:Protons	1:25	1:6.25	1:3.8	1:1.7	1:7.8
100 Muons (Extrapolated)	1805 s	620 s	482 s	430 s	1731.6 s

Table 4.4: Performance analysis of 100 primary protons through $5m$ radius simplified asteroid, set to $1 g/cm^3$ density. Muon simulation time extrapolated from generated muons-per-proton and 100 proton simulation time. *Simplified asteroid model with the regular $1.9 g/cm3$ density.

Additionally, high kinetic energy protons have a higher chance of producing energetic muons, which are of most interest to this research. The choice is therefore made to use $200 GeV$ proton primaries for this section. As simulating high energy proton primaries is computationally more intensive than muons, the simulations will yield much less usable data in the same computation time. Less detected muons will result in a much lower resolution and contrast [187]. To partially mitigate this, the resolution is lowered to 10 by 10 bins of $1 \times 1 m^2$ each, increasing the number of muons per bin available. The axis labels on the plots in this section, located at the bins' centres, denote the bin number starting from the axis' minimum, which is $-5m$ for both axes. For example, the the bin located at $(2,3)$ represents the data of the $1 \times 1 m^2$ detector square centred at $(Y,Z) = (-3.5m, -2.5m)$.

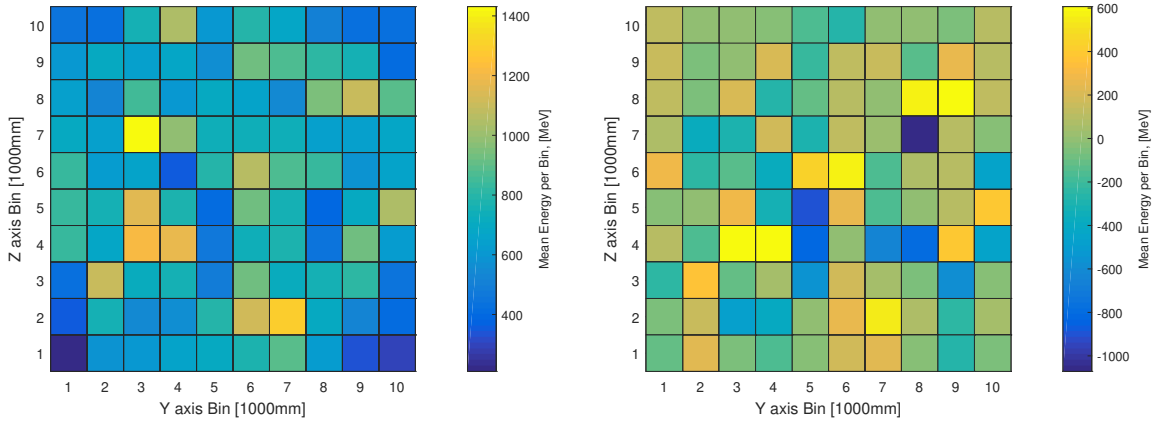

(a) 7 monolith and 3 void inclusions asteroid (figure 4.11)

(b) Energy difference with homogeneous asteroid (figure 4.12).

Figure 4.15: Average kinetic energy per muon per bin of $1 \times 1m^2$, resulting from 16k $100GeV$ proton primaries.

It is evident from figure 4.15 that lowering the resolution alone will not mitigate the problems resulting from a lack of muons. The simulation time for the above figures was 4.6 hours for the inclusions test, and 4.4 hours for the control. Increasing the amount of proton primaries will result in more muons, but will decrease the turnaround time of the simulation, which is not preferred. The high contrast simplified asteroid model (figure 4.4b), containing merely 2 voids and 2 monolithic solids, is used for most of the following simulations, as higher contrast will be easier to detect. As an additional measure the regolith density is lowered for some of the simulations, which will yield more muons in less simulation time according to table 4.4.

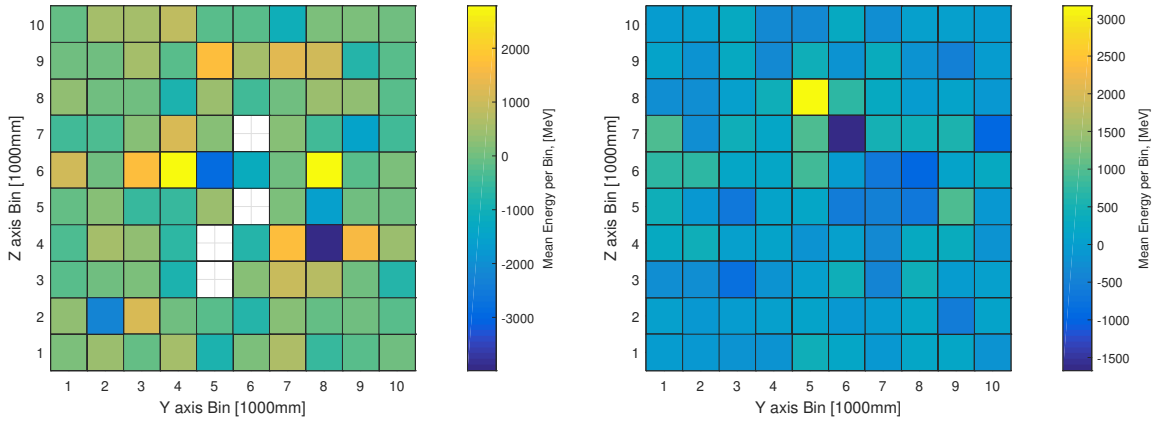

(a) Normal regolith density; $1.92g/cm^3$.

(b) Lowered regolith density; $1g/cm^3$

Figure 4.16: Average kinetic energy difference per muon per bin of $1 \times 1m^2$, resulting from 6.5k $200GeV$ proton primaries. Difference calculated between simulation results of 2 void, 2 monolithic inclusions asteroid (figure 4.4b) and homogeneous asteroid.

These results show that vast amounts of simulation time are needed to yield enough results to be able to draw conclusions using the same data processing method as for muons, in section 4.3.2. The empty squares, visible in figure 4.16a, are the result of a complete absence of muon counts in those detector areas. The crossing lines visible in these empty areas are merely the axis grid lines, denoting the bin's centre.
The velocity vector of the muons arriving at the detector varies much more compared to the muons detected when using a pure muons source. This results in an unfocused, unclear histogram, as seen in figures 4.15 and 4.16. Higher energy muons tend to scatter less when travelling through matter [125]. A threshold is therefore used to remove muons with kinetic energy levels lower than $1GeV$. This threshold was only applied on the $1g/cm^3$ model (figure 4.17b), since too little data would remain when applied on the normal regolith density model. Higher energy muons arriving at oblique angles are discarded as well, as they most likely scattered in their creation process and will not form the right 2D representation on the histogram. The resulting plots are shown in figure 4.17.

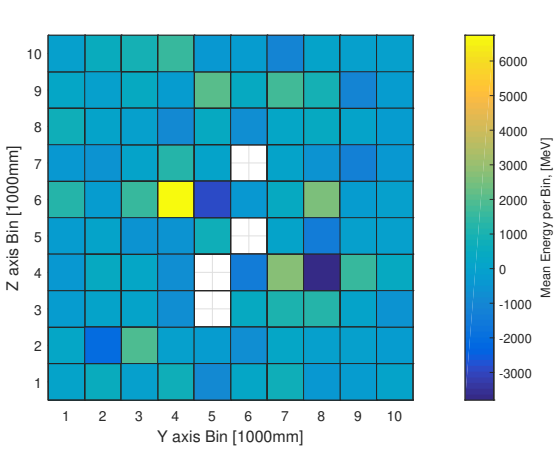

(a) Normal regolith density; $1.92 g/cm^3$.

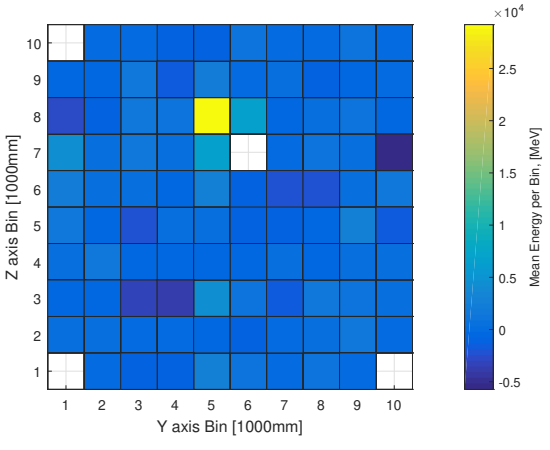

(b) Lowered regolith density; $1 g/cm^3$. $1 GeV$ minimum muon energy threshold.

Figure 4.17: Average kinetic energy difference per muon per bin of $1 \times 1 m^2$, resulting from 6.5k $200 GeV$ proton primaries. Difference calculated between simulation results of 2 void, 2 monolithic inclusions asteroid (figure 4.4b) and homogeneous asteroid. The minimum velocity unit vector threshold in the X direction is set at 0.9.

Again, these resulting figures show very little detail, partly due to the removal of many detector hits, which were already very little in number to begin with. To reveal some detail lost by this removal process, a completely new approach is employed.

Straight Track Fitting

A plot of all the muon travel paths is created, based on the available information at the detector. The path from the asteroid surface to the detector plate is considered to be linear, as almost no matter is present to induce scattering. The path within the asteroid is considerably less linear. The following plot 4.18 shows the extrapolated muon travel paths, based on their velocity vector on arrival at the detector plate. The extrapolation takes place in two separate steps: the first step provides a linear plot from the detector to the asteroid's surface (in red), the next extrapolates linearly from the surface exit point to the surface entry point (in blue). This straight-track approximation is assumed to be relatively accurate when applied to high energy muons [186]. The further back this line is tracked through the asteroid material, the larger the probable deviation from this linear vector, and the less likely it is the muon existed at the determined point. This phenomenon is discussed in further detail in section 4.4.3, and shown graphically in figure 4.29.

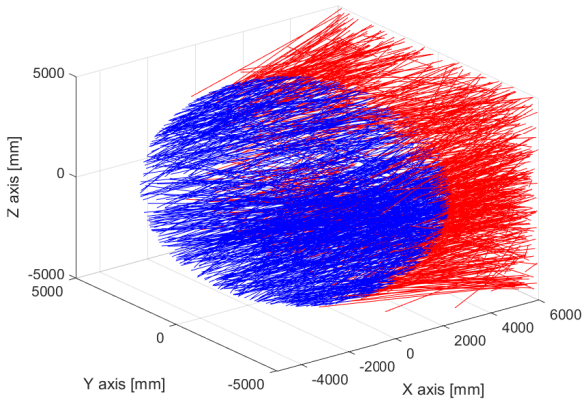

Figure 4.18: Extrapolated muon travel paths from simulation of 6.5k $200 GeV$ protons through a $5m$ radius, simplified, 4 inclusions asteroid (figure 4.4b), along the X-axis. Red line shows travel path after asteroid exit, blue line shows interior travel path.

Nonetheless, this muon vector extrapolation can reveal quite some detail of the interior structure. For comparison, two simulation runs of 6,500 $200 GeV$ proton primaries are performed on both the four inclusions model (figure 4.4b) as the homogeneous control model. The computation time, 4.3 hours and 4 hours

respectively, is considerably higher compared to using muon primaries, limiting the amount of proton primaries used. For the following plot, higher energy muon vectors are shown with bigger line thickness, as they are assumed to have scattered less on their path through the asteroid. The increasing thickness therefore is used as a gauge to show path probability. As the travelled path outside the asteroid is not of interest for this plot, geared towards revealing interior composition, only the muon vector within the asteroid is shown.

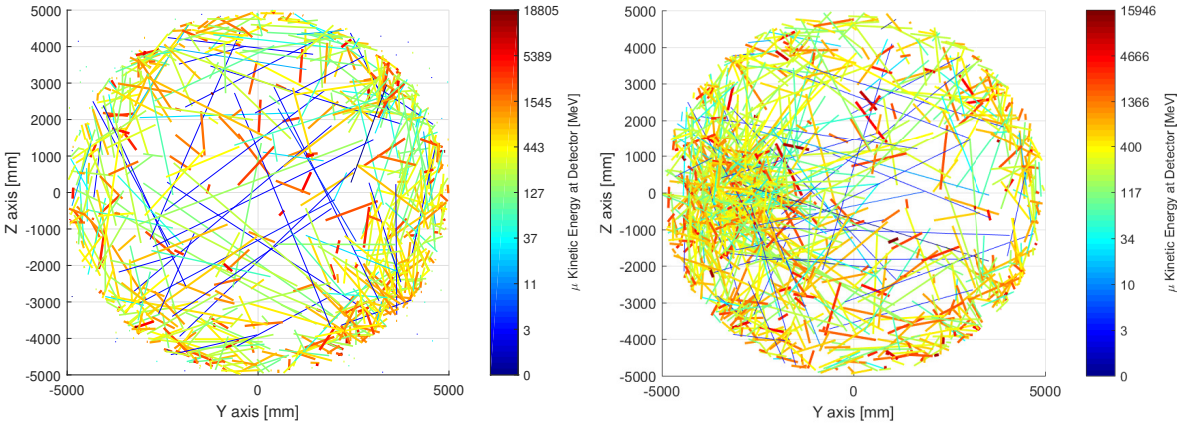

(a) Control

(b) 2 monolithic and 2 void inclusions

Figure 4.19: Extrapolated interior muon travel paths from simulation of 6.5k 200GeV protons through 5m radius simplified asteroids, along the X-axis. Line width increases with kinetic energy.

It is clear that more numerous and higher energy muons are present in the $Y < 0$ area of figure 4.19b, whereas less muons are present in the $Y > 0$ area. This increase is the result of the void inclusions present in the model. For ease of comparing, the 2D representation of the inclusions present in the 4 inclusion mode (figure 4.4b), in the $Y - Z$ plane, is superimposed on the figure. The void inclusion are represented as blue circles, the monolithic higher density inclusions as red circles. The resulting figure 4.20 shows, albeit crudely, that the extrapolation of the muon velocity vector is a viable method for determining an asteroid's interior structure.

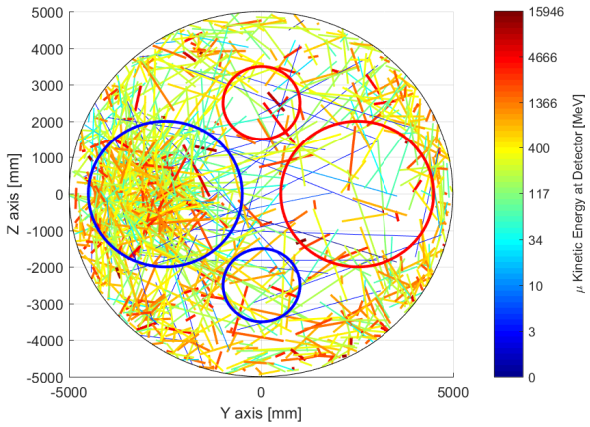

Figure 4.20: Figure 4.19 with the 2D circular representation of the inclusions shown in the $Y - Z$ plane. Red circles denote higher density monoliths, blue circles depict void inclusions.

4.3.4. Galactic Cosmic Ray Primaries

As the amount of muons received from a cosmic ray primaries source is expected to be quite low per computing time, as shown in section 4.2.3, the high contrast 2 inclusion, 2 voids simplified asteroid model visible in figure 4.3b is used for the simulations in this section. The simulation is set up with a spherical particle source of radius $R_s = 5.1m$, completely enveloping the concentric $R_a = 5m$ radius spherical model, contrary to the previous sections where a square planar particle source was employed. The direction of the emitted particles

is set inwards, shown schematically in figure 4.21. It must be noted that the infinitesimal sections shown are merely added for clarification and depict a subset of the full 3D sphere. The blue arrows are drawn randomly, but their distribution in the simulation is cosine-law dependent.

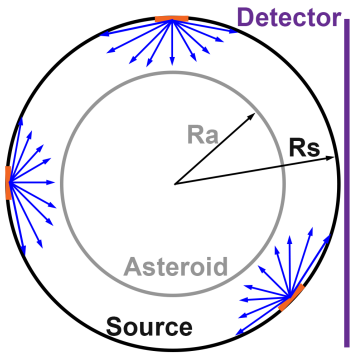

Figure 4.21: Schematic 2D representation of simulation setup. Three randomly placed, infinitesimal sections of the source surface depicted in orange show the velocity vectors of particles originating within, in blue. R_a and R_s denote the asteroid an particle source radius respectively. Not to scale.

As previously mentioned in section 4.2.3, the GCR spectrum will mostly be simplified to a pure proton source, adhering to the differential energy flux as provided by SPENVIS. Additionally, a simulation run with alpha particles (Helium ions) was performed to provide some new results and take a preliminary look at how big of an increase in muon count the additional flux will provide.

Normalisation Factor

The normalisation factor for this spherical particle source is calculated using equation 4.4. Two of the three input arguments for this equation, when using the modified GCR flux spanning from $1GeV$ to $100TeV$, are previously calculated in section 4.2.3 and equal $n_{1(p)} = 2.4587[cm^{-2}s^{-1}]$ for protons, $n_{1(\alpha)} = 0.3382[cm^{-2}s^{-1}]$ for alpha particles and $n_2 = 1/4$ for both. The surface area of the emitter is calculated using equation 4.12.

$$S = 4\pi R_s^2 = 3,268,512.99[cm^2] \tag{4.12}$$

The resulting normalisation factors then equate to:

$$N_{r(p)} = n_{1(p)} n_2 S = 2009073.22 \approx 2.01 \cdot 10^6 [s^{-1}] \tag{4.13}$$

$$N_{r(\alpha)} = n_{1(\alpha)} n_2 S = 276,390.03 \approx 2.764 \cdot 10^5 [s^{-1}] \tag{4.14}$$

This represents the total number of GCRs fired from the source's surface in a single real-world second. Using equation 4.3, this normalisation factor N_r can be divided by the total number of particles fired in the simulation N_s to create the factor by which the scored number of particles in the simulated detector X_s can be converted to the real world expected number X_r.

Muon Count

A proton GCR simulation using $N_{s(p)} = 502,268$ particles, which represents exactly $N_{s(p)}/N_{r(p)} = 0.25s$ of real-world time, took 9.4 hours to complete. An entire real-world second would take 37.6 hours, which is quite close to the predicted 44 hours in section 4.2.3 for an asteroid without such large voids, showing that computing time can quite reasonably be extrapolated. The simulation time for alpha particles was quite a bit shorter, with $N_{s(\alpha)} = 138,196$ representing $0.5s$ of real-world time taking $5.4hours$ to complete.
The total amount of muons reaching the $10 \times 10m^2$ detector in the proton simulation is $X_{s(p)} = 2635$, of which only $X_{s(p)}(> 1GeV) = 30$ surpass the aforementioned $1GeV$ lower energy limit for backscatter removal. The muon count for the alpha simulation, divided by 2 to match the real-world run time of the proton simulation, was $X_{s(\alpha)} = 723$ and $X_{s(\alpha)}(> 1GeV) = 10.5$. The muon count results are extrapolated for longer real-world durations, and simulation times are extrapolated according to the performance comparison shown in table 4.2. The results are tabulated in table 4.5.

Real World Time	0.25s	1s	1 day	1 month	6 months	1 year
Total Primary GCR Protons	5.02E+5	2.01E+06	1.74E+11	5.28E+12	3.17E+13	6.34E+13
Total Muons	**2635**	*1.05E+04*	*9.11E+08*	*2.77E+10*	*1.66E+11*	*3.33E+11*
Total $E_{kin} > 1GeV$ Muons	**30**	*120*	*1.04E+07*	*3.16E+08*	*1.89E+09*	*3.79E+09*
$E_{kin} > 1GeV$ Muons / m^2	**0.3**	*1.2*	*1.04E+05*	*3.16E+06*	*1.89E+07*	*3.79E+07*
Total Primary GCR α	6.91E+4	2.76E+5	2.39E+10	7.27E+11	4.36E+12	8.72E+12
Total Muons	**723**	*2892*	*2.5E+08*	*7.61E+09*	*4.56E+10*	*9.13E+10*
Total $E_{kin} > 1GeV$ Muons	**10**	*42*	*3.63E+06*	*1.1E+08*	*6.63E+08*	*1.33E+09*
$E_{kin} > 1GeV$ Muons / m^2	**0.1**	*0.42*	*3.63E+04*	*1.1E+06*	*6.63E+06*	*1.33E+07*
Simulation Time HP 8560W(p&α)	**9.4&2.7h**	*37.5&10.7h*	*N/A&N/A*	*N/A&N/A*	*N/A&N/A*	*N/A&N/A*
Simulation Time Magdalena(p&α)	*131&37s*	*524&150s*	*524&150d*	*N/A&N/A*	*N/A&N/A*	*N/A&N/A*

Table 4.5: Extrapolated muon counts and simulation times for longer duration simulations. Simulation subject is the $5m$ radius, 2 inclusions, 2 voids simplified asteroid model. Values in **bold** are simulation results, values in *italics* are extrapolated.

This shows that if the alpha particle flux is included in the simulation, a 35% increase in muon count can be expected at the detector. This is a significant increase, and should therefore be taken into account for conclusions drawn on feasibility.
To show the expected muon flux values for asteroids larger than the $10m$ diameter model used thus far, the simulation results are extrapolated. The equations to extrapolate with are the best-fit power-laws applied to the simulation results of J. Keerl [125] and T.H. Prettyman [187]. The following table 4.6 shows these simulation results as well as the extrapolated results of this study.

Asteroid Depth	10	50	100	200	500	[m]	Source ⇓
$\rho_b = 1.6g/cm^3$	*1.89E+6*	**14 134**	*1791*	**320**	**12.6**	$[sr^{-1}h^{-1}m^{-2}]$	J.Keerl[125]
Asteroid Diameter	10	50	100	200	500	[m]	Source ⇓
$\rho_b = 2g/cm^3$	*1.01E+05*	**960**	**144**	**20.4**	*1.45*	$[m^{-2}day^{-1}]$	T.H.Prettyman[187]
		[Extrapolated Simulation Results]					Extrapolation ⇓
$\rho_b = 1.9g/cm^3$	**1.40E+05**	*1118*	*140*	*17.5*	*1.12*	$[m^{-2}day^{-1}]$	$\propto$ J.Keerl
$\rho_b = 1.9g/cm^3$	**1.40E+05**	*1425*	*197*	*27.3*	*2*	$[m^{-2}day^{-1}]$	$\propto$ T.H.Prettyman

Table 4.6: Muon counts per day per square meter detector on the surface, for larger asteroid diameters. Values in **bold** are obtained directly from sources, values in *italics* are extrapolated using best-fit power law from available data per source. Simulation results including the alpha particle contribution in **bold** are extrapolated in *italics* proportional to source data, indicated in the right-most column.

As the amount of muons to work with is quite low, a similar method to the proton primaries section 4.3.3 will be applied. Figure 4.22 characterises the number of muons reaching the detector versus the incident location in the $Y-Z$ plane.

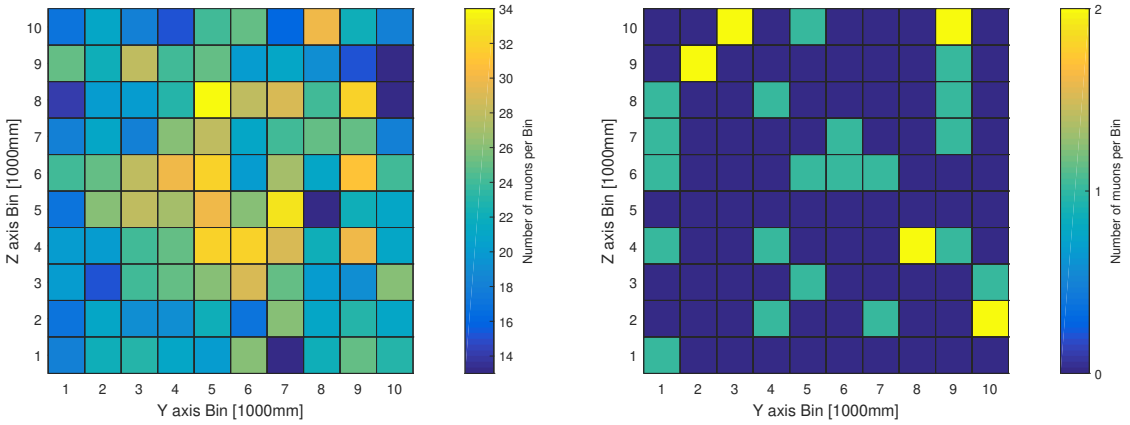

(a) Full kinetic energy spectrum.

(b) $1GeV$ lower kinetic energy threshold.

Figure 4.22: Muon count per $1 \times 1m^2$ bin.

There seems to be no representation of the 2 voids, 2 inclusions simplified asteroid model visible based on transmission tomography. A similar story unfolds when considering energy absorption tomography, as visible in figure 4.23.

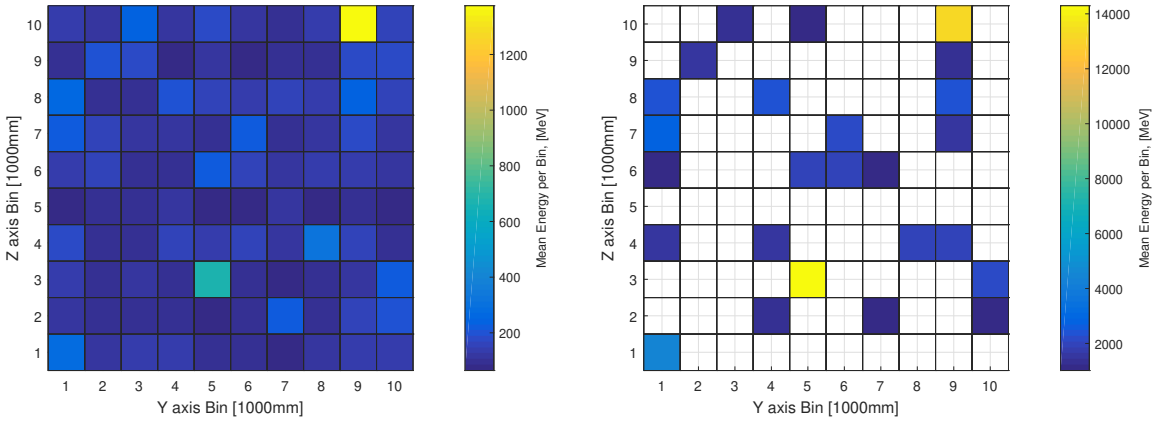

(a) Full kinetic energy spectrum.

(b) $1GeV$ lower kinetic energy threshold.

Figure 4.23: Average kinetic energy of muons reaching the detector, per $1 \times 1m^2$ bin.

To try and recover some interior structure information from the muon data, the straight track fitting method is employed, similar in setup to section 4.3.3. The $1GeV$ kinetic energy limit should remove all the potential backscattered muons [186].

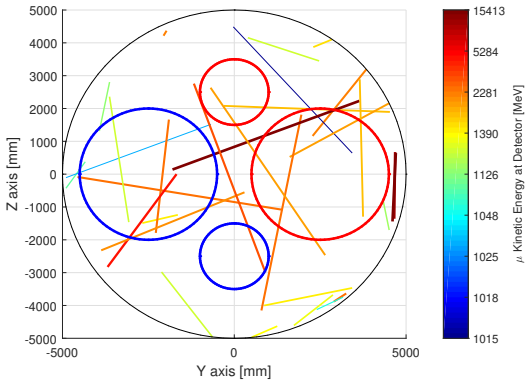

(a) Travel paths through a $5m$ radius simplified asteroid.

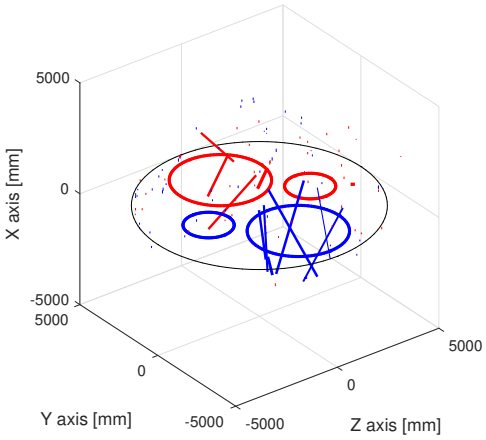

(b) Travel paths through inclusions (red) and voids (blue).

Figure 4.24: Extrapolated $E_{kin} > 1GeV$ muon travel paths from simulation of ~ $500k$, $1GeV - 100TeV$ GCR protons. 2D circular representation of the spherical inclusions (red) and voids (blue) shown in the $Y - Z$ plane. Line width increases with kinetic energy.

The 2D view along the $x - axis$ in figure 4.24a already shows the increase in muon travel paths through the larger void. To increase the clarity, a 3D view is created in which only the travel paths through the voids and inclusions are shown, in figure 4.24b. This very clearly shows that more high energy muons transected the void compared to the monolithic inclusion. Although in this situation this could be considered cherry picking the data, as the location of the inclusions is known beforehand, a similar process of density model fitting can be employed for reconstruction purposes, which will be discussed in further detail in section 4.4. This simulation of merely $0.25s$ of real-world time already shows some promising results for asteroid muon tomography. When including the alpha particles, the amount of muon tracks transecting the large void is twice the number of those transecting the large inclusion.

4.4. Reconstruction

In this section, the exploratory research and numerical modelling of reconstruction algorithms applicable to the muon tomography performed in this project, are discussed. Reconstructing a 3D model from 2D observations is an inverse problem, as one attempts to reconstruct the cause from the effects. This is almost never directly analytically possible, and requires a tuned algorithm to minimise artefacts.
As a preliminary high-level algorithm, an orthogonal 3-axis projection made with muon energy absorption mapping is used to reconstruct the 10 inclusions model. The process used to create these energy absorption difference maps is discussed in section 4.3.2, where the view along the $z - axis$ is shown in figure 4.13. The views along the x and y axes are shown in figure 4.25, for both the 10 monolithic inclusion model as well as the 7 monolithic, 3 void inclusion model.

4.4.1. Back Projection

The first reconstruction algorithm explored is called "Back Projection" (BP). This is a very intuitive but unsophisticated approach of resolving detail in 2D or 3D space, from lower dimensional projections. Stepping away from mathematical terms, this process is performed by smearing the acquired 2D image back through 3D space along the direction in which it was originally obtained. The 3D resultant is the sum of all 2D back projected smearing operations [209]. For resolving 3D structures, the 2D pixel data of the measurement image is essentially copied and pasted on all the voxels (3D pixels) orthogonal to the detector plane. For resolving 2D figures, the measurement graph data is pasted on all the pixels along a line orthogonal to the sensor. A graphical 2D example of the latter, created from three 45 degrees offset views, is shown in figure 4.26a. The first step in processing the data from these figures involves the use of a Gaussian filter. Through this filter, the individual peaks per bin are smoothed out without resorting to a lower resolution. An energy threshold is applied to these data-sets, below which the value of a bin will be set to NaN. The resulting figures are similar to figure 4.14. The next step creates a 100 by 100 by 100 matrix, where each of the individual entries consists

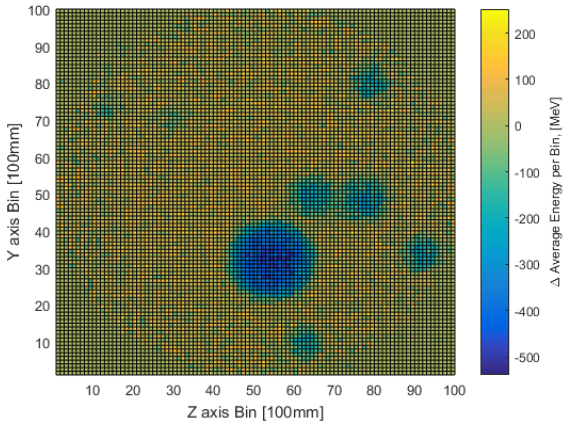

(a) 10 monolithic inclusions, $Z-Y$ plane.

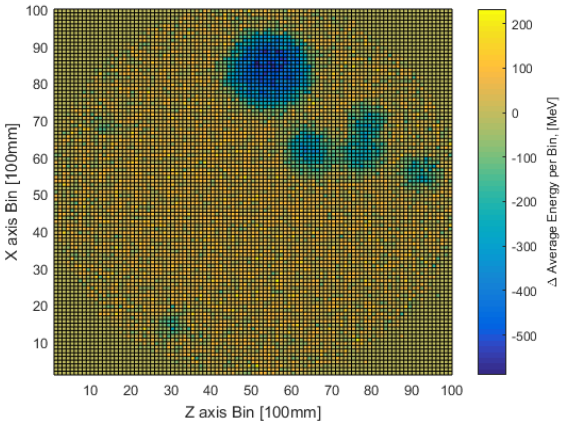

(b) 10 monolithic inclusions, $Z-X$ plane.

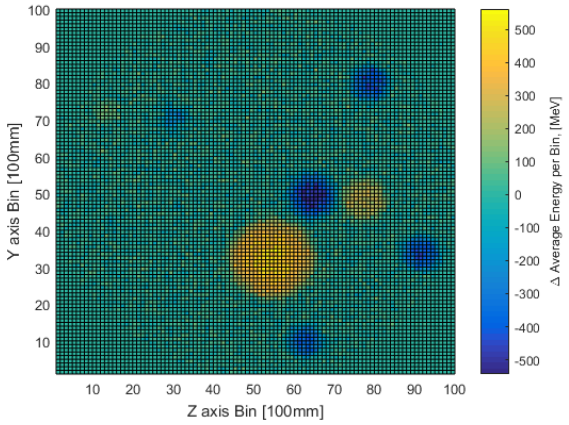

(c) 7 monolithic and 3 void inclusions, $Z-Y$ plane.

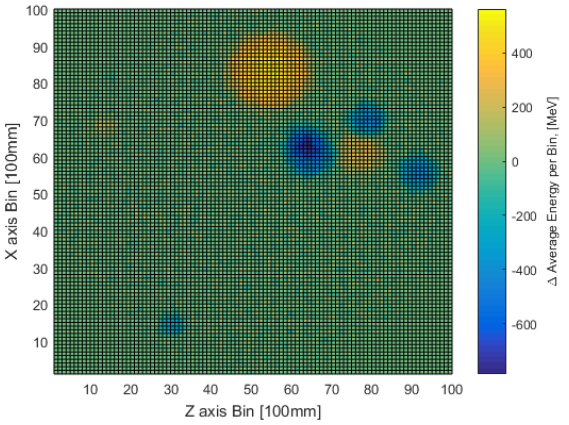

(d) 7 monolithic and 3 void inclusions, $Z-X$ plane.

Figure 4.25: Average kinetic energy difference per muon per bin, heterogeneous asteroid (figure 4.11) compared to homogeneous asteroid (figure 4.12).

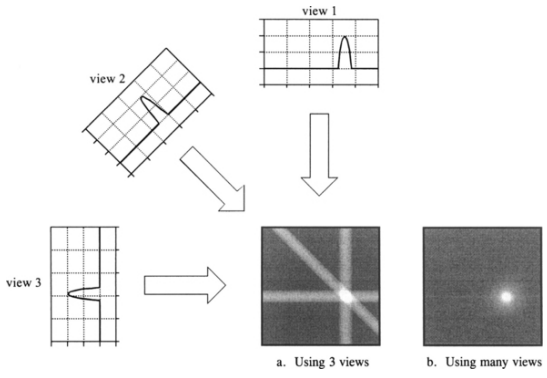

(a) Back Projection

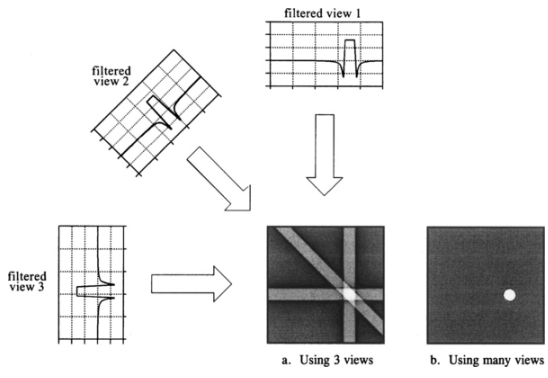

(b) Filtered Back Projection

Figure 4.26: Tomographic reconstruction of a circle using 3 views. From "Digital Signal Processing: A Practical Guide for Engineers and Scientists", by S.W. Smith, 2013 [209]. Adapted with permission.

of 3 values: the energy difference measured along the $x-axis$, $y-axis$ and $z-axis$. Each of these entries can be seen as a voxel with location (X,Y,Z) in 3D space, containing the data from three views. For each of the voxels, the sum of all three the values is calculated. When one or more of the three values was set to NaN, the entire entry will be deleted. This prevents ghosting of inclusions: when a spot in 3D space aligns in one or two axis, with one or two different inclusions, it will result in that spot getting modelled as an inclusion as well. The 2D version of this ghosting is clearly visible in figure 4.26a.a, where it materialises as the three white bands across the image. This problem still persists in the following graphs, as a few spots align with 3 different inclusions along 3 different axis. This ghosting is easily mitigated once more views are available, as shown in figure 4.26a.b, for instance by means of the data received from an orbiting spacecraft. The resulting 3D reconstruction of the monolithic inclusions is shown in figure 4.27.

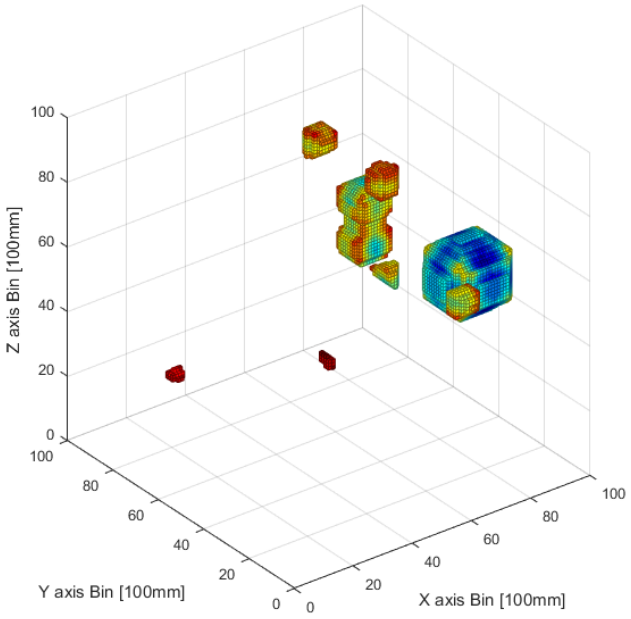

Figure 4.27: Reconstruction of monolithic inclusions contained within the ten inclusions simplified asteroid model.

The triangular shape, to the left of the largest inclusion in figure 4.27, is one of the aforementioned ghosted shapes. It is in line with 3 different inclusions, along three different axis. The three orthogonal views of the reconstruction are compared with the size and location of the inclusions in the model, in appendix B. This process can be applied as well to find void inclusions. The resulting reconstruction result is shown in figure 4.28. The red and yellow shapes are denoted as voids, whereas the turquoise and blue shapes indicate higher density regions.

4.4.2. Filtered Back Projection

All the spherical inclusions and voids depicted seem to be reconstructed slightly cubic. This is a manifestation of the BP algorithm's mathematically incorrect reconstruction. Every single point in the original 3D space will be reconstructed as a "blurry" sphere where the intensity scales with the inverse of the radius, graphically shown in figure 4.26a.b. To mitigate this problem, a filter can be applied to the measurement data. The algorithm using such filtered data is called "Filtered Back Projection" (FBP), and is one of the most used reconstruction algorithms for tomography. The resulting 3D image will be a mathematically exact representation of the original when infinite views are used [209], graphically shown in figure 4.26b.
As a Gaussian filter is applied to the muon measurements, as well as an exclusion algorithm for NaN values, the used method in this section can be seen as an intermediate process between BP and FBP.

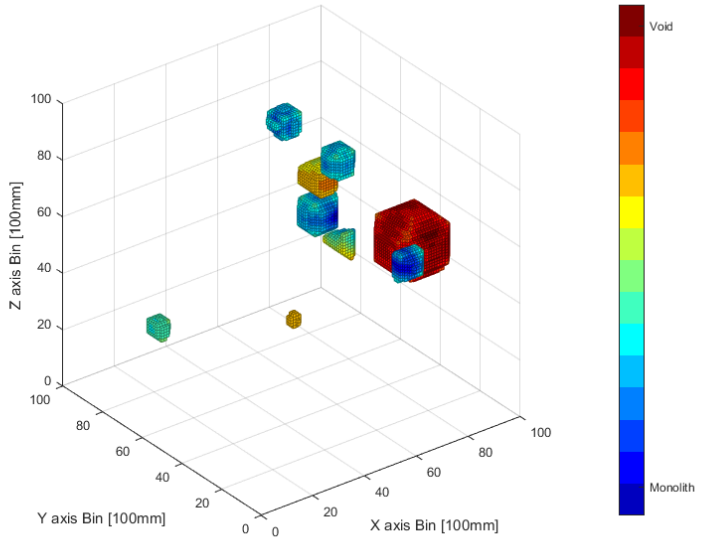

Figure 4.28: Reconstruction of monolithic and void inclusions contained within the seven inclusions, three voids simplified asteroid model.

4.4.3. Iterative Reconstruction

Another method of reconstructing the 3D interior is performed with iterations. Instead of solving the inverse problem of recreating the cause from the effects, "Iterative Reconstruction" (IR) essentially guesses the cause and compares the resulting simulated effects with the measurements [209]. This process is iterated, where every iteration aims to modify the cause to fit the resultant measurements better. Multiple variations of IR exist, but all adhere to this general description and all tend to be much more computationally intensive than BP and FBP.

Density Determination

IR can be applied to the simulations of this chapter, where the cause is the 3D interior structure and the effects the muon measurements. The iterations can then adjust parameters in such a way that the reconstructed voxels fit the 3D simplified asteroid model.

The straight track fitting method described in section 4.3.3 can be extended by including the formation location probability. As shown in figure 4.2, most muons are formed within the first $10-30m$ below the surface. For larger asteroid diameters than surveyed in this research, this would limit the possible formation locations of the muon. Combined with the muon kinetic energy measured at the hodoscope and its velocity vector, the muon's probable path can be traced back to a section of this formation layer. An exaggerated visual representation of this probable path is shown in figure 4.29. As higher energy muons undergo less scattering, their probable path is more condensed as compared to lower energy muons. Integrating all the measured muons' probable paths and their corresponding energies will yield a 3 dimensional model of average energy probability clouds, which is essentially a 3D version of figure 4.20. Sections of the asteroid where more muons passed through and retained more of their kinetic energy as compared to homogeneous asteroid simulation result, will prove to be lower density inclusions or voids.

Composition Determination

Not only density differences effect the path of the detected muon, but material and composition differences, to varying degrees, as well. As discussed in section 4.3.1, the amount of muon scattering depends on material radiation length L_0 (equation 4.8), which in turn depends on both material density and material type (equation 4.10). The higher the atomic number Z of the atoms comprising the material, the more scattering is expected.

Using straight track fitting, areas within the asteroid can be found from which a lot of muon tracks seem to diverge, which indicates that the material strongly scatters muons. When this amount of scattering is higher than what would be expected from the density in that region, found with energy absorption tomography, one

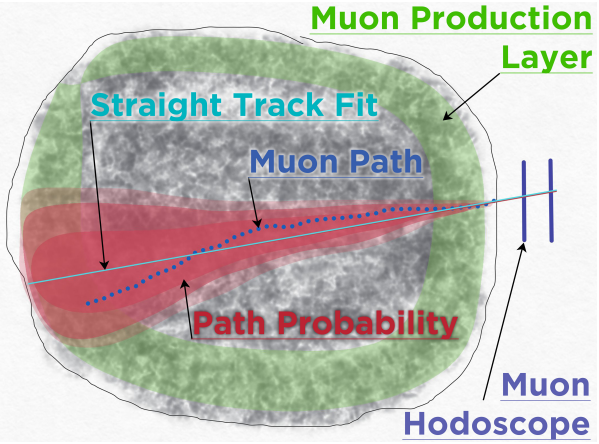

Figure 4.29: Schematic drawing of muon travel path probability through an asteroid. Not to scale.

can draw the conclusion that the material comprising said region will have on average a higher atomic number Z than the reference material used in the model. In short, applying IR to scattering tomography data, paired with absorption tomography data, can not only deliver information on asteroid interior structure and density distribution, but on material composition as well.

Iteration

All these findings can be applied to the control asteroid model used in simulations, essentially fitting a density and composition model to the results. This new asteroid model must be used to remake and narrow down the 3D average energy path probability model. Graphically, this would look like the red area in figure 4.29 shrinking, converging towards the actual muon path shown in dark blue. This new model must also undergo new simulation rounds, to provide results to compare to the in-situ measurements. This iterative process can be repeated until simulation results of the adjusted model correspond to the measurement results, which is therefore a method fitting the IR denominator.

4.4.4. Neural Networks & Machine Learning

Artificial intelligence, the overarching term used for intelligence displayed by machines, is applied more and more in the field of space exploration. These machines are often designed to mimic perks of biology, such as neural cognitive functions and evolution. Per example, NASA used an evolutionary algorithm to automate antenna design for multiple missions [113].
The steps described in the previous algorithms in this chapter are quite complex but require little parameters to work. These parameters require human input or problem-solving strategies to be modified so that the algorithm yields the best result. Examples of such parameters are the choice of threshold energy and method of filtering.

Neural Network

Artificial neural networks can be used to replace the need for human pragmatism in such strategies, as optimal parameters can be found using trial and error and other methodologies by non-biological machines [209]. Neural networks similarly remove the need for an algorithm choice, as again the optimum should be found by the network itself.
Such a neural network will require relatively basic algorithms, so basic that one might not even consider calling it an algorithm. Most of the processes in such a network involve linear or non-linear equations applied to data inputs. A basic neural network starts with an input layer, consisting of nodes where the input data is read. These values are then forwarded to the hidden layer, where weights (w) or parameters on nodes are applied mathematically to the input values. The final step moves these adjusted values to the output nodes in the output layer, once again applying weights. The theoretical "lines" connecting the nodes depict the flow of information, and represent the neural network, reminiscent of the neuron structure within the brain. A schematic example of a basic neural network is shown in figure 4.30.

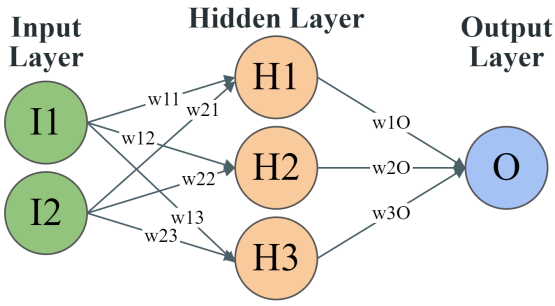

Figure 4.30: Schematic drawing of basic neural network.

This examples shows only six nodes, whereas in reality the amount of nodes used is many orders of magnitude larger. With more complex networks, information might travel backwards in the hidden layer, and more layers can be used. Once more than one hidden layer is employed in the network, the machine learning process described hereafter is called "Deep Learning", as more layers will more closely resemble biological neural networks.

Supervised Machine Learning

The weights of the artificial neural network are adjusted at each iteration by the machine itself, using its learning algorithm. This type of machine learning tries to mimic the current understanding of how biological neurons work, hence the name. The neural network can be "trained" on known data, by using simulation results and measurement data of known subjects as the inputs. The learning algorithm essentially conditions the neural network by "rewarding" weight changes that lead to results more closely resembling the real-life 3D interior structure of those known subjects or simulation models. In essence, during the machine learning process the weights of the neural network will get optimised such that the output statistically resembles the corresponding example data-sets the closest [209]. This is called supervised learning, as the algorithm constantly compares the output with known data, essentially supervising its learning progress. Once such a network manages to reconstruct the interior structure of a wide range of asteroid sizes, materials and density distributions, it can be employed on actual measurement data where the interior structure is yet unknown.

Unsupervised Machine Learning

Unsupervised machine learning uses unlabelled input data for the neural network, and does not compare the output to known data. It merely asks the neural network to categorise and group the data. As the neural network is not trained to sort the data by any externally imposed criterion, it will try and identify clusters and structures in the input data on its own. The labelling of the output clusters can take place in post-processing. The main advantages of unsupervised learning are the lack of a need for training data, and the absence of training data imposed bias, which could lead to new scientific discoveries on the internal structures. Little to no training data will be available for a future muon tomography mission, making unsupervised machine learning a prime candidate for interior reconstruction from tomography data.

Neural networks are proven to yield better reconstruction results, depending on the size and type of the network. The learning process does take time, but once the network weights are established, the neural network outperforms IR processes in quality [209], and in computational intensity for tomographic reconstruction [119].

It should be mentioned that the use of neural networks and machine learning carries one huge caveat: once such a network is trained and performs to requirements, it might not be possible or feasible to infer the inner workings from reading the values for the weights, the code or even from the way it performs. The lack of such an analytical equivalent to the neural network's process might create the situation where it is practically impossible to thoroughly validate the resulting reconstructions. Especially in the situation where the amount of example material for the network to train on is very small, it is hard to even heuristically validate the neural network. Unsupervised machine learning shows similar problems, as one can not know for certain the resulting clusters and anomalies found by the algorithm actually match up to real-world interior properties.

Another caveat is the fact that neural networks tend to end up in local optimums, whilst the aim is to find

the global optimum. Specific measures exist to mitigate this, such as stochastic gradient descent, but with a lack of sample material to compare to, a local optimum is where most types of neural networks are bound to arrive.

5

Top Level Requirements

As touched upon several times in the first few chapters of this report, this document does not envelop a complete and definitive synthesis of design for an asteroid tomography mission. Rather, the aim is to showcase the high-level feasibility of such a mission through the use of systems engineering tools and methods, by formulating basic preliminary requirements and performing case feasibility studies. The focal point of this chapter will logically lie on the tomographic muon-detecting instrument, as it plays a pivotal role in the feasibility study. A need and mission statement for asteroid muon tomography were defined as follows:

> Knowledge on asteroid internal structure and composition is invaluable to the fields of planetary science, planetary defence and in-situ resource utilisation. The space science community needs to characterise these interior properties to enable future exploration, mining and planetary defence applications.
> Muon tomography will provide a method to measure the particle flux through asteroids induced by galactic cosmic rays, allowing for the characterisation of their interior.

This chapter initiates with a description of the method employed to guide the requirement discovery process, as well as alternative considerations. The seconds section provides a comprehensive overview of assumptions made during the project, which both limits the scope of the research performed and puts preliminary constraints on the design. This is followed by the presentation of the top level requirements, which were formed based on spaceflight heritage, literature research and simulation results. The chapter concludes with multiple levels of design feasibility studies, partially in the form of case studies, applying the simulation results and demonstrating the feasibility of the muon tomography concept.

5.1. Method

As the presented content in this chapter forms a part of what is conventionally included in a design synthesis, an effort was made to adhere to System Engineering standards. This sections provides a description of the chosen design method, and briefly treats an alternative consideration.

5.1.1. Systems Engineering

The choice was made to use Systems Engineering (SE) practises as top-level guidance for this chapter, such as the ones described in the "NASA Systems Engineering Handbook"[108]. Various chapters from both "Space Mission Engineering: The New SMAD" [233] and "Spacecraft Systems Engineering" [80] are used for reference. The oft-mentioned concept study report by T.H. Prettyman et al. [186] was submitted as part of a 2013 NASA Institute for Advanced Concepts (NIAC) phase I project. This report mirrors its breadth and depth, and is therefore used as a guide in picking the project life-cycle phase. The three different phases of NIAC studies all couple the best into NASA's "Pre-Phase A" of a program's life-cycle [108], where the focus lies on performing concept studies for a specific goal. As this thesis aims to build upon the previous work, and its focus mainly lies in the tomographic muon-detecting instrument, a next step is performed by including some SE normally destined for Phase A of a program. The SE product maturity from NASA Procedural Requirements (NPR) 7123.1 [108] states which SE products should be created or updated in which phase, and will therefore guide the SE performed in this thesis project.

5.1.2. Model Based Systems Engineering

The experience gained during a 4 month internship at IMPACT, working with researchers of LASP on the IDEX instrument to be flown on the IMAP mission, sparked the initial consideration of the use of Model Based Systems Engineering (MBSE) for this thesis project. The SUDA (Surface Dust Analyser) instrument for the Europa Clipper mission was being developed concurrently at the same facility. As this mission is one of the first adopting MBSE for space exploration [19], it allowed for a peak into the perks and pains one encounters when applying MBSE.
MBSE revolves around the use of a system model, hence the name, to synthesise a final design. The model accepts new inputs and requirements, keeps everything updated and connected, provides the documentation and updates the design accordingly. With MBSE, ideally the model should directly govern the final design. The main advantages of using MBSE boil down to reducing complexity, providing traceability of data and requirements and greatly increasing the speed at which design updates and iterations can be applied. The downside however is that it requires more upfront engineering cost as compared to conventional Systems Engineering (SE), as well as experience in MBSE tools such as the open source Systems Modelling Language *SysML* [214]. As not much iterative design is to be expected in such a preliminary phase, and the complexity of the SE is restricted mostly to a single instrument, the advantages of using MBSE were deemed to not outweigh the extra upfront cost.

5.2. Assumptions and Constraints

This section presents the assumptions and constraints that helped shape research for the thesis project, and will aid in the formation of requirements and constraints. Taking a leaf from the book of formal requirement generation, as so often taught in SE courses, these assumptions are ordered, named and tabulated categorically. This will aid in traceability and allow for ease of reference later on. The source for each assumption, whether external or internal, will be included as well.
Some of the assumptions will revolve around using preliminary estimates based on comparable data, such as from previous missions, spacecraft or current commercial off the shelf (COTS) solutions. Shaping initial requirements based of spaceflight heritage and currently available parts is often performed in such preliminary stages of design [233].
It must be noted that all the following assumptions will state the absolute maximum values, unless mentioned otherwise. The decision for this approach was taken due to the nature of the feasibility study. In case the required instrument or mission parameters far exceed the maximums posed in the assumptions, one can conclude such a mission might ultimately not be feasible. When averages are stated for the assumptions, no such conclusion can be drawn other than that the mission requirements show a deviation from the heritage mean.

5.2.1. Simulation

Apart from the assumptions and simplifications stated in section 4.1, a few general assumptions for the simulation setup are stated in the following list.

Table 5.1: Simulation Assumptions and Constraints.

ID	Sub-Categories	Assumption	Rationale	Source
SIM.0.0.0	Muon Decay	The muons with $E_{kin} > 1GeV$ exiting the asteroid surface will not decay en route to the instrument at orbit altitude.	Average range of $1GeV$ muons is approximately $6km$. Maximum expected travel distance is less than $2km$.	MIS.0.0.2 MIS.1.0.0 Fig. 3.30
SIM.1.0.0	*Geant4* Validate	*Geant4* validation efforts in medium to high energy ranges implies validation for edge cases.	*Geant4* is currently in use for test and validation purposes at various high-profile particle experiments.	[3]

Continued on next page

Table 5.1 – *Continued from previous page*

ID	Sub-Categories		Assumption	Rationale	Source
SIM.1.0.1	*Geant4*	Validate	The use of a pure proton GCR spectrum, to provide a basis for validation with literature, should not negatively effect resulting total muon count.	The total GCR flux consists of ~ 90% protons. Including the ~ 10% Helium ions increased the muon count 35%. The other ions in the GCR flux should also only increase muon count.	Fig. 2.13 Table 4.5 [187]
SIM.1.0.2	*Geant4*	Validate	The simulation results can be linearly extrapolated with real-world run time.	Due to a constant input flux, particle detection count increases proportionally with run time for sufficiently large sample sets.	[125] [187]

To allow for extrapolation of the muon flux at an asteroid's surface to the spacecraft altitude, it is assumed (SIM.0.0.0) that no muons will decay within this leg of their journey to the detector. The muon flux at altitude then scales with the radius to the SSSB core squared.

Geant4 is a very capable tool to accurately simulate particle and quantum physics. Simulating the passage of particles through matter however is a very complex problem to solve. Ongoing validation studies aim to provide larger validated ranges of energies within the software program, but for this project, the entire range of interest is deemed (SIM.1.0.0) validated.

As a simulation focusing on the alpha particle spectrum of GCRs showed an increase in muon flux, the logical conclusion (SIM.1.0.1) is drawn that a pure proton source will result in a lower flux compared to a real-world simulation.

A crucial assumption (SIM.1.0.2) for this project states that the simulation results of very short real-world run-times are representative of longer duration runs. As computational limitations restricted the run-times, this assumption is critical to allow for comparison with other literature.

5.2.2. Physics

Table 5.2: Physics Assumptions and Constraints.

ID	Sub-Categories		Assumption	Rationale	Source
PHY.0.0.0	GCR	Surface	The effect of the surface structure and composition on muon production shall be characterised or not significant.	A surface porosity of 50% caused a muon increase of 12.5% compared to homogeneous material in a single study.	[125]
PHY.0.1.0	GCR	Energy	GCRs with $E_{kin} < 1GeV$ are assumed to not produce muons with $E_{kin} > 1GeV$.	Protons with $E_{kin} = 10GeV$ produced no muons with $E_{kin} > 1GeV$ in simulations.	[125]
PHY.1.0.0	Muon	Energy	All back-scattered muons have a kinetic energy lower than $E_{kin} < 1GeV$.	Prettyman et al. and J. Keerl state a significant upper limit of $1GeV$ for back-scattered muons in simulations.	[125] [187]

Variations in surface topography are thought to influence the muon production. The assumption (PHY.0.0.0) is made that this effect is either characterised and the surface topography is known, or that the effect will not significantly alter results. If the topography does influence the production locally, resulting in a higher muon production in one region compared to another, this effect must be taken into account.

The total energy of a proton with $1GeV$ kinetic energy is much higher than a muon with similar kinetic energy, because a muon is approximately 9 times less massive. Based on the law of conservation of energy, it should be possible for a muon to end up with more kinetic energy than the proton it was created from. However, this is practically never a one-to-one process, as multiple particles are created and momentum is transferred to other particles. The assumption (PHY.0.1.0) is therefore made that sub $1GeV$ protons do not produce muons with kinetic energies above $1GeV$. Because muons below $1GeV$ are omitted from results to remove the signal from backscattered muons, which are deemed to always be below this energy threshold (PHY.1.0.0), $1GeV$ is the lower threshold for the proton particle source as well.

5.2.3. Mission

Although the focal point of this thesis project does not lie on mission design, a minimum of constraints is researched and assumptions are made to aid in the design of the hodoscopic instrument, and better tailor the research to potential future missions.

Table 5.3: Mission Assumptions and Constraints.

ID	Sub-Categories		Assumption	Rationale	Source
MIS.0.0.0	Flight	Orbit	The mission shall contain an in-orbit phase at the target.	Long muon tomography integration times discard fly-by's as an option.	[187]
MIS.0.0.1	Flight	Orbit	The duration of the in-orbit science mission should be at least 1.5 years.	The previous 6 minor planet missions show a median in-orbit time of 1.5 years.	Table 5.4
MIS.0.0.2	Flight	Orbit	The lowest orbit altitude should be not more than 680m.	The lowest achieved orbit altitude around a minor planet was $\sim 680m$.	Table 5.4
MIS.0.0.3	Flight	Orbit	The duration of the lowest orbit phase shall be no less then 95 days.	The scheduled + overrun time for OSIRIS-REx lowest Orbit-B was 95 days.	[139]
MIS.0.1.0	Flight	Attitude	The muon tomography instrument shall point nadir during the lowest orbit phase.	Muon tomography instruments require nadir pointing.	[187] [109]
MIS.1.0.0	Target	Diameter	The target diameter shall be no more than $1km$.	The upper limit of muon tomography feasibility.	[186]
MIS.1.1.0	Target	Shape	The target shape model shall be known.	Previous minor planet orbit missions always retrieved shape models of their target.	[85] [70]
MIS.1.2.0	Target	Density	The target average density shall be known.	Previous minor planet orbit missions always lead to mass and volume calculations.	[83] [232]

Continued on next page

Table 5.3 – *Continued from previous page*

ID	Sub-Categories		Assumption	Rationale	Source
MIS.1.3.0	Target	Surface	The target surface structure and composition shall be known.	Previous minor planet orbit missions often used imaging, spectroscopy or even sample return.	[83] [232] [139]
MIS.1.4.0	Target	Status	The target is currently unexplored by an orbiting spacecraft.	Previous minor planet orbit missions targets were never re-explored by an orbiting spacecraft.	[234] [76] [210]
MIS.1.5.0	Target	Orbit	The target's perihelion will be approximately $0.9AU$, and its aphelion $1.3 \sim 1.7AU$.	NEA's are of particular interest due to low delta-V cost and potential hazard. Previous mission NEA targets were within this range.	Table 5.4 [79]

Assumption MIS.0.0.0 heads the list with a constraint on mission type. As shown by Prettyman et al. [187], measurement integration times of more than a day, close to the target asteroid's surface, are to be expected for a muon tomography mission. Fly-by missions usually provide much shorter close-to-asteroid integration times, as slow fly-by's are nonsensical from a scientific standpoint. Fly-by missions are therefore discarded as an option. Assumptions MIS.0.0.1-3 all involve the same close-to-asteroid integration time requirement, but state their assumption based on past minor planet mission data, tabulated in table 5.4.

Mission	Target & Avg. Diameter	Orbit Duration	Min. Orbit Altitude	Launch
NEAR Shoemaker	433 Eros $\sim 16.84km$	$\sim 1year$	$\sim 18km$ (Landed)	1996
Hayabusa	25143 Itokawa $\sim 330m$	$\sim 1.5year$	$\sim 3km$[83] (Touch&Go)	2003
Rosetta	67P/C-G $\sim 4.2km$	$\sim 2.1year$	$\sim 10km$	2004
Dawn	4 Vesta $\sim 525.4km$	$\sim 1.2year$	210km	2007
	1 Ceres 946km	$\sim 3.5year$	$375km$	
Hayabusa2	162173 Ryugu $\sim 870m$	$\sim 1.5year$	$\sim 20km$ (Touch&Go)	2014
OSIRIS-REx	101955 Bennu $\sim 525m$	$\sim 2.3year$	$\sim 680m$ (Touch&Go)	2016

Table 5.4: List of missions that orbited small Solar System bodies.[234]

As the instrument is most likely required to point nadir, towards the SSSB, the assumption (MIS.0.1.0) is made that is does so during the science phase of the mission.

The assumptions MIS.1.X.X all revolve around the knowledge on the target. A few of these (MIS.1.0.0 & MIS.1.5.0) need to be known before the target is selected. Larger than $1km$ diameter SSSBs will require measurement integration times much longer than average mission science phase duration[186]. The orbit of the target should logically be known before launch. The selection of targets is restricted to NEAs for their low delta-V requirements, high solar energy and scientific interest.

The remaining assumptions (MIS.1.1.0 & MIS.1.2.0 & MIS.1.3.0) essentially show the auxiliary information needed for interior reconstruction, which must be provided by other on-board instruments (MIS.1.4.0). As both shape and density were resolved for all past minor planet mission targets, the assumption of availability of this data is made.

5.2.4. Spacecraft

Preliminary assumptions and constraints on spacecraft design possibilities will help constrain the design of the muon tomography instrument. These assumptions will mostly effect the available mass and power budgets for the instrument. Similar to the subsection on mission assumptions, this subsection relies heavily on the use of previous missions as example and comparison material.

Table 5.5: Spacecraft Assumptions and Constraints. Superscript "2" denotes assumptions concerning a secondary spacecraft.

ID	Sub-Categories		Assumption	Rationale	Source
SPC.0.0.0	Mass	Dry	The dry mass of the main spacecraft should be 400 ~ 1200kg, average 693kg.	All previous SSSB orbiting spacecraft were within this dry mass range.	Table 5.6
SPC.0.1.0	Mass	Payload	The payload mass of the main spacecraft should be 5% ~ 24%, average 15%, of the dry mass.	All previous SSSB orbiting spacecraft and selected interplanetary spacecraft, were within this payload mass range.	Table 5.6 [233]
SPC.0.1.1	Mass	Payload	The mass of the auxiliary instrument suite needed for the muon tomography instrument should be no more than approximately 52kg, and could be ~ 39.2kg.	Based on the instruments of OSIRIS-REx that delivered on assumption MIS.1.1.0, MIS.1.2.0 and MIS.1.3.0.	MIS.1.4.0 [56] [210] [47] [190] [151]
SPC.1.0.0	Mass[2]	Dry	The mass of a secondary spacecraft should be lower than 100kg.	All secondaries to SSSB orbiting spacecraft, often landers or rovers, were approximately either ~ 100kg,~ 10kg or 1 ~ 2kg.	Table 5.6
SPC.1.1.0	Mass[2]	Payload	The mass of the payload of a secondary spacecraft should be approximately 27% of its dry mass.	The payload mass of all secondaries to SSSB orbiting spacecraft was approximately ~ 27%.	Table 5.6
SPC.2.0.0	Power	Solar	The minimum total available solar power during the science mission should be 0.4 ~ 1.2kW for conventional and 0.9 ~ 1.4kW for electric propulsion. Average 1kW.	Values from the past missions to SSSBs, solar power at 1AU extrapolated to 1.7AU for Hayabusa.	Table 5.6
SPC.2.1.0	Power	Payload	The available power for the payload in the main spacecraft should be 5 ~ 20%, average 15%, of the total solar power.	All previous SSSB orbiting spacecraft and selected interplanetary spacecraft, were within this power percentage range	Table 5.6 [233]

Continued on next page

Table 5.5 – *Continued from previous page*

ID	Sub-Categories		Assumption	Rationale	Source
SPC.2.1.1	Power	Payload	The maximum nominal power usage of the auxiliary instrument suite needed for the muon tomography instrument should be no more than approximately $91W$, and could be $67.8W$.	Based on the instruments of OSIRIS-REx that delivered on assumption MIS.1.1.0, MIS.1.2.0 and MIS.1.3.0.	[56] [210] [47] [190] [151]
SPC.3.0.0	Power[2]	Solar	The available solar power for secondary landers at $1.7AU$ should be approximately 19 ~ 100, average ~ $31W$, per m^2 zenith facing area.	Extrapolated from all SSSB lander spacecraft solar power statistics, to assumed target aphelion $1.7AU$ and m^{-2}.	Table 5.6 MIS.1.5.0
SPC.4.0.0	Payload	Location	The auxiliary instrument suite needed for the muon tomography instrument will be located on the primary spacecraft.	Most instruments of the auxiliary suite require observations from orbit altitude, or a direct communication link with Earth, which is best fulfilled by the primary spacecraft.	[56] [210] [47] [190] [151]

The mass of the spacecraft (SPC.0.0.0) is determined from all previous orbiting SSSB missions. The choice is made not to include fly-by missions for the mass estimation, as these would have quite different requirements in terms of propulsion and instrument suite. Similarly, to calculate the budget for the payload mass (SPC.0.1.0), only spacecraft with a lower mass than Rosetta's $1200kg$ were considered. The payload budgets were taken from the interplanetary mission mass budget list in SMAD [233], excluding missions such as Cassini-Huygens.

In a similar manner, the mass (SPC.1.0.0) and payload mass (SPC.1.1.0) for a secondary spacecraft are determined. The values are all based off secondary spacecraft in previous SSSB missions, as shown in table 5.6, in italics.

Assumptions SPC.0.1.1 and SPC.2.1.1 are based on the fact that the most recent asteroid mission, OSIRIS-REx, provided the shape model (MIS.1.1.0), average density (MIS.1.2.0), surface structure and composition (MIS.1.3.0) of its target Bennu.
The 3D shape model, and the resulting surface structure and volume, were found using the OLA laser altimeter instrument, with a mass of $21.4kg$ and nominal power usage of $59W$ [56]. The spacecrafts high gain communications antenna paired with the Deep Space Network on Earth allowed for the application of radio science techniques, such as Doppler and Delta-Differential One-Way-Ranging, to resolve the spacecraft's dynamics around Bennu[210]. Paired with volume and shape model data, knowledge on the spacecraft's dynamics allowed for the calculation of the mass and density of Bennu. The surface composition was determined using a suite of 3 different spectrometers. OTES, focusing op thermal spectroscopy, weighed in at $6.27kg$ with a total average power consumption of $10.8W$ [47]. The main visible and infra-red spectroscope OVIRS has a mass of $17.8kg$ and uses $8.8W$ on average [190]. The X-Ray spectroscope REXIS has a total mass of $6.5kg$ and total power consumption of $12.4W$ [151]. Together, this lavish instrument suite has a mass of ~ $52kg$ and requires $91W$ if used simultaneously. As surface composition does not directly imply interior composition and the mineralogy of the surface is only needed as a starting point for interior reconstruction, a muon tomography mission could make do with only a single spectroscope. This would drastically lower the mass and power budgets for the auxiliary instrument suite, to $39.2kg$ and $67.8W$ respectively. Due to the size of these instruments, they are constraint to the primary spacecraft only (SPC.4.0.0).

The available solar power of each spacecraft (SPC.2.0.0) in table 5.6 is calculated at the aphelion position

of their science mission. The Rosetta mission for example ventured out to 5.25AU from the sun, but its science mission did not start until it returned to 3.4AU, which is why its minimum available solar power was determined at this point. It is worth noting that spacecraft with electric propulsion tend to carry larger solar panels, which could be a two birds with one stone situation for power hungry instruments. The payload power budget (SPC.2.1.0) as a function of total solar power is derived from previous missions in the same table, and in SMAD [233], again excluding missions with a mass higher than 1200kg.

The available power for a secondary spacecraft (SPC.3.0.0) is quite a tough one to deduce from previous missions. Most of these spacecraft were either rovers or landers, and therefore depended heavily on the day and night cycle at their landing location. Literature stating their specifications is often not clear on whether the power is stated as a maximum, or diurnal average. The large range stated in the assumption is extrapolated from all the values found in literature, and converted to a wattage per square meter. A future lander, called MASCOT-II, is expected to provide 80Wh per day Dimorphos day (~ 12h), at a Solar distance of 1.0 ~ 1.2AU. This can be increased to 127Wh when deployable Solar panels are included [136]. With a top surface area of 0.109m^2 [137], this lander would provide 21W/m^2 at a Solar distance of 1.7AU, which is very close to the denoted average. With the deployable panels, this would increase to 34W/m^2 zenith facing area.

Table 5.6: List of science spacecraft that orbited around or landed on small Solar System bodies [234][76][210]. Spacecraft in *italics* formed part of their parent mission above, * denotes the use of electric propulsion.

Spacecraft	Dry Mass	Size	Payload Mass & Power		Solar Power
NEAR Shoemaker	487kg	⊘1.7x2.8m	56kg	81W	1.8kW (1AU) 400W (2.2AU)
Hayabusa*	415kg	1.0x1.6x2.0m	-	-	2.6kW (1AU) 900w (1.7AU)
-*MINERVA*[237]	591g	⊘12x10cm			~ 1.9W (1AU)
Rosetta	1180kg	2.8x2.1x2.0m	165kg	-	12kW (1AU) 850w (3.4AU)
-*Philae*	100kg	1.0x1.0x0.8m	~27kg	15-20W	10~32W (3AU)
Dawn*	725kg	1.6x1.3x1.8m	~35kg	~60W	10.3kW (1AU) 1.3kW (3AU)
Hayabusa2*	493kg	1.6x1.0x1.2m	-	-	2.6kW (1AU) 1.4kW (1.4AU)
-*MASCOT*	11kg	30x28x20cm	3kg	N/A	N/A
-*MINERVA-II1A*	1.15kg	⊘18x7cm	-	-	2W(1.4AU)
-*MINERVA-II1B*	1.13kg	⊘18x7cm	-	-	2W(1.4AU)
-*MINERVA-II2*	~ 1kg	⊘15x16cm			~2W(1.4AU)
-*DCAM3*	~2kg	⊘6x6cm	-	-	N/A
OSIRIS-REx	860kg	2.4x2.4x3.2m	-	-	1.2kW~3kW

5.2.5. Muon Tomography Instrument

This final assumptions section discusses all the goals and target values for the muon tomography instrument. The requirement section 5.3 hereafter lists the absolute maximum values to which the instrument should adhere, whereas this section focuses on the general averages found thus far.

Table 5.7: Muon Tomography Instrument Assumptions and Constraints. Superscript "2" denotes assumptions specifically concerning instrument integration on a secondary spacecraft.

ID	Sub-Categories	Assumption	Rationale	Source
TOM.0.0.0	Resolution Time	The instrument should have a time resolution of ~ 120ps or better for particles with a single charge $Z = 1$.	Current techniques allow for sub ~ 60ps time resolutions. Instruments in space applications such as AMS-02 reached ~ 140ps.	[187][22]

Continued on next page

Table 5.7 – *Continued from previous page*

ID	Sub-Categories		Assumption	Rationale	Source
TOM.0.1.0	Resolution	FOV	The small Solar System body will fully occult the field of view (FOV) of the instrument.	The instrument will be partially shielded from unwanted radiation entering front-to-back.	MIS.0.0.2 MIS.1.0.0 [109]
TOM.0.1.1	Resolution	FOV	Most of the small Solar System body will be contained within the field of view (FOV) of the instrument.	The received muon flux is the largest when the entire SSSB is in view.	MIS.0.0.2 MIS.1.0.0
TOM.1.0.0	Power	Total	The instrument shall have sufficient power available at all times during the science phase, to operate.	Orbiting spacecraft around SSSBs are often almost continuously illuminated by the Sun. In a worst case scenario (lowest orbit, largest asteroid, Solar opposition), basic trigonometry shows that less than 14% of the orbit is in the asteroid's shadow.	MIS.0.0.2 MIS.1.0.0
TOM.1.0.1	Power	Total	The instrument should use less than $82.2W$ of power during the science phase, to operate.	This value is found from the remaining payload power budget after required auxiliary payload power usage subtraction, calculated with previous mission averages.	SPC.2.0.0 SPC.2.1.0 SPC.2.1.1
TOM.2.0.0	Power[2]	Total	When used on a secondary spacecraft, the instrument should use less than $31W$ per square meter zenith facing spacecraft area, during the science phase.	This value is found from the total secondary spacecraft payload power budget, calculated with previous missions, extrapolated to a science phase aphelion of $1.7AU$.	MIS.1.5.0 SPC.3.0.0 SPC.4.0.0
TOM.3.0.0	Mass	Total	The instrument should weigh less than $\sim 65kg$.	This value is found from the remaining payload mass budget after required auxiliary payload mass subtraction, calculated with previous mission averages.	SPC.0.0.0 SPC.0.1.0 SPC.0.1.1 SPC.4.0.0
TOM.4.0.0	Mass[2]	Total	The instrument should weigh less than $\sim 27kg$ when used on a secondary spacecraft.	This value is found from the total secondary spacecraft payload mass budget, calculated with previous missions.	SPC.1.0.0 SPC.1.1.0 SPC.4.0.0

The time resolution of the instrument is the discrete resolution with respect to time. Any measurements taken in shorter succession than this value, will be registered as a single event. For Time-Of-Flight instruments, the temporal resolution is a major performance factor. The assumed time resolution for the muon detector (TOM.0.0.0) is set at $120ps$, but could be cut in half depending on the type of configuration.

To make use of the in-situ available radiation shielding provided by the SSSB of interest, the aperture of the instrument must be fully occulted by it (TOM.0.1.0). This reduces the amount of shielding needed at the

instrument. Conversely, as much of the SSSB much be in view as possible (TOM.0.1.1) to receive most of the available muon flux leaving the surface.

The instrument should be designed to operate within the available power budget (TOM.1.0.1). Since the spacecraft is nearly continuously illuminated by the Sun, the instrument should always have sufficient power during the science phase (TOM.1.0.0). When used on a secondary spacecraft, the instrument's power budget is quite a bit lower (TOM.2.0.0), but can be scaled up when deployable panels are used [136].

The mass of the instrument (TOM.3.0.0&TOM.4.0.0) should be equal or lower than these assumptions, which are deemed very feasible and will not tremendously impact the design of the rest of the spacecraft. This prevents the mission from becoming a single-issue type, where the entire mission will revolve around one instrument.

5.3. Requirements

The establishment of requirements for a project is a crucial step, as it forms the basis for the agreement between developers and stakeholders on what the resulting product should do. Although this thesis project currently has no clear separation of developer and stakeholder, the generation of requirements will clarify and constrain the products design, and provide a basis for a verification and validation process. Additionally, requirements facilitate the transfer of such a project for future work, and provide a baseline on which improvements can be made to the design [108].
The NASA Systems Engineering Handbook states the metadata requirements should contain, similar to the tabulated assumptions of the previous section 5.2. Some of this metadata, such as requirement owner and verification lead, can be omitted as it is extraneous in a single author report.
To minimise the amount of **TBD** "To Be Determined" statements within the requirements, a first order estimate will always be presented together with a **TBR** "To Be Resolved" mark [108]. These estimates are based on literature and the assumptions in the previous section, and are naturally linked for traceability. They all show the absolute maximum values, as these are the most import values for a feasibility study. It is worth noting that a combination of all edge-cases into a single design might ultimately not end up to be feasible, and this should therefore be avoided.

Table 5.8: Muon Tomography Instrument Requirements. Superscript "2" denotes requirements specifically concerning instrument integration on a secondary spacecraft.

ID	Sub-Categories		Assumption	Rationale	Source
R.TOM.0.0.0	Mass	Total	The total instrument mass shall be less than **<TBR>** (248.8kg).	The preliminary instrument mass limit is determined from the most forgiving edge case: A spacecraft mass of 1200kg, 24% of which is payload, and subtracted with the minimum auxiliary payload mass.	SPC.0.0.0 SPC.0.1.0 SPC.0.1.1
R.TOM.1.0.0	Mass[2]	Total	The total instrument mass shall be less than **<TBR>** (27kg) when used on a secondary spacecraft.	The preliminary instrument mass limit is determined from the most forgiving edge case: A spacecraft mass of 100kg, 27% of which is payload.	SPC.1.0.0 SPC.1.1.0 SPC.4.0.0
R.TOM.2.0.0	Perf.	Prop.	The instrument shall be able to resolve the incident muon track arrival angles with an accuracy of **TBR** degrees.	The determination of muon arrival angle is required to perform straight track fitting.	[187]

Continued on next page

Table 5.8 – *Continued from previous page*

ID	Sub-Categories		Assumption	Rationale	Source
R.TOM.2.0.1	Perf.	Prop.	The instrument shall be able to resolve muon within the $1GeV$ ~**<TBR>** ($100TeV$) range.	Measurements on muon energy are required for absorption tomography. The lower limit of $1GeV$ eliminates backscattered muons, the upper limit is the maximum energy for hadronic processes in *Geant4*.	PHY.1.0.0 [29]
R.TOM.2.1.0	Perf.	Life.	The instrument shall be able to operate for at least then 3 months.	Basen on heritage and future mission designs, the science phase closest to the asteroids lasts approximately three months.	MIS.0.0.3 [136]

5.4. Design Feasibility Study

For this feasibility study, two fairly different mission design options for the instrument will be pursued. The choice for a clear separation for these options is based on mission heritage data. The first option is the minimal viable design needed for such an instrument to function on-board a spacecraft similar in parameters to previous missions. The second and possible more adventurous option, discussed in section 5.4.2, surveys the feasibility of utilising such an instrument on a micro- to picosatellite platform, with a total mass lower than $100kg$ [80].
This section starts off with an analysis on instrument integration time requirements for certain mission configurations. Statistical analysis methods are employed to determine the time needed for the instrument to detect interior features with a sufficient level confidence. The section concludes with an application of the acquired knowledge on integration time to a case study, demonstrating such a mission concept's capability.

5.4.1. Integration Time

It is apparent from literature and the simulation results, that the muon count received by the instrument plays a pivotal role in the feasibility of this muon tomography mission concept. The muon count depends on various factors, the most notable ones being:

- asteroid size;
- asteroid density;
- detector area;
- integration time;
- and orbit altitude.

To test the feasibility of two proposed mission concepts, the edge cases providing the highest muon count were taken for most of these aspects. Additionally, the amount of muons received during the mission dictates what level of contrast can be resolved between the imaged interior density variations.

Transmission Tomography

According to T.H. Prettyman et al. [186], the integration time needed to reach the 3σ Poisson detection limit for certain density inclusions depends directly on the mean muon counting rates. The following equation expresses the integration time in terms of mean count rates:

$$t_{Integration} > \frac{9 \cdot Rate_{ROI}}{(Rate_{ROI} - Rate_{Ref})^2} \text{ [186]} \tag{5.1}$$

In this equation, $Rate_{ROI}$ describes the muon count rate in the region of interest, and $Rate_{Ref}$ describes the count rate for the same region, but for the homogeneous "control" asteroid with uniform density. The

reference count rate depends on asteroid size, mass, composition, detector area and detector altitude. The count rate in the region of interest diverts from the reference value when higher or lower density inclusions are within the detectors line of sight. Equation 5.1 allows for the creation of a chart, from which the expected integration time can be read to reach the 3σ Poisson detection limit. The horizontal axis denotes the reference rate per day, the vertical axis shows the ratio between both rates. For clarity, integration times lower than $1hour$ or higher than $5years$ are shown as one single contour colour.

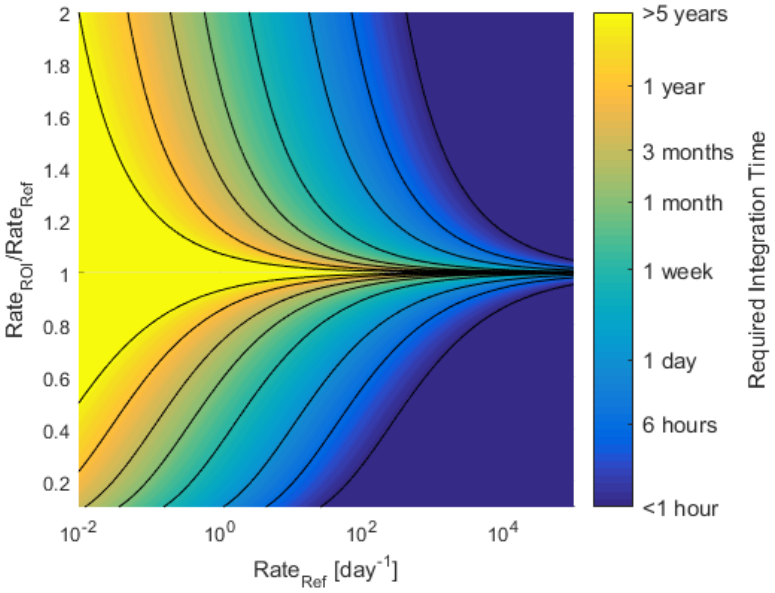

Figure 5.1: Contour plot describing the required integration time to reach the 3σ Poisson detection limit, depending on reference muon count rate, and count rate ratio. Created with equation 5.1[186]

Energy Absorption Tomography

The previous section discussed the integration time of the instrument when transmission tomography is the method of choice for the detection of inclusions. Equation 5.1 shows the minimum integration time needed to reach a 3σ Poisson detection limit. The Poisson distribution is especially suited for discrete count rates, whereas a normal distribution is better suited for continuous data. When reaching the detector, the muon energy spectrum would, over time, be better described by a continuous distribution. This subsection treats the relation between this measured energy spectrum and the confidence level is supplies.
The mono-energetic pure muon source simulation as discussed in section 4.3.2 will be the subject of the following demonstration. The 10-inclusions model (figure 4.4a) is subjected to 500,000 primary $5GeV$ muons along the $X-axis$, but unlike the results shown in figure 4.25a, bins of $1x1m^2$ were used. The histogram of all the muons and their energies that reached the bin representing the biggest inclusion, is plotted in figure 5.2 on the following page, for both the 10-inclusions model and the control model. A normal distribution is fitted to each of these two histograms, and the mean and $\pm3\sigma$ locations on the $X-axis$ are denoted.
It is immediately clear than the mean of the test simulation is lower in energy compared to the control. This is expected, as a high density inclusion was in the path of the muons in the test simulation. However, the confidence at which we can state the measured mean is actually the true mean still needs to be determined.
If the same 3σ detection limit is maintained, the only measurements counted as true positives, indicating a higher density inclusion, would be in the area denoted in green in figure 5.2. All the data in the test fit that is within the $\pm3\sigma$ of the control fit, will be a false negative. The graph area (=probability) of false negatives is called β, and for false positives it is called α [55]. When using the $\pm3\sigma$ detection limit, the value for α is very close to zero.

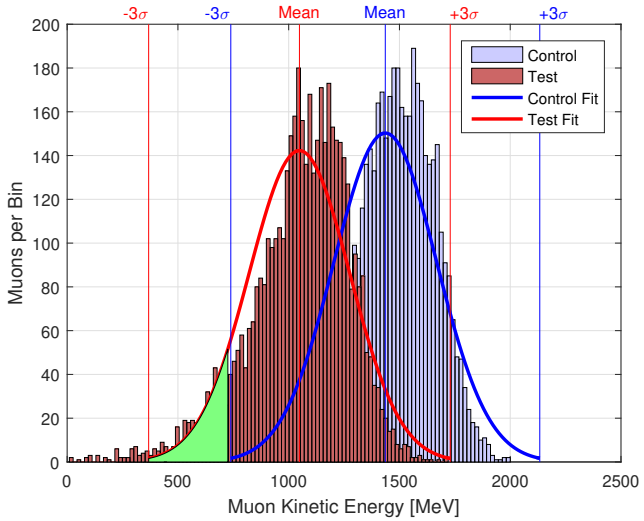

Figure 5.2: Histogram of muon kinetic energy distribution, as detected by a $1x1m^2$ detector section with its field of view through the largest inclusion. Data from 500,000 $5GeV$ muon simulation. Test data from 10 inclusions model, control data from homogeneous model. Normal distribution plot best-fit overlaid on both histograms.

As a rather large portion of the measurement results would be identified as false negative, a very long integration time would be needed to reach sufficient confidence levels. It is therefore possible to choose the limits for α and β beforehand, and try to choose the detection limit such that these are not exceeded. The value for α should be chosen carefully, as it directly describes the possibility that the results are wrongly positive. One method to set the detection limit using available data, is to choose the mean of the measurements as the limit. The probability of a false negative is then, assuming a normal distribution for the measurement, equal to $\beta = 50\%$. The resulting plot is shown in figure 5.3a. This is quite a large proportion of false negatives. The minimum of false negatives and positives combined is achieved when $\alpha = \beta$, shown in figure 5.3b. In the field of chemistry, both are advised to be set at $\alpha = \beta = 0.05$ [55].

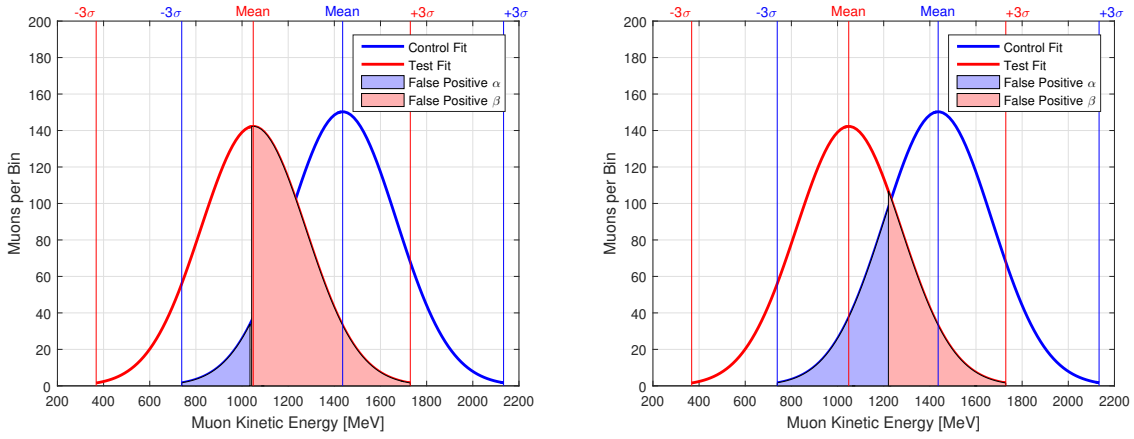

(a) Detection Limit equal to measurement mean.

(b) $\alpha = \beta$

Figure 5.3: The two normal distribution best-fit plots for the histograms in figure 5.2. *(Erratum: [False Positive β] should be [False Negative β].)*

In this example, the histograms seem to follow a normal distribution quite nicely. The variance for a normal distribution is equal to its standard deviation squared. As sample sets rarely exactly follow a normal distribution, the standard deviation σ and mean μ are estimated with the sample standard deviation s and the sample mean $\overline{X}$. To determine whether the means of these two normal distributions are actually significantly different from each other, they are subjected to the Student's t-test. In this demonstration case, the variance

of both distributions is quite similar, allowing the use of the following equations.

$$t = \frac{\overline{\mathrm{X}}_{ROI} - \overline{\mathrm{X}}_{Ref}}{s_p \cdot \sqrt{\frac{1}{n_{ROI}} + \frac{1}{n_{Ref}}}} \tag{5.2}$$

$$s_p = \sqrt{\frac{(n_{ROI}-1)s^2_{X_{ROI}} + (n_{Ref}-1)s^2_{X_{Ref}}}{n_{ROI}+n_{Ref}-2}} \tag{5.3}$$

The mean of each of the two sample sets are denoted with $\overline{\mathrm{X}}$, where the test set is shown with "Region of Interest" (ROI) and the control is shown as "Reference" (Ref). The number of samples is denoted with n and s^2 is the unbiased estimator of the variance.
The Student's t-test (equation 5.2) is applied to the two sample-sets shown in figure 5.2. The resulting values are $s_p = 230$ and $t = -83$. The total Degrees of Freedom, used to find the significance of the difference, is calculated with $DOF = n_{ROI} + n_{Ref} - 2 = 9650$. The value found for t is so large that the confidence level in stating that the two means are different, is practically 100%. Reversing this equation can yield the required sample size to reach a certain confidence level, versus the mean difference in muon energy. Per example, figure 5.4 shows the confidence level that the mean muon energy measured is in fact different from the mean muon energy simulated with the reference asteroid. The sample set and mean of the reference asteroid are set at $n_{Ref} = 4920$ and $\overline{\mathrm{X}}_{Ref} = 1.436 GeV$.

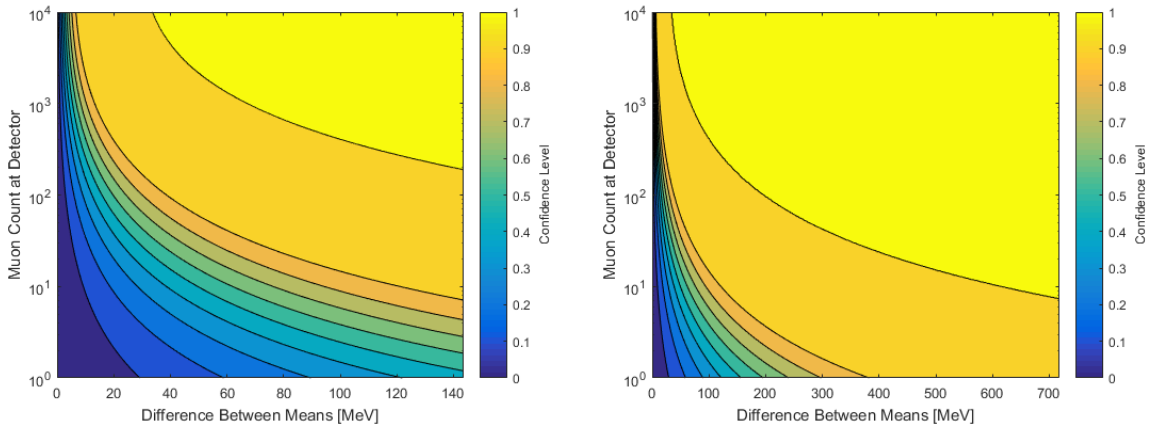

(a) $MAX|\overline{\mathrm{X}}_{ROI} - \overline{\mathrm{X}}_{Ref}| = 140[MeV]$ (b) $MAX|\overline{\mathrm{X}}_{ROI} - \overline{\mathrm{X}}_{Ref}| = 700[MeV]$

Figure 5.4: Muon count at the detector, versus difference in mean muon kinetic energy between the detector and simulation. Colour scale shows achieved confidence level. Example case with $10m$ diameter simplified asteroid as referece subject.

Although these graphs are created for demonstration purposes, they indicate the relation between confidence level on the one hand, versus muon count and energy difference on the other. For smaller asteroids, the differences in energy absorption are thought to vary a lot from region to region [186], as differences in structure and density are less likely to even-out over the shorter distances travelled. It is also shown that confidence level depends positively on total sample size. In other words, when simulations on Earth are used as the reference test, running longer and highly detailed simulations will increase the confidence level of deductions on the measurement results around the asteroid. A mere 10 muons detected with a mean energy difference of $200[MeV]$ as compared to the simulation with $n_{Ref} = 4920$, already yields a confidence level of 80% that the detected mean is indeed different from the simulation mean, as read from figure 5.4b.
The major disadvantage of this method is the limited amount of real-world run time one can simulate. Table 4.5 shows that 1 day of real world run time on a $10m$ diameter model, including both protons and alpha particles in the cosmic ray spectrum, would take approximately $2 years$ on a purpose build system. Running such a simulation for larger asteroids would require exponentially more computational resources. Super computer networks such as the previously mentioned *Nikhef* Data Processing Facility might be up to the task, be the extrapolation of computing time to such a network's performance is deemed out of scope for this project.

5.4.2. Case Study

Primary Spacecraft

During the lowest orbit phase around the SSSB, at $680m$ altitude (MIS.0.0.2), the instrument will have an integration time of 95 days (MIS.0.0.3). We can extrapolate the muon flux at the SSSB surface ($j_{\mu(@Surface)}$) to the flux at spacecraft altitude h with the following equation:

$$j_{\mu} = \frac{j_{\mu(@Surface)} R^2}{(h+R)^2} \tag{5.4}$$

In this equation, R denotes the radius of the SSSB, and j_{μ} denotes the flux at the spacecraft altitude. For example, with a SSSB radius of $R = 500m$ (MIS.1.0.0), the flux reaching the spacecraft is approximately 18% of the flux at the surface.
As secondary spacecraft often carry a much less varied set of instruments compared to their parent spacecraft, with less volume and mass required for aspects like propulsion and communications, the muon detection area for a secondary lander-type spacecraft is not assumed to be significantly smaller than for primary spacecraft. A lander with a similarly sized muon tomography instrument would receive a five times increase in muon flux compared to an orbiting spacecraft. A landing spacecraft is therefore the preferred design option, and therefore taken as the subject of the following case study.

Secondary Spacecraft

There are quite few arguments why the muon detector instrument would better serve its purpose on a secondary spacecraft. The biggest of these must be the removal of mutually imposed constraints between the main spacecraft and the muon detecting instrument. Even at the lowest assumed orbit altitude, the spacecraft only receives a small fraction of the muon flux that is available at the SSSB surface (equation 5.4). Similarly, the primary spacecraft is not likely to orbit at this lowest altitude for very long, as a maximum of 95 days is assumed (MIS.0.0.3). A secondary spacecraft could be allowed to orbit much closer to the asteroid, or even land on its surface. These landers would not necessarily be constraint to a single site, as "hopping" rovers, such as the MINERVA-II's and MASCOT, have already been put to use on an asteroid's surface. Additionally, the orbit of the lander or rover would not have to be determined in detail. This brilliant lack of complications removes the need for time-based determination of position and orientation, removing constraining requirements on the additional instrument suite.
Table 5.6 shows various secondary spacecraft that hitched a ride on larger spaceprobes to their ultimate destination. Unfortunately, not all of these are feasible for muon tomography missions. A first constraint is imposed by assumption TOM.0.0.0, which states the instrument should have a time resolution of at least $120ps$, and possible $60ps$. At close to the speed of light, a particle travels $3.6cm$ in $120ps$. This is more than 1/3 the size of the picosats included in the list. As this would severely limit the actual time of flight resolution the instrument can achieve, TOM.0.0.0 renders picosats such as the MINERVA's and DCAM3 on Hayabusa and Hayabusa2 infeasible.
This leaves microsat and nanosat platforms, such as Philae and MASCOT respectively, as the remaining secondary spacecraft options. The future Hera mission to Dimorphos, the smaller moon of the 65803 Didymos system, is planned to include the MASCOT-II lander. The heritage of this lander is easily traced back to the original MASCOT lander of the Hayabusa2 mission, with the notable difference being the addition of solar panels, which should be able to supply $127Wh$ per $\sim 12h$ day [136]. The following case study uses MASCOT-II as its subject, and compares some of the results to a larger microsat platform.
Dimorphos has an average diameter of approximately $D = 168m \pm 18m$, shown in table 2.3. The muon count per square meter per day on the surface is found by extrapolating the values in table 4.6 to this diameter. The resulting flux equals for $32\mu^{\pm}m^{-2}day^{-1}$ protons GCRs only. Assuming an increase of 35% caused by alpha particles in the primary GCR flux, the total flux equals $43\mu^{\pm}m^{-2}day^{-1}$. The MASCOT-II dimensions are set to be $330x330x210mm$ [137], resulting in a detector area of $0.109m^2$. The muon flux expected through the MASCOT-II lander would then be approximately $4.7\mu^{\pm}day^{-1}$, or a total of $426\mu^{\pm}$ over its envisaged three month lifetime [136]. When larger dimensions are assumed, such as the Philae lander's $1x1m^2$, the total muon count over three months would be $3,913\mu^{\pm}$.
These muon flux per day values can be used in figure 5.1 to retrieve the muon rate ratios these landers can achieve within a 3 month integration time.

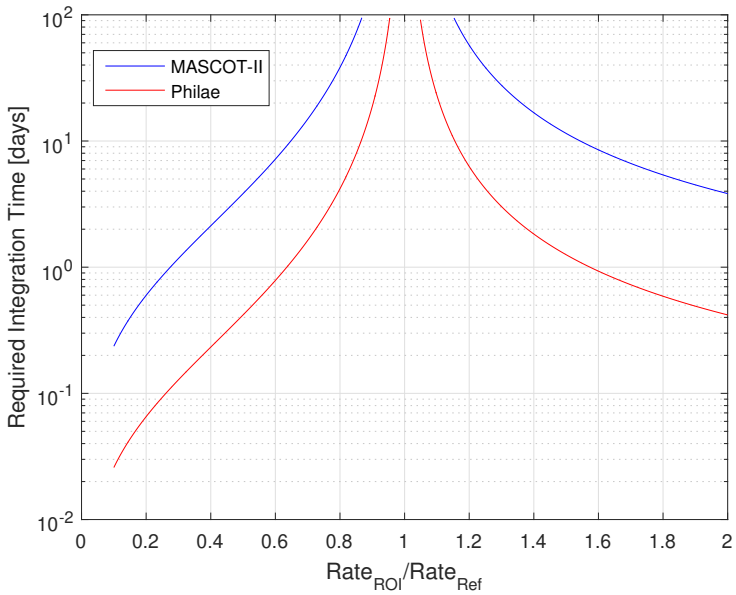

Figure 5.5: Plot describing the required integration time to reach the 3σ Poisson detection limit versus the muon count ratio on Dimorphos, for the MASCOT-II ($330x330mm$) and Philae ($1x1m$) sized landers. Created with equation 5.1[186]

Figure 5.5 shows that in a three month time frame, based on count rates, a MASCOT-II sized lander would be able to distinguish muon count rate ratios lower than 0.867 and higher than 1.152. A Philae sized lander with approximately 10 times the detector area, would reach 0.9541 and 1.048.

6

Verification & Validation

It is of paramount importance for any project dependant on simulation based results that the involved simulation model is validated. This validation process tests whether the model accurately represents the real world. Although real-world data was not always available, an effort was made nonetheless to validate the result using other sources of information. The outcome of this verification and validation process is shown in the following paragraphs.

Asteroid Model
The ultimate goal is to discover the interior properties of small Solar System bodies, which drives the entire feasibility study on a method to measure this. It is therefore logically not possible to completely validate a model of the interior of such a body. The choice was therefore made to not settle on a single model, but rather create multiple models using the various hypotheses on interior structure available. Additionally, the contrasting differences between these hypotheses are thought to not significantly effect the overall muon flux, the parameter of highest importance to this feasibility study.
The knowledge on the material composition of small Solar System bodies is similarly limited, as the only available data is from surface sample return missions and inference based on spectral signature comparison with meteorites. The choice was made to use the most direct information available, which was that of the sample return mission Hayabusa. The same molecular bulk composition as found in these surface samples (table 3.2) was used in the asteroid model.

Radiation Environment
The galactic cosmic ray flux used to model the radiation environment near the small Solar System body was created with ESA's Space Environment Information System (SPENVIS) [69][105]. The cosmic ray flux is calculated with this online tool, which bases its results on one of four different models. Since the models are practically identical above $1GeV$, as shown in figure 4.5, the choice of the CREME96 was not of effect to the produced flux.
CREME96 is based on an analytical model of the galactic cosmic ray fluxes by R.A. Nymmik et al. (1992) [176], adjusted with results of the Solar Anomalous and Magnetospheric Particle Explorer (SAMPEX) space mission [69]. It has subsequently been validated with on-orbit cosmic ray spectrum measurements by the AMS experiment flown on the International Space Station [13].
The differential spectral index of $\alpha = -2.7$, as presented by T.K. Gaisser et al. (2016) [220], is derived from, and validated by many cosmic ray experiments, which are shown in the legend of figure 2.14.

Geant4
The software toolkit *Geant4* in which all of the particle passage simulations were performed is validated with a large number of experiments, such as the ones at the Large Hadron Collider [3]. The physics lists governing the way processes are run in the toolkit are validated with these experiment results [6]. The physics lists used in the simulations, as discussed in section 4.1.1, all come as standard with the toolkit, and form part of its overall validity. The slight bias induced by the use of the *EMV* suffixed lists [7] is deemed negligible for the purpose of such a feasibility study, where the order of magnitude of the expected muon flux is of higher importance than the energy flux accuracy. This project did not make use of any non-standard physics plugins for the *Geant4* simulation toolkit.

Simulation Results

The verification process of the simulation was performed for the most part by comparing the results with their expected values. Different parts of the simulation, such as the passage of muons, were separated from the full simulation run and tested individually. As shown in section 4.3.2, the simulation results for a pure muon source are in line with what is logically expected. Additionally, the simulation performed by T.H. Prettyman et al. [187], who's results are used for validation later in this section, were verified using analytical methods and equations by T.K. Gaisser [220]. The semi-empirical Gaisser cascade model scales the atmospheric muon production to a different density material. The Gaisser model positively compares to the Prettyman simulation results [187], which in turn indirectly analytically verifies the simulation results of this report through a validation process.

To validate a simulation, its results should be compared with real-world measurements. As muon tomography interior mapping is only used once in space [2] and the subject (*Mir*) does not represent the characteristics of small Solar System bodies, the choice was made to validate the simulation instead with a comparison to results of other studies. Table 4.6 shows the extrapolated results of the NIAC study by T.H. Prettyman[187] and the master thesis by J. Keerl [125]. As these studies as well as the thesis by D. Hodge [109] used a proton-only GCR spectrum in their simulations, the validation efforts will focus on the proton contribution to the resulting muon flux only.

The proton simulation results found in this study were extrapolated using a power-law fit on simulation data of larger asteroids, shown in table 6.1, similar to the method described in section 4.3.4. The simulations by both T.H. Prettyman, (2019) [187] and D. Hodge, (2018) [109] used a spherical representation, of which only the composition and average bulk density are chosen differently. The particle source for both simulations should, albeit through different methods of construction, represent the expected primary proton GCR flux. The simulation results by J. Keerl, (2020) [125] used a $500 \times 500 m^2$ slab with a particle source not directly representing GCR flux. These results are shown separately. The simulation results from this project are extrapolated proportionally to the best-fit power-laws for the both the Prettyman and Keerl results, as these provide values for multiple depths of material.

Asteroid Depth	10	50	100	200	500	[m]	Source ⇓
$\rho_b = 1.6 g/cm^3$	*1.89E+6*	**14 134**	*1791*	**320**	**12.6**	$[sr^{-1}h^{-1}m^{-2}]$	J.Keerl[125]
Asteroid Diameter	10	50	100	200	500	[m]	Source ⇓
$\rho_b = 3.4 g/cm^3$	N/A	N/A	**1-2**	N/A	N/A	$[m^{-2}day^{-1}]$	D.Hodge[109]
$\rho_b = 2 g/cm^3$	*1.01E+05*	**960**	**144**	**20.4**	*1.45*	$[m^{-2}day^{-1}]$	T.H.Prettyman[187]
	[Extrapolated Simulation Results]						Extrapolation ⇓
$\rho_b = 1.9 g/cm^3$	**1.04E+05**	*829*	*104*	*13*	*0.83*	$[m^{-2}day^{-1}]$	$\propto$ J.Keerl
$\rho_b = 1.9 g/cm^3$	**1.04E+05**	*1056*	*146*	*20.2*	*1.48*	$[m^{-2}day^{-1}]$	$\propto$ T.H.Prettyman

Table 6.1: Muon counts per day per square meter detector on the surface, for larger asteroid diameters. Values in **bold** are obtained directly from sources, values in *italics* are extrapolated using best-fit power law from available data per source. Simulation results in **bold** are extrapolated in *italics* proportional to source data, indicated in the right-most column.

The results of the simulations performed in this thesis project are in very high accordance with the T.H. Prettyman results. The difference for the $100 m$ diameter asteroid is 1.4% and 38.5% when scaled proportional to the best-fit power law for the results of T.H. Prettyman and J. Keerl respectively. This slight discrepancy can be explained by the use of a different Monte Carlo transport simulation software (*Geant4* in this study versus *FLUKE* for Prettyman [187]). Another possible cause is the difference in asteroid material, which was so-called "standard rock" for the Prettyman study, comprised of $(SiO_2)_{0.8}$ and $(FeO)_{0.2}$ [187]. A third possible cause is the density difference as shown in table 6.1, which is known to effect the muon flux.

The resulting muon flux showed a 100× increase compared to the results of D. Hodge [109]. This can partially be explained by the higher bulk density of $3.4 g/cm^3$ used in the Hodge model, which not only decreases the muon production in the upper regolith layers, but decreases the surviving muon flux as well.

Compared to the results of J. Keerl [125], the resulting flux is much smaller. Again, this could partially be caused by the difference in model bulk density, which in the Keerl study was set to $1.6 g/cm^3$. A more likely culprit is the difference in particle source, which did not represent a GCR flux in the Keerl simulation.

As the results of this thesis's simulations seem to line up with those of Prettyman et al., the simulation can be

considered validated with the best available data. It is worth re-iterating that the muon fluxes stated in table 6.1 do not include the contribution from the alpha particles in the GCR flux, which was shown to increase the flux by as much as 35%.

The real-world data needed for validation studies does not always have to sourced from in-situ measurements. A great alternative to aid in the (partial) validation of these results, would be the use of experimental data. Although performing such experiments did not fit within the limited scope of this thesis project, a few recommendations are made for future research.
Since the muon production rate from GCR collisions with regolith is poorly characterised, a helpful experiment would quantify this rate and aid in determining the surface parameters effecting it. The experimental setup could for instance consist of a proton or alpha particle accelerator aimed at a regolith analogue, with a muon detector behind the regolith. Similarly, one could prove the feasibility of using the resulting muon flux to distinguish features and density variation within the regolith.
Another possible option is to involve the AMS-02 instrument aboard the International Space Station in the experiment. This unique instrument grants the ability to detect muons outside of Earth's atmosphere [22]. An experimental setup in this case could be to measure the produced muon flux from cosmic ray collisions with the matter of a visiting spacecraft, or an on-board regolith analogue. A similar experiment used the first version of this instrument, AMS-01, to map the *Mir* space station with muons and pions induced from primary cosmic rays [2].

Charge Ratio Discrepancy
Unexpected simulation results could not only lead to interesting auxiliary findings for a research project, they could also challenge the validity of the simulation itself. Since the validity of the simulation is of paramount importance to the validity of the end results, it is worth discussing this unexpected discrepancy. Checking a simulation for correct and bug-free performance is a part its the verification process.
The simulation performed on the simplified asteroid model using a cosmic ray primaries source, as shown in section 4.3.4, yielded an interesting but controversial result. On Earth, the surface flux charge ratio for muons is found to be $N_{\mu^+}/N_{\mu^-} \approx 1.2766$ [127], below $p_\mu = 100 GeV/c$. Conversely, the stopping power for positive muons is higher than for negative muons in the low energy ranges due to the Barkas effect (figure 2.16), leading one to expect a lower charge ratio after a large amount of material is traversed. The charge ratio at the detector in the simulation, $N_{\mu^+}/N_{\mu^-} = 1833/802 \approx 2.29$ for the proton source and ≈ 1.73 for the alphas, shows a rather large discrepancy with the expected value. When considering only muons with kinetic energies above $1 GeV$, this ratio is exactly $15/15 = 1$, and above $500 MeV$ this is even slightly reversed, $48/59 = 0.81$. This is an unexpected result of the simulation, and its cause should therefore be researched to verify the justness of the results.
The histogram of the positive and negative muons that reached the detector in the simulation is plotted in figure 6.1.

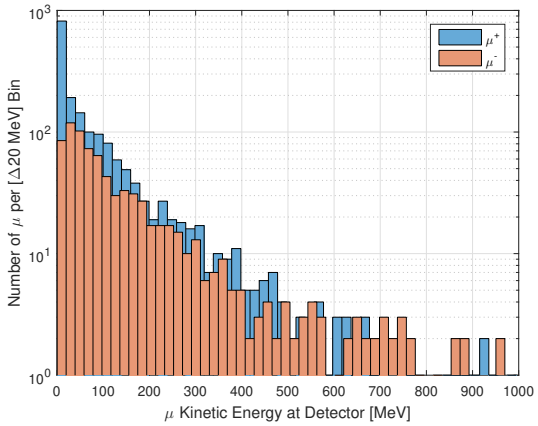

Figure 6.1: Histogram of positive and negative muons up to $1 GeV$, from pure proton GCRs, reaching the detector versus kinetic energy, binned per $20 MeV$.

D. Hodge (2018)[109] characterised the backscatter of particles caused by GCRs on an asteroid's surface

and found a charge ratio of $(N_{\mu^+}/N_{\mu^-}) \propto (\sim 8\%/\sim 4.8\%) \approx 1.67$, which shows a similar discrepancy towards a larger ratio. It is clear from the histogram that at the lowest regions of this energy spectrum, positive muons are much more present compared to negative muons. As the latter experience less energy loss at those low energy regions, the inverse would be expected. However, when considering the equation for muon scattering 4.8, one finds the scattering standard deviation σ_θ to depend inversely on muon energy. A theorem for the possible cause of this charge ratio discrepancy is therefore the fact that low energy positive muons lose energy faster, and therefore scatter faster, allowing positive muons travelling at oblique angles in the upper surface to escape the surface with less distance travelled within the asteroid, possibly allowing more of those to survive. Another possible cause is the poor validation of the lowest energy regions in *Geant4* [3]. Efforts are being made to mitigate this, and results of these efforts are already available in certain physics models. Physics list with the *EMY* or *EMX* suffix, as shown in section 4.1.1, use these models to provide the highest available levels of precision for electromagnetic interactions, at the cost of performance. These low energy regions are not of interest for muon tomography, justifying the use of *EMV* suffixed physics lists.

7

Business Plan

This chapter forms the concluding deliverable for the course MoT9611 *Project Entrepreneurship Thesis Related*. It marks the end of the Master Annotation Entrepreneurship elective track, performed parallel to the main Space Flight MSc track. The aim of this course is to educate engineering students how to generate value from their master thesis work in a commercial context [226]. It was therefore decided, in consultation with the supervisors and the entrepreneurship coordinator of the Aerospace Engineering faculty, that the deliverable would best serve its purpose as an integrated part of the thesis.

Disclaimer: This chapter is not to be included for the formal grading process of the Master's Thesis Project. The members of the graduation committee are of course free to read the chapter, as it forms an interesting addition to the main thesis project in a different field of research.

7.1. Introduction

Opportunity is described by the *Merriam-Webster* dictionary as a favourable juncture of circumstances[157]. During the final phase of my MSc in Space Engineering, whilst working on my MSc thesis, I found myself at the crossroads of such circumstances. The results of the research performed during the thesis project formed an ideal subject for identifying and analysing business opportunities in a learning environment.

7.1.1. Technology

At this moment, there exists no tried and tested solution to accurately map the interior of asteroids and comets in space. A few methods have been proposed, but none have yet seen the light of day[187]. Moreover, in the past few years, an increasing amount of scientific missions was launched to these smaller bodies in the solar system, with more being planned for the upcoming years. The need to gain scientific knowledge on the interior of these objects in space grows with every launch. A system capable of mapping these interiors and reconstructing them would satisfy this need.
The proposed solution revolves around the use of already-present muons from cosmic rays to map interior features. Derivatives of this technology are currently sparsely used on Earth to map the magma chambers of volcanoes [215][149], pyramid interiors [165], detect contraband materials for homeland security [93][166] and even look for radioactive material inside the Fukushima-Daiichi nuclear reactor [162][163].

7.1.2. Plan

This thesis, to which this chapter on entrepreneurship is a tangent, shows that with a combination of a spacecraft-based instrument and capable data processing on Earth, such a system can be realised. The focus of this chapter lies on identifying the path on which this system can successfully be brought to market. This is achieved by showcasing the commercial value of the system, followed by an investigation into the appropriate business model for the route to market. The research performed revolves around the start of a new company, although the line between this and an entrepreneurial venture within an established company tends to blur for these kinds of projects. This is caused by the strong involvement of the intended customer in the development process. The scientific and societal value of the system, from which its commercial value is derived, are discussed in the main thesis report.

The customer pool for scientific spacecraft systems is traditionally small (research groups, governments, universities and space organisations). These relatively small markets have a history of quick adaptation of bleeding edge technology, and are often willing to spend a vast amount of resources to obtain it. This theoretically makes them the ideal beachhead market for this service and technology, allowing to gain a dominant position within this specific market before branching out, elaborated in section 7.2.2. Paraphrasing Elon Musk FRS on the mission of the successful electric car company Tesla: bringing a product to mass market is impossible for a start-up with only a single technology iteration and no economy of scale [168]. He therefore chose to compete with the conventional fossil fuel alternatives in the niche high-performance section of the intended market, which in the case of Tesla was the sports car segment of the much larger automobile market. A similar approach will be surveyed in this chapter, focusing on leapfrogging the competition in performance first with the space application of the technology, before moving to the much larger market for Earth applications.

7.1.3. Method

In the research proposal, a two pronged approach was planned for the business strategy development research. One branch would tackle the business development around the muon tomography instrument, the other describes the strategy for the data processing business. The framework for this research is shown graphically in the following figure 7.1.

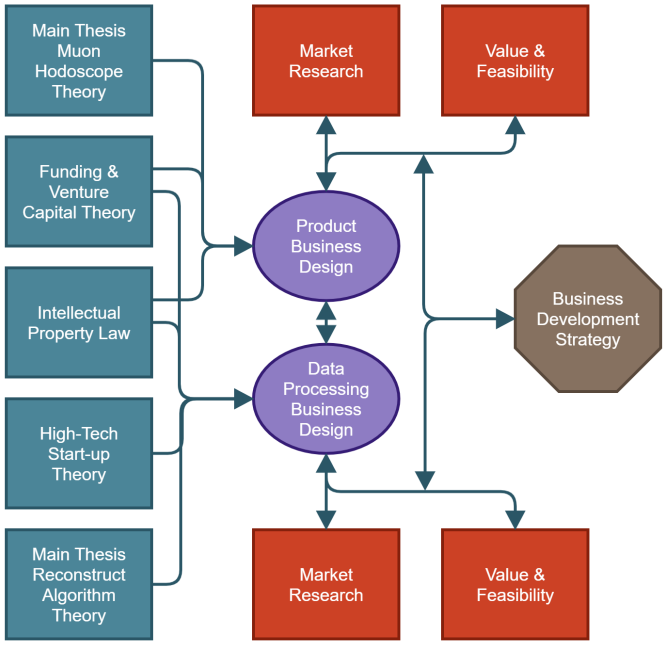

Figure 7.1: Research Framework for the *Project Entrepreneurship Thesis Related.*

The following sections in this chapter each treat a different aspect of the research performed to discover the best-fit business development strategy for this product. The oft-referenced work "Disciplined Entrepreneurship: 24 Steps to a Successful Startup" by Bill Aulet (2013) [12] will roughly dictate the order by which these sections are presented. Although this work will form the thread this chapter follows, not every dictated step will be treated in similar detail as it would not fit the scope for this chapter.
Space flight has been a traditionally government-run branch of the technology industry. Most space organisations around the world are transitioning to commercial solutions, for both hardware and human space flight. The available literature on entrepreneurship in the field of space engineering is therefore considerably sparse. To augment the available data from literature and online sources, interviews were held with Dr. Michael Küppers, who is the Mission Scientist for the asteroid mission Hera at the European Space Agency (ESA), and with Dr. Alessandra Menicucci, who has close to a decade of working experience at ESA and currently works as assistant professor at the Space Systems Engineering faculty of the Delft University of Technology. Furthermore, Surya Pradesh of NeoStove B.V. conveyed his first-hand experience with creating business from space

technology though the use of the ESA space Business Incubation Centre (BIC).
It became apparent that other applications of the technology warranted a literature study as well. Therefore, in addition to a business development plan for the space application of the aforementioned technology, this chapter seeks out to lightheartedly discuss possible next steps in the business development as well.

7.2. Customer & Market

The first steps in creating a successful business plan involves the search for a potential market and therefore a paying customer. The introduction lightly touched upon the idea of using the space industry as the beachhead market for the muon tomography technology before branching out to other markets. This will be further elaborated in this section, with the main focus on the technology's space application and some illustrative notions of other market applications. It is worth mentioning that as a general rule for entrepreneurship, one should only select a single market opportunity to pursue [12]. This justifies the sole focus on the space market application. The treatment of other applications within this chapter should therefore be seen as additional but nonetheless interesting exploratory research.

7.2.1. Market Segmentation

The main market to focus on will be the space flight market. All the missions to small Solar System bodies thus far, shown in table 5.4, have been launched by large governmental space organisations such as ESA, NASA and JAXA for scientific purposes. Although commercial and planetary defence applications have been considered, where a future asteroid mining business would especially be of interest, creating a start-up within a not yet existent branch of industry was deemed infeasible. With this in mind, one can already state that the aforementioned space organisations, with collaborating universities and research groups included, form the most likely market segment to focus on. This can be further narrowed down to the segment of interplanetary space flight, or the field of small Solar System body research.
With only a few asteroid missions every decade, this market is very specialised and is considered niche. Briefly touched upon in section 7.1.2, this market segment devoid of competition utilising similar technology will form the ideal breeding grounds for the muon tomography instrument. As economy of scale is not required for this niche market, the focus can lie on perfecting the technology.

Follow-On Market Segment

Although not the main focus of this business development plan, it is interesting to look forward to the next step for the product. The intended mass market for the product, once it is used and proven in space, will be that of border and port security. The market segment of homeland security is the largest by far, compared to the other existing applications of the technology mentioned in section 7.1.1. The budget for the United States Customs and Border Protection (CBP) alone, for the year 2019, was 16.7 billion USD [62]. The budget for the Countering Weapons of Mass Destruction Office (CWMD) was 430 million USD for the same year. The figure for both these offices increases steadily each year, shown graphically for the CBP in figure 7.2. Such a large and steadily increasing market is a prime candidate for the envisioned business application. The specifics of this application will be further discussed in the section on product value 7.3.

7.2.2. Beachhead

The term "beachhead market" is derived from the use of a beachhead landing point in military strategy. The famous D-Day landings used the beaches of Normandy as the beachhead for the liberation of the European mainland. The goal of this strategy is to take control of a small section or segment of a market, the so-called beachhead, and gain a dominant position within this segment before branching out to adjacent markets. The control of the beachhead market will give the business the strength to leap into other markets.
Suitable beachhead markets are generally void of entrenched competition, contain well-funded customers and the proposed product is a compelling solution to a pain of said customers. Scientific payload instruments typically range in cost from hundreds of thousands of dollars to tens of millions, with exceptions ranging up to multiple billions [45], confirming the "well-funded" requisite.
Generally, the member states of ESA are asked whether they would like to take up a specific challenge. These states in turn will provide a large part of the funding, and consequently stimulate their own industry and technological know-how. In case no specific member state wants to tackle a problem, it is outsourced to industry. It became apparent from the interviews with (former) ESA personnel that a space organisation like

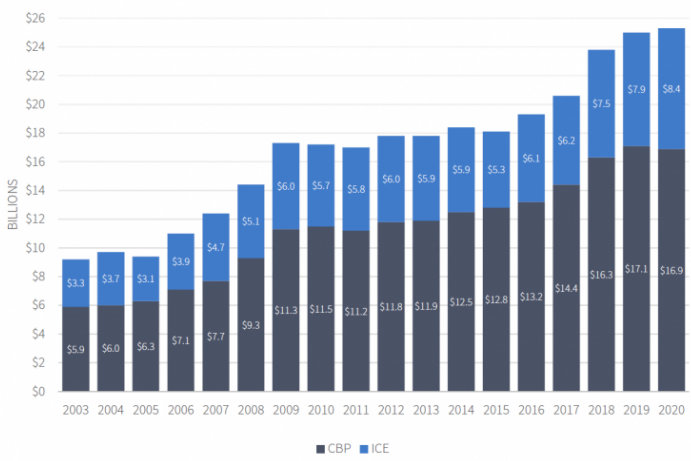

Figure 7.2: The annual budgets of the United States Immigration and Customs Enforcement (ICE) and CBP, fiscal year 2003 to 2020. From "The Cost of Immigration Enforcement and Border Security", by the American Immigration Council, (2020)[4].

ESA will put out invitation-to-tenders (ITT) to request commercial solutions for their problems and needs. When a company wins with its bid, ESA will often not only pay for the proposed technological product, but will support and fund the development of the product as well. This again supports the denotation of the space instrumentation market as a suitable beachhead for the muon tomography instrument.

7.2.3. End User Profile

B. Aulet notes that customers consist of both an individual who will use the product, as well as a decision-making unit that decides whether the customer will buy the product [12]. A clear example of this would be children's toys, where generally the parents form the decision-making unit and their child the end user. In the case of the muon tomography a few separate end users can be identified, ranging from personnel integrating the instrument into the spacecraft to scientist using the provided sensor data. As scientists are very involved in the decision making process when choosing a specific payload for a mission, they form the focus for the following end user profile. By creating such a profile and even including a specific example (called the "Persona" [12]), the target customer becomes concrete, facilitating customer-focused product development instead of the pursuing the fallacious idea that the first iteration is best. The following table 7.1 shows this end user profile, with Hera mission scientist Dr. Michael Küppers as the chosen Persona.

Table 7.1: Profile of typical end user within the segmented space instrumentation beachhead market. The specific example persona is based on Dr. Michael Küppers of ESA.

	Typical End User	**Persona**
Gender	60% Male 40% Female [75]	Male
Age	40-60	~ 50
Job	Mission Scientist or Engineer	Hera Project Scientist at ESA since 2007
Location	Europe	Madrid, Spain
Education	University Level	PhD
History	Often worked all over the world, almost always science related jobs at research groups, universities or space organisations.	Studied physics at university, PhD on the plasma torus of Io at the Georg-August-Universität Göttingen, postdoc in Bern, and worked at Max-Planck-Institut für Aeronomie in Katlenburg-Lindau and LASP in Colorado.

Continued on next page

Table 7.1 – *Continued from previous page*

	Typical End User	Persona
Product feature requests	Data processing. Involvement of the general public with missions, to improve the image of ESA and connect the tax payers to the fruits of their support.	Service that makes instrument data available to general public. Data processing services. Everyday applications of space instrument data. Data archiving.
Passion	Generally very gifted, chooses to philanthropically improve quality of life and our understanding of the Universe. Generally seem to dislike the politics and paperwork involved with their jobs.	Planetary sciences, physics, and science in general. Moving around the world.

7.2.4. Decision Making Unit

It is vital for a business to determine the decision making unit (DMU) of the customer, as this unit is ultimately responsible for the acquisition of your product. Often the DMU consists of multiple entities, all with different roles and degrees of influence on the purchase. The DMU for ESA is determined based on interview results, literature and data available from ESA.

The first part of the DMU to note are the ESA member state governments. Ultimately these member states control a large part of the budget, and therefore have quite a bit of say in the decision making process. This is especially true when a specific country initially took responsibility for the development of the instrument, making it a national contribution to an ESA project. Governing the budget, it would give the government Veto-power over the product's implementation.

Customer Acquisition Process

The acquisition process of a paying customer by a company can be seen as the reverse of the product acquisition process of the customer. Each of these steps taken by the customer in this process could prove to be a potential pitfall in the sales process, and must therefore be identified as such.

Within ESA, a potential mission follows a set track before a specific implementation of said mission is chosen [66]. It starts with a "Call for Mission Proposals" with certain boundary constraints from ESA to the science community, which makes the science community a secondary influencer. The different proposals naturally include different hardware solutions and payloads, so the company must make sure to be included in as much of these proposals as possible.

The proposals are subsequently checked for feasibility by ESA's Science Advisory Structure and a scientific review is performed by the Space Science Advisory Committee. The requirements and method of testing influence the final choice, and these committees are therefore influencers in the DMU as well. From the missions that passed all scrutiny, a winner is selected by the Science Programme Committee, which is therefore considered the Primary Economic Buyer [12] in the DMU. Most of these aforementioned committees form a part of the Future Mission Department, which could be considered the DMU of ESA.

It must be noted that this entire process, called the Mission Preparation Phase, can take anywhere from less than two years for smaller missions all the way up to 8 years for the largest flagship missions [66]. Missions to asteroids and comets vary greatly in cost, with the previous JAXA missions costing 25% ~ 50% of the missions by ESA and NASA. This puts such missions in the medium M-Class and large L-Class by ESA, for which the Mission Preparation Phase should take up 4 ~ 8 years. However, faster tracks are available, as ESA recently rolled out the new fast F-Class mission type which can be used for events that require a quick response time, such as comet interception.

7.2.5. Total Addressable Market

The Total Addressable Market (TAM) size is calculated from the total amount of revenue one expects per end user in the chosen market segment, multiplied by the amount of end users in the segment.

Beachhead Market
The TAM is used to determine whether the chosen beachhead market segment is appropriately sized, or whether it needs to be segmented further. The end users in this case are the decision making unit, as they will choose what instrument best suits their need. However, they are generally not responsible for the budget, which complicates the calculation of the TAM size for this beachhead market. As a solution, an estimation using the JPL developed NASA Instrument Cost Model [233] (NICM) is made for non-recurring hardware development costs for a particle detection payload. The approximate resulting cost is 30M\$, which is very close to values found for similar instrument types. It must be noted that the NICM model is based on fiscal year 2010, resulting in a under-approximation due to inflation, which is approximately 19.3% from 2010 to 2020. The adjusted cost would then equate to 35.8M\$.
In the past 20 years, an orbiting mission to a small Solar System body was launched roughly once every 3 years, when considering all space organisations combined. As a first order approximation, the calculated development cost is divided by 3 to find the TAM size. In this case, the TAM size would equate to 11.9M\$. A TAM size of twenty to a hundred million dollars is considered to be an adequate size for the beachhead market [12]. However, in case not a lot of personnel is needed and the margins can be large, smaller market segments would be fit as well. This market should therefore be a good starting point, especially considering the financial and development aid from the intended customer. Although the initial intended customer is ESA, most other space organisations should be interested in this system as well, justifying their inclusion in the TAM.

Follow-On Market
As briefly touched upon in the market segmentation section 7.2.1, a potential follow-on market could be that of border and port security. As shown in said segment, the yearly budget for the United States alone dwarfs the market size for the beachhead market. Various estimations put the total worldwide container scanning market at a few billion dollars per year, which could be the TAM size. Obtaining even a sliver of this market will vastly expand the business.
To better quantify the possibilities, the numbers provided by the main competitor "Decision Sciences" are used to calculate their market share [60]. Over the past eight years, the company installed their product in two major ports, and supplied to two nuclear agencies. Extrapolating from a single contract, these four contracts should be worth around twenty-one million dollars in total [60]. This excludes all the US backed research and development contracts.

7.2.6. Full Life Cycle Use Case
In this section, the interactions of the persona with the product are treated, which encompasses everything from their realisation a (better) solution to their need exists and their acquisition and use of the product, to the spreading of awareness of the product to others. The flow chart in figure 7.3 visually depicts essential parts of this process in sequence.

7.2.7. Next Ten Customers
As a follow on to the selection of a "Persona", B. Aulet [12] advises to identify and interview 10 more such potential customers to validate the created end user profile (section 7.2.3). The interview with Dr. A. Menicucci was used in this case to validate the findings, although her willingness to buy such a product was deemed biased as she supervises the muon tomography research project. An interview with eight additional persona was not performed due to time constraints, but is recommended to complete the business plan.
In a broader sense, when considering ESA as the customer, one can define potentially interested parties to be:

1. **European Space Agency (ESA), Europe**
    (a) Canadian Space Agency (CSA), Canada
2. **National Aeronautics and Space Administration (NASA), United States of America**
3. **Japan Aerospace Exploration Agency (JAXA), Japan**
4. *Roscosmos, Russia*
5. *China National Space Administration (CNSA), China*

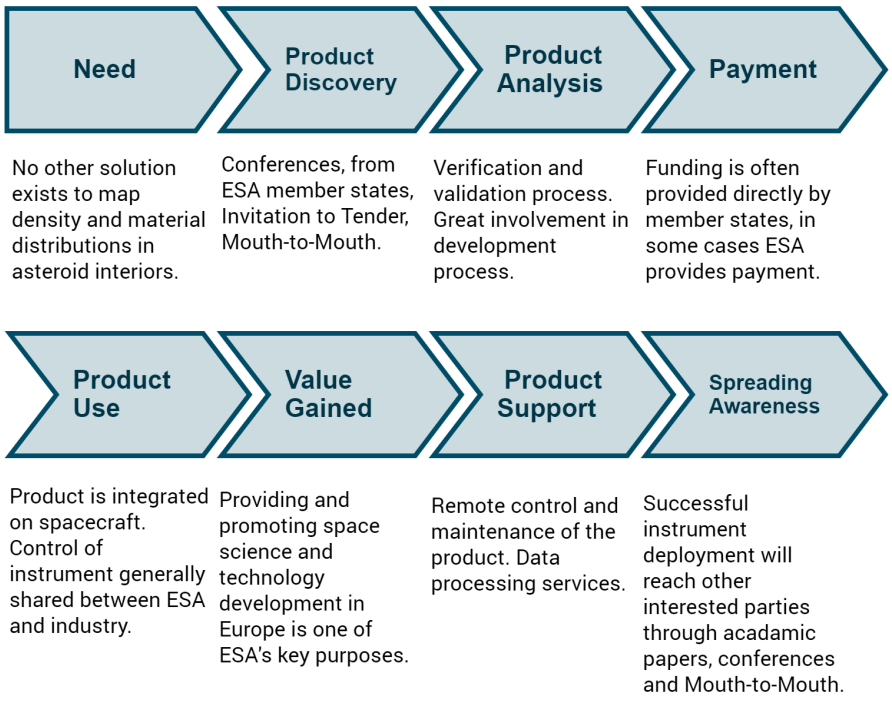

Figure 7.3: Visual representation of essential parts of the Full Life Cycle Use Case for the muon tomography instrument, applied to the ESA beachhead market segment. Based in part on interview results.

6. Indian Space Research Organisation (ISRO), India
7. Brazilian Space Agency (AEB), Brazil

This list comprises seven additional space agencies with capabilities or ambitions to go beyond Earth orbit. Agencies in bold have already orbited small Solar System bodies, agencies in italics have performed fly-byes. Some governmental agencies with similar capabilities are omitted because they are currently full member states of ESA as well.

7.3. Product & Value

This section treats the product created by the business as well as the created value. To add clarity and conciseness, small deviations are made from the order of steps as presented by B. Aulet [12].

7.3.1. Product Specification

Contrary to an engineers intuition, the features and specifications of a product are often not the sole cause for a successful venture. Other factors can play large roles in the success of a product as well, evident from the large sales of items some might consider to be nearly worthless gadgets. Nonetheless, formulating a high level product specification will aid in refining the product outline, which will in turn help define the business plan. Although a visual representation of the product is often preferred [12], a verbal statement is used in this chapter to aid conciseness.

> The product consists of a muon tomography instrument, capable of passively mapping a small Solar System body interior structure from orbit, together with data processing services on Earth, reconstructing said structure from the instrument data.

7.3.2. Minimum Viable Business Product

The selection of a Minimum Viable Business Product (MVBP) is normally performed at the end of the business plan development process, but for the sake of clarity it is treated earlier in this chapter. The goal of the MVBP is to find the most basic version of the envisioned product that the customer will still get value out off, and still

pay for. The intent is to start a customer feedback loop, where the customer helps to create a better product. The MVBP is used to system test key assumptions made during the business development process, such as the assumption that a customer will buy the product.
The MVBP for the space application would be the muon tomography instrument with small Solar System body interior mapping capabilities. The extra whistles and bells, such as the data processing or the service contracts, are features which will generate extra revenue and profit but should not be included in the MVBP.

MVBP Test

The next step is to test the MVBP in the field. Metrics need to be collected on how engaged potential customers are with the MVBP, how the word of mouth travels and if current customers would advocate the MVBP. This step should demonstrate that customers are willing to pay for the MVBP, testing the assumption that they will. In case a less than desirable response is observed, the MVBP needs to be adjusted or the product plan failed altogether. For example, a possible outcome could be that space agencies need the service contract to be included in the MVBP, something which is easy to adjust.

7.3.3. Product Plan

The product plan describes how the product which is optimised for the beachhead market will have to develop to enter other (adjacent) markets. As touched upon in previous sections, the envisioned business plan involves expansion into the border and port security market. This requires the product to evolve from its space application, as described in section 7.3.1, to an Earth-bound application.
Entrenched competition exists in this market, even in the specific field of using muon tomography for contraband detection. The "Discovery - A Multi-Mode Passive Detection System (MMPDS)" by Decision Sciences builds upon initial research performed by the U.S. Department of Energy's Los Alamos National Laboratory, and uses the muons from cosmic rays to map contraband within shipping containers. However, only a small market share is held by Decision Sciences, with only a single U.S. harbour equipped with their technology. Their latest version still takes a minute to scan a single container, time which adds up for large ports. The advantage of deriving such equipment from space technology are the innovations developed for interior reconstruction with the sparsely available muons in space. The use of these innovations will lead to much faster scanning times. Additionally, ports only scan the small percentage of cargo they deem high risk, which saves costs but leaves holes in border security. An increase in scanning speed will therefore increase safety as well.
The product will be shaped similarly to the MMPDS, with a detector above and below the container. This configuration is shown in figure 7.4.

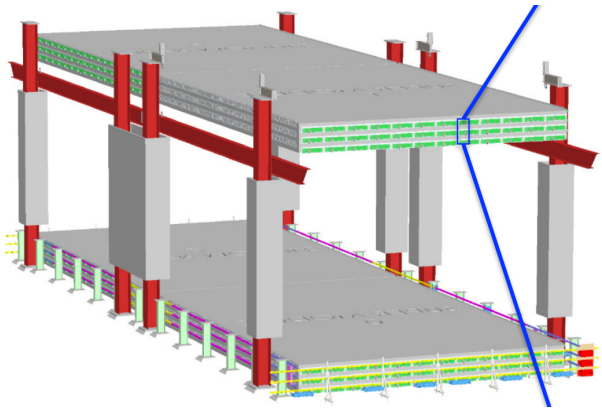

Figure 7.4: 3D model of the "Discovery - A Multi-Mode Passive Detection System" internal structure, by Decision Sciences. Modified, from "Scanning of vehicles for nuclear materials" by J.I. Katz (2014) [124]. ©2013 Decision Sciences International Corporation.

The contract with port and border security agencies will include service and maintenance, which is the industry standard for scanners of this size. Although these scanners should have a long lifetime, it is of vital importance for border security agencies to use the latest technologies in order to stay ahead of wrongdoers. The product could therefore be upsold with upgrade and update packages, which can be a viable business plan in its own right.

7.3.4. Value Proposition

The quantification of the value proposition is outlined by the top priorities of the Persona, shown in section 7.2.3. These top priorities, found from interview results, are shown in table 7.1. Generally, the value of a certain product for the customer is found by comparing the quantified current "as-is" state with the "possible" state [12]. The differences can arise in product life cycle as well as in product properties or capabilities. Customers like ESA are deemed not likely to radically change their Full Life Cycle Use Case (section 7.2.6) for a single product, which is why the focus for the value proposition lies on product and service performance and properties. Whilst features and services are quantifiable in some way, the value of scientific gain is not, as this has to be decided upon by the scientific community. The value proposition, shown hereafter graphically in the form of a value proposition canvas (figure 7.5), should therefore be validated by the Persona or typical end users instead of merely relying on a numbers game.

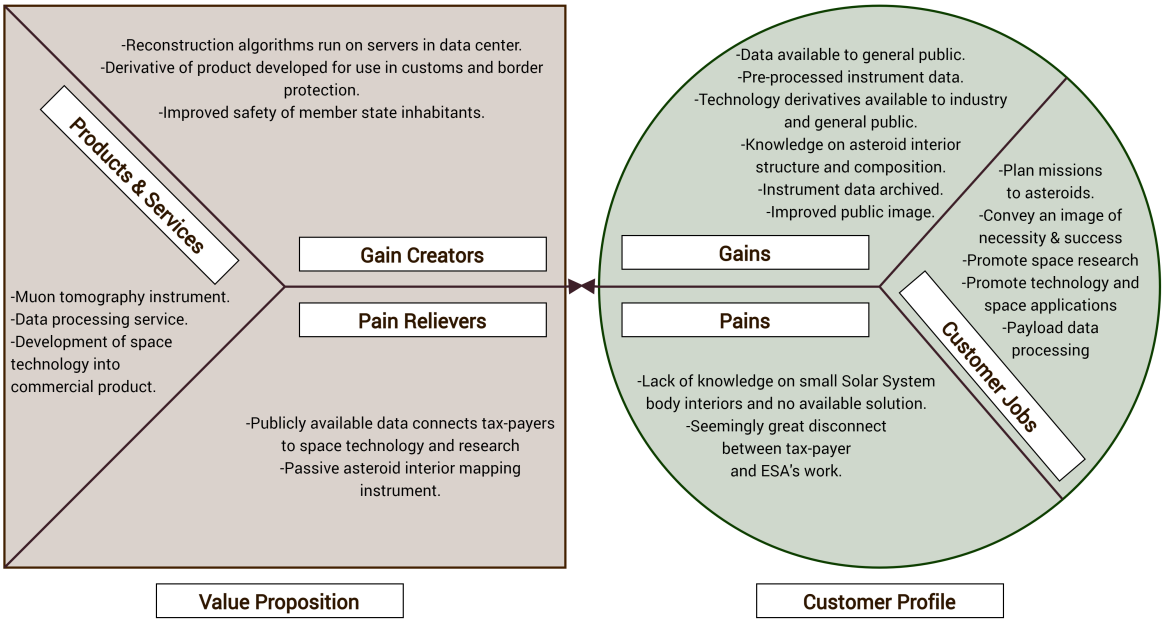

Figure 7.5: Value Proposition Canvas, with the envisioned business providing the value proposition and the customer profile based in part on interview results.

The goal of the value proposition canvas is to visually aid the understanding of whether the value proposition matches up with the customers expectations. In short, is shows whether the target audience is understood well enough. The muon tomography instrument combined with data processing services is deemed to provide a good fit between the left and right side of the canvas, justifying the choice of customer and product.

7.3.5. Core

The "Core" is in this case defined as the single thing the envisioned business brings to the table that potential competitors cannot. This can for example be a technological achievement protected by intellectual property laws, or it can be the lowest cost, the best customer service, the best user experience, or even the prettiest design. The core must prevent competitors from simply copying your product.
The core for this business will be the customer benefits of combining an instrument with unparalleled capabilities together with data processing services on Earth.

Network Effect

As the product outperforms the current competition, the chances are very high that muon tomography becomes the standard for asteroid interior mapping. The competing solutions are often derivatives of other technologies, not purpose build for this specific application. One can therefore state that there is no entrenched competition in this specific market segment. As the intended market is quite small, chances are that the company quickly gains a critical mass and it no longer makes sense for customers to use other products. Comparable situations arose for other payload instruments. The French Aerospace Lab ONERA for example

has provided the high accuracy accelerometers for all previous geodesic gravity missions [48] described in section 2.1.5, dominating this niche market segment.

Intellectual Property
Although software is to some extent automatically copyright protected as literary work, the underlying idea on which the workings of the software are based are not protected by this copyright [132].
As proposed in section 4.4.4, the reconstruction algorithm software could be created through the use of artificial intelligence (AI). This forms another problem for the legal protection of this work. Directive 2009/24/EC, the "Computer Programs Directive", states that software must be "The author's own intellectual creation" to fulfil the originality criterion [132]. Similarly, the "Database Directive" 96/6/EC states the database selection or arrangement of its content to be "The author's own intellectual creation" [132]. The AI creates the database or the algorithm without the intervention or intellectual input of a person, which is the root cause of this issue. AI is currently not considered to be a legal person, and can therefore not hold these legal rights. The reconstruction algorithm created by a form of artificial intelligence software is therefore much more difficult to protect.
Two alternative protection solutions exist. The produced database *sui generis* rights belong to the maker of the database, whom is defined as "the person who takes the initiative and the risk of investing". In this case, one could argue the *sui generis* rights of the AI produced database would still belong to the entrepreneur.
The other solution flows from the fact that a trained neural network, in this case the reconstruction algorithm, is notoriously difficult to comprehend. Without access to the actual code, copying the code based on its workings is close to impossible. This prevents competitors from simply reconstructing the code based on its publicly available results.

7.3.6. Competitive Position
Comparing the competitive position of the proposed start-up is performed by charting the business proposition and the competitors versus the Persona's top priorities. This provides a clear visual representation of the advantages of the envisioned product compared to the competition. However, a few of the Persona's top priorities are not quantifiable, but follow a binary "met" or "not met" status. The previously flown instruments to map small Solar System body interiors did not meet all these priorities, whereas the muon tomography product will. A comparison with alternative mapping methods is shown in table 2.5.

The core of the border security application is twofold. Most container X-Ray scanners claim to be low-dosage, and this seems to be partially true when empty containers are used for the test [114]. However, the dose increases when filled containers are used, as well as the amount of scattering towards the driver [43]. A driver could therefore, depending on the cargo, receive a dose equivalent to a medical X-Ray every time a drive-through X-Ray scanner is passed. Compared to the currently standard X-Ray machines, muon tomography is passive and not harmful to biological life. This would be a major improvement to the safety of truck drivers who pass the X-Ray scanner many times per year. It would also allow for safely scanning radiation sensitive cargo such as photographic film, or possible living beings such as humans or animals.
The other part of the core is the improvement in scanning speed. The only muon tomography competitor, Decision Sciences, is approaching scanning times of one minute, during which the container must maintain stationary. This limits the scanning capability to sixty containers per hour, whereas X-Ray systems approach 150 containers an hour. A decrease in scan integration time would give a competitive edge over other companies.

7.4. Business Model
The adaptation or creation of a business model is arguably the most important step in starting a business. It describes how the business will capture some of the value it provides to the customer with its product. Innovation in the business model has great potential for the growth of the company, possibly even more so than product innovation. This section describes the chosen business model, as well as the strategies employed to bring the business to fruition.

7.4.1. Business Model Canvas
The business model canvas is a visual template to aid in the development of a new business. It is closely linked with the value proposition canvas shown in figure 7.5 by means of the value propositions and customer

segments. The following figure 7.6 shows the canvas applied to both the business model revolving around the initial space application of the product (green) and the business model aimed at border security (magenta). Entries applying to both business cases are shown in green with a magenta border.

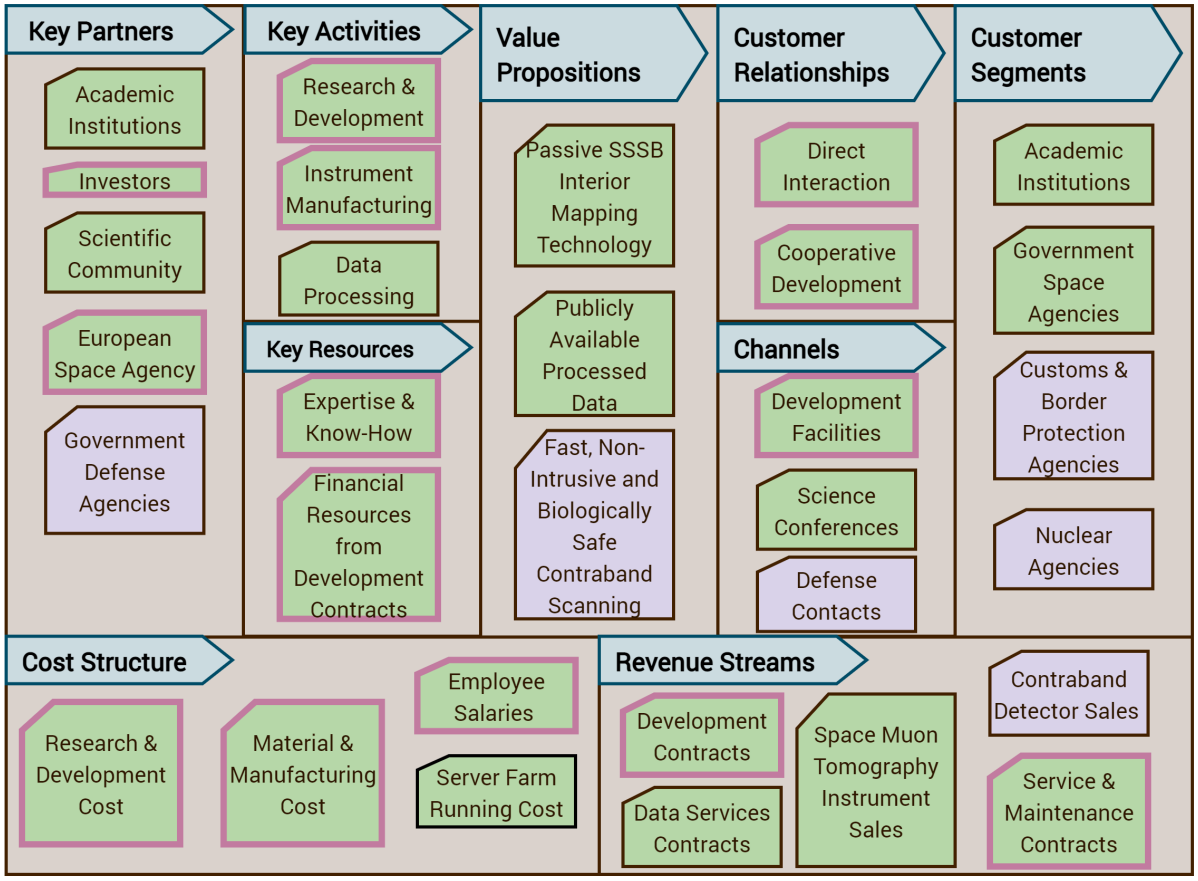

Figure 7.6: Hybrid Business Model Canvas, showing the entries for the space application of the technology in green, and for the follow-on border security application in magenta.

Since knowledge and technical know-how are deemed a key resource for both business applications, the venture is determined to be a High-Tech Start-up. Without proper institutions for development, the Business Incubation Centre of ESA is deemed key in the development phase.

7.4.2. Pricing Framework

The initial pricing framework is based on the business model and the value proposition for the customer. The pricing of the product should not be based on cost, but rather on the value it creates for the customer [12]. Initially, when products are still under development, some of the product risk is transferred to the customer. This is why early bird price tags are generally lower. However, the exclusivity of using the bleeding edge of technology should raise the price as well.

In this case, the initial product price can be on the high side, which should be in the ballpark of $30 \sim 45 M\$$, or around $100 \sim 150\%$ the price of similar instruments as calculated in section 7.2.5. The agency aiding the research and development process, for this case assumed to be ESA, will receive a hefty "Early-Adopter" discount and will therefore essentially only pay for direct expenses made by the company. In other words, little or no profit is expected from the first sale, but the profit is subsequently made with the after-sales services such as maintenance contracts and data services. The subsequent sales can slowly decrease from the initial product price all the while staying competitive with other solutions and maintaining healthy profit margins.

A similar strategy can be employed for the border protection application. The agencies investing in development will receive discounts on prototypes and first products. The subsequent first sales can err on the high side of product pricing, which are expected to be around $5 M\$$ per unit, based on Decision Sciences' first contract values [60]. Competing X-Ray based solutions seem to be priced in the order of $2 \sim 3 M\$$ per unit, a price

the product will need to approach to attract more sales.

7.4.3. Profitability

To determine the profitability of the business within the beachhead market, one first needs the determine the Cost Of Customer Acquisition (COCA) and the customer Lifetime Value (LTV). These values are deemed critical in the business plan development process [12].

Cost of Customer Acquisition

The COCA depends first and foremost on the sales process the company goes through for each paying customer. B. Aulet [12] divides this into three categories: Short, Medium and Long term sales.
In the short term, the company must create demand for the product. This would be achieved by applying to Invitation to Tenders, presenting on conferences and generally getting the word out there. Specialised salespeople can be hired to establish communication and sales channels with space organisations.
In the Medium term, word of mouth marketing takes over some of the company's burden of demand creation, while the focus for the company shifts towards customer management and service up-selling.
In the third phase, the focus shifts towards customer retention, whilst the sales department focuses on fulfilling customer orders. In this phase, it is assumed that most potential customers already know about the product and the focus lies on maintaining or adjusting the company's position to the current sales landscape.
In short, the COCA is driven by the cost of the marketing and sales process. In the case of ESA, a large portion of this cost will consist of applying for the Invitation to Tender (ITT). Quantifying this cost is very difficult, as ESA provides support and subsidies for almost every phase of the development project. For the first sale, ESA can even supply up to $150K€$ for a feasibility study. Setting up the necessary documentation for the ITT will be an investment in time and salary, and the risk here is that cost to tender is not covered by ESA.
To conclude, the COCA for the first customer will be much higher than for subsequent customers. Although research and development costs are not included in the COCA, entering the market with no sales record and no experience will logically result in high cost. As ESA intents to cover the feasibility study cost with $150K€$, it is safe to assume the application for the ITT will not cost more. Combined with the marketing cost, and the cost of the rest of the sales process, one can guesstimate the COCA to not exceed $0.5 \sim 5M\$$.

Customer Lifetime Value

The customer LTV serves as a checkpoint to test the viability of the business [12]. It is calculated by adding up the expected value a customer provides, which equates to summing all the revenue streams multiplied by their gross margins from a single customer. The found value is the profit obtained from a single customer over its customer lifetime. Generally, the LTV is taken from year 0 to year 5 of a customer lifetime. However, the cost of capital still needs to be subtracted. Investors partially carry the risk of the start-up and are recouped with interest on their investment.
A heuristic high level approximation for the customer LTV, in the case of a space agency customer and assuming no investment from entities other than ESA, would be calculated as follows. The one-time revenue for the instrument would be $30M\$$, with a guesstimated gross margin of 65%. The recurring revenue from maintenance contracts and data services is guesstimated to be $1M\$$ per year, with a profit margin of 80%. The assumption is made that only a single customer uses the service at a time, and this happens back-to-back every 3 years. The customer LTV would then equate to $21.9M\$$.

A rule of thumb for testing business viability is to make sure the customer LVT is at least 3 times the COCA [12]. The performed back of the envelope calculations of the customer LVT and the COCA show that in this case, the LVT is much larger than the COCA, even for the first customer. The resulting conclusion is, purely based on these guesstimated figures and assuming investment from ESA, that this is a viable business concept.

7.5. Conclusion & Recommendations

Starting with a space application of a technology is a business plan not often used in the industry from the outset. This explains in part the willingness of ESA to invest in and fund start-ups with their Business Incubation Centres, as this will increase the amount of products available to the public derived from space technology. As ESA is willing to invest in development of technology for space applications as well, this was deemed a relatively low-risk proving ground for the muon tomography instrument.
Subsequently, the gained experience and technical knowledge can be applied to an Earth application. Again,

European grants and investments from port authorities such as the Port of Rotterdam's "PortXL" innovation program could help accelerate development.
Based on the results from the research performed in this project, the conclusion is drawn that this is a viable business plan.

There are naturally quite a few caveats worth mentioning. The first is the limited scope of this project. The development of High-Tech requires a lot of investments of time and money, requiring a very well thought out business plan. Due to time constraints, a few untested key assumptions were made to create this chapter. The first key assumption is that ESA covers the development cost. This is true is some cases, but to what extent this process is funded is not yet known. It is recommended that this assumption is tested before any further steps are taken.
A second assumption is the willingness of ESA to fly an unproven instrument on a M-class or L-class mission. Some of these missions do contain technology demonstration hardware, but these instruments are rarely mission critical. It will require a leap of faith for ESA to include the instrument on their spacecraft, especially since this type of hardware is hard to validate in the radiation environment of Earth.
Thirdly, it is assumed that ESA will grant a licence to use the technology of the muon tomography instrument. Generally, the intellectual property of the technological development flows automatically to ESA when they are involved financially in the development process. Because one of the goals of ESA is to aid technological development, it is assumed the company will be allowed to use the technology for the Earth application.
The fourth assumption is that no part of the IP will belong to the Delft University of Technology. The scientific basis of the instrument was researched during a MSc Thesis project. This could complicate things legally and would therefore demand further investigation.
Lastly, it must be noted that R&D cost are not taken into account for the calculation of the customer LVT, whilst this forms a large portion of the total cost for High-Tech start-ups. In case external investments are required for the R&D process, the customer LVT would lower dramatically due to compounding interest, posing a risk to company viability. This should therefore be examined further in follow-up studies.

The personal reflection for the *Project Entrepreneurship Thesis Related* can be found in appendix C.

8

Conclusions & Recommendations

Many of the conclusions to the findings presented in this report are treated in their relevant chapters. This chapter contains the discussion of the research results and the conclusions that can be drawn from them, providing a concise overview and therefore forming the keystone to this entire thesis report. The first section 8.1 starts with a review of the original research questions, followed by the conclusions that were drawn from the findings in this project. The section subsequently treats the interpretations of the results and discusses the major findings of the research and simulations performed during the thesis project. The chapter concludes with recommendations and suggested future directions for new research on the topic, in section 8.2.

8.1. Conclusions & Discussion

To complete the literary circle of this report, the research questions posed in the introduction (chapter 1) are re-stated hereafter. The results and findings of the research performed over the course of the thesis project allow for at least a partial answering of all the following questions.

Review of Research Questions

Question 1. Which methods and techniques can be used to model small Solar System bodies for accurate particle transmission simulations?

The simulation toolkit *Geant4* chosen to simulate the passage of particles through matter requires the three dimensional asteroid model to be either hard-coded into the software, or read from a *GDML* geometry file. The choice fell on the latter, as this would provide the greatest amount of control for quick adjustments. The outer shape models for various comets and asteroids are available from NASA's Planetary Data System [85], and can be converted to the right format for *GDML* using the steps described in figure 3.5. As no direct information is available on the interior of these models, a system was created to adjust the interior according to many of the current hypotheses. A randomly distributed, spherical representation of the many monolithic structures and voids thought to be present within these small space bodies was chosen. Their composition, size and placement within the body can be adjusted by the user to fit the hypothesis to be tested. Additionally, a method to model a comet's tenuous coma was devised, as this gaseous atmosphere could influence the muon flux.

Question 1a. What are the interior characteristics of asteroids and comets?

Most asteroids and comets are thought to be so-called rubble-piles: loose agglomerates of monolithic boulders, regolith grains, dust and ices. Figure 3.1 graphically shows all the relevant terms. Sand-like regolith consists of very small dust and grains with void spaces in between. The larger monoliths can contain void spaces as well as round chondrules encased within. Macroscopic voids between such boulders are expected to exist. Comets additionally contain a large fraction of volatiles such as water ice, which lowers their average density compared to asteroids. The interior of these small Solar System bodies has thus far always been inferred from surface observations. The interior dynamics are poorly understood, but at least some form of convection or subduction is thought to take place. This creates a discrepancy between surface observations and interior characteristics, which is one of the reasons why not much is known of small Solar System body interiors.

Question 1b. Which simplifications can be made to the model to increase performance with minimal loss of accuracy?

The biggest performance increase was found when the model size was decreased. This did not reduce the accuracy, but did result in a decrease of realism. The use of a sphere to model the complex asteroid shape mainly improved the model creation performance. The simplification of homogeneous regolith as opposed to discrete grains creates a huge increase in both model creation and simulation performance, but also decreases the accuracy.

Question 1c. What are the characteristics of a comet's coma that are relevant to muon tomography?

The most important characteristic relating to muon tomography was deemed the density of the coma, more specifically the column density. Galactic cosmic rays can collide with particles in the coma, forming cosmic ray showers which produce muons. The limited range of muons caused by their short decay time, combined with the fact that most of a coma's column density is close to the surface as shown in figure 3.32, restricted the radius of interest for a coma to no more than $100km$. A coma is very heterogeneous spatially in density and composition, and shows a lot of temporal variations, all of which are deemed relevant to muon tomography.

Question 2. How can the radiation environment responsible for muon production around small Solar System bodies be simulated?

To answer this research question, extensive use was made of ESA's Space Environment Information System (SPENVIS) [69][105]. This online science interface hosts a tool to calculate the expected galactic cosmic flux at a defined location and time in the Solar System. The energy spectrum produced by this tool ($10^0 \sim 10^5 MeV$) displays a mismatch with the energy range of interest for muon tomography simulation in *Geant4*, which ranges from the significant maximum energy of back-scattered muons ($\sim 1GeV$) to the maximum energy allowed in a *Geant4* simulation ($\sim 100TeV$) for hadronic processes. To adjust the produced cosmic ray flux, the spectrum was limited on the lower end at $1GeV$, and extended using the differential spectral index $\alpha = -2.7$ to $100TeV$. This flux was subsequently converted to a macro file for use in *Geant4*, and the relevant normalisation factors were calculated. The flux particles are generated with isotropically distributed velocity vectors, originating from the interior surface of a sphere enveloping the asteroid model. Both the proton spectrum as well as the alpha particle spectrum are shown to effect the muon production, and both should therefore be simulated.

Question 2a. Which simplifications can be made to simulation parameters to increase performance with minimal loss of accuracy?

The use of *EMV* suffixed physics lists decreased the simulation time by as much as 25% at a relatively small cost of accuracy. Another simplification was the use of a detector with the same size as the subject volume, which greatly increased the muon count without reducing accuracy if the resulting counts are divided by its area. The biggest improvement in performance was the use of a pure muon source. This completely removed the connection with the cosmic ray spectrum and therefore all accuracy in that respect, but it was a very useful simplification for parameter studies.

Question 2b. What are the properties of the muon flux through a small Solar System body?

The muons are created in the upper surface layers of the SSSB, up to approximately $18m$ depth for the infrequent, high energy $100TeV$ protons in the galactic cosmic ray flux. Literature shows that the resulting muon flux is expected to be very small, varying from $1 \sim 2$ [109] to 1791 [125] per square meter per day, on the surface of a $100m$ diameter asteroid with a representative composition and density. The simulation results paint a similar picture with a muon count of $104 \sim 146$, closely matching the results presented in the oft-mentioned NASA report by T.H. Prettyman [187], as shown in table 6.1.

Question 2bi. How are the characteristics of the muon flux altered by various aspects of the small Solar System body interior?

Three fundamental muon flux characteristics are altered during the passage through the SSSB interior. The muons lose energy proportional to the amount of material they traverse. This energy loss scales with the material opacity, which is the density per unit length integrated over the total muon path length. Higher density and longer path lengths will result in larger energy losses experienced by the muon flux. Through this

process, muons can reach a critical energy at which they are no longer able to traverse the material and either decay or are absorbed. This alters the quantity of muons surviving the journey, with less muons for higher densities and longer path lengths. The third property altered by the interior is the flux' velocity vector angle. The amount by which this value is changed through a process called scattering, is governed not only by the flux properties and material density, but by atomic number and atomic mass number as well. This causes the flux to scatter more in a material with heavier atoms as compared to a material similar in density.

> *Question 3. How can the interior characteristics of a small Solar System body be reconstructed from muographic measurements?*

Since the incoming galactic cosmic ray spectrum arrives from isotropic distributed angles, deviations from this distribution in the outgoing muon flux are caused by SSSB interior features. Both the muon count as well as the muon energy is indicative of the opacity of the material it traversed. By reconstructing the path each muon is thought to have followed, a three dimensional density model can be constructed. Deviations for the expected angles at which the muons arrive can be used to determine the average atomic number and atomic mass number of the material in this model.

> *Question 3a. Which current algorithms and techniques are best fit to reconstruct the interior of a muographically mapped small Solar System body?*

The technique best suited depends heavily on the amount of data to work with. When a large sample set is available, commonly used tomographic reconstruction techniques such as Back Projection and Filtered Back Projection can be employed. For sparse data, a technique called Straight Track Fitting is shown to produce promising results. Another auspicious technique makes use of the up-and-coming applications of artificial intelligence. Unsupervised machine learning shows to be able to interpret data features from very small sample-sets without the need of training data, making it a prime candidate for reconstruction activities.

> *Question 3b. Can the interior characteristics of an asteroid model be reconstructed from particle transmission simulation results?*

Yes. This report unequivocally demonstrated that this, based on *Geant4* simulation results, is possible. The simulations in this report did however rely on best case scenarios, with high contrast between density regions and rather large muon counts due to the small asteroid size. Nonetheless, this proves the feasibility of asteroid muon tomography as a concept.

> *Question 4. Which constraints and requirements imposed by muon tomography are put on key design aspects of a space mission to a small Solar System body?*

It is clear that due to the less than desirable muon flux near SSSBs and the realistic limitations on detector size and mass, a long integration time would be required. This removed the possibility of a fly-by mission. To increase the flux as much as possible, it is favourable to use a large detector area, close to the SSSB surface. The SSSB size is limited to a few hundred metres, the larger this diameter the longer integration times are required.

> *Question 4a. What type and size of small Solar System bodies are best suited to tomographically map using a hodoscopic muon instrument?*

The diameter of an asteroid with a density of $1.9 g/cm^3$ is realistically limited to a few hundred metres. For larger diameters, only a single muon per day flux is expected for a square meter detector, as shown in table 6.1. Large density contrasts would nonetheless still be resolvable in such a scenario, depending on the amount of integration time.
On the other end of the spectrum, one could define a realistic minimum asteroid size for muon tomography. Based on asteroid lightcurve data, presented in figure 2.6, it is concluded that most asteroids with a diameter $< 120m$ are monoliths [231]. These are subsequently assumed to have a higher average density than rubble-piles and less interior composition variation, which makes them less suitable for muon tomography. Additionally, their much higher spin rates not only complicates the reconstruction process, it also restricts the feasible landing sites for a lander/rover mission to the poles. Seeing as measurements from multiple angles are preferred, a hopping rover would have to anchor itself to the surface after every hop, greatly decreasing the feasibility of such a mission.
Comets, due to their much lower density, could prove to be a better suited target for this technology, as larger diameters would still be feasible. The effect of their coma on the muon production and the variability thereof would need the be resolved in detail, which complicates this specific application.

Question 4b. What instrument characteristics are required to fulfil a small Solar System body muon tomography mission?

A square meter detector area is shown to detect enough muons for the reconstruction of high contrast regions in a ten meter diameter asteroid, from a mere quarter second of integration time. For larger SSSB, an as large as possible detector area is trade off with required integration time. The instrument should be able to resolve the incoming muon's trajectory, its energy, and discriminate it against background radiation.

Question 4c. What are the differences in performance between the application of a micro- or nanosatellite platform, versus a conventional spacecraft platform?

For a performance evaluation, both platforms were assessed in chapter 5. For the assessment it was assumed based on spaceflight heritage that a micro- or nanosatellite platform used on an asteroid or comet mission would be a secondary, lander-type spacecraft. At the lowest thus far achieved orbit altitude around an SSSB, a primary orbiting spacecraft would receive only 18% the muon flux of what a lander would receive. A detector area one-fifth the size of that on the primary spacecraft would therefore still experience a higher muon flux. Although a lander brings extra complications to the envisioned mission, this flux increase combined with the longer integration time possible close to the surface puts this solution ahead.

Conclusions
Based on the research question answers, as well as additional findings and results, a few major conclusions can be drawn. As this project is a feasibility study at heart, the nature of these conclusions will lie more towards qualitative validity instead of exact numerical conclusions. The following list sums up these conclusion:

- the application of muon tomography technology in space, to detect small Solar System body interior features, is feasible;
- the preferred location for the instrument is as close to the surface as possible, imaging the body through along a minor axis;
- a good technique to resolve interior features from sparse muon data is straight track fitting;
- accurate and plentiful reference data from simulations with homogeneous asteroid models is required to increase the statistical confidence level of density variations inferred from in-situ measurement data;
- alpha particles in the GCR flux positively increase the muon flux by 35% and therefore increase the feasibility of a muon tomography mission;
- feasible muon tomography target asteroids range from approximately $\sim 120m$ to $\sim 500m$ in diameter, with a strong preference towards the lower end of this range;
- feasible muon tomography target comets extend the aforementioned range towards larger diameters due to their lower density.

The latter two conclusions carry a few caveats worth mentioning. The mentioned limits for asteroid diameters are not absolute limits, but rather a logical conclusion from the presented data. Naturally, not all sub $120m$ asteroids are monolithic, but since most of them seem to be solid based on the limited available data, this value was chosen. Similarly, the $500m$ is chosen as the limit as this is shown to marginally result in a high enough muon flux for some tomography to be performed, but this is once again not a hard limit.
Comets are mentioned to be feasible targets, with their lower density aiding this feasibility. However, the effect of a comet's coma is approximated based on models and measurements which were not all validated. Although it looks like the presence of a coma would only increase the muon flux, this is not proven unequivocally and therefore omitted from the conclusion.

Discussion
While the single most important result of this thesis project is the determination of the feasibility of a muon tomography mission, it is worth discussing some of the collateral findings. It was found that including the alpha particle flux present in the galactic cosmic ray spectrum, increases the muon flux noticeably. As these particles were omitted in previous simulations performed in other studies [187][109], the approximately 35%

increase in muon flux increases the perceived feasibility significantly.
Another interesting finding was the discrepancy in muon flux at different altitudes as compared to other literature. The resulting muon flux in this research decreased, on average, proportional to the square of the altitude of the detector, as is expected. The results of D. Hodge [109] show variations in flux for different altitudes, prompting his recommendation for the determination of a "sweet-spot". The increase in muon flux at some higher altitudes is a very counter-intuitive result. Although it does not definitive disproof that such a phenomenon exits, two empirical deductions are made to try and explain this discrepancy.
One possible cause of the variation found by Hodge might be the use of the standard "random seed" used by *Geant4*. For small sample sets this would result in great variability between simulation runs, not altitude dependant but rather "run-dependant".
Another cause could be the very small data-set the conclusion was based on. Without the averaging effects of large data-sets, certain sweet-spots could arise where multiple muon paths intersect in space. These sweet-spots are consequently thought to only exist in the simulation they are based on, and are thought move or disappear altogether if the simulation run was extended or a different initial seed was used. The search for this sweet-spot was subsequently called off as no increase in muon flux was found at higher altitudes.
An unexpected result, discussed in the verification and validation chapter 6, showed a discrepancy in the charge ratio of the low energy muons. As these muons are mostly below the threshold of $1GeV$ used to discriminate against backscattered muons, this charge ratio discrepancy is not of importance to muon tomography. It is however indicative of a not yet understood process taking place in the *Geant4* simulation, which is worth researching.
All in all the simulation results are shown to be in line with the findings by T.H. Prettyman [187].

8.2. Recommendations

Due to the limited resources available for this research project, quite a few simplifications had to be made to get enlightening results. Naturally, it is recommended that future research with more resources at its disposal would revert to more realistic models. The accurate three-dimensional models of an asteroid an a comet presented in the modelling chapter 3 would result in the most realistic simulation setup to date, but would require the simulation to be run on a system with modern workstation performance or better.
The design and modelling of a muon detecting instrument would further increase the accuracy of the simulation, as *Geant4* allows for the testing of detectors as well. Seeing as this research assumed a 100% muon detection efficiency, quantifying this value and optimising for it is a logical next step in muon tomography research. This is especially true for the instrument on a lander configuration, seeing as how the aperture of this instrument would have to be huge to accept muons from all possible angles.
With the recent arrival of the sub-surface sample of 162173 Ryugu on-board the Hayabusa 2 mission, as well as the impending arrival of a surface sample of 101955 Bennu on-board OSIRIS-REx, an increased amount of information will become available on asteroid composition. It is recommended that the asteroid simulation models are adjusted to these findings.
Additionally, the inclusions and voids in the SSSB models were modelled using a spherical representation. Section 3.1.4 shows that, based on literature, boulders created in fragmentation events generally assume an aspect ratio of 1 : 0.7 : 0.5 (Length:Width:Height). To further increase the model accuracy, the monolithic spherical inclusions should be replaced by these tri-axial ellipsoid shapes.
Similarly, the presented models should be adjusted to include a physically porous top-layer of $18m$ in depth, as this is demonstrated to affect and increase the muon flux. Although mineral structures do not seem to effect the passage of muons through the asteroid, rare scintillation effects could prove otherwise and should therefore be included in the model as well.
A final recommendation is to test the waters of neural networks and machine learning, applied to asteroid interior reconstruction from muon tomography data. These artificial intelligence methods could prove to play a pivotal role in future missions, enabling to resolve detail from sparse data where conventional methods fail to do so.

A

Solar System

Group	Sub-Group	Sub-Group	Sub-Group	Types	Orbit [AU]
Inner Solar System	Sun	-	-	Star	0
Inner Solar System	Mercury	-	-	Planet	0.4
Inner Solar System	Venus	-	-	Planet	0.7
Inner Solar System	NEOs	NEAs	Atiras	Asteroids	<0.983
Inner Solar System	NEOs	NEAs	Atens	Asteroids	<0.983&>1.017
Inner Solar System	Earth	-	-	Planet	$0.983 < x < 1.017$
Inner Solar System	NEOs	NEAs	Apollos	Asteroids	<0.983&>1.017
Inner Solar System	NEOs	NEAs	Amors	Asteroids	1.017<x<1.3
Inner Solar System	NEOs	NECs	-	Comets	-
Inner Solar System	Mars	-	-	Planet	1.5
Inner Solar System	Main Belt	-	-	SSSBs/ Dwarf Planet	2.2-3.3
Inner Solar System	Main Belt	Hildas	-	SSSBs	3.7-4.2
Inner Solar System	Trojans	-	-	SSSBs	5.2
Outer Solar System	Jupiter	-	-	Planet	5.2
Outer Solar System	Saturn	-	-	Planet	9.5
Outer Solar System	Uranus	-	-	Planet	19.2
Outer Solar System	Centaurs	-	-	SSSBs	5.5-30
Outer Solar System	Neptune	-	-	Planet	30.1
Trans-Neptunian	TNOs	KBOs	Classical	SSSBs/ Dwarf Planet	39.4-47.7
Trans-Neptunian	TNOs	KBOs	Resonant	SSSBs/ Dwarf Planet	30-50
Trans-Neptunian	TNOs	SDOs	-	SSSBs/ Dwarf Planet	30-200
Interstellar Space	TNOs	Oort Cloud	-	SSSBs	$1 \cdot 10^3 - 2 \cdot 10^5$

B

Comparison between model and reconstruction.

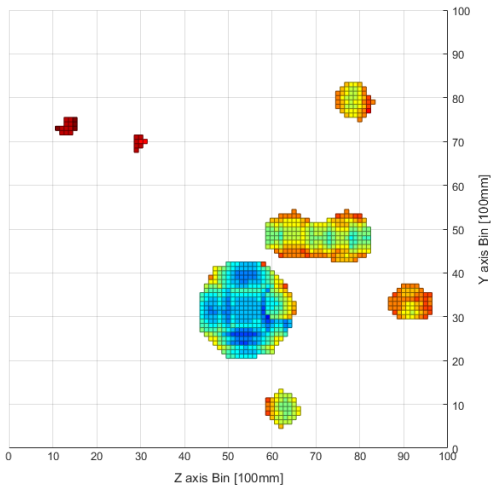

(a) Reconstruction from simulation data.

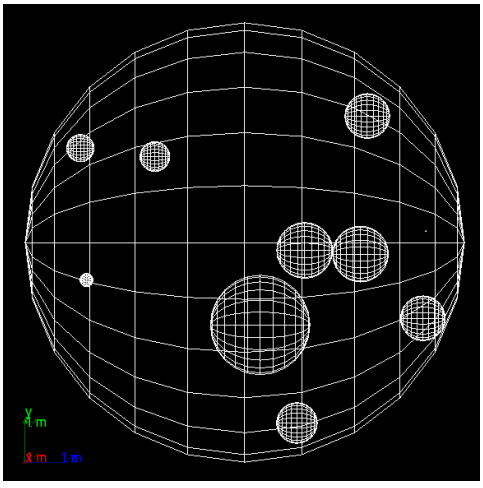

(b) 2D view of GDML model in *Geant4*.

Figure B.1: Comparison between 3D model showing spherical inclusions, and inclusion reconstruction from particle simulation results, along $X - axis$.

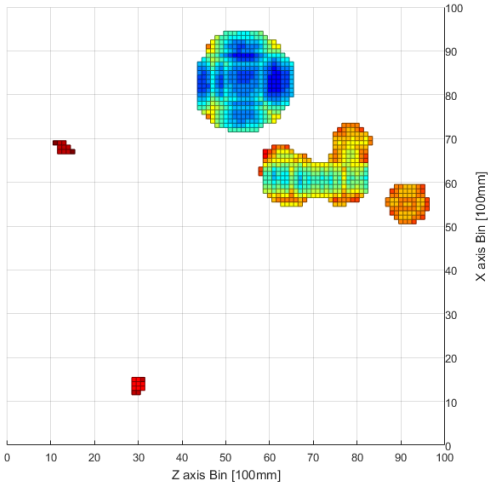

(a) Reconstruction from simulation data.

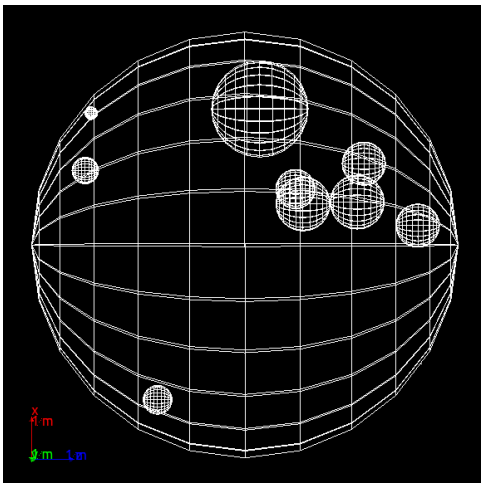

(b) 2D view of GDML model in *Geant4*.

Figure B.2: Comparison between 3D model showing spherical inclusions, and inclusion reconstruction from particle simulation results, along $Y-axis$.

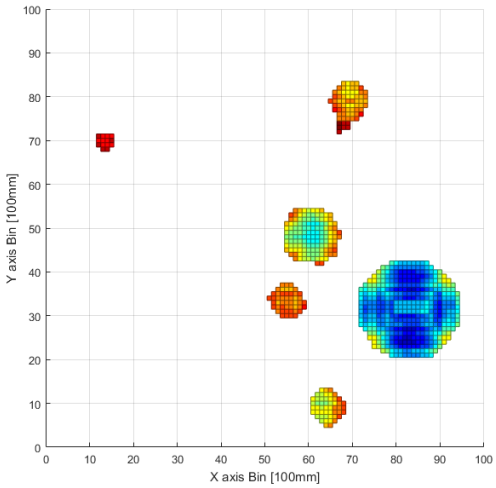

(a) Reconstruction from simulation data.

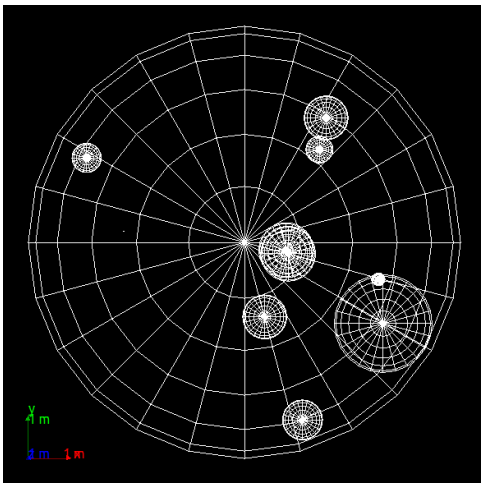

(b) 2D view of GDML model in *Geant4*.

Figure B.3: Comparison between 3D model showing spherical inclusions, and inclusion reconstruction from particle simulation results, along $Z-axis$.

C

Entrepreneurship: Personal Reflection

The *Project Entrepreneurship Thesis Related* was one of the most enjoyable projects of the entire annotation. It required me to put everything I have learned from the annotation courses to use in one final project. This was especially true since I could apply the knowledge to a subject of my own choosing. Unfortunately, the onset of the COVID-19 pandemic limited the research possibilities, as I would have liked to go to ESTEC and interview the ESA scientists and engineers face-to-face. Luckily, I managed to get an interview with Dr. Michael Küppers and Dr. Alessandra Menicucci, who were very kind and helpful in answering all my questions using a video link. I noticed that they both enjoyed discussing the entrepreneurial tangent to their day-to-day work. Similarly, I would like to thank Dr. L. (Dap) Hartmann for the inspiring talks on the matter. It was an eye-opener to step away from the science and product capabilities, and instead learn to focus on the entrepreneurial job at hand. This aided me through the process of business plan creations better than any book or course would.
The *Project Entrepreneurship Thesis Related* was performed in part simultaneously with the main thesis project, which complicates the calculation of time spend on the subject. The two interviews and other meetings add up to about a day in preparation and execution time. The research plan and proposal similarly took a few days to formulate, with an additional few hours of brainstorming and literature search. The project itself took quite a bit longer. This was caused in part due to regulatory complications, such as gaining approval to include the deliverable as a chapter in the main thesis and discovering whom is supposed to grade the document. Another cause was my own difficulty with the fast switching from a purely scientific mindset employed during the main thesis project, to a more pragmatic entrepreneurial mindset for the entrepreneurship project. Naturally, the main contributors to the time spend were the literature research, the plan development, the creation of visual aids and the writing of the chapter. All in all, the entire project is estimated to have taken four full-time weeks to complete.

Bibliography

[1] S. Abe, T. Mukai, N. Hirata, O. S. Barnouin-Jha, A. F. Cheng, H. Demura, R. W. Gaskell, T. Hashimoto, K. Hiraoka, T. Honda, T. Kubota, M. Matsuoka, T. Mizuno, R. Nakamura, D. J. Scheeres, and M. Yoshikawa. Mass and local topography measurements of itokawa by hayabusa. *Science*, 312(5778): 1344–1347, jun 2006. doi: 10.1126/science.1126272.

[2] M. Aguilar, J. Alcaraz, J. Allaby, and et al. A study of cosmic ray secondaries induced by the mir space station using AMS-01. *Nuclear Instruments and Methods in Physics Research Section B: Beam Interactions with Materials and Atoms*, 234(3):321–332, jun 2005. doi: 10.1016/j.nimb.2005.01.015.

[3] K. Amako, S. Guatelli, V. Ivanchencko, M. Maire, B. Mascialino, K. Murakami, L. Pandola, S. Parlati, M.G. Pia, M. Piergentili, T. Sasaki, and L. Urban. Geant4 and its validation. *Nuclear Physics B - Proceedings Supplements*, 150:44–49, jan 2006. doi: 10.1016/j.nuclphysbps.2004.10.083.

[4] American Immigration Council. The cost of immigration enforcement and border security. :https://www.americanimmigrationcouncil.org/research/the-cost-of-immigration-enforcement-and-border-security, July 2020.

[5] Carl D. Anderson. The positive electron. *Physical Review*, 43(6):491–494, mar 1933. doi: 10.1103/physrev.43.491.

[6] J. Apostolakis, G. Folger, V. Grichine, A. Howard, V. Ivanchenko, M. Kosov, A. Ribon, V. Uzhinsky, and D. H. Wright. GEANT4 physics lists for HEP. In *2008 IEEE Nuclear Science Symposium Conference Record*. IEEE, oct 2008. doi: 10.1109/nssmic.2008.4774655.

[7] J Apostolakis, A Bagulya, S Elles, V N Ivanchenko, J Jacquemier, M Maire, T Toshito, and L Urban. Validation and verification of geant4 standard electromagnetic physics. *Journal of Physics: Conference Series*, 219(3):032044, apr 2010. doi: 10.1088/1742-6596/219/3/032044.

[8] Juan Carlos Arteaga-Velázquez, Karen Salomé Caballero Mora, David Curtin, Arturo Fernández Téllez, M. Rodríguez Cahuantzi, and Martin Alfonso Subieta Vásqueze. Cosmic ray physics at mathusla. resreport, Instituto de Física y Matemáticas, Universidad Michoacana, Morelia, México, April 2018. `https://twiki.cern.ch/twiki/pub/MATHUSLA/MATHUSLAPublic/cosmic-ray-physics_MATHUSLA.pdf`.

[9] E. Asphaug and W. Benz. Density of comet shoemaker-levy 9 deduced by modelling breakup of the parent 'rubble pile'. *Nature*, 370(6485):120–124, jul 1994. doi: 10.1038/370120a0.

[10] Erik Asphaug and Willy Benz. Size, density, and structure of comet shoemaker–levy 9 inferred from the physics of tidal breakup. *Icarus*, 121(2):225–248, 1996.

[11] ATLAS Collaboration. *ATLAS detector and physics performance: Technical Design Report, 1*. Technical Design Report ATLAS. CERN, Geneva, 1999. URL `http://cds.cern.ch/record/391176`.

[12] Bill Aulet. *Disciplined entrepreneurship: 24 steps to a successful startup*. John Wiley & Sons, 2013.

[13] G.D Badhwar, A.G Truong, P.M O'Neill, and Vitaly Choutko. Validation of the galactic cosmic ray and geomagnetic transmission models. *Radiation Measurements*, 33(3):361–367, jun 2001. doi: 10.1016/s1350-4487(00)00166-9.

[14] Adriano Campo Bagatin, Rafael A. Alemañ, Paula G. Benavidez, Manuel Pérez-Molina, and Derek C. Richardson. Gravitational re-accumulation as the origin of most contact binaries and other small body shapes. *Icarus*, 339:113603, mar 2020. doi: 10.1016/j.icarus.2019.113603.

[15] Enrico Bagli, Makoto Asai, Andrea Dotti, Luciano Pandola, and Marc Verderi. Allowing for crystalline structure effects in geant4. *Nuclear Instruments and Methods in Physics Research Section B: Beam Interactions with Materials and Atoms*, 402:304–307, jul 2017. doi: 10.1016/j.nimb.2017.03.092.

[16] R.-L. Ballouz, D.C. Richardson, P. Michel, S.R. Schwartz, and Y. Yu. Numerical simulations of collisional disruption of rotating gravitational aggregates: Dependence on material properties. *Planetary and Space Science*, 107:29–35, mar 2015. doi: 10.1016/j.pss.2014.06.003.

[17] Anaïs Bardyn, Donia Baklouti, Hervé Cottin, Nicolas Fray, Christelle Briois, John Paquette, Oliver Stenzel, Cécile Engrand, Henning Fischer, Klaus Hornung, Robin Isnard, Yves Langevin, Harry Lehto, Léna Le Roy, Nicolas Ligier, Sihane Merouane, Paola Modica, François-Régis Orthous-Daunay, Jouni Rynö, Rita Schulz, Johan Silén, Laurent Thirkell, Kurt Varmuza, Boris Zaprudin, Jochen Kissel, and Martin Hilchenbach. Carbon-rich dust in comet 67p/churyumov-gerasimenko measured by COSIMA/rosetta. *Monthly Notices of the Royal Astronomical Society*, 469(Suppl_2):S712–S722, jul 2017. doi: 10.1093/mnras/stx2640.

[18] Walter H. Barkas, Wallace Birnbaum, and Frances M. Smith. Mass-ratio method applied to the measurement ofL-meson masses and the energy balance in pion decay. *Physical Review*, 101(2):778–795, jan 1956. doi: 10.1103/physrev.101.778.

[19] T. J. Bayer, Seung Chung, B. Cole, B. Cooke, F. Dekens, C. Delp, I. Gontijo, K. Lewis, M. Moshir, R. Rasmussen, and D. Wagner. Model based systems engineering on the europa mission concept study. In *2012 IEEE Aerospace Conference*. IEEE, mar 2012. doi: 10.1109/aero.2012.6187337.

[20] Zane W Bell. Scintillation counters. In *Handbook of Particle Detection and Imaging*, pages 349–375. Springer Berlin Heidelberg, 2012. doi: 10.1007/978-3-642-13271-1_15.

[21] W. Benz and E. Asphaug. Simulations of brittle solids using smooth particle hydrodynamics. *Computer Physics Communications*, 87(1-2):253–265, may 1995. doi: 10.1016/0010-4655(94)00176-3.

[22] V. Bindi, G.M. Chen, H.S. Chen, E. Choumilov, V. Choutko, A. Contin, A. Lebedev, Y.S. Lu, N. Masi, A. Oliva, F. Palmonari, L. Quadrani, and Q. Yan. Calibration and performance of the AMS-02 time of flight detector in space. *Nuclear Instruments and Methods in Physics Research Section A: Accelerators, Spectrometers, Detectors and Associated Equipment*, 743:22–29, apr 2014. doi: 10.1016/j.nima.2014.01.002.

[23] Richard P. Binzel, Andrew S. Rivkin, Schelte J. Bus, Jessica M. Sunshine, and Thomas H. Burbine. MUSES-c target asteroid (25143) 1998 SF36: A reddened ordinary chondrite. *Meteoritics & Planetary Science*, 36(8):1167–1172, aug 2001. doi: 10.1111/j.1945-5100.2001.tb01950.x.

[24] Richard P. Binzel, Ettore Perozzi, Andrew S. Rivkin, Alessandro Rossi, Alan W. Harris, Schelte J. Bus, Giovanni B. Valsecchi, and Stephen M. Slivan. Dynamical and compositional assessment of near-earth object mission targets. *Meteoritics & Planetary Science*, 39(3):351–366, mar 2004. doi: 10.1111/j.1945-5100.2004.tb00098.x.

[25] Blender Online Community. *Blender - a 3D modelling and rendering package*. Blender Foundation, Stichting Blender Foundation, Amsterdam, 2020. URL `http://www.blender.org`.

[26] Dominique Bockelée-Morvan. An overview of comet composition. *Proceedings of the International Astronomical Union*, 7(S280):261–274, jun 2011. doi: 10.1017/s1743921311025038.

[27] Dominique Bockelée-Morvan, J Crovisier, MJ Mumma, and HA Weaver. *Comets II*, volume 1, chapter The composition of cometary volatiles, pages 391–423. University of Arizona Press, 2004.

[28] Hermann Boehnhardt, Jean-Pierre Bibring, Istvan Apathy, Hans Ulrich Auster, Amalia Ercoli Finzi, Fred Goesmann, Göstar Klingelhöfer, Martin Knapmeyer, Wlodek Kofman, Harald Krüger, Stefano Mottola, Walter Schmidt, Klaus Seidensticker, Tilman Spohn, and Ian Wright. The philae lander mission and science overview. *Philosophical Transactions of the Royal Society A: Mathematical, Physical and Engineering Sciences*, 375(2097):20160248, may 2017. doi: 10.1098/rsta.2016.0248.

[29] A. Bolshakova, , I. Boyko, G. Chelkov, D. Dedovitch, A. Elagin, M. Gostkin, A. Grishin, A. Guskov, Z. Kroumchtein, Yu. Nefedov, K. Nikolaev, A. Zhemchugov, F. Dydak, J. Wotschack, A. De Min, V. Ammosov, V. Gapienko, V. Koreshev, A. Semak, Yu. Sviridov, E. Usenko, and V. Zaets. Comparison of geant4 hadron generation with data from the interactions with beryllium nuclei of 8.9 gev/c protons and pions and 8.0 gev/c pions. *The European Physical Journal C*, 56(3):323–332, aug 2008. doi: 10.1140/epjc/s10052-008-0679-2.

[30] Konstantin N. Borozdin, Gary E. Hogan, Christopher Morris, William C. Priedhorsky, Alexander Saunders, Larry J. Schultz, and Margaret E. Teasdale. Radiographic imaging with cosmic-ray muons. *Nature*, 422(6929):277–277, mar 2003. doi: 10.1038/422277a.

[31] Edward Bowell, Clark R. Chapman, Jonathan C. Gradie, David Morrison, and Benjamin Zellner. Taxonomy of asteroids. *Icarus*, 35(3):313–335, sep 1978. doi: 10.1016/0019-1035(78)90085-4.

[32] J.C. Bridges, H.G. Changela, S. Nayakshin, N.A. Starkey, and I.A. Franchi. Chondrule fragments from comet wild2: Evidence for high temperature processing in the outer solar system. *Earth and Planetary Science Letters*, 341-344:186–194, aug 2012. doi: 10.1016/j.epsl.2012.06.011.

[33] D. T. Britt and G. J. S. J. Consolmagno. Stony meteorite porosities and densities: A review of the data through 2001. *Meteoritics & Planetary Science*, 38(8):1161–1180, aug 2003. doi: 10.1111/j.1945-5100.2003.tb00305.x.

[34] Dan T Britt, Don Yeomans, Kevin Housen, and G Consolmagno. Asteroid density, porosity, and structure. 2003.

[35] R Brun, R Hagelberg, M Hansroul, and J C Lassalle. *Simulation program for particle physics experiments, GEANT: user guide and reference manual*. CERN, Geneva, 1978. URL `https://cds.cern.ch/record/118715`.

[36] R Brun, F Bruyant, M Maire, A C McPherson, and P Zanarini. *GEANT 3: user's guide Geant 3.10, Geant 3.11; rev. version*. CERN, Geneva, 1987. URL `https://cds.cern.ch/record/1119728`.

[37] Albino Carbognani. The spin-barrier ratio for s and c-type main asteroids belt. *Planetary and Space Science*, 147:1–5, nov 2017. doi: 10.1016/j.pss.2017.07.019.

[38] Kieran Carroll. Astrorecon asteroid surface gravimetry presentation. `https://www.researchgate.net/publication/271373015_201501_AstroRecon_Asteroid_Surface_Gravimetry_presentation`, January 2015.

[39] Kieran A. Carroll. Asteroid and comet surface gravimetric surveying can reveal interior structural details. In *Conference on Spacecraft Reconnaissance of Asteroid and Comet Interiors*, number 1829, page 8, 3600 Bay Area Boulevard Houston TX 77058-1113, 2015. Lunar and Planetary Institute.

[40] B. Carry. Density of asteroids. *Planetary and Space Science*, 73(1):98–118, dec 2012. doi: 10.1016/j.pss.2012.03.009.

[41] A Cellino, SJ Bus, A Doressoundiram, D Lazzaro, et al. *Asteroids III*, volume 1, chapter Spectroscopic properties of asteroid families, pages 633–643. University of Arizona Press, Tucson, 2002.

[42] Clark R. Chapman, David Morrison, and Ben Zellner. Surface properties of asteroids: A synthesis of polarimetry, radiometry, and spectrophotometry. *Icarus*, 25(1):104–130, may 1975. doi: 10.1016/0019-1035(75)90191-8.

[43] Nishant Chaudhary, Dhritiman Bhattacharjee, V. Yadav, S.D. Sharma, Shuvajit Acharya, Kapil Dixit, and K.C. Mittal. Monte carlo simulation and measurement of x-ray dose from 9 mev rf electron linac for cargo scanning. *Indian Journal of Pure and Applied Physics*, 50:517–519, 07 2012.

[44] A.F. Cheng, J. Atchison, B. Kantsiper, A.S. Rivkin, A. Stickle, C. Reed, A. Galvez, I. Carnelli, P. Michel, and S. Ulamec. Asteroid impact and deflection assessment mission. *Acta Astronautica*, 115:262–269, oct 2015. doi: 10.1016/j.actaastro.2015.05.021.

[45] Adrian Cho. Two billion dollar cosmic ray detector confirms possible signs of dark matter. : https://www.sciencemag.org/news/2013/04/two-billion-dollar-cosmic-ray-detector-confirms-possible-signs-dark-matter, April 2013.

[46] Mathieu Choukroun, Kathrin Altwegg, Ekkehard Kührt, Nicolas Biver, Dominique Bockelée-Morvan, Joanna Drążkowska, Alain Hérique, Martin Hilchenbach, Raphael Marschall, Martin Pätzold, Matthew G. G. T. Taylor, and Nicolas Thomas. Dust-to-gas and refractory-to-ice mass ratios of comet 67p/churyumov-gerasimenko from rosetta observations. *Space Science Reviews*, 216(3), apr 2020. doi: 10.1007/s11214-020-00662-1.

[47] P. R. Christensen, V. E. Hamilton, G. L. Mehall, D. Pelham, W. O'Donnell, S. Anwar, H. Bowles, S. Chase, J. Fahlgren, Z. Farkas, T. Fisher, O. James, I. Kubik, I. Lazbin, M. Miner, M. Rassas, L. Schulze, K. Shamordola, T. Tourville, G. West, R. Woodward, and D. Lauretta. The OSIRIS-REx thermal emission spectrometer (OTES) instrument. *Space Science Reviews*, 214(5), jul 2018. doi: 10.1007/s11214-018-0513-6.

[48] B. Christophe, B. Foulon, F. Liorzou, V. Lebat, D. Boulanger, P.-A. Huynh, N. Zahzam, Y. Bidel, and A. Bresson. Status of development of the future accelerometers for next generation gravity missions. In *International Symposium on Advancing Geodesy in a Changing World*, pages 85–89. Springer International Publishing, 2018. doi: 10.1007/1345_2018_42.

[49] R. Chytracek, J. Mccormick, W. Pokorski, and G. Santin. Geometry description markup language for physics simulation and analysis applications. *IEEE Transactions on Nuclear Science*, 53(5):2892–2896, oct 2006. doi: 10.1109/tns.2006.881062.

[50] Paolo Cignoni, Marco Callieri, Massimiliano Corsini, Matteo Dellepiane, Fabio Ganovelli, and Guido Ranzuglia. Meshlab: an open-source mesh processing tool, 2008.

[51] Michael R Combi, Walter M Harris, and William H Smyth. *Comets II*, volume 1, chapter Gas dynamics and kinetics in the cometary coma: Theory and observations, pages 523–552. University of Arizona Press, 2004.

[52] United States Nuclear Regulatory Commission. Nrc picture of cerenkov radiation surrounding the underwater core of the reed research reactor, reed college, oregon, usa. `https://commons.wikimedia.org/wiki/File:Cerenkov_Effect.jpg`, November 2007. Public Domain.

[53] G.J. Consolmagno, D.T. Britt, and R.J. Macke. The significance of meteorite density and porosity. *Geochemistry*, 68(1):1–29, apr 2008. doi: 10.1016/j.chemer.2008.01.003.

[54] JF Crifo, F Fulle, NI Kömle, and K Szego. *Comets II*, chapter Nucleus-coma structural relationships: lessons from physical models, pages 471–503. University of Arizona Press, 2004.

[55] Lloyd A Currie. Nomenclature in evaluation of analytical methods including detection and quantification capabilities (iupac recommendations 1995). *Pure and applied chemistry*, 67(10):1699–1723, 1995.

[56] M. G. Daly, O. S. Barnouin, C. Dickinson, J. Seabrook, C. L. Johnson, G. Cunningham, T. Haltigin, D. Gaudreau, C. Brunet, I. Aslam, A. Taylor, E. B. Bierhaus, W. Boynton, M. Nolan, and D. S. Lauretta. The OSIRIS-REx laser altimeter (OLA) investigation and instrument. *Space Science Reviews*, 212(1-2):899–924, aug 2017. doi: 10.1007/s11214-017-0375-3.

[57] G. Danby, J-M. Gaillard, K. Goulianos, L. M. Lederman, N. Mistry, M. Schwartz, and J. Steinberger. Observation of high-energy neutrino reactions and the existence of two kinds of neutrinos. *Physical Review Letters*, 9(1):36–44, jul 1962. doi: 10.1103/physrevlett.9.36.

[58] Mathieu de Naurois and Daniel Mazin. Ground-based detectors in very-high-energy gamma-ray astronomy. *Comptes Rendus Physique*, 16(6-7):610–627, aug 2015. doi: 10.1016/j.crhy.2015.08.011.

[59] P. S. Decarli, E. Bowden, and L. Seaman. Shock-induced compaction and porosity in meteorites. *Meteoritics & Planetary Science*, 36(9):A47, September 2001.

[60] Decision Sciences. Press releases. : https://decisionsciences.com/category/press-releases, April 2017.

[61] Jakob Deller. *Introduction*, pages 1–48. Springer International Publishing, 2017. ISBN 978-3-319-47985-9. doi: 10.1007/978-3-319-47985-9_1.

[62] Department of Homeland Security. Fiscal year 2019 budget-in-brief. :https://www.dhs.gov/publication/fy-2019-budget-brief, 2019.

[63] P. A. M. Dirac. The quantum theory of the electron. *Proceedings of the Royal Society A: Mathematical, Physical and Engineering Sciences*, 117(778):610–624, feb 1928. doi: 10.1098/rspa.1928.0023.

[64] Line Drube, Alan W. Harris, Kilian Engel, Albert Falke, Ulrich Johann, Siegfried Eggl, Juan L. Cano, Javier Martín Ávila, Stephen R. Schwartz, and Patrick Michel. The NEOTωIST mission (near-earth object transfer of angular momentum spin test). *Acta Astronautica*, 127:103–111, oct 2016. doi: 10.1016/j.actaastro.2016.05.009.

[65] Anton I. Ermakov, Maria T. Zuber, David E. Smith, Carol A. Raymond, Georges Balmino, Roger R. Fu, and Boris A. Ivanov. Constraints on vesta's interior structure using gravity and shape models from the dawn mission. *Icarus*, 240:146–160, sep 2014. doi: 10.1016/j.icarus.2014.05.015.

[66] ESA. Future missions department. :https://sci.esa.int/web/future-missions-department/, December 2020.

[67] ESA - European Space Agency. Comet activity, 21 june. :https://www.esa.int/var/esa/storage/images/esa_multimedia/images/2015/06/comet_activity_21_june/15497201-1-eng-GB/Comet_activity_21_June.jpg, June 2015.

[68] ESA/ESTEC Space Environment and Effects Section (TEC-EPS) and Belgian Institute for Space Aeronomy (BIRA-IASB). Geant4 source particles. :https://www.spenvis.oma.be/help/models/g4_source_new.html, April 2018.

[69] ESA/ESTEC Space Environment and Effects Section (TEC-EPS) and Belgian Institute for Space Aeronomy (BIRA-IASB). Gcr fluxes near earth. :https://www.spenvis.oma.be/help/background/gcr/gcr.html, March 2018.

[70] ESA/Rosetta/MPS for OSIRIS Team MPS/UPD/LAM/IAA/SSO/INTA/UPM/DASP/IDA. Measuring comet 67p/c-g. `http://blogs.esa.int/rosetta/2014/10/03/measuring-comet-67pc-g/`, October 2014.

[71] D.C. Richardson et al. Dynamical and physical properties of 65803 didymos, the proposed aida mission target. In *AAS/Division for Planetary Sciences Meeting Abstracts, nr 48*, volume 48, 2016.

[72] A. Aab et al.; The Pierre Auger Colleboration. Observation of a large-scale anisotropy in the arrival directions of cosmic rays above $8{\cdot}10^{18} ev$. *Science*, 357(6357):1266–1270, sep 2017. doi: 10.1126/science.aan4338.

[73] *GDML Userś Guide*. European Organization for Nuclear Research (CERN), 2.8 edition, May 2020. :https://gdml.web.cern.ch/GDML/doc/GDMLmanual.pdf.

[74] "European Southern Observatory". Schematic view of asteroid (25143) itokawa. :https://www.eso.org/public/images/eso1405a/, February 2014. Acknowledgement: JAXA.

[75] European Space Agency. International women's day: Esa promotes gender diversity for sustainable development. :https://www.esa.int/Enabling_Support/Preparing_for_the_Future/Space_for_Earth/International_Women_s_Day_ESA_promotes_gender_diversity_for_sustainable_development, March 2019.

[76] European Space Agency and Earth Observation Community. Earth observation portal - satellite missions database. `https://directory.eoportal.org/web/eoportal/satellite-missions`, 2020.

[77] Gianrico Filacchione, Olivier Groussin, Clémence Herny, David Kappel, Stefano Mottola, Nilda Oklay, Antoine Pommerol, Ian Wright, Zurine Yoldi, Mauro Ciarniello, Lyuba Moroz, and Andrea Raponi. Comet 67p/CG nucleus composition and comparison to other comets. *Space Science Reviews*, 215(1), feb 2019. doi: 10.1007/s11214-019-0580-3.

[78] Center for Near Earth Object Studies (CNEOS). Discovery statistics. https://cneos.jpl.nasa.gov/stats/totals.html, October 2020. Accessed on 2020.10.06.

[79] Center for Near Earth Object Studies (CNEOS). Discovery statistics. https://cneos.jpl.nasa.gov/stats/totals.html, October 2020. Accessed on 2020.10.06.

[80] Peter Fortescue, Graham Swinerd, and John Stark, editors. *Spacecraft Systems Engineering*. John Wiley & Sons Ltd., 4 edition, 2011.

[81] Leonor Frazao, S. Maddrell-Mander, C. Thomay, J. Velthuis, and C. Steer. Imaging and discrimination of high-z materials with muon scattering tomography. *Defence and Security Doctoral Symposium*, 2017. doi: 10.17862/CRANFIELD.RD.5589958.V1.

[82] Daniel Frisch. point2trimesh. MATLAB Central File Exchange :https://www.mathworks.com/matlabcentral/fileexchange/52882-point2trimesh-distance-between-point-and-triangulated-surface, September 2016.

[83] A. Fujiwara, J. Kawaguchi, D. K. Yeomans, M. Abe, T. Mukai, T. Okada, J. Saito, H. Yano, M. Yoshikawa, D. J. Scheeres, O. Barnouin-Jha, A. F. Cheng, H. Demura, R. W. Gaskell, N. Hirata, H. Ikeda, T. Kominato, H. Miyamoto, A. M. Nakamura, R. Nakamura, S. Sasaki, and K. Uesugi. The rubble-pile asteroid itokawa as observed by hayabusa. *Science*, 312(5778):1330–1334, jun 2006. doi: 10.1126/science.1125841.

[84] M. Galand, P. D. Feldman, D. Bockelée-Morvan, N. Biver, Y.-C. Cheng, G. Rinaldi, M. Rubin, K. Altwegg, J. Deca, A. Beth, P. Stephenson, K. L. Heritier, P. Henri, J. Wm. Parker, C. Carr, A. I. Eriksson, and J. Burch. Far-ultraviolet aurora identified at comet 67p/churyumov-gerasimenko. *Nature Astronomy*, sep 2020. doi: 10.1038/s41550-020-1171-7.

[85] R. Gaskell, J. Saito, M. Ishiguro, T. Kubota, T. Hashimoto, N. Hirata, S. Abe, O. Barnouin-Jha, and D. Scheeres. Gaskell itokawa shape model v1.0. hay-a-amica-5-itokawashape-v1.0. NASA Planetary Data System, :https://sbn.psi.edu/pds/resource/itokawashape.html, 2008.

[86] Robert Gaskell, Olivier Barnouin-Jha, Daniel Scheeres, T Mukai, Naru Hirata, Shinsuke Abe, Jun Saito, M Ishiguro, T Kubota, T Hashimoto, et al. Landmark navigation studies and target characterization in the hayabusa encounter with itokawa. In *AIAA/AAS Astrodynamics Specialist Conference and Exhibit*, page 6660, 2006.

[87] Geant4 Collaboration. Geant4 10.0 release notes. :http://geant4-data.web.cern.ch/geant4-data/ReleaseNotes/ReleaseNotes4.10.0.html, December 2013.

[88] Geant4 Collaboration. Physics reference manual. :https://indico.cern.ch/event/679723/contributions/2792554/attachments/1559217/2454299/PhysicsReferenceManual.pdf, December 2017.

[89] Geant4 Collaboration and National Institute for Standards and Technology. Geant4 material database. :http://geant4-userdoc.web.cern.ch/geant4-userdoc/UsersGuides/ForApplicationDeveloper/html/Appendix/materialNames.html, 2020.

[90] Donald S. Gemmell. Channeling and related effects in the motion of charged particles through crystals. *Reviews of Modern Physics*, 46(1):129–227, jan 1974. doi: 10.1103/revmodphys.46.129.

[91] EP George. Cosmic rays measure overburden of tunnel. *Commonwealth Engineer*, 455, 1955.

[92] Douglas C. Giancoli. *Physics Principles with Applications*, volume 1. Pearson, 7th edition, 2014. ISBN 0-321-62592-7.

[93] Kondo Gnanvo, Leonard V Grasso III, Marcus Hohlmann, Judson B Locke, Amilkar Quintero, and Debasis Mitra. Imaging of high-z material for nuclear contraband detection with a minimal prototype of a muon tomography station based on gem detectors. *Nuclear Instruments and Methods in Physics Research Section A: Accelerators, Spectrometers, Detectors and Associated Equipment*, 652(1):16–20, 2011.

[94] Jennifer A. Grier and Andrew S. Rivkin. Comparing sample and remote-sensing data—understanding surface composition. In *Airless Bodies of the Inner Solar System*, pages 95–119. Elsevier, 2019. doi: 10.1016/b978-0-12-809279-8.00005-6.

[95] Donald E. Groom, Nikolai V. Mokhov, and Sergei I. Striganov. Muon stopping power and range tables 10 mev-100 tev. *Atomic Data and Nuclear Data Tables*, 78(2):183–356, jul 2001. doi: 10.1006/adnd.2001.0861.

[96] Crater Analysis Techniques Working Group et al. Standard techniques for presentation and analysis of crater size-frequency data. *Icarus*, 37(2):467–474, 1979.

[97] Thomas Hales, Mark Adams, Gertrud Bauer, Tat Dat Dang, John Harrison, Hoang Le Truong, Cezary Kaliszyk, Victor Magron, Sean McLaughlin, Tat Thang Nguyen, et al. A formal proof of the kepler conjecture. 5, 2017.

[98] Hamamatsu Photonics K.K., Electron Tube Division. *micro PMT*. Hamamatsu Photonics K.K., 314-5, Shimokanza, Iwata City, Shizuoka Pref., 438-0193, Japan., tpmz1019e edition, February 2020. :https://www.hamamatsu.com/resources/pdf/etd/MicroPMT_TPMZ1019E.pdf.

[99] Bruce Hapke. Space weathering from mercury to the asteroid belt. *Journal of Geophysical Research: Planets*, 106(E5):10039–10073, may 2001. doi: 10.1029/2000je001338.

[100] Trent Hare. Platevertex2obj.py. GitHub :https://github.com/USGS-Astrogeology/GDAL_scripts/tree/master/PlateVertex2Obj, April 2013.

[101] L. Haser. Distribution d'intensité dans la tête d'une comète. *Bulletin de la Societe Royale des Sciences de Liege*, 43:740–750, January 1957.

[102] Thomas Hebbeker and Kerstin Hoepfner. Muon spectrometers. In *Handbook of Particle Detection and Imaging*, pages 473–496. Springer Berlin Heidelberg, 2012. doi: 10.1007/978-3-642-13271-1_19.

[103] A. Herique, B. Agnus, E. Asphaug, A. Barucci, P. Beck, J. Bellerose, J. Biele, L. Bonal, P. Bousquet, L. Bruzzone, C. Buck, I. Carnelli, A. Cheng, V. Ciarletti, M. Delbo, J. Du, X. Du, C. Eyraud, W. Fa, J. Gil Fernandez, O. Gassot, R. Granados-Alfaro, S.F. Green, B. Grieger, J.T. Grundmann, J. Grygorczuk, R. Hahnel, E. Heggy, T-M. Ho, O. Karatekin, Y. Kasaba, T. Kobayashi, W. Kofman, C. Krause, A. Kumamoto, M. Küppers, M. Laabs, C. Lange, J. Lasue, A.C. Levasseur-Regourd, A. Mallet, P. Michel, S. Mottola, N. Murdoch, M. Mütze, J. Oberst, R. Orosei, D. Plettemeier, S. Rochat, R. RodriguezSuquet, Y. Rogez, P. Schaffer, C. Snodgrass, J-C. Souyris, M. Tokarz, S. Ulamec, J-E. Wahlund, and S. Zine. Direct observations of asteroid interior and regolith structure: Science measurement requirements. *Advances in Space Research*, 62(8):2141–2162, oct 2018. doi: 10.1016/j.asr.2017.10.020.

[104] Alain Herique and Wlodek Kofman. Definition of the consert/rosetta radar performances. In *Proceedings of the CEOS SAR Workshop, Tokyo, Japan*, 2001.

[105] D. Heynderickx, B. Quaghebeur, E. Speelman, and E. Daly. ESA's space environment information system (SPENVIS) - a WWW interface to models of the space environment and its effects. In *38th Aerospace Sciences Meeting and Exhibit*. American Institute of Aeronautics and Astronautics, jan 2000. doi: 10.2514/6.2000-371.

[106] N. Hirata and M. Ishiguro. Properties and Possible Origin of Black Boulders on the Asteroid Itokawa. In *Lunar and Planetary Science Conference*, Lunar and Planetary Science Conference, page 1821, March 2011.

[107] Takahiro Hiroi, Masanao Abe, Kohei Kitazato, Shinsuke Abe, Beth E. Clark, Sho Sasaki, Masateru Ishiguro, and Olivier S. Barnouin-Jha. Developing space weathering on the asteroid 25143 itokawa. *Nature*, 443(7107):56–58, sep 2006. doi: 10.1038/nature05073.

[108] Steven R. Hirshorn, Linda D. Voss, and Linda K. Bromley. *NASA Systems Engineering Handbook: SP-2016-6105 Rev2*, volume 2. NASA Technical Report Server (NTRS), February 2017. :https://ntrs.nasa.gov/citations/20170001761.

[109] David Hodge. Asteroid muography: Design feasibility of a hodoscopic, spacecraft-based, detector intended for muon tomography of asteroid interiors. mathesis, Delft University of Technology, October 2018. `http://resolver.tudelft.nl/uuid:8fa057fc-10c3-4480-9441-4b00343b99b4`.

[110] Sven Holcombe. Growbubbles - maximum radius packing. MATLAB Central File Exchange :https://www.mathworks.com/matlabcentral/fileexchange/33213-growbubbles-maximum-radius-packing, October 2011.

[111] Sebastian Hollenberg and Palash B Pal. Cpt-violating effects in muon decay. *Physics Letters B*, 701(1): 89–92, 2011.

[112] K. Hong. Algorithms - uniform distribution of points on the surface of a sphere. :https://www.bogotobogo.com/Algorithms/uniform_distribution_sphere.php, March 2019.

[113] Gregory Hornby, Al Globus, Derek Linden, and Jason Lohn. Automated antenna design with evolutionary algorithms. In *Space 2006*. American Institute of Aeronautics and Astronautics, sep 2006. doi: 10.2514/6.2006-7242.

[114] F.Y. Hsu, W.F. Lee, C.J. Tung, J.S. Lee, T.H. Wu, S.M. Hsu, H.T. Su, and T.R. Chen. Ambient and personal dose assessment of a container inspection site using a mobile x-ray system. *Applied Radiation and Isotopes*, 70(3):456–461, mar 2012. doi: 10.1016/j.apradiso.2011.10.017.

[115] International Astronomical Union. Resolution b5: Definition of a planet in the solar system. `https://www.iau.org/static/resolutions/Resolution_GA26-5-6.pdf`, August 2006. IAU 2006 General Assembly.

[116] International Astronomical Union. Resolution b6: Pluto. `https://www.iau.org/static/resolutions/Resolution_GA26-5-6.pdf`, August 2006. IAU 2006 General Assembly.

[117] International Astronomical Union. Iau approves name of target of first nasa and esa planetary defence missions. Press Release: :https://www.iau.org/news/pressreleases/detail/iau2007/, June 2020.

[118] Eugene Jarosewich. Chemical analyses of meteorites: A compilation of stony and iron meteorite analyses. *Meteoritics*, 25(4):323–337, dec 1990. doi: 10.1111/j.1945-5100.1990.tb00717.x.

[119] Kyong Hwan Jin, Michael T. McCann, Emmanuel Froustey, and Michael Unser. Deep convolutional neural network for inverse problems in imaging. *IEEE Transactions on Image Processing*, 26(9):4509–4522, sep 2017. doi: 10.1109/tip.2017.2713099.

[120] Jkrieger. Scheme of a photomultiplier tube (pmt) in english. :https://en.m.wikipedia.org/wiki/File:Photomultiplier_schema_en.png, May 2007. Public Domain.

[121] L. Jorda, R. Gaskell, C. Capanna, S. Hviid, P. Lamy, J. Ďurech, G. Faury, O. Groussin, P. Gutiérrez, C. Jackman, S.J. Keihm, H.U. Keller, J. Knollenberg, E. Kührt, S. Marchi, S. Mottola, E. Palmer, F.P. Schloerb, H. Sierks, J.-B. Vincent, M.F. A'Hearn, C. Barbieri, R. Rodrigo, D. Koschny, H. Rickman, M.A. Barucci, J.L. Bertaux, I. Bertini, G. Cremonese, V. Da Deppo, B. Davidsson, S. Debei, M. De Cecco, S. Fornasier, M. Fulle, C. Güttler, W.-H. Ip, J.R. Kramm, M. Küppers, L.M. Lara, M. Lazzarin, J.J. Lopez Moreno, F. Marzari, G. Naletto, N. Oklay, N. Thomas, C. Tubiana, and K.-P. Wenzel. The global shape, density and rotation of comet 67p/churyumov-gerasimenko from preperihelion rosetta/OSIRIS observations. *Icarus*, 277:257–278, oct 2016. doi: 10.1016/j.icarus.2016.05.002.

[122] Kevin Jourde, Dominique Gibert, Jacques Marteau, Jean de Bremond d'Ars, and Jean-Christophe Komorowski. Muon dynamic radiography of density changes induced by hydrothermal activity at the la soufrière of guadeloupe volcano. *Scientific Reports*, 6(1), sep 2016. doi: 10.1038/srep33406.

[123] Masanori Kanamaru, Sho Sasaki, and Mark Wieczorek. Density distribution of asteroid 25143 itokawa based on smooth terrain shape. *Planetary and Space Science*, 174:32–42, sep 2019. doi: 10.1016/j.pss.2019.05.002.

[124] J. I. Katz. Scanning of vehicles for nuclear materials. AIP Publishing LLC, 2014. doi: 10.1063/1.4876473.

[125] Julian Keerl. Characterization of radiation in the proximity of smallcelestial bodies and the respective implication on muontomography in space. mathesis, Delft University of Technology, May 2020.

[126] Johannes Kepler. *Vom sechseckigen Schnee*, volume 273 of *Ostwalds Klassiker der Exakten Wissenschaften [Ostwald's Classics of the Exact Sciences]*. Akademische Verlagsgesellschaft Geest & Portig K.-G., Leipzig, 1987. ISBN 3-321-00021-0. Strena seu de Nive sexangula, Translated from the Latin and with an introduction and notes by Dorothea Goetz.

[127] V. Khachatryan, A.M. Sirunyan, A. Tumasyan, and et al. Measurement of the charge ratio of atmospheric muons with the CMS detector. *Physics Letters B*, 692(2):83–104, aug 2010. doi: 10.1016/j.physletb.2010.07.033.

[128] K. Kodama, N. Ushida, C. Andreopoulos, N. Saoulidou, G. Tzanakos, P. Yager, B. Baller, D. Boehnlein, W. Freeman, B. Lundberg, J. Morfin, R. Rameika, J.C. Yun, J.S. Song, C.S. Yoon, S.H. Chung, P. Berghaus, M. Kubantsev, N.W. Reay, R. Sidwell, N. Stanton, S. Yoshida, S. Aoki, T. Hara, J.T. Rhee, D. Ciampa, C. Erickson, M. Graham, K. Heller, R. Rusack, R. Schwienhorst, J. Sielaff, J. Trammell, J. Wilcox, K. Hoshino, H. Jiko, M. Miyanishi, M. Komatsu, M. Nakamura, T. Nakano, K. Niwa, N. Nonaka, K. Okada, O. Sato, T. Akdogan, V. Paolone, C. Rosenfeld, A. Kulik, T. Kafka, W. Oliver, T. Patzak, and J. Schneps. Observation of tau neutrino interactions. *Physics Letters B*, 504(3):218–224, apr 2001. doi: 10.1016/s0370-2693(01)00307-0.

[129] W. Kofman, A. Herique, Y. Barbin, J.-P. Barriot, V. Ciarletti, S. Clifford, P. Edenhofer, C. Elachi, C. Eyraud, J.-P. Goutail, E. Heggy, L. Jorda, J. Lasue, A.-C. Levasseur-Regourd, E. Nielsen, P. Pasquero, F. Preusker, P. Puget, D. Plettemeier, Y. Rogez, H. Sierks, C. Statz, H. Svedhem, I. Williams, S. Zine, and J. Van Zyl. Properties of the 67p/churyumov-gerasimenko interior revealed by CONSERT radar. *Science*, 349 (6247):aab0639–aab0639, jul 2015. doi: 10.1126/science.aab0639.

[130] Tobias Kramer and Matthias Noack. ON THE ORIGIN OF INNER COMA STRUCTURES OBSERVED BY ROSETTA DURING a DIURNAL ROTATION OF COMET 67p/CHURYUMOV–GERASIMENKO. *The Astrophysical Journal*, 823(1):L11, may 2016. doi: 10.3847/2041-8205/823/1/l11.

[131] Manfred Krammer and Winfried Mitaroff. Tracking detectors. In *Handbook of Particle Detection and Imaging*, pages 265–295. Springer Berlin Heidelberg, 2012. doi: 10.1007/978-3-642-13271-1_12.

[132] Annette Kur and Thomas Dreier. *European Intellectual Property Law*. Edward Elgar Publishing, 1 edition, 2013. ISBN 9781848448803.

[133] Commissariat à l'énergie atomique Saclay L. Chevalier. Muon detection. `https://indico.cern.ch/event/472305/contributions/1982405/attachments/1228365/1799493/Muon-I.pdf`, February 2016.

[134] California Institute of Technology Lance A. M. Benner, Jet Propulsion Laboratory. Near-earth asteroid delta-v for spacecraft rendezvous. `https://echo.jpl.nasa.gov/~lance/delta_v/delta_v.rendezvous.html`, January 2018.

[135] L.D. Landau. On the energy loss of fast particles by ionization. *USSR J. Phys*, 8:201–205, 1944.

[136] Caroline Lange, Jens Biele, Stephan Ulamec, Christian Krause, Barbara Cozzoni, Oliver Küchemann, Simon Tardivel, Tra-Mi Ho, Christian Grimm, Jan Thimo Grundmann, Elisabet Wejmo, Silvio Schröder, Michael Lange, Josef Reill, Alain Hérique, Yves Rogez, Dirk Plettemeier, Ian Carnelli, Andrés Galvez, Christian Philippe, Michael Küppers, Björn Grieger, Jesus Gil Fernandez, Jerzy Grygorczuk, Marta Tokarz, and Christian Ziach. MASCOT2 – a small body lander to investigate the interior of 65803 didymos′ moon in the frame of the AIDA/AIM mission. *Acta Astronautica*, 149:25–34, aug 2018. doi: 10.1016/j.actaastro.2018.05.013.

[137] Michael Lange, Christian Hühne, Caroline Lange, and Olaf Mierheim. A trade-off study on the mechanical support structure of the mascot-2 small body lander package. 2017.

[138] L. M. Lara, S. Lowry, J.-B. Vincent, P. J. Gutiérrez, A. Rożek, F. La Forgia, N. Oklay, H. Sierks, C. Barbieri, P. L. Lamy, R. Rodrigo, D. Koschny, H. Rickman, H. U. Keller, J. Agarwal, A.-T. Auger, M. F. A'Hearn, M. A. Barucci, J.-L. Bertaux, I. Bertini, S. Besse, D. Bodewits, G. Cremonese, B. Davidsson, V. Da Deppo, S. Debei, M. De Cecco, M. R. El-Maarry, F. Ferri, S. Fornasier, M. Fulle, O. Groussin, P. Gutiérrez–Marques, C. Güttler, S. F. Hviid, W.-H. Ip, L. Jorda, J. Knollenberg, G. Kovacs, J.-R. Kramm, E. Kührt, M. Küppers, M. Lazzarin, Z.-Y. Lin, J. J. López-Moreno, S. Magrin, F. Marzari, H. Michalik, R. Moissl–Fraund,

F. Moreno, S. Mottola, G. Naletto, M. Pajola, A. Pommerol, N. Thomas, M. D. Sabau, and C. Tubiana. Large-scale dust jets in the coma of 67p/churyumov-gerasimenko as seen by the OSIRIS instrument onboard rosetta. *Astronomy & Astrophysics*, 583:A9, oct 2015. doi: 10.1051/0004-6361/201526103.

[139] D. S. Lauretta, S. S. Balram-Knutson, E. Beshore, W. V. Boynton, C. Drouet d'Aubigny, D. N. DellaGiustina, H. L. Enos, D. R. Golish, C. W. Hergenrother, E. S. Howell, C. A. Bennett, E. T. Morton, M. C. Nolan, B. Rizk, H. L. Roper, A. E. Bartels, B. J. Bos, J. P. Dworkin, D. E. Highsmith, D. A. Lorenz, L. F. Lim, R. Mink, M. C. Moreau, J. A. Nuth, D. C. Reuter, A. A. Simon, E. B. Bierhaus, B. H. Bryan, R. Ballouz, O. S. Barnouin, R. P. Binzel, W. F. Bottke, V. E. Hamilton, K. J. Walsh, S. R. Chesley, P. R. Christensen, B. E. Clark, H. C. Connolly, M. K. Crombie, M. G. Daly, J. P. Emery, T. J. McCoy, J. W. McMahon, D. J. Scheeres, S. Messenger, K. Nakamura-Messenger, K. Righter, and S. A. Sandford. OSIRIS-REx: Sample return from asteroid (101955) bennu. *Space Science Reviews*, 212(1-2):925–984, aug 2017. doi: 10.1007/s11214-017-0405-1.

[140] D. S. Lauretta, , D. N. DellaGiustina, C. A. Bennett, D. R. Golish, K. J. Becker, S. S. Balram-Knutson, O. S. Barnouin, T. L. Becker, W. F. Bottke, W. V. Boynton, H. Campins, B. E. Clark, H. C. Connolly, C. Y. Drouet d'Aubigny, J. P. Dworkin, J. P. Emery, H. L. Enos, V. E. Hamilton, C. W. Hergenrother, E. S. Howell, M. R. M. Izawa, H. H. Kaplan, M. C. Nolan, B. Rizk, H. L. Roper, D. J. Scheeres, P. H. Smith, K. J. Walsh, and C. W. V. Wolner. The unexpected surface of asteroid (101955) bennu. *Nature*, 568(7750):55–60, mar 2019. doi: 10.1038/s41586-019-1033-6.

[141] Dante S Lauretta and Harry Y McSween. *Meteorites and the early solar system II*. University of Arizona Press, 2006.

[142] Xi-zhi Li, René Weller, and Gabriel Zachmann. Astrogen–procedural generation of highly detailed asteroid models. In *2018 15th International Conference on Control, Automation, Robotics and Vision (ICARCV)*, pages 1771–1778. IEEE, 2018.

[143] J.J. Lissauer and I. de Pater. *Fundamental planetary science: Physics, chemistry and habitability*. Cambridge University Press, 32 Avenue of the Americas, New York, September 2013. ISBN 9780521618557.

[144] S. Lowry, S. R. Duddy, B. Rozitis, S. F. Green, A. Fitzsimmons, C. Snodgrass, H. H. Hsieh, and O. Hainaut. The nucleus of comet 67p/churyumov-gerasimenko. *Astronomy & Astrophysics*, 548:A12, nov 2012. doi: 10.1051/0004-6361/201220116.

[145] S. C. Lowry, P. R. Weissman, S. R. Duddy, B. Rozitis, A. Fitzsimmons, S. F. Green, M. D. Hicks, C. Snodgrass, S. D. Wolters, S. R. Chesley, J. Pittichova, and P. van Oers. The internal structure of asteroid (25143) itokawa as revealed by detection of YORP spin-up. *Astronomy & Astrophysics*, 562:A48, feb 2014. doi: 10.1051/0004-6361/201322602.

[146] Matthew Lawrence Lund. High-performing simulations of the space radiation environment for the international space station and apollo missions. mathesis, Department of Civil and Environmental Engineering, University of Utah, May 2016.

[147] R. Marschall, L. Rezac, D. Kappel, C.C. Su, S.-B. Gerig, M. Rubin, O. Pinzón-Rodríguez, D. Marshall, Y. Liao, C. Herny, G. Arnold, C. Christou, S.K. Dadzie, O. Groussin, P. Hartogh, L. Jorda, E. Kührt, S. Mottola, O. Mousis, F. Preusker, F. Scholten, P. Theologou, J.-S. Wu, K. Altwegg, R. Rodrigo, and N. Thomas. A comparison of multiple rosetta data sets and 3d model calculations of 67p/churyumov-gerasimenko coma around equinox (may 2015). *Icarus*, 328:104–126, aug 2019. doi: 10.1016/j.icarus.2019.02.008.

[148] Raphael Marschall, Johannes Markkanen, Selina-Barbara Gerig, Olga Pinzón-Rodríguez, Nicolas Thomas, and Jong-Shinn Wu. The dust-to-gas ratio, size distribution, and dust fall-back fraction of comet 67p/churyumov-gerasimenko: Inferences from linking the optical and dynamical properties of the inner comae. *Frontiers in Physics*, 8, jun 2020. doi: 10.3389/fphy.2020.00227.

[149] J Marteau, D Gibert, N Lesparre, F Nicollin, P Noli, and F Giacoppo. Muons tomography applied to geosciences and volcanology. *Nuclear Instruments and Methods in Physics Research Section A: Accelerators, Spectrometers, Detectors and Associated Equipment*, 695:23–28, 2012.

[150] F. Marzari, A. Rossi, and D.J. Scheeres. Combined effect of YORP and collisions on the rotation rate of small main belt asteroids. *Icarus*, 214(2):622–631, aug 2011. doi: 10.1016/j.icarus.2011.05.033.

[151] R. A. Masterson, M. Chodas, L. Bayley, B. Allen, J. Hong, P. Biswas, C. McMenamin, K. Stout, E. Bokhour, H. Bralower, D. Carte, S. Chen, M. Jones, S. Kissel, F. Schmidt, M. Smith, G. Sondecker, L. F. Lim, D. S. Lauretta, J. E. Grindlay, and R. P. Binzel. Regolith x-ray imaging spectrometer (REXIS) aboard the OSIRIS-REx asteroid sample return mission. *Space Science Reviews*, 214(1), feb 2018. doi: 10.1007/s11214-018-0483-8.

[152] MATLAB. *version 8.6.0.267246 (R2015b)*. The MathWorks Inc., Natick, Massachusetts, August 2015.

[153] Soko Matsumura, Derek C. Richardson, Patrick Michel, Stephen R. Schwartz, and Ronald-Louis Ballouz. The brazil nut effect and its application to asteroids. *Monthly Notices of the Royal Astronomical Society*, 443(4):3368–3380, aug 2014. doi: 10.1093/mnras/stu1388.

[154] Clara Maurel, Ronald-Louis Ballouz, Derek C. Richardson, Patrick Michel, and Stephen R. Schwartz. Numerical simulations of oscillation-driven regolith motion: Brazil-nut effect. *Monthly Notices of the Royal Astronomical Society*, 464(3):2866–2881, oct 2016. doi: 10.1093/mnras/stw2641.

[155] S. Mazrouei, M.G. Daly, O.S. Barnouin, C.M. Ernst, and I. DeSouza. Block distributions on itokawa. *Icarus*, 229:181–189, feb 2014. doi: 10.1016/j.icarus.2013.11.010.

[156] Mdf. The inner solar system, from the sun to jupiter. [rendering]. `https://commons.wikimedia.org/wiki/File:InnerSolarSystem-en.png`, September 2006. Public Domain.

[157] Merriam-Webster.com Dictionary. "opportunity". :https://www.merriam-webster.com/dictionary/opportunity, December 2020. Accessed Dec 2020.

[158] Patrick Michel, Michael Küppers, and Ian Carnelli. The hera mission: European component of the esa-nasa aida mission to a binary asteroid. In *42nd COSPAR Scientific Assembly*, volume 42, pages B1.1–42–18, Jul 2018.

[159] Tatsuhiro Michikami, Akiko M. Nakamura, Naru Hirata, Robert W. Gaskell, Ryosuke Nakamura, Takayuki Honda, Chikatoshi Honda, Kensuke Hiraoka, Jun Saito, Hirohide Demura, Masateru Ishiguro, and Hideaki Miyamoto. Size-frequency statistics of boulders on global surface of asteroid 25143 itokawa. *Earth, Planets and Space*, 60(1):13–20, jan 2008. doi: 10.1186/bf03352757.

[160] Tatsuhiro Michikami, Axel Hagermann, Tokiyuki Kadokawa, Akifumi Yoshida, Akira Shimada, Sunao Hasegawa, and Akira Tsuchiyama. Fragment shapes in impact experiments ranging from cratering to catastrophic disruption. *Icarus*, 264:316–330, jan 2016. doi: 10.1016/j.icarus.2015.09.038.

[161] MissMJ. Standard model of elementary particles: the 12 fundamental fermions and 5 fundamental bosons. `https://upload.wikimedia.org/wikipedia/commons/0/00/Standard_Model_of_Elementary_Particles.svg`, June 2006. Public Domain.

[162] Haruo Miyadera. Next step for fukushima daiichi muon tomography. August 2012.

[163] Haruo Miyadera, Konstantin N Borozdin, Steve J Greene, Zarija Lukić, Koji Masuda, Edward C Milner, Christopher L Morris, and John O Perry. Imaging fukushima daiichi reactors with muons. *Aip Advances*, 3(5):052133, 2013.

[164] H. Miyamoto, H. Yano, D. J. Scheeres, S. Abe, O. Barnouin-Jha, A. F. Cheng, H. Demura, R. W. Gaskell, N. Hirata, M. Ishiguro, T. Michikami, A. M. Nakamura, R. Nakamura, J. Saito, and S. Sasaki. Regolith migration and sorting on asteroid itokawa. *Science*, 316(5827):1011–1014, may 2007. doi: 10.1126/science.1134390.

[165] Kunihiro Morishima, Mitsuaki Kuno, Akira Nishio, Nobuko Kitagawa, Yuta Manabe, Masaki Moto, Fumihiko Takasaki, Hirofumi Fujii, Kotaro Satoh, Hideyo Kodama, et al. Discovery of a big void in khufu's pyramid by observation of cosmic-ray muons. *Nature*, 552(7685):386, 2017.

[166] CL Morris, CC Alexander, JD Bacon, KN Borozdin, DJ Clark, R Chartrand, CJ Espinoza, AM Fraser, MC Galassi, JA Green, et al. Tomographic imaging with cosmic ray muons. *Science & Global Security*, 16(1-2):37–53, 2008.

[167] H. Motz and L. I. Schiff. Cherenkov radiation in a dispersive medium. *American Journal of Physics*, 21 (4):258–259, apr 1953. doi: 10.1119/1.1933417.

[168] E. Musk. The mission of tesla. :https://www.tesla.com/blog/mission-tesla, November 2013.

[169] Matthias E. Möbius, Benjamin E. Lauderdale, Sidney R. Nagel, and Heinrich M. Jaeger. Size separation of granular particles. *Nature*, 414(6861):270–270, nov 2001. doi: 10.1038/35104697.

[170] Tomas Möller and Ben Trumbore. Fast, minimum storage ray-triangle intersection. *Journal of Graphics Tools*, 2(1):21–28, jan 1997. doi: 10.1080/10867651.1997.10487468.

[171] T. Nakamura, T. Noguchi, M. Tanaka, M. E. Zolensky, M. Kimura, A. Tsuchiyama, A. Nakato, T. Ogami, H. Ishida, M. Uesugi, T. Yada, K. Shirai, A. Fujimura, R. Okazaki, S. A. Sandford, Y. Ishibashi, M. Abe, T. Okada, M. Ueno, T. Mukai, M. Yoshikawa, and J. Kawaguchi. Itokawa dust particles: A direct link between s-type asteroids and ordinary chondrites. *Science*, 333(6046):1113–1116, aug 2011. doi: 10.1126/science.1207758.

[172] NASA, ESA, STScI, H. Weaver, and E. Smith. Panoramic picture of comet p/shoemaker-levy 9. :https://hubblesite.org/contents/media/images/1994/26/168-Image.html?news=true, July 1994.

[173] NASA/JPL-Caltech. Oort cloud and scale of the solar system. (pia22921) [infographic]. `https://photojournal.jpl.nasa.gov/catalog/PIA22921`, December 2018.

[174] M. Neugebauer, G. Gloeckler, J. T. Gosling, A. Rees, R. Skoug, B. E. Goldstein, T. P. Armstrong, M. R. Combi, T. Makinen, D. J. McComas, R. von Steiger, T. H. Zurbuchen, E. J. Smith, J. Geiss, and L. J. Lanzerotti. Encounter of the ulysses spacecraft with the ion tail of comet mcnaught. *The Astrophysical Journal*, 667(2):1262–1266, oct 2007. doi: 10.1086/521019.

[175] S Nishihara, M Abe, S Hasegawa, M Ishiguro, K Kitazato, N Miura, H Nonaka, Y Ohba, M Okyudo, T Ozawa, et al. Ground-based lightcurve observation of (25143) itokawa, 2001/2004, lunar planet. In *Sci. Conf. XXXVI, abstr*, volume 2005, 1833.

[176] R.A. Nymmik, M.I. Panasyuk, T.I. Pervaja, and A.A. Suslov. A model of galactic cosmic ray fluxes. *International Journal of Radiation Applications and Instrumentation. Part D. Nuclear Tracks and Radiation Measurements*, 20(3):427–429, jul 1992. doi: 10.1016/1359-0189(92)90028-t.

[177] R.A Nymmik, M.I Panasyuk, and A.A Suslov. Galactic cosmic ray flux simulation and prediction. *Advances in Space Research*, 17(2):19–30, jan 1996. doi: 10.1016/0273-1177(95)00508-c.

[178] C. Patrignani, et al., and Particle Data Group. Review of particle physics. *Chinese Physics C*, 40(10): 100001, oct 2016. doi: 10.1088/1674-1137/40/10/100001. (Particle Data Group).

[179] Gene Mosca Paul A. Tipler. *Physics for Scientists and Engineers with Modern Physics*, volume Extended, chapter 41, page 1405. Susan Finnemore Brennan, 6 edition, 2008.

[180] Viranga Perera, Alan P. Jackson, Erik Asphaug, and Ronald-Louis Ballouz. The spherical brazil nut effect and its significance to asteroids. *Icarus*, 278:194–203, nov 2016. doi: 10.1016/j.icarus.2016.06.014.

[181] M. L. Perl, G. S. Abrams, A. M. Boyarski, M. Breidenbach, D. D. Briggs, F. Bulos, W. Chinowsky, J. T. Dakin, G. J. Feldman, C. E. Friedberg, D. Fryberger, G. Goldhaber, G. Hanson, F. B. Heile, B. Jean-Marie, J. A. Kadyk, R. R. Larsen, A. M. Litke, D. Lüke, B. A. Lulu, V. Lüth, D. Lyon, C. C. Morehouse, J. M. Paterson, F. M. Pierre, T. P. Pun, P. A. Rapidis, B. Richter, B. Sadoulet, R. F. Schwitters, W. Tanenbaum, G. H. Trilling, F. Vannucci, J. S. Whitaker, F. C. Winkelmann, and J. E. Wiss. Evidence for anomalous lepton production in e^+ - e^- annihilation. *Physical Review Letters*, 35(22):1489–1492, dec 1975. doi: 10.1103/physrevlett.35.1489.

[182] Jeffrey Plescia. Seismic exploration of small bodies. techreport, National Aeronautics and Space Administration, March 2016. NASA Innovative Advanced Concepts (NIAC) Phase I.

[183] L.A. McFadden P.R. Weissman, M.F. A'Hearn and H. Rickman. *Asteroids III*, volume 1, chapter Evolution of comets into asteroids, page 669. University of Arizona Press, Tucson, 2002.

[184] Petr Pravec and Alan W Harris. Fast and slow rotation of asteroids. *Icarus*, 148(1):12–20, 2000.

[185] T. H. Prettyman, L. S. Pinsky, A. Empl, R. S. Miller, M. V. Sykes, S. L. Koontz, M. C. Nolan, D. J. Lawrence, D. W. Mittlefehldt, and B. D. Redell. Muon vision for planetary geology: A look inside asteroids, comets and surface features. `https://www.lpi.usra.edu/sbag/meetings/jun2016/presentations/prettyman.pdf`, June 2016.

[186] T.H. Prettyman, S. Koontz, L. Pinsky, A. Empl, D.W. Mittlefehldt, B. Reddell, and M. Sykes. Deep mapping of small solar system bodies with galactic cosmic ray secondary particle showers. techreport, May 2014.

[187] Thomas H Prettyman, A Empl, LS Pinsky, MV Sykes, and MC Nolan. Deep mapping of small solar system bodies with galactic cosmic ray secondary particle showers. 2019.

[188] Fred Reines and Clyde Cowan. The reines-cowan experiments: detecting the poltergeist. *Los Alamos Sci.*, 25:4–27, 1997.

[189] Frederick Reines and Clyde L. Cowan. The neutrino. *Nature*, 178(4531):446–449, sep 1956. doi: 10.1038/178446a0.

[190] D. C. Reuter, A. A. Simon, J. Hair, A. Lunsford, S. Manthripragada, V. Bly, B. Bos, C. Brambora, E. Caldwell, G. Casto, Z. Dolch, P. Finneran, D. Jennings, M. Jhabvala, E. Matson, M. McLelland, W. Roher, T. Sullivan, E. Weigle, Y. Wen, D. Wilson, and D. S. Lauretta. The OSIRIS-REx visible and InfraRed spectrometer (OVIRS): Spectral maps of the asteroid bennu. *Space Science Reviews*, 214(2), mar 2018. doi: 10.1007/s11214-018-0482-9.

[191] D Richardson. Direct large-scale n-body simulations of planetesimal dynamics. *Icarus*, 143(1):45–59, jan 2000. doi: 10.1006/icar.1999.6243.

[192] Derek C. Richardson, William F. Bottke, and Stanley G. Love. Tidal distortion and disruption of earth-crossing asteroids. *Icarus*, 134(1):47–76, jul 1998. doi: 10.1006/icar.1998.5954.

[193] Derek C Richardson, Zoe M Leinhardt, HJ Melosh, WF Bottke Jr, Erik Asphaug, et al. *Asteroids III*, volume 1, chapter Gravitational Aggregates: Evidence and Evolution, pages 501–515. University of Arizona Press, Tucson, 2002.

[194] Derek C. Richardson, Kevin J. Walsh, Naomi Murdoch, and Patrick Michel. Numerical simulations of granular dynamics: I. hard-sphere discrete element method and tests. *Icarus*, 212(1):427–437, mar 2011. doi: 10.1016/j.icarus.2010.11.030.

[195] A.V. Rodionov and J.-F. Crifo. Time-dependent, three-dimensional fluid model of the outer coma, with application to the comet hale-bopp gas spirals. *Advances in Space Research*, 38(9):1923–1927, jan 2006. doi: 10.1016/j.asr.2006.03.019.

[196] AV Rodionov, J-F Crifo, K Szegő, J Lagerros, and M Fulle. An advanced physical model of cometary activity. *Planetary and space science*, 50(10-11):983–1024, 2002.

[197] Léna Le Roy, Kathrin Altwegg, Hans Balsiger, Jean-Jacques Berthelier, Andre Bieler, Christelle Briois, Ursina Calmonte, Michael R. Combi, Johan De Keyser, Frederik Dhooghe, Björn Fiethe, Stephen A. Fuselier, Sébastien Gasc, Tamas I. Gombosi, Myrtha Hässig, Annette Jäckel, Martin Rubin, and Chia-Yu Tzou. Inventory of the volatiles on comet 67p/churyumov-gerasimenko from rosetta/ROSINA. *Astronomy & Astrophysics*, 583:A1, oct 2015. doi: 10.1051/0004-6361/201526450.

[198] J. Saito, H. Miyamoto, R. Nakamura, M. Ishiguro, T. Michikami, A. M. Nakamura, H. Demura, S. Sasaki, N. Hirata, C. Honda, A. Yamamoto, Y. Yokota, T. Fuse, F. Yoshida, D. J. Tholen, R. W. Gaskell, T. Hashimoto, T. Kubota, Y. Higuchi, T. Nakamura, P. Smith, K. Hiraoka, T. Honda, S. Kobayashi, M. Furuya, N. Matsumoto, E. Nemoto, A. Yukishita, K. Kitazato, B. Dermawan, A. Sogame, J. Terazono, C. Shinohara, and H. Akiyama. Detailed images of asteroid 25143 itokawa from hayabusa. *Science*, 312(5778):1341–1344, jun 2006. doi: 10.1126/science.1125722.

[199] Giovanni Santin and ESA / ESTEC. Geant 4: Normalisation modelling sources. :http://geant4.in2p3.fr/2007/prog/GiovanniSantin/GSantin_Geant4_Paris07_Normalisation_v07.pdf, June 2007.

[200] Paul Sava and Erik Asphaug. 3d radar wavefield tomography of comet interiors. *Advances in Space Research*, 61(8):2198–2213, apr 2018. doi: 10.1016/j.asr.2018.01.040.

[201] D.J. Scheeres, M. Abe, M. Yoshikawa, R. Nakamura, R.W. Gaskell, and P.A. Abell. The effect of YORP on itokawa. *Icarus*, 188(2):425–429, jun 2007. doi: 10.1016/j.icarus.2006.12.014.

[202] Petr Scheirich. Asteroid (and comet) groups. :http://sajri.astronomy.cz/asteroidgroups/groups.htm, April 2005.

[203] Paul M. Schenk, Erik Asphaug, William B. McKinnon, H.J. Melosh, and Paul R. Weissman. Cometary nuclei and tidal disruption: The geologic record of crater chains on callisto and ganymede. *Icarus*, 121 (2):249–274, jun 1996. doi: 10.1006/icar.1996.0084.

[204] L.J. Schultz, K.N. Borozdin, J.J. Gomez, G.E. Hogan, J.A. McGill, C.L. Morris, W.C. Priedhorsky, A. Saunders, and M.E. Teasdale. Image reconstruction and material z discrimination via cosmic ray muon radiography. *Nuclear Instruments and Methods in Physics Research Section A: Accelerators, Spectrometers, Detectors and Associated Equipment*, 519(3):687–694, mar 2004. doi: 10.1016/j.nima.2003.11.035.

[205] Peter Shearer. A brief history of seismology. `https://earthquake.usgs.gov/static/lfs/nshm/workshops/thailand2007/CSMpp1_History.pdf`, 2007. Cambridge University Press.

[206] Troy Shinbrot, Tapan Sabuwala, Theo Siu, Miguel Vivar Lazo, and Pinaki Chakraborty. Size sorting on the rubble-pile asteroid itokawa. *Physical Review Letters*, 118(11), mar 2017. doi: 10.1103/physrevlett.118.111101.

[207] Frank H. Shu. *The physical universe: an introduction to astronomy*. University science books, 55D Gate Five Road, Sausalito, CA 94965, 1982. ISBN 0-935702-05-9.

[208] H. Sierks, C. Barbieri, P. L. Lamy, R. Rodrigo, D. Koschny, H. Rickman, H. U. Keller, J. Agarwal, M. F. A'Hearn, F. Angrilli, A.-T. Auger, M. A. Barucci, J.-L. Bertaux, I. Bertini, S. Besse, D. Bodewits, C. Capanna, G. Cremonese, V. Da Deppo, B. Davidsson, S. Debei, M. De Cecco, F. Ferri, S. Fornasier, M. Fulle, R. Gaskell, L. Giacomini, O. Groussin, P. Gutierrez-Marques, P. J. Gutierrez, C. Guttler, N. Hoekzema, S. F. Hviid, W.-H. Ip, L. Jorda, J. Knollenberg, G. Kovacs, J. R. Kramm, E. Kuhrt, M. Kuppers, F. La Forgia, L. M. Lara, M. Lazzarin, C. Leyrat, J. J. Lopez Moreno, S. Magrin, S. Marchi, F. Marzari, M. Massironi, H. Michalik, R. Moissl, S. Mottola, G. Naletto, N. Oklay, M. Pajola, M. Pertile, F. Preusker, L. Sabau, F. Scholten, C. Snodgrass, N. Thomas, C. Tubiana, J.-B. Vincent, K.-P. Wenzel, M. Zaccariotto, and M. Patzold. On the nucleus structure and activity of comet 67p/churyumov-gerasimenko. *Science*, 347(6220):aaa1044–aaa1044, jan 2015. doi: 10.1126/science.aaa1044.

[209] Steven W. Smith. *Digital Signal Processing: A Practical Guide for Engineers and Scientists*. Newnes: An imprint of Elsevier Science, 2013. ISBN 0-750674-44-X.

[210] Spacecraft 101. Satellite library. :https://spaceflight101.com/spacecraft/dawn-spacecraft-mission-overview/, November 2020.

[211] Splarka. An example of phosphorescence. europium doped strontium silicate-aluminate oxide powder (cyan pigmented). shown under visible light, long-wave uv light, and in total darkness. `https://commons.wikimedia.org/wiki/File:Phosphorescent.jpg`, August 2005. Public Domain.

[212] Abhishek Srinivas, Rene Weller, and Gabriel Zachmann. Fast and accurate simulation of gravitational field of irregular-shaped bodies using polydisperse sphere packings. In *ICAT-EGVE*, pages 213–220, 2017.

[213] J. Street and E. Stevenson. New evidence for the existence of a particle of mass intermediate between the proton and electron. *Physical Review*, 52(9):1003–1004, nov 1937. doi: 10.1103/physrev.52.1003.

[214] SysML Partners. Sysml open source project. :https://sysml.org/, November 2020.

[215] Hiroyuki KM Tanaka, Hideaki Taira, Tomihisa Uchida, Manobu Tanaka, Minoru Takeo, Takao Ohminato, Yosuke Aoki, Ryuichi Nishitama, Daigo Shoji, and Hiroshi Tsuiji. Three-dimensional computational axial tomography scan of a volcano with cosmic ray muon radiography. *Journal of Geophysical Research: Solid Earth*, 115(B12), 2010.

[216] Valeriy Tenishev, Michael Combi, and Björn Davidsson. A global kinetic model for cometary comae: The evolution of the coma of the rosetta target comet churyumov-gerasimenko throughout the mission. *The Astrophysical Journal*, 685(1):659–677, sep 2008. doi: 10.1086/590376. URL `https://doi.org/10.1086%2F590376`.

[217] Tsuyoshi Terai, Jun Takahashi, and Yoichi Itoh. High ecliptic latitude survey for small main-belt asteroids. *The Astronomical Journal*, 146(5):111, sep 2013. doi: 10.1088/0004-6256/146/5/111.

[218] Jörn Teuber, René Weller, Gabriel Zachmann, and Stefan Guthe. Fast sphere packings with adaptive grids on the gpu. *GI AR/VRWorkshop*, 4, 2013.

[219] P. C. Thomas and Mark S. Robinson. Seismic resurfacing by a single impact on the asteroid 433 eros. *Nature*, 436(7049):366–369, jul 2005. doi: 10.1038/nature03855.

[220] Elisa Resconi Thomas K. Gaisser, Ralph Engel. *Cosmic Rays and Particle Physics*. Cambridge University Press, second edition edition, 2016. ISBN 978-0-521-01646-9.

[221] J. J. Thomson. XL. cathode rays. *The London, Edinburgh, and Dublin Philosophical Magazine and Journal of Science*, 44(269):293–316, oct 1897. doi: 10.1080/14786449708621070.

[222] Maxim Titov. Gaseous detectors. In *Handbook of Particle Detection and Imaging*, pages 239–264. Springer Berlin Heidelberg, 2012. doi: 10.1007/978-3-642-13271-1_11.

[223] Yung-Su Tsai. Decay correlations of heavy leptons in $e^+ + e^- \rightarrow l^+ + l^-$. *Physical Review D*, 4(9):2821–2837, nov 1971. doi: 10.1103/physrevd.4.2821.

[224] P. Tsou. Wild 2 and interstellar sample collection and earth return. *Journal of Geophysical Research*, 108 (E10), 2003. doi: 10.1029/2003je002109.

[225] A. Tsuchiyama, M. Uesugi, T. Matsushima, T. Michikami, T. Kadono, T. Nakamura, K. Uesugi, T. Nakano, S. A. Sandford, R. Noguchi, T. Matsumoto, J. Matsuno, T. Nagano, Y. Imai, A. Takeuchi, Y. Suzuki, T. Ogami, J. Katagiri, M. Ebihara, T. R. Ireland, F. Kitajima, K. Nagao, H. Naraoka, T. Noguchi, R. Okazaki, H. Yurimoto, M. E. Zolensky, T. Mukai, M. Abe, T. Yada, A. Fujimura, M. Yoshikawa, and J. Kawaguchi. Three-dimensional structure of hayabusa samples: Origin and evolution of itokawa regolith. *Science*, 333(6046):1125–1128, aug 2011. doi: 10.1126/science.1207807.

[226] TU Delft Faculty of Technology, Policy and Management. Mot9611 - project entrepreneurship thesis related - description. `https://brightspace.tudelft.nl/d2l/le/content/45304/viewContent/1609149/View`, 2018.

[227] Jarek Tuszynski. in_polyhedron. MATLAB Central File Exchange :https://www.mathworks.com/matlabcentral/fileexchange/48041-in_polyhedron, August 2018.

[228] V. Uzhinsky. String models for (fast) pedestrians. :https://indico.cern.ch/event/27302/contributions/615516/, February 2008.

[229] Stefaan Van Wal, Simon Tardivel, and Daniel Scheeres. Parametric study of ballistic lander deployment to small bodies. *Journal of Spacecraft and Rockets*, 54(6):1330–1355, nov 2017. doi: 10.2514/1.a33832.

[230] K Walsh and D Richardson. Binary near-earth asteroid formation: Rubble pile model of tidal disruptions. *Icarus*, 180(1):201–216, jan 2006. doi: 10.1016/j.icarus.2005.08.015.

[231] Brian D. Warner, Alan W. Harris, and Petr Pravec. The asteroid lightcurve database. *Icarus*, 202(1): 134–146, jul 2009. doi: 10.1016/j.icarus.2009.02.003.

[232] S. Watanabe, M. Hirabayashi, N. Hirata, and et al. Hayabusa2 arrives at the carbonaceous asteroid 162173 ryugu - a spinning top - shaped rubble pile. *Science*, 364(6437):268–272, April 2019. doi: 10.1126/science.aav8032.

[233] James R Wertz, David F Everett, and Jeffery J Puschell, editors. *Space mission engineering: the new SMAD*. Microcosm Press, 2011.

[234] David R. Williams. Nasa space science data coordinated archive. :https://nssdc.gsfc.nasa.gov/, September 2018.

[235] H. Yano, T. Kubota, H. Miyamoto, T. Okada, D. Scheeres, Y. Takagi, K. Yoshida, M. Abe, S. Abe, O. Barnouin-Jha, A. Fujiwara, S. Hasegawa, T. Hashimoto, M. Ishiguro, M. Kato, J. Kawaguchi, T. Mukai, J. Saito, S. Sasaki, and M. Yoshikawa. Touchdown of the hayabusa spacecraft at the muses sea on itokawa. *Science*, 312(5778):1350–1353, jun 2006. doi: 10.1126/science.1126164.

[236] D. K. Yeomans. Radio science results during the NEAR-shoemaker spacecraft rendezvous with eros. *Science*, 289(5487):2085–2088, sep 2000. doi: 10.1126/science.289.5487.2085.

[237] T Yoshimitsu, S Sasaki, M Yanagisawa, and T Kubota. Scientific capability of minerva rover in hayabusa asteroid mission. *LPI*, page 1517, 2004.

[238] Hideki Yukawa. On the interaction of elementary particles. *Proceedings of the Physico-Mathematical Society of Japan. 3rd Series*, 17:48–57, 1935.

[239] V. V. Zakharov, J.-F. Crifo, A.V. Rodionov, M. Rubin, and K. Altwegg. The near-nucleus gas coma of comet 67p/churyumov-gerasimenko prior to the descent of the surface lander PHILAE. *Astronomy & Astrophysics*, 618:A71, oct 2018. doi: 10.1051/0004-6361/201832883.

[240] F. Zappa, S. Tisa, A. Tosi, and S. Cova. Principles and features of single-photon avalanche diode arrays. *Sensors and Actuators A: Physical*, 140(1):103–112, oct 2007. doi: 10.1016/j.sna.2007.06.021.

[241] Yun Zhang and Patrick Michel. Tidal distortion and disruption of rubble-pile bodies revisited. *Astronomy & Astrophysics*, 640:A102, aug 2020. doi: 10.1051/0004-6361/202037856.